2021 Midwest American Society of Biomechanics Regional Meeting

CHMS
Center for Human-Machine Systems
chms.csuohio.edu

Cleveland State University

September 16-17th Cleveland, Ohio

engineering.csuohio.edu/midwestasb2021/midwest-american-society-biomechanics-conference

CHMS

This meeting is hosted by the Center for Human-Machine Systems (CHMS).

The Center for Human-Machine Systems is a consortium of Cleveland State University labs with the aim of improving human-machine systems by combining the unique capabilities of the engineered and natural subsystems. The center provides its members a synergistic environment and resources to promote the development of high-quality, well-funded, and high-impact research projects. http://chms.csuohio.edu/

Location

Cleveland State University
Wolstein Center
2000 Prospect Ave E
Cleveland, OH 44115

Lodging

Hilton Garden Inn Downtown Cleveland
1100 Carnegie Ave
Cleveland, OH 44115
(216) 658-6400

Comfort Inn Downtown Cleveland
1800 Euclid Ave
Cleveland, OH 44115
(216) 861-0001

Website

https://engineering.csuohio.edu/midwestasb2021/midwest-american-society-biomechanics-conference

WELCOME TO MIDWEST ASB 2021 IN CLEVELAND, OHIO!

We are so excited to welcome you to Cleveland! This conference is a long time in the making. Originally scheduled for Spring 2020, moved again to Fall 2020, and finally here in Fall 2021.

While COVID has not disappeared, we knew that with the right safety measures in place, we could bring everyone together for two days of presentations, networking, and scientific and personal development. In order to keep everyone safe and have a successful conference, masks are required anytime you are within the Wolstein center.

If you are a returning ASB conference goer – welcome back! We hope you have a fantastic time at the first in person ASB conference in almost two years. If this is your first time, we hope you take in all that ASB has to offer. ASB conferences are friendly, student focused environments. Don't be afraid to ask questions! This is your chance to learn and grow as a researcher. For more information on becoming a member of ASB, check out their website: https://asbweb.org/membership/

Sincerely,

The Midwest ASB 2021 Organizing Committee at Cleveland State University

Midwest ASB would like to thank its generous sponsors for making this conference possible! Donations were given by the American Society of Biomechanics (ASB), the Center for Human Machine Systems (CHMS), Parker Hannifin, Motek, Novel, Bertec, AMTI, Motion Monitor, and XSENSOR.

Keynote Speaker: Dr. Tamara Reid Bush

Keynote Presentation: "Small body part but huge role in daily activities – understanding the thumb"

Dr. Tamara Reid Bush is Professor and Interim Chairperson in the Department of Mechanical Engineering at Michigan State University. She earned a BS in Mechanical Engineering along with a MS and PhD in Engineering Mechanics. Broadly, Dr. Bush's area of research is whole-body biomechanics. She conducts *in-vivo* experimentation, methods development, and modeling to better understand clinically motivated problems. More specifically, her research includes seating mechanics, hand function, prosthetics and soft tissue injury. Today's talk will focus on her group's work associated with the biomechanics of thumb function.

Her research has been funded by NIH, NSF, Blue Cross Blue Shield of Michigan and several industry sponsors. These industry sponsors include Haworth, Abbott Labs, Sage Medical, Steelcase, Johnson Controls and the Michigan District Attorney's Office. Dr. Bush is a Fellow in the American Society of Mechanical Engineers, two-time recipient of the Withrow Teaching Award, and completed her term as Treasurer on the Executive Board of the American Society of Biomechanics. Most recently she received MSU's Inspirational Woman Award for Professional Achievement, the Founder's Award from the American Society of Biomechanics and became a Fellow of the American Institute for Medical and Biological Engineering (AIMBE).

Dr. Bush is an active mentor. She has mentored over 58 undergraduates and over 41 graduate students. Dr. Bush has established a program within her lab where she helps her graduate students learn how to mentor undergraduate students. Diversity in her research group helps creativity and enriches her lab environment. Dr. Bush is in mechanical engineer, her students come from many disciplines including – material science, bioengineering, biosystems, kinesiology, orthotic/prosthetics and medicine. By having a diverse group, the perspectives and knowledge of those in her group are expanded leading to unique solutions and research ideas.

Keynote Speaker: Dr. Jillian Beveridge

Keynote Presentation: The Impact of ACL Function on Knee Biomechanics and PTOA Risk

Abstract: Anterior cruciate ligament (ACL) tear is a known risk factor for post-traumatic osteoarthritis (PTOA), and ACL reconstruction does not appear to reduce this risk. It is widely accepted that both biomechanics and biology play important roles in PTOA initiation and progression, but the contribution of each to the long-term risk of PTOA remains a challenge to discern. Therefore, non-invasive in vivo measures that quantify both joint mechanics and soft tissue function - and how the biological milieu modulates these measures - are critical to developing and monitoring individualized treatments that successfully mitigate PTOA. This research talk will present biomechanical and magnetic resonance imaging methods developed in translational models that are now being applied in clinical studies. Significant results that have formed the basis for my research program will be presented, along with an overview of planned studies that will further extend our understanding of in vivo ACL structure and function.

Bio: Dr. Beveridge is Assistant Staff in the Biomedical Engineering Department at the Cleveland Clinic and Assistant Professor at Case Western Reserve University where her research investigates the mechanisms that drive PTOA after intra-articular joint injury. She completed her undergraduate degree from Acadia University with specializations in Biomechanics and Sport Rehabilitation and her PhD in Biomedical Engineering at the University of Calgary. She then pursued two postdoctoral fellowships, the first at the University of Calgary, and the second at Brown University. Dr. Beveridge's career development and research has been supported by the Canadian Institutes of Health Research, Alberta Innovates Health Solutions, The Arthritis Society, the Natural Sciences and Engineering Research Council of Canada, and the National Institutes of Health as a K99/R00 scholar.

Biomechanics Panelist: Dr. Antonie J. van den Bogert

Antonie J. (Ton) van den Bogert currently holds the Parker-Hannifin Endowed Chair in Human Motion and Control in the Department of Mechanical Engineering at Cleveland State University. He has previously been on the faculty at the University of Calgary (1993-1998) and the Cleveland Clinic (1998-2010).

His academic degrees are from the University of Utrecht (Netherlands), including a BS/MS degree in Physics and Applied Mathematics, and a PhD degree in Veterinary Science for work on locomotion in horses.

For most of his career, Ton has worked on computational modeling of human movement and computer-aided movement analysis, with applications in rehabilitation, sports, and animation. His work has been supported by numerous federal grants and contracts with industry. Ton has served as President of the International Society of Biomechanics and also well known as the moderator of Biomch-L, an online discussion forum on human and animal movement science. He has published over 150 journal articles and book chapters and holds four patents in the area of rehabilitation technology. Notable awards are the Sports Injury Research Award of the American Orthopaedic Society for Sports Medicine (2004), and a Technical Achievement Award from the Academy of Motion Picture Arts and Sciences (2005). He is a Fellow of the International Society of Biomechanics and a Fellow of the American Institute for Medical and Biological Engineering.

Current research interests are: control of powered prosthetic and orthotic devices, predictive simulation for design of sports equipment and assistive devices, and novel methods for analysis of human movement.

Biomechanics Panelist: Dr. Musa Audu

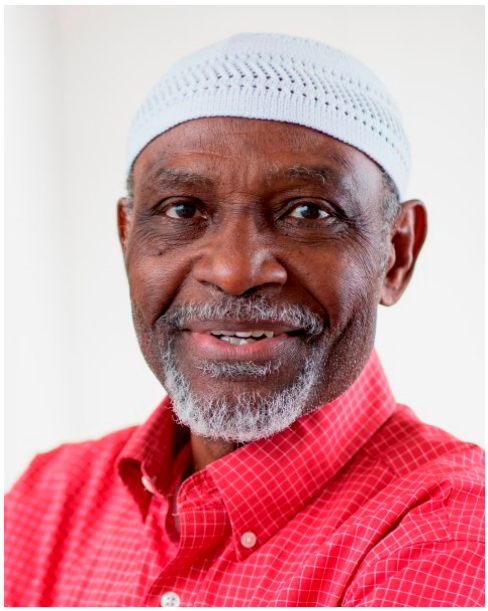

Musa L. Audu received the B.E. and M.E. degrees in mechanical engineering from Ahmadu Bello University, Zaria, Nigeria, and the Ph.D. degree in mechanical engineering with a major in biomechanics from Case Western Reserve University, Cleveland, OH, USA. He was an Associate Professor of Mechanical Engineering at Abubakar Tafawa Balewa University, Bauchi, Nigeria, and the Rector (President) of the Federal Polytechnic in Bauchi, Nigeria. He is currently a Research Professor in the Department of Biomedical Engineering, Case Western Reserve University and a Principal Investigator with the Advanced Platform Technology Center at the Cleveland VA Medical Center. His current research interests include applications of musculoskeletal modeling, simulation of dynamic systems, and optimal control of biomechanical systems. Dr. Audu is a member of the American Society of Biomechanics and the International Functional Electrical Stimulation Society.

Biomechanics Panelist: Dr. Lise Worthen-Chaudhari

Lise Worthen-Chaudhari, PhD, MFA, CCRC connects health science to the creative arts at The Ohio State University Wexner Medical Center. Seeking to make sensorimotor recovery following central nervous system injury more engaging, data-driven, and evidence-based, Worthen-Chaudhari applies principles from dance, biomechanics, and motor learning to improve human neurorecovery. Her work is funded by the National Institutes of Health and has been commercialized by Columbus-based startup, *Rekovo*.

A former professional contemporary dancer, Worthen-Chaudhari holds the role of Research Scientist in OSU's Department of Physical Medicine and Rehabilitation. is the Associate Director of Dodd Hall's Motion Analysis and Recovery Laboratory (MARBL) and a faculty a ffiliate of OSU's Neurological Institute and Chronic Brain Injury Discovery Themes Initiative. Worthen-Chaudhari has served in leadership roles for the American Society of Biomechanics (Program Committee) and The American College of Rehabilitation Medicine (founding member of the Arts & Neuroscience Networking group) and teaches within the OSU School of Health and Rehabilitation Sciences.

Biomechanics Panelist: Dr. Prabaha Sikder

Prabaha Sikder is an Assistant Professor in the Department of Mechanical Engineering and a faculty at the Center for Human-Machine Systems. His research focuses on the development of state-of-the-art regenerative technologies, especially biomaterials for tissue regeneration. He develops medical implants and scaffolds which aims to treat orthopedic and musculoskeletal defects. Some of the solutions developed by him include antibacterial coatings, biodegradable bone-grafting materials, 3-D printed bioactive polymer-ceramic scaffolds and cell-laden implants.

Midwest ASB 2021 Conference Schedule

Wednesday, September 15 – Wolstein Center 5th Floor	
6:00 pm to 8:00 pm	Reception and Early Registration

Thursday, September 16 – Wolstein Center 4th Floor	
8:00 am to 9:15 am	Registration and Breakfast Location: Wolstein 4th floor atrium
9:15 am to 9:30 am	Welcome Address: **Dr. Brian Davis, Associate Dean of Engineering at Cleveland State University** Location: Wolstein 4th floor, Room 411
9:30 am to 10:30 am	Keynote Address 1: **Dr. Tamara Reid Bush, Associate Professor, and Interim Chair of Mechanical Engineering at Michigan State University** Location: Wolstein 4th floor, Room 411
10:30 am to 11:30 am	Coffee Break and Poster Session A Location: Wolstein 4th floor, Room 410
11:30 am to 12:30 pm	Keynote Address 2: **Dr. Jillian Beveridge, Assistant Staff and Research Group Leader at Cleveland Clinic Lerner Research Institute** Location: Wolstein 4th floor, Room 411
12:30 pm to 1:30 pm	Lunch Location: Wolstein 4th floor atrium
1:30 pm to 2:45 pm	Parallel Podium Sessions *Podium Session 1A: Upper Extremity* Location: Wolstein 4th floor, Room 411 *Podium Session 1B: Bone, Tissue, and Imaging* Location: Wolstein 4th floor, Room 410

2:45 pm to 3:00 pm	Coffee Break Location: Wolstein 4th floor atrium
3:00 pm to 4:00 pm	Parallel Podium Sessions *Podium Session 2A: Lower Body Exoskeletons and Biomechanics* Location: Wolstein 4th floor, Room 411 *Podium Session 2B: Clinical Biomechanics 1* Location: Wolstein 4th floor, Room 410
4:00 pm to 5:00 pm	Washkewicz College of Engineering Tours

Friday, September 17

8:00 am to 8:30 am	Breakfast
8:30 am to 9:00 am	Black Biomechanics Association Speaker (Virtual) **Dr. Erica Bell, Research Fellow at the Mayo Clinic (Assistive and Restorative Technology Laboratory)** Location: Wolstein 4th floor, Room 411
9:00 am to 10:00 am	Podium Session *Podium Session 3: Gait and Running* Location: Wolstein 4th floor, Room 411
10:00 am to 11:00 am	Coffee Break and Poster Session B Location: Wolstein 4th floor, Room 410
11:00 am to 12:00 pm	Open Forum Discussion on Biomechanics Panelists: **Dr. Ton van den Bogert, Cleveland State University** **Dr. Musa Audu, Case Western Reserve University** **Dr. Lise Worthen-Chaudhari, The Ohio State University** **Dr. Prabaha Sikder, Cleveland State University** Location: Wolstein 4th floor, Room 411

12:00 pm to 1:00 pm	Lunch Location: Wolstein 4th floor atrium
1:00 pm to 2:00 pm	Poster Session C Location: Wolstein 4th floor, Room 410
2:00 pm to 3:15 pm	Parallel Podium Sessions *Podium Session 4A: Knee Modeling and Biomechanics* Location: Wolstein 4th floor, Room 411 *Podium Session 4B: Clinical Biomechanics 2* Location: Wolstein 4th floor, Room 410
3:15 pm	Closing Address Location: Wolstein 4th floor, Room 411

Thursday, September 16th

Poster Session A: 10:30 am – 11:30 am

Room 410

Presenter	Poster Number	Title
Manaswini Chennoju	PA1	Comparison of the Levator Ani Muscle and the Apical Support Ligaments in Women With and Without Pelvic Organ Prolapse
Austin Cook	PA2	Effects of Rotator Cable and Crescent Tear Propagation on Humeral Abduction Strength
Justin Buce	PA3	Anatomy of the Rotator Cuff and Superior Capsular Complex
Amanda Laxganger	PA4	Intensity of Balance Challenge During Videogaming
Sydney Mountcastle	PA5	Adapting Stroke Hybrid Exoskeleton Electronics for Increased Ease of Use
Emily Szabo	PA6	Validation of Digital Image Correlation to Evaluate 4-Point Bending of Maturing Porcine Fibulae
Christopher Slater	PA7	Quantitative Measurement of Nanoscale Collagen Fiber Mechanical Damage
Marianna Morillo	PA8	Modeling Selective Activation of the Median Nerve
Walid Abuhashim	PA9	Biomechanics of the Praying Mantis Foreleg Strike
Michael Haupt	PA10	Quantitative Analysis of Hemiplegic Gait Following Forced Exercise Intervention
Bridget Gagnier	PA11	Validating the Use of an IMU-Based System to Capture Patient-Handling Tasks
Lauren Long	PA12	Importance of Including BMI, Weight, and Height in Arthroplasty Revision Data Analyses
Abigail Tolstyka	PA13	The Impact Balance Training Has on Kinematic Measurements Post Stroke

Thursday, September 16th

Parallel Podium Sessions 1A and 1B: 1:30 pm – 2:45 pm

Parallel Podium Session 1A – Upper Extremity – Room 411		
Presenter	**Time**	**Title**
Jack Schultz	1:30-1:45	Controlling an Effector with Eye Movements: The Effect of Entangled Sensory and Motor Responsibilities
Lanna Klausing	1:45-2:00	Upper Extremity Motion Assessments in Virtual Reality Environments
Garrett Weidig	2:00-2:15	Using Studies of Octopuses to Aid the Design of Smart Prosthetics
Adam Chrzan	2:15-2:30	Initial Work Towards a More Complete Understanding of the Healthy Thumb
David Williams	2:30-2:45	The Effects of Environmental Factors on Ladder Overreaching

Parallel Podium Session 1B – Bone, Tissue, and Imaging – Room 410		
Presenter	**Time**	**Title**
Ryan Rosario	1:30-1:45	Effect of Bony Mismatches Caused by Osteochondral Allograft Repair on Cartilage Deformation
Dylan Crocker	1:45-2:00	Fatigue and Fracture Toughness of Cortical Bone are Radiation Dose-Dependent
Phillip McClellan	2:00-2:15	Mesenchymal Stem Cell Delivery via Topographically Tenoinductive Collagen Biotextile Enhances Regeneration of Segmental Tendon Defects
Juliana Azuero	2:15-2:30	Design-Specific Muscle Tissue Constructs for Treating Severe Musculoskeletal Defects
Ronald Fortunato	2:30-2:45	Combining multiple imaging modalities to develop a finite element model of cerebral aneurysm with variable thickness and comparison to a constant thickness model

Thursday, September 16th

Parallel Podium Session 2A and 2B: 3:00 pm – 4:00 pm

Podium Session 2A – Lower Body Exoskeletons and Biomechanics – Room 411		
Presenter	**Time**	**Title**
Shanpu Fang	3:00-3:15	Added Mass Changes Kinematics and Kinetics of Adults During Walking
Sai Gunti	3:15-3:30	Optimization Based Postural Control System in an Underactuated Exoskeleton
Vinayak Vijayan	3:30-3:45	Spatiotemporal and Muscle Activation Adaptations During Overground Walking in Response to Lower Body Added Mass
Marshaun Fitzpatrick	3:45-4:00	An Adjustable Pelvic-Trunk Corset for Lower-Limb Exoskeletons

Podium Session 2B – Clinical Biomechanics I – Room 410		
Presenter	**Time**	**Title**
Khaled Adjerid	3:00-3:15	The Effect of Nipple Stiffness and Hole Size on Infant Sucking Behaviors
Homa Eskandri	3:15-3:30	Decay Rates of Generated Particles and Aerosolized Droplets in Dental Practices
Niloufar Sadoughipour	3:30-3:45	Aerosol Characterization in a Dental Setting
Chloe Edmonds	3:45-4:00	Oropharyngeal Capsaicin Application Alters Swallowing Kinematics to Improve Performance

Friday, September 17th

Podium Session 3: 9:00 am – 10:00 am

Podium Session 3 – Gait and Running – Room 411		
Presenter	**Time**	**Title**
Hala Osman	9:00-9:15	Quantifying Gait Perturbation Responses Using the Hotelling T-Squared Statistic: A Novel Approach
Dana Lorenz	9:15-9:30	A Treadmill Perturbation Method for Assessment of Reflex Modulation During Gait
Loubna Baroudi	9:30-9:45	Contextualizing Walking Speed in the Real World
Micah Garcia	9:45-10:00	Run Type Influences Running and Physiologic Parameters for High School Cross-Country Runners

Friday, September 17th

Poster Session B: 10:00 am – 11:00 am

Room 410

Presenter	Time	Title
Mikayla Bulson	PB1	Incorporating Additive Manufacturing in Hand Splinting and Designing a New Palm Cone
Ells Mine Saint Paul	PB2	Error in Joint Angle Measurement Through Simulated Motion Capture
Maria Gamez	PB3	Increased Load Transfer Heterogeneity in Chiari Malformation Suggests Less Interlimb Coordination
Dawud Sharrieff	PB4	EMG-IMU Instrumentation and Sensor Fusion
Brendan Otani	PB5	Bioprinting of a Design-Specific Implant for Treating Volumetric Muscle Loss (VML)
Raven Foust	PB6	Developing a Biomechanical Analysis for Softball Pitching
Zachary Hubbard	PB7	Quantifying Balance Through Step Length and Single-Leg Stance
Sofia Urbina	PB8	Manipulability of a Multilink Mobile Arm Support
Isaias Trevino	PB9	Identification of Feedback Control for Human Posture Using SCONE
Kyra Stovicek	PB10	Effectiveness of a Motor Point Pen in Finding Muscle Motor Points
Tayluer Streat	PB11	A case study of Chiari Malformation Type 2 gait abnormalities in a pediatric population
Kaitlin Skurnak	PB12	Pediatric Partial Body Weight Support System for the Aid of Movement for Children with Cerebral Palsy

Friday, September 17th

Poster Session B: 1:00 pm – 2:00 pm

Room 410

Presenter	Time	Title
Jack Schultz	PC1	Robot-Assisted Feeding for Individuals with Movement Disorders
Michael Dube	PC2	In Silico Modeling of Achilles Tendon Function in Running Humans: Effects of Foot Geometry, Speed, and Gait
Reese Moschetta	PC3	Feasibility of the Lifting Full-Body Model to Simulate Squatting Tasks
Cameron LaMack	PC4	Improving Neuromusculoskeletal Models with Tactile Feedback: A Proof of Concept Simulation Study
Nicole Arnold	PC5	Kinematic Data of Healthy Thumbs
Archana Lamsal	PC6	Understanding Head Movement and Shoulder Rounding in Seated and Standing Postures
Loay Al Zube	PC7	Modeling Human Arm Configuration Holding a Tennis Racket Using a 2-Dimensional 4-Segments Coupled Pendulum System
Lauren Eichaker	PC8	Determination of L5/S1 Loads During Lifting Using a Simplified Conservative Model
Kenneth Munyuza	PC9	Application of Artificial Neural Networks in Estimating Ground Reaction Forces Using Inertial Data of the Lower Body
Grace VanDellen	PC10	EEG Analysis of Referred Sensations Caused by Electrical Stimulation for Treatment of Phantom Limb Pain
Jessi Martin	PC11	The Viability of In-Shoe Insoles to Measure Pressure and Shear in Patients with Charcot Arthropathy
Sudeep Gummadi	PC12	3D Printing of Biomedical Implants
Ryan O'Quinn	PC13	Additive Insert Molding: Feasibility and Applications

Friday, September 17th

Podium Session 4A and 4B: 2:00 – 3:15 pm

Podium Session 4A – Knee and Ankle Modeling – Room 411		
Presenter	**Time**	**Title**
Lexie Mallinos	2:00-2:15	Pivot Shift and Anterior Drawer Test Simulations in Juvenile Patient Populations
Mohamed Hefzy	2:15-2:30	Knee Mechanics During Anterior and Posterior Lunge
Skye Carlson	2:30-2:45	Novel Implant Device for Plantar Plate Repair
Will Zaylor	2:45-3:00	Sensitivity of ACL Force and Stress to Kinematic Error
Jeffrey Watts	3:00-3:15	Anatomical Characteristics Contributing to Patellar Dislocations Following MPFL Reconstruction

Podium Session 4B – Clinical Biomechanics II – Room 410		
Presenter	**Time**	**Title**
Jae-Won Choi	2:00-2:15	A Preliminary Study on Measuring Normal and Tangential Force Using Stretch Polymeric Sensors for Smart Insoles
Justin Scott	2:15-2:30	Isolated Seat Pan Tilt Reduces Buttock and Lower Back Pressure on Able-Bodied Individuals and Wheelchair Users While Seated
Jeremiah Ukwela	2:30-2:45	Development of Foot Displacement Detection Algorithm for Power Wheelchair Footplate Pressure and Positioning
Mark Morkos	2:45-3:00	Accuracy of Cranial and Brain Morphometric Measurements across Parasagittal Planes as compared to Midsagittal Plane Measurements on Adult Females with Chiari I Malformation
Shraddha Sudhir	3:00-3:15	The Effects of Compression Garments on Hip and Knee Kinematics During a Swim Start

COMPARISON OF THE LEVATOR ANI MUSCLE AND THE APICAL SUPPORT LIGAMENTS IN WOMEN WITH AND WITHOUT PELVIC ORGAN PROLAPSE

[1] Manaswini Chennoju

[1]Cleveland State University, Cleveland, OH, USA

Email: chennoju.manaswini@gmail.com

INTRODUCTION

According to the National Institutes of Health(NIH), almost 24% of US women are affected by pelvic organ prolapse. There is a 50% chance of women above 80 and older to be affected by any pelvic floor disorders and a 40% chance for women in theirs 60s to 70s [1]. There are many reasons for a woman to be diagnosed with a pelvic organ prolapse, including menopause, aging, genetics, and obesity, etc. [2]. Pelvic organ prolapse is when the organs in the pelvis slip down from their normal position and bulge into the vagina. In pelvic organ prolapse, the apical support ligaments i.e., the cardinal and the uterosacral ligaments, the levator ani muscle, the vagina, and the pubovisceral muscle play an important role. The forces from the intra-abdominal pressure which are applied on the vagina are counterbalanced with the vaginal and the levator ani closure reaction force which holds the hiatus from tearing. When the pressure from the intra-abdominal pressure increases due to various reasons such as obesity, genetic factor, etc., and the levator ani muscle cannot generate the counterbalance force to balance the force, due to the pressure difference, and the loss of strength in the support ligaments the pelvic organs slowly descend.

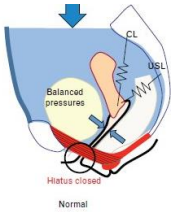

Figure 1. shows the normal function of the pelvic floor [3].

METHODS

The pelvic floor is developed as a 2D biomechanical model using multi-body modelling software (MSC ADAMS). The dimensions and angles of the muscles in the biomechanical model are considered as listed in [7].

Figure 2 shows the snapshot of the biomechanical 2D model that was developed in the MSC ADAMS software.

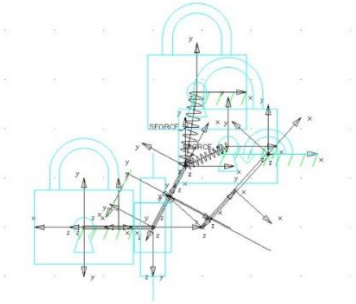

Figure 2. the biomechanical model developed in the MSC ADAMS

RESULTS

When the conditions are applied and the model is simulated with normal conditions, with 70cm H2O intra-abdominal pressure on the system. There was no deformation in the anterior walls of the vagina. The forces calculated using the equation in Table 1[7] are used to simulate the model with normal levator function. The tensions in the cardinal, the uterosacral ligaments, and the tension in the levator muscle were plotted. Figures 3 show the tension in the levator ani muscle at normal loading and the tensions in the cardinal and the uterosacral ligaments at PVM loading respectively.

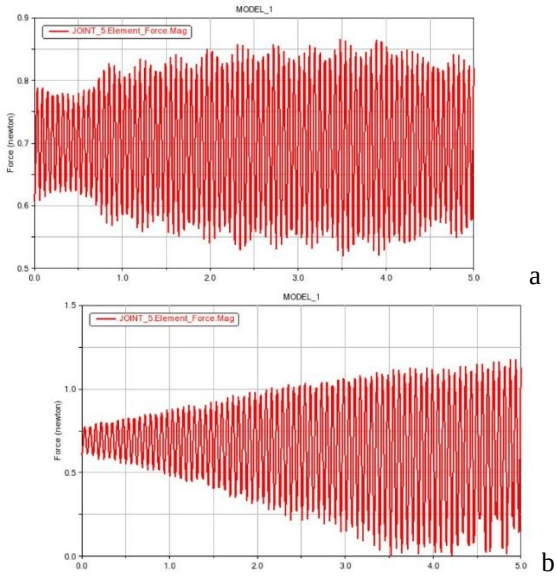

Figure 3. tension in the levator muscle at normal loading and a PVM impairment loading

When the model was loaded with a PVM defect and the forces which were derived from the levator injury, deformation in the anterior vaginal wall could be seen.
Comparing the plots of the normal loading and the prolapse loading we can see that when the model was loaded with the appropriate forces calculated the equations and the theoretical forces, deformation in the anterior vaginal wall could be seen. The levator muscle at normal loading shows the plot with 0.8 to 0.6N and when the forces generated due to PVM impairment were loaded, the tension in the levator plate was tending towards 0N which shows the reduced tensions in the levator plate.

CONCLUSION

Pelvic organ prolapse is caused due to multiple muscle failures like pubovisceral muscle, levator injury, etc. It can cause due to many factors affecting the intra-abdominal pressures to increase. In the pelvic organ prolapse, the tension in the apical support ligaments is seen to increase and the tension in the levator muscle seems to be reduced. The biomechanical model created in this paper broadens the scope of understanding these disorders or dysfunctions in the human body with a clearer picture using these computer softwares.

REFERENCES

1. 1.Nygaard, Ingrid et al. “Prevalence of symptomatic pelvic floor disorders in US women.” *JAMA* vol. 300,11 (2008): 1311-6. doi:10.1001/jama.300.11.1311
2. Weintraub, Adi Y., Glinter, Hannah, & Marcus-Braun, Naama. (2020). Narrative review of the epidemiology, diagnosis and pathophysiology of pelvic organ prolapse. *International braz j urol*, *46*(1), 5-14. Epub January 13, 2019.https://doi.org/10.1590/s1677-5538.ibju.2018.0581.
3. DeLancey, John O L. “What's new in the functional anatomy of pelvic organ prolapse?.” *Current opinion in obstetrics & gynecology* vol. 28,5 (2016): 420-9. doi:10.1097/GCO.0000000000000312.
4. DeLancey, John O L. Surgery for cystocele III: do all cystoceles involve apical descent?: observations on cause and effect. Int Urogynecol J 2012; 23:665–667.
5. Ashton-Miller, James A, and John O L DeLancey. “Functional anatomy of the female pelvic floor.” *Annals of the New York Academy of Sciences* vol. 1101 (2007): 266-96. doi:10.1196/annals.1389.034
6. Ramanah, Rajeev; Berger, Mitchell B.; Parratte, Bernard M.; DeLancey, John O. L. (2012). *Anatomy and histology of apical support: a literature review concerning cardinal and uterosacral ligaments. International Urogynecology Journal, 23(11), 1483–1494.* doi:10.1007/s00192-012-1819-7
7. Chen L, Ashton-Miller JA, Hsu Y, DeLancey John O L. Interaction among apical support, levator ani impairment, and anterior vaginal wall prolapse. Obstetrics and Gynecology. 2006 Aug;108(2):324-332. DOI: 10.1097/01.aog.0000227786.69257.a8.

EFFECTS OF ROTATOR CABLE AND CRESCENT TEAR PROPAGATION ON HUMERAL ABDUCTION STRENGTH

[1,2]A. Cook (Presenter), [1,2]R. Blake, MS, [2]L. Carrazana-Suarez, MD, [2]D. Papadopoulos, MD, [1,2]M. Smolinski, MS, [2]J. Greenwell, BS, [1,2]M. Miller, PhD, [1,2]P. Smolinski, PhD, [2]C. Schmidt, MD

[1]University of Pittsburgh, Pittsburgh, PA, USA

[2]Shoulder and Elbow Mechanical Research Laboratory, Department of Orthopaedic Surgery, UPMC, Pittsburgh, PA

Email: ajc201@pitt.edu

INTRODUCTION

The rotator cable (RCa) is a semilunar fibrous band of collagen that is hypothesized to transmit forces and protect the crescent area (CA) [1]. Despite this, patients with full-thickness tears and an intact RCa present with clinical dysfunction. The purpose of this study is to evaluate the biomechanical effect of tear propagation along the CA. The researchers hypothesized that the humeral abduction strength will decrease as the tear propagates through the CA, even with an intact RCa, and strength loss will be independent of direction.

METHODS

Twenty fresh-frozen cadavers (68.5 ± 12.1 years) without rotator cuff pathology were dissected leaving the rotator cuff muscles and tendons intact. An acromion osteotomy, inferior capsulectomy, and anatomic neck osteotomy were performed to reveal the articular surface of the rotator cuff and the RCa. A running silk suture was passed from the articular to bursal surface along the borders of the RCa (Figure 1a), and the CA was sectioned into quarters (Figure 1c).

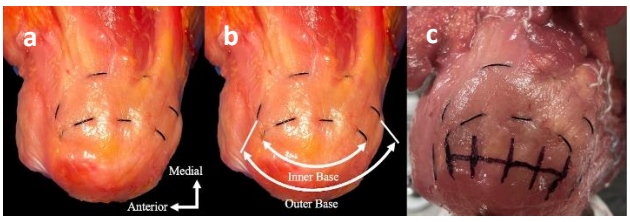

Figure 1: (a) Outlined rotator cable on the bursal surface, (b) inner and outer base measurements, (c) crescent area sectioned into quarters

Loading sutures were placed in each rotator cuff muscle with two on the subscapularis, upper and lower. The humeral shaft and scapula were potted into a plastic sleeve and custom scapular box, respectively. The specimens were loaded into a custom shoulder simulator (Figure 2) comprised of actuators and a pulley system replicating lines of action. The specimens were loaded to physiological values simulating abduction at 0° and neutral rotation[2,3]. A 6 degree of freedom load cell located at the distal humerus measured force (strength) in the scapular plane.

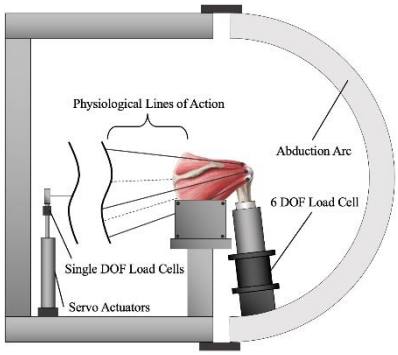

Figure 2: Shoulder simulator schematic highlighting key features

Specimens were randomized into two groups: initial release of the anterior quarter (anterior group) or posterior quarter (posterior group) of the CA. After statically loading the native specimen for 5 minutes, a simulated tear was introduced to either the anterior/posterior quarter of the CA. The tear was then extended into the neighboring quarters one at a time (Figure 1b), leaving the RCa intact. The propagation continued into the posterior and anterior RCa insertion for the anterior and posterior group, respectively. The final condition was release of the

remaining RCa insertion. The specimens remained loaded for the entirety of the test and each sequence was held for 5 minutes. The output humeral abduction force was averaged over the final two minutes of each condition and normalized to the native strength.

RESULTS AND DISCUSSION

One specimen was removed from the posterior group based on an outlier analysis. The decrease in strength is shown below for the anterior (Figure 3a) and posterior groups (Figure 3b). The decreases were significant ($p<0.05$) when the tear affected ¾ of the CA for both the anterior ($p=0.008$) and posterior groups ($p=0.033$), both the entire CA for anterior ($p=0.001$) and posterior ($p=0.023$), extension into the posterior RCa insertion ($p=0.001$) for the anterior group, extension into the anterior RCa insertion for the posterior group ($p=0.019$), and the final extension into both RCa insertions for both anterior ($p=0.001$) and posterior groups ($p=0.001$).

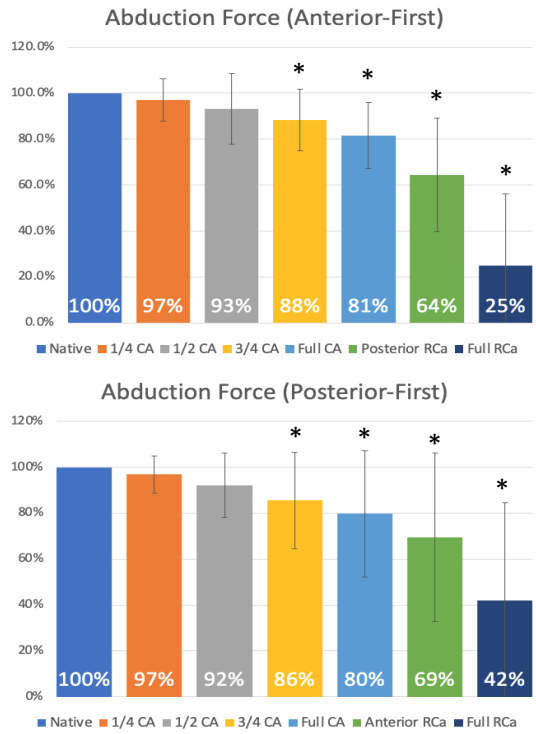

Figure 3: Abduction force for both anterior- and posterior-first groups for each stage of tear progression. Significance is marked with (*).

This study indicates that significant decreases in humeral abduction strength occurred as tears in the CA increased in size. Also, these findings occurred while both insertions of the RCa were intact, suggesting the CA also transmits load during abduction. The biggest drop in abduction force resulted after both RCa insertions and the entire CA were torn, and the strength losses were similar, which suggest symmetry among the rotator cuff. Both facets of the original hypothesis, that the humeral abduction strength would decrease as the tear propagates through the CA and be independent of tear propagation, were upheld by these results. These results can be correlated clinically with pseudoparalysis after massive rotator cuff tears. Although the RCa plays a crucial role in maintaining abduction strength, it can be concluded that the entire complex is necessary for unaltered shoulder function.

CONCLUSION

Humeral abduction strength is significantly decreased by tears in the crescent area. The effect on humeral strength is independent of tear propagation direction. Tears larger than 14.2 ± 1.8 mm are at risk to cause loss in humeral abduction strength and surgical intervention may be needed.

REFERENCES

1. Burkhart, et al., Arthroscopy 1993.

2. Kedgley, et al., J Biomech 2007.

3. Omi, et al., J Anatomy 2010.

ANATOMY OF THE ROTATOR CUFF AND SUPERIOR CAPSULAR COMPLEX

[1,2]J. Buce (Presenter), BS, [2]L. Carrazana-Suarez, MD, [1,2]M. Smolinski, MS, [2]J. Greenwell, BS, [1,2]R. Blake, MS, [1,2]M. Miller, PhD, [1,2]P. Smolinski, PhD, [1,2]C. Schmidt, MD

[1]Department of Mechanical Engineering and Material Science, University of Pittsburgh, Pittsburgh, PA, USA

[2]Shoulder and Elbow Mechanical Research Laboratory, Department of Orthopaedic Surgery, UPMC, Pittsburgh, PA

Email: jgb35@pitt.edu

INTRODUCTION

Superior capsular reconstruction (SCR) has become a popular procedure for management of irreparable rotator cuff (RC) tears [1]. Although good patient outcomes have been reported, the structural failure rate can reach 75% [2]. A more anatomic repair of the rotator cuff superior capsular complex may increase healing rates. Using laser imaging, this anatomy can be visualized in 3D. We hypothesize that the superior capsule (SC) is: bound to the coracohumeral ligament (CHL), thinner than the CHL, attaches to the RC at a consistent location, and has specialized attachments to the humerus and scapula.

METHODS

Ten fresh-frozen cadavers (66.6±8.6 years) without RC pathology were dissected leaving the rotator cuff capsular complex intact; the rotator cable (RCa) was outlined from the articular side with stitches (Fig. 1A). Each specimen was mounted in a fixator (Fig. 1B) and dissected in a stepwise protocol. Steps of dissection were: 1) specimen with RC and humeral attachments intact, 2) blunt separation of the RC off the capsule, 3) sharp dissection separating the tendons off of the SC under Loupe magnification, 4) removal of the RC from their humeral insertions, and 5) dissection of the SC from its humeral and scapular insertions. After each step, 3D models were made using a laser scanning system (FaroArm, FL, USA) and geometric software (3D Systems, NC, USA). Measurements of the supraspinatus (SS), infraspinatus (IS) tendons, SC, and location of the RC/SC junction were made using the software and verified using a scientific caliper (accuracy 0.01mm, $p \geq 0.150$).

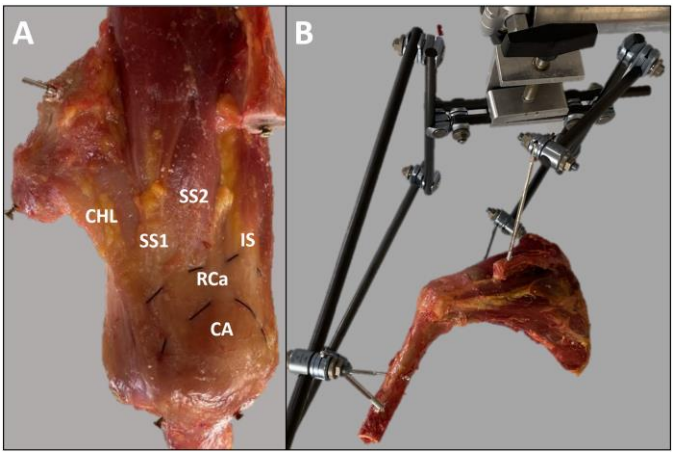

Figure 1: (A) The rotator cable (RCa) outlined with running silk suture from the bursal side, (B) specimen mounted to fixator (CHL coracohumeral ligament, SS supraspinatus, IS infraspinatus, RCa rotator cable, CA crescent area).

RESULTS AND DISCUSSION

The CHL and SC formed a continuous structure in all steps. The CHL was measured in Steps 1-4 and the SC was measured in Steps 3 and 4. The CHL (4.5±2.1mm) was 4 times thicker than the SC (1.2±1.0mm). The rotator cuff capsular complex thickness was measured laterally (4.66±1.50mm SS and 5.76±1.67mm IS) and medially (5.05±1.91mm SS and 6.35±1.78mm IS) in step 1. The IS was found to be significantly thicker than SS laterally ($p<0.04$) but not medially ($p \geq 0.04$). The IS and SS tendons inserted into the SC at the medial border of the (RCa) and their insertion locations were measured (22.6±4.7mm and 17.6±4.2mm respectively) (Fig. 2A-B). The SC attached to the humerus with its

broadest area surrounding the biceps tunnel, between the infraspinatus and teres minor, on the scapula at the coracoid, and adjacent to the scapular spine.

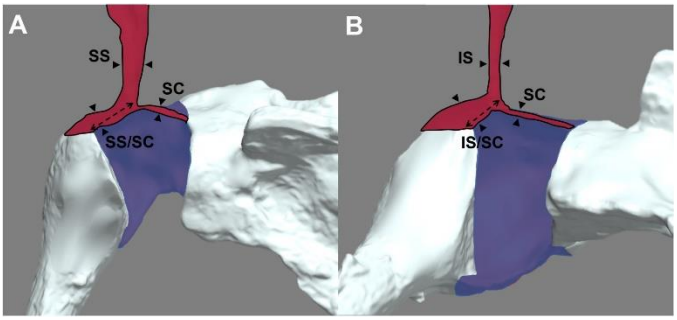

Figure 2: (A) Coronal cut through supraspinatus (SS), (B) coronal cut through infraspinatus (IS), dashed lines represent the distance from the tendon humeral insertion to its capsular insertion (SC superior capsule, SS/SC supraspinatus inserting to superior capsule, IS/SC infraspinatus insertion to superior capsule).

Our study shows that an anatomic SC reconstruction requires restoration of the thickness of the CHL, repair of the SS and IS to their respective humeral footprints, and anchor placement for the SC graft at the broadest SC attachments. 3D scanning from this study adds to the current understanding of the anatomy by confirming our hypothesis. These steps can serve as a template for an anatomic SCR, restoring anatomy, and improving biomechanics and function of the glenohumeral joint.

CONCLUSION

The current measures of tissue thickness and of the attachment of the CHL highlight opportunities for improvement of SCR. Future work can examine whether repairs restore the mechanical behavior dictated by the present research.

REFERENCES

1. Mihata, T, et al. *Am J Sports Med.* 2012.

2. Kovacevic, D, et al. *JSES.* 2020.

INTENSITY OF BALANCE CHALLENGE DURING VIDEOGAMING

Amanda Laxganger, Debbie Espy, and Ann Reinthal

Cleveland State University, Cleveland, OH, USA

Email: a.m.lowe9@vikes.csuohio.edu

INTRODUCTION

Poor balance and falls remain a large concern for older adults and individuals with physical disability. Clinicians use adapted commercial video gaming as one intervention technique to address balance impairments. However, a lack of standardized balance intensity measures poses a significant challenge in prescribing appropriate dosage for balance rehabilitation interventions such as gaming [1]. Movement kinematics provide one method for quantifying functional demands of a therapeutic intervention. This study's objective was to use kinematics to investigate how varied balance training game demands and gaming surface increase the intensity of balance challenge, specifically movement of the center of mass (COM) relative to base of support (BOS).

METHODS

Twenty-seven self-reported community ambulators, ages 50-79, played four randomly selected video-gaming conditions. Each condition consisted of a specific game (Microsoft Kinect) and play surface combination. Game conditions were grouped into those requiring kicking (4 conditions), stepping (5 conditions), or no stepping (6 conditions). Participants played about five minutes per condition. They rated their self-perceived balance challenge of each condition using the visual Rate of Perceived Stability (RPS) Scale [2]. Three-dimensional motion capture was collected using the Helen Hayes marker set, an eight-camera system and Cortex software (Motion Analysis Corp., Rohnert Park, CA). Capture data were processed through Cortex and custom MATLAB code to determine the fraction of game play time that the COM moved outside of the BOS (FX) as well as the maximum excursion range of the COM (EX). Descriptive statistics were calculated for these measures in each condition.

RESULTS AND DISCUSSION

Tables 1-3 display the mean and ranges for RPS scores (maximum challenge 10 on 1 to 10 scale), the fraction of time the COM was outside of the BOS (FX: %), and the maximum excursion of the COM (EX: mm).

Table 1: Data for Kicking Games

Condition description	n	RPS mean	RPS range	Frac. BOS mean	Frac. BOS range	max excursion Mean*	max excursion Range*
Intermediate Target Kick on Mats/Rafts	18	3.61	1-7	0.32	0.10 - 0.56	44.0	5-273
Hard Target Kick on floor	4	3.25	2-5	0.18	0.04 - 0.34	16.7	4-29
Hard Target Kick on rocker	13	4.31	2-7	0.14	0.03 - 0.34	18.5	3-90
Hard Target Kick on slider	16	5.31	4-8	0.15	0.06 - 0.37	7.2	2-33

Table 2: Data for Stepping Games

Condition description	n	RPS mean	RPS range	Frac. BOS mean	Frac. BOS range	max excursion Mean*	max excursion Range*
Ship shapes on Floor	7	1.29	1 - 2	0.06	0.02 - 0.13	179.2	7 - 536
Cruiser Reflex Ridge on Floor	8	1.63	1 - 3	0.05	0.01 - 0.12	56.4	6 - 318
Dodger Reflex Ridge on Floor	3	2.33	2 - 3	0.10	0.02 - 0.14	14.8	6 - 25
Crab Crazy & Fish Frenzy on Floor	11	1.82	1 - 3	0.13	0.03 - 0.35	94.0	7 - 360
Cruiser Reflex Ridge on Mats/Rafts	5	3.20	2 - 5	0.11	0.06 - 0.20	83.9	9 - 369

Table 3: Data for Non-Stepping Games

Condition description	n	RPS mean	RPS range	Frac. BOS mean	Frac. BOS range	max excursion Mean*	max excursion Range*
Amateur Table Tennis on Floor	8	1.50	1 - 2	0.03	0.00 - 0.10	29	2 - 113
Amateur Table Tennis on Mats/Rafts	8	2.13	1 - 4	0.08	0.00 - 0.38	11	1 - 20
Hard Table Tennis on Rocker	7	2.43	1 - 4	0.13	0.00 - 0.65	4	0 - 10
Funnel Cake Falls on Rocker	8	4.25	2 - 7	0.10	0.00 - 0.41	6	1 - 10
Amateur Table Tennis on Slider	7	2.71	1 - 4	0.00	0.00 - 0.00	1	1 - 4
Funnel Cake Falls on Slider	7	1.71	1 - 3	0.01	0.00 - 0.05	1	1 - 1

During the kicking games (Table 1), EX and FX increased on the mat while decreasing on the slider and rocker surfaces. EX especially decreased on the slider while having the highest RPS score. Since there were three conditions using the same game (Hard Target Kick) with three different surfaces, RPS scores ranked these surfaces from easiest to hardest as floor, rocker, and slider, respectively. During stepping games, FX was highest on the mats and the two harder floor games, while RPS and EX increased on the mat surface in the one game played on both floor and mats (Cruiser Reflex Ridge). In the non-stepping games, EX was highest on the floor/mat surfaces and lowest on the slider. FX was lowest in the slider and highest on the rocker surface while RPS was highest on the rocker.

CONCLUSION

Overall, FX and EX were highest in the stepping games, where the games demanded more movement, and lowest in the non-stepping games where the games demanded stability. They also decreased on the two mobile surfaces, especially on the slider. Thus, kinematic analysis of balance intensity in terms of EX and FX must be coupled with an understanding of the game condition.

REFERENCES

1. Farlie M, et al. Intensity of challenge to the balance system is not reported in the prescription of balance exercises in randomised trials: a systematic review. Journal of Physiotherapy, 59(4), 227–235, 2013.
2. Espy D. Intensity of balance task intensity, as measured by the rate of perceived stability, is independent of physical exertion as measured by heart rate. *J Nov Physiother*, *7*(343), 2, 2017.

ACKNOWLEDGEMENTS

We acknowledge support from the Cleveland State University Undergraduate Summer Research Award as well as the assistance of Lorenzo Bianco, Summer Gaglione, Kathryn Kroszkewicz, and Emily Meisterheim in data collection and analysis.

ADAPTING STROKE HYBRID EXOSKELETON ELECTRONICS FOR INCREASED EASE OF USE

[1]Sydney Mountcastle, [1,2]Marshaun Fitzpatrick, [1]Roger Quinn, [1,2]Ronald Triolo, and [1,2,3]Nathaniel Makowski

[1]Case Western Reserve University, Cleveland, OH, USA

[2]Louis Stokes Cleveland Veterans Affairs Medical Center, Cleveland, OH, USA

[3]MetroHealth Medical Center, Cleveland, OH, USA

Email: sem204@case.edu

INTRODUCTION

Powered exoskeletons are being developed for rehabilitation to improve walking ability in people with neurologic impairments (e.g. spinal cord injury (SCI) and stroke) [1]. Our team is developing a hybrid modular system for improving mobility. The approach prioritizes incorporating the user's muscles via volitional activation or through electrical stimulation with the motors assisting as needed. The modular approach allows the device to be customized to the individual's needs. For example, for people with SCI, the system can be configured with bilateral actuators at the hip, knee, and ankles [2]. For individuals with poststroke hemiparesis, the system could only contain an actuator at one knee with electrical stimulation assisting the knee and ankle.

The first prototype for the untethered system incorporated a small backpack containing the battery and electronics. Feedback from a stroke survivor testing the system indicated that the pack was annoying and made the system more challenging to don and doff.

To improve ease of use and facilitate eventual implementation in home and community settings outside the laboratory, this project developed a method for mounting the battery and electronics with the hardware on the leg in order to eliminate the need for the backpack. This abstract describes the first prototype for these modifications.

METHODS

Table 1 shows the relevant clinical goals as well as the resulting design requirement.

Table 1: Design Requirements

Clinical Need	Design Requirement
Maintain functionality of existing components.	Enclosures cannot impede access to or functionality of control board, battery, or actuator.
Remove secondary elements to simplify ease of use.	Mount components on the existing structure.
Enclosures must not cause injury to user and protect internal components.	Corners must be rounded to avoid discomfort; wires must be protected.
Size adjustability must be maintained for multiple body types.	The enclosures cannot block access to the device's adjustment mechanisms.
Component relocation cannot increase strain on the user.	The added moment on the hip due to the extra weight should be minimized.

Based on these constraints, mounting configurations for the control board and battery were drafted. Options included mounting it on a pelvic band or along the various dimensions of the knee actuator. After determining effective mounting locations, models were developed in Onshape. The enclosure pieces were then printed on a 3D resin printer. Acrylic components that allow visibility of internal components were fabricated via laser cutting. Metal structural aspects of the actuator that required modification were manufactured on a CNC mill.

After assembly, an able-bodied user walked with the new system to verify that the updated battery and control board mounting did not adversely affect use.

The additional joint moments added by shifting the battery and control board locations were also calculated. Based on the estimated center of mass and distance from the point of rotation, the additional moments were determined for the frontal plane in stance and the sagittal plane in swing.

RESULTS AND DISCUSSION

The prototype for the new mounting system includes a holder for the battery along the anterior face of the actuator (Figure 1). This location was selected to limit additional lateral size. The control board was mounted superior to the actuator, adjacent to a turnbuckle for an optional pelvic attachment. These locations reduce additional size while maintaining adjustability for individuals of varied heights to use the pelvic band. Additionally, this configuration minimizes wire routing. The battery holder is incorporated directly into the actuator enclosure while the control board enclosure is a separate component that attaches to the actuator.

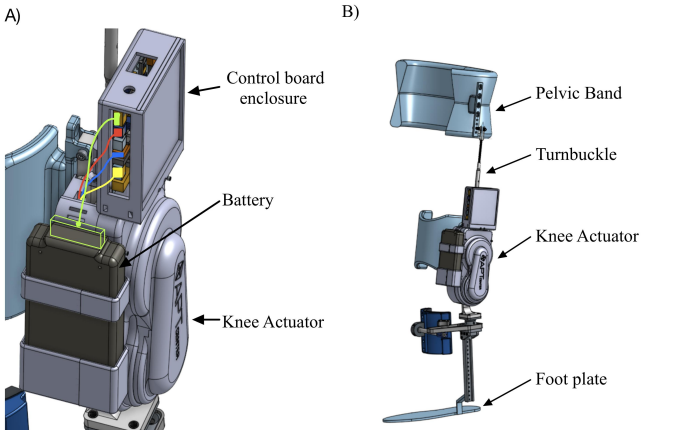

Figure 1: Model of components integrated with actuator a) close up of new elements b) view of full device

The increased moments due to both the battery, the control board, and the additional parts is 1.403 Nm within the coronal plane, at 0 degrees abduction. Based on a maximum hip flexion of 30 degrees during walking [3], the maximum moment within the sagittal plane is approximately 1.583Nm. These increases are relatively small compared to the moment generated by the knee actuator placed on the hip: 4.991 Nm in the coronal plane and 4.351 Nm in the sagittal plane.

Tests on an able-bodied user support that the changes simplify use and donning and doffing without negatively impacting functionality. Next the device will be tested with a stroke survivor to confirm the changes are effective for someone with hemiparesis.

CONCLUSION

The control board and the battery were relocated to the leg without reducing functionality, adjustability, durability, or safety. The added moments due to relocating these components were relatively small. Further testing will determine how these effects are perceived by users.

REFERENCES

1. Louie, DR, et al. *BioMed Central.* 35, 2020.

2. Nandor, Mark, et al. *Frontiers in Robotics and AI.* 8, 2021.

3. Bowker, J, et al. *Atlas of Limb Prosthetics.* American Academy of Orthopedic Surgeons, 1992.

ACKNOWLEDGEMENTS

This work was supported by VA Merit Review 3056, the SOURCE Program at Case Western Reserve University, and the Case Alumni Association.

VALIDATION OF DIGITAL IMAGE CORRELATION TO EVALUATE 4-POINT BENDING OF MATURING PORCINE FIBULAE

Emily Szabo[1], Jay Bensusan[1], Clare Rimnac[1]

[1]Case Western Reserve University, Cleveland, OH, USA

Email: emily.szabo@case.edu

INTRODUCTION

Long bone fractures in young children (1-5 years) occur in both accidental and non-accidental (i.e., child abuse) trauma instances [1]. Criteria to assess the likelihood of non-accidental trauma is subjective and limited in clinical practice [1]. There is an interest in analyzing and predicting the mechanical loading conditions associated with long bone diaphyseal fractures attributed to trauma in children.

Human bone from young donors is difficult to obtain for ethical reasons; thus, few studies have investigated it. Surrogate animal models with similar geometrical aspect ratio and microstructure (e.g., porcine, ovine) have been used to characterize maturing human bone [2].

Examining whole-bone mechanical behavior of maturing bone can be done to simulate the conditions associated with fracture. Whole-bone bending is a clinically relevant loading mode leading to long bone fracture. Digital image correlation (DIC) is a non-contacting method in which displacement and strain of small dots (speckles) are traced with imaging techniques and analysis software. Experimental mechanical testing methods using DIC are useful to evaluate local displacement and strain behavior during loading of whole bone geometries; they also can serve as a basis to conduct theoretical (i.e., finite element) analyses (FEA). In turn, FEA can also be used to validate the experimental results from DIC.

The purpose of this study is to report the whole bone behavior of young, maturing porcine fibulae up to failure using experimental methods with DIC.

METHODS

Six hind limbs from maturing male white domestic porcine were obtained from the National Swine Resource and Research Center (NSRRC). Two limbs from each time point (newborn, 1-month, 3-months) were obtained. This age-range of porcine bone is approximately equivalent to humans 1-3 years [3]. The limbs were cleaned of soft tissue, and the bones were stored at -20°C wrapped in water-soaked gauze.

The fibulae were mechanically tested until fracture with a custom 4-point bending fixture using ASTM D6272-17 as a guide. Prior to testing, each fibula was thawed to room temperature. DIC was used to determine the strain in the tensile region of the specimens. White acrylic, water-based paint was applied to the inferior bone surface undergoing tension and on the surface orthogonal to that and facing the camera. Black acrylic, water-based paint was applied on top of the white paint in speckles. The remainder of the specimen was kept wrapped in saline-soaked gauze. VIC-Snap (correlated solutions) was used for image acquisition, and VIC-2D (correlated solutions) was used to calculate displacement and strain. A mirror was mounted on the fixture directly beneath each specimen to observe the posterior aspect of the bone, corresponding with the tensile surface, to collect DIC data.

Engineering stress from the load and whole bone geometrical data, and engineering strains from DIC were converted to true stress and true strain. The elastic modulus was determined from the linear region of the true stress-strain behavior for each fibula.

RESULTS AND DISCUSSION

Of the 6 porcine fibulae, one newborn, both 1-month, and one 3-month specimen underwent visible fracture through the periosteum. Both newborn specimens, both 1-month specimens, and one 3-month specimen experienced impingement in the bending fixture between the loading noses and lower supports. The tensile displacement and strain at the initial point of yielding are reported in Table 1.

Table 1: Displacement and Strain at Yielding, Maturing Porcine Fibulae.

Specimen	Displacement at Yielding (mm)	DIC Strain at Yielding (%)	Elastic Modulus (GPa)
Newborn_1	0.75	1.03	0.45
Newborn_2	0.75	0.74	0.54
1Month_1	0.66	0.67	1.21
1Month_2	0.67	0.78	1.01
3Month_1	0.75	1.10	3.53
3Month_2	0.60	0.80	2.83

Qualitatively, as maturation progressed from newborn to 3-months, elastic modulus, yield stress and stress at fracture increased, as expected (Figure 1). Both newborn fibulae underwent a maximum true stress of 10.8MPa, both 1-month fibulae underwent a maximum true stress of 10.1MPa, and the two 3-month fibulae experienced a maximum true stress of 20MPa and 86MPa. Displacement at the initial point of yielding decreased as the fibulae matured in all specimens except one 3-month fibula. In contrast, the strain behavior of maturing porcine femora at yielding did not produce a clear trend; however, strain to fracture appeared to generally decrease with maturation, consistent with Öhman et al.'s study of pediatric bone [4].

The reported elastic moduli are in good agreement with Bertocci et al.'s [3] elastic moduli for 3-month porcine femora, as well as the elastic moduli reported in Ambrose et al.'s [5] study of children 0-1 year, suggesting a satisfactory equivalence of 0-3 months porcine fibulae and 1-3 years children.

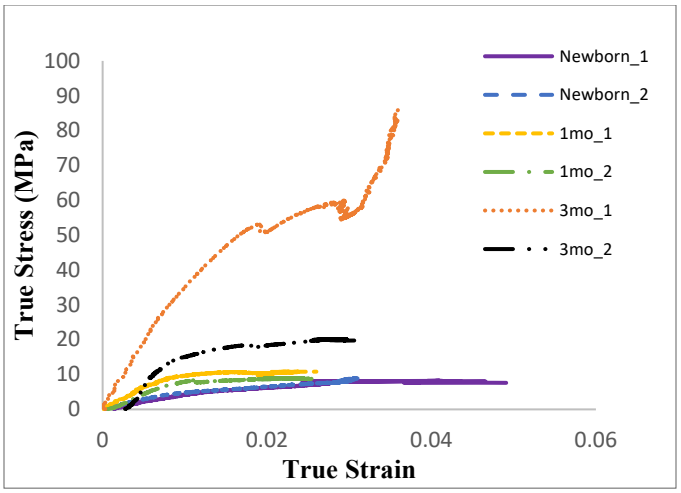

Figure 1: Mean true-stress, true-strain (from DIC measurements) of maturing porcine fibulae from the posterior tensile surface showing an increase in elastic modulus, yield, and fracture stress, and overall decrease in fracture strain with maturation.

CONCLUSION

Using DIC to quantify displacement and strain of maturing porcine fibulae in bending is a promising approach to characterize the whole-bone mechanical behavior of maturing bone. Further study is underway to correlate findings with FEA, in which stresses and strains will be compared up to failure.

REFERENCES

1. Theobald, P, et al. *Journal of Clinical Orthopaedics and Trauma*. 24-27, 2012.

2. Cheong, V, et al. *Journal of the Mechanical Behavior of Biomedical Materials.* 68-76, 2017.

3. Bertocci, G, et al. *Journal of Forensic and Legal Medicine.* 5-11, 2017.

4. Öhman, C, et al. *Bone*. 769-776, 2011.

5. Ambrose, C, et al. *Bone*. 151-160, 2018.

ACKNOWLEDGEMENTS

This study was supported by Case Western Reserve University's Flora Stone Mather for Women and MalwareBytes. Porcine limbs were provided by NSRRC grant U42 OD011140.

QUANTITATIVE MEASUREMENT OF NANOSCALE COLLAGEN FIBER MECHANICAL DAMAGE

[1,2]Christopher Slater and [1]Steven J. Eppell

[1]Case Western Reserve University, Cleveland, OH, USA

[2]The Ohio State University College of Medicine, Columbus, OH, USA

Email: cas291@case.edu

INTRODUCTION

In the United States it is estimated that over 16 million people experience injury to tendons or ligaments each year [1]. Healing from such injury takes many months and can have a significant impact on quality of life and ability to work. Current treatments often do not lead to a full recovery [2]. Finding better options for assessing tendon injuries and treating them is limited by our basic understanding of the tendon tissue [2] and its response to mechanical load.

We aim to improve the basic understanding of tendon tissue by elucidating it's nanoscale mechanical behavior. This abstract describes a method of detecting tendon damage of single collagen fibrils. We use a fluorescently labeled collagen hybridizing protein (CHP), that binds to damaged collagen molecules indicating molecular level damage. For the first time, we use a micro-electromechanical system (MEMS) device to damage isolated fibrils and then look at molecular level damage in gauge regions only a few microns long. This work is expected to aid understanding of how we can detect early tendon damage at the single collagen fibril level. Such early detection is expected to allow for treatments and/or recommendations for lifestyle changes that will obviate tendinopathies.

METHODS

Collagen fibrils are isolated from rat tail tendons [3]. Using micromanipulators, single collagen fibrils are placed on a MEMS and epoxied down for testing using a UV curing epoxy. After straining to a level expected to induce damage, the fibrils were stained with CHP to determine the level of damage. Damage was associated with fluorescent intensity which was, in turn, associated with molecular level damage due to straining.

To find correlations between fluorescence intensity and mechanical parameters like ultimate strain and fibril modulus, it was necessary to take into account: variations in preexisting damage between collagen fibrils, variations in damage along single fibrils, and photobleaching. To address this, we created the Relative Fluorescent Increase (RFI) method. This method assumes there is variation in preexisting damage both along a fibril and among fibrils. The method uses the fact that the control region experiences no strain. However, photobleaching and the need to restain with CHP after straining both cause the raw fluorescence intensity value of the control region to change between the pre and post straining images. These changes affect the gauge and control regions equally. Thus, a ratio of ratios allows us to recover an RFI of one for a fibril that experiences no damage during the strain.

$$RFI = \frac{Intensity_{Post-gauge}/Intensity_{Post-control}}{Intensity_{Pre-gauge}/Intensity_{Pre-control}}$$

RESULTS AND DISCUSSION

We observed an inverse relationship between modulus and pre-damage fluorescence intensity in the gauge region (Fig. 1). This is likely due to using a fibril area to compute the stress needed to determine modulus that was based on SEM images

of fibril diameter. This measurement doesn't take into account that some of the collagen molecules in the fibril are damaged and can't carry any load. The effect of this is that, as more molecules are damaged, the lower the apparent modulus. This makes it

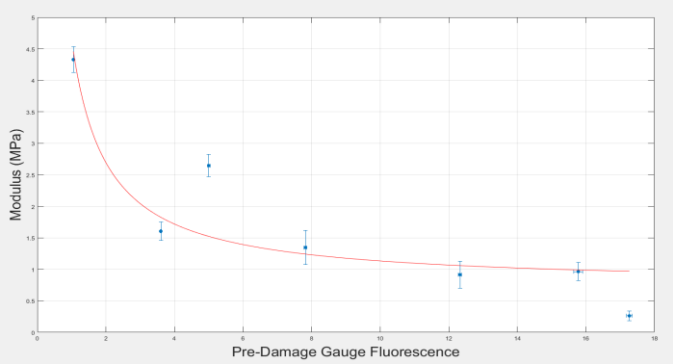

Figure 1. Inverse relationship between modulus and pre damage control fluorescence. Red line shows best fit line of inverse relationship (y = A + B/x).

important to take into account modulus when relating damage and final strain.

Based on this, we constructed a 3D plot with axes for: RFI, final strain, and modulus (Fig. 2).

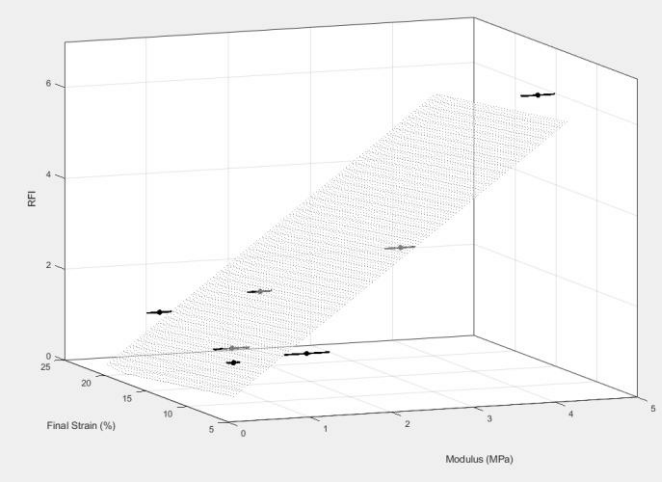

Figure 2. Three Dimensional Relationship of Final Strain, Modulus and Damage (RFI). There is a strong planar relationship between Final Strain, Modulus and RFI (R^2 = 0.93).

The parameters correlated well with each other fitting on a plane with an R^2 value of 0.93. This supports the notion that it is quite important to properly control for the various inhomogenieties that exist in populations of collagen fibrils when looking at their mechanical behavior at the nanoscale.

CONCLUSION

Using seven individual collagen fibrils we developed a novel method for accurately measuring molecular level damage using CHP. Using the RFI method showed a significant increase in florescence intensity with a Wilcoxon signed rank test returning a p value of 0.02. This shows that detecting molecular level damage of isolated collagen fibrils using MEMS devices with gauge regions of a few microns to strain and CHP fluorescence to assay for damage is possible. By taking into account variations in modulus we were able to find a strong correlation between fluorescent intensity and ultimate strain. While enticing data suggesting specific structure/function mechanisms at play in the damaging of the fibrils was obtained, improvements to the technique are warranted to improve the control that is possible during the experiments. Real time fibril strain measurements are needed. In addition, use of quantum dots rather than organic fluorophores would substantially improve the method as they do not photobleach.

REFERENCES

1. Roshan, J., et al. *The Journal of Hand Surgery*. 102-112, 2008.

2. Wu, F., et al. *The Journal of Hand Surgery. EFORT Open Reviews,* 332-342, 2017.

3. Liu, Y., et al. *A Novel Method to Extract Type-I Collagen Fibrils From Mammalian Tendons*. Master's thesis, Case Western Reserve University, 2015.

Modeling Selective Activation of the Median Nerve

[1]Marianna Urdaneta Morillo and [1]Katharine Polasek

[1]Hope College, Holland, MI, USA

Email: polasek@hope.edu

INTRODUCTION

Achieving referred sensation via surface electrical stimulation for the median nerve experimentally has been found to be difficult and time consuming. Our goal is to design an electrode array to be placed over the cubital fossa area, and have the ability to adjust the voltage combinations used for stimulation until a good referred sensation is achieved. The goal of this research was to investigate stimulation techniques that resulted in selective activation and to compare activation when varying the nerve anatomy.

METHODS

A 3-dimensional, anatomically-based finite element method model of the arm was used to model nerve activation due to electrical stimulation at the skin [1]. The model included electrodes near the elbow and electrical properties for each tissue type. Different median nerve cross-sections were used to test the effects of human variability in the predicted selectivity. These cross-sections consisted of the same number and size of fascicles, but rearranged. This abstract covers nerve arrangements C and D (Fig. 1).

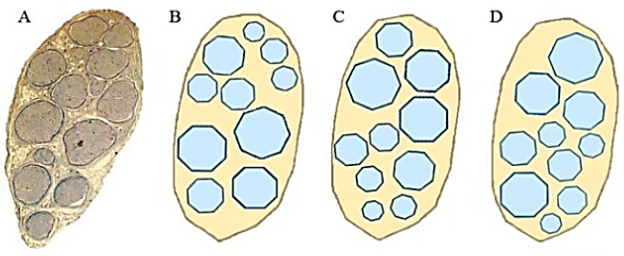

Figure 1: (A) Actual cross section of the median nerve near the elbow. (B)-(D) Nerve cross-section used in a previous study and used here to look at anatomical variations [1].

The NEURON programming environment [2] was used to test every axon in every fascicle and determine which axons fired, giving the percentage activation of every fascicle for different voltage combinations used as stimulus. The number of axons in each fascicle was based on the area of the fascicle and ranged from 50 to 125.

A quality of activation was created in order to quantify and compare the selectivity of the simulation data. The key contributors to quality of activation are as follows: reachability which included the distance from fascicle center to the skin and resistivity of the perineurium, type of selectivity (singular, dual, group of 3), and delta of activation between the lowest selective fascicle and the next highest non-selective fascicle. Voltage combinations were considered selective if one to three fascicles had an activation that had at least 25% difference from the lowest selective fascicle to the highest non-selective fascicle.

$$Q_{act} = \frac{reachability_1 + \cdots + reachability_n}{n} * \Delta$$

To look at effects of varying anatomy, simulations were performed in cross sections C and D (Fig.1) using the same voltage combinations. The results were compared using the quality of activation.

RESULTS AND DISCUSSION

This summer 3,442 simulations were run, which resulted in 2,003 unique results and 1,011 unique and selective results (selectivity >= 25%). Out of the selective results, 16% produced activation of a single fascicle, 57% a pair of fascicles, and 27% groups of 3 fascicles. The average quality of activation was: 2.06±0.44 for single fascicles,

2.54±0.49 for pairs of fascicles, and 2.09±0.32 for groups of fascicles. The fact that the quality of activation was similar across groups is likely due to the way the quality of activation was defined but does suggest that good selectivity was obtained for each group.

Nineteen unique voltage combinations were simulated for nerve internal arrangements C and D. The quality of activation of each voltage combination is compared in Fig. 2.

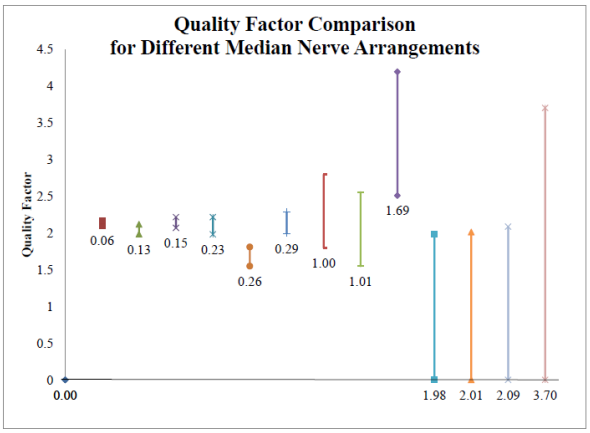

Figure 2: Quality of activation difference for voltage combinations between internal nerve arrangements C and D

In figure 2 the single point at the origin represents the six voltage combinations that resulted in a quality factor of zero for both nerve arrangements. Furthermore, six others had a quality factor difference less than 3% between the two nerve arrangements. The rest of the voltage combinations show a higher quality factor discrepancy as only one of the nerve arrangements succeeded in achieving a selective result. This suggests that voltage combinations that give a selective result in one person or model will not necessarily give a similar result in another person. However, the fact that many were similar was an encouraging result.

CONCLUSION

Computer modeling was used to evaluate different stimulation parameters with the goal of selective nerve activation. These simulations suggest that selective activation is possible and maybe even similar across differences in anatomy. Further investigations are underway to develop general techniques that can produce selective activation in all people and experimental testing of these predictions is planned.

REFERENCES

[1] J. Gaines, K. Finn, J. Slopsema, L. Heyboer, and K. Polasek, "A model of median nerve activation using surface electrical stimulation," *J. Comput. Neurosci.*, vol. Accepted P, 2018.

[2] M. L. Hines and N. T. Carnevale, "The NEURON simulation environment," *Neural Comput*, vol. 9, no. 6, pp. 1179–1209, 1997.

ACKNOWLEDGEMENTS

This material is based upon work supported by the National Science Foundation under Grant No. 1805447.

Biomechanics of the Praying Mantis Foreleg Strike

[1]Walid Abuhashim, [1]Colleen Unsworth, [2]Gavin Svenson, [2] Sydney Brannoch [1]Henry Astley

[1]The University of Akron, Akron, OH, USA

[2]Case Western Reserve University, Cleveland, OH, USA

Email: waa23@zips.uakron.edu

INTRODUCTION

Praying mantises (*Mantodea*) catch prey via rapid motion of their specialized forelegs. Due to the high speed requirements to catch quick prey items, a mantis must accelerate their limb segments rapidly, which depends upon mechanical power. Besides increase in muscle mass organisms can increase mechanical power output by coupling muscle with an elastic tissue to generate relatively greater power than muscle alone. In this phenomenon, known as power-amplification, elastic potential energy is stored in elastic structures and rapidly released, resulting in power outputs beyond those of muscle, as seen in the flea jump. This research investigates the foreleg strike of the Chinese Mantis (*Tenodera sinensis*) capturing live prey (*Periplaneta americana*) to determine whether power-amplification is used in the mantis strike.

METHODS

The praying mantises were collected from the Cleveland Metro Parks. From the mantises collected, we recorded 11 strikes at 700 frames/second with two Edgertronic high-speed cameras, of the mantises striking at cockroaches attaches to strings. The use of 2 cameras allowed us to track the movements of points in three dimensions. We used a calibration device to convert the pixels to metric units.

There were 8 points that were being tracked for the strikes. The points were digitized via MATLAB DLTdv5 software package. These 8 points then made 4 vectors. Upon which we calculated angular displacement, velocity, and acceleration for the 3 joint angles.

The strikes of the mantis were split into 2 phases an extension phase, where the mantis was extending its forearms to attain its pray, and a grabbing phase, where the mantis was closing its arms to grab its prey.

RESULTS AND DISCUSSION

From the 11 strikes, the angles were calculated and plotted as shown in figure 1.

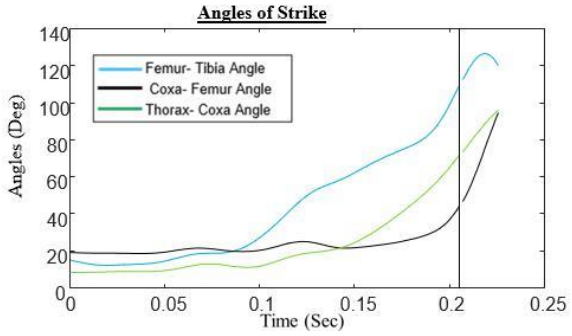

Figure 1: 1 of the strikes joint angular displacements over time, the vertical line denotes the split.

The angular acceleration was then calculated from the angles. the fastest average joint angular acceleration was the Femur Tibia Joint during extension with a velocity of 2,180 deg/sec, as seen from table 1.

Table 1: Average max angular velocity of 11 strikes, split into 2 parts: Extension and Grabbing.

	Peak Angular Velocity	
	Extension (deg/s)	Grabbing (deg/s)
Femur Tibia Joint	2,180	2,130
Coxa Femur Joint	970	2,700
Thorax Coxa Joint	1,260	1,320

Compared to Dr. Patek's study of mantis shrimp, which was found to exhibit power amplification, had an angular velocity of 38,888 deg/sec [1]. More then 10 times faster then the preying mantis strikes. Hence, the angular velocity's suggest purely muscular actuation. To confirm this we will use inverse dynamics to compare joint angles, angular acceleration, torque, and power across individual foreleg segments (coxae, femora, tibiae, tarsi) to identify coordination and control patterns and which joints are primarily responsible for generating power. The apparent lack of power amplification in *T. sinensis* forelegs suggests that tradeoffs may preclude some animals from using it, such as the dual function of *T. sinensis* forelegs for both prey capture and locomotion.

CONCLUSION

The results suggest an apparent lack of power amplification in *T. sinensis* forelegs. For the praying mantis had a fraction of the mantis shrimp speeds. Which had two phases of behavior, extension and grab. The trade-offs may deter some animals from using power amplification, such as the dual function of *T. sinensis* forelegs for both prey capture and locomotion.

REFERENCES

1. Patek, S, et al. *Nature*. Page 428 (2004).

ACKNOWLEDGEMENTS

We would like to acknowledge the University of Akron Biology Department Tiered mentoring program for funding part of this research, and pairing the student with the lab. As well as Stephen Howe for demonstrating how to use and setup the cameras.

Quantitative Analysis of Hemiplegic Gait Following Forced Exercise Intervention

[1]Michael Haupt, BS, [1,2]Susan M Linder, PT, DPT, [2]Matt Streicher, MS, [1]Sara Davidson, BS, PTA, [2]Jay L Alberts, PhD
1. Cleveland Clinic, Department of Physical Medicine and Rehabilitation, Cleveland, OH, USA
2. Cleveland Clinic, Department of Biomedical Engineering, Cleveland, OH, USA
Email: hauptm@ccf.org

INTRODUCTION

Residual motor deficits post-stroke can significantly limit activities of daily living and reintegration into personal and professional settings. Repetitive task related sensorimotor training is a rehabilitation technique used to induce motor learning and neuroplasticity in order to regain motor function post stroke [1]. Aerobic exercise training has previously been shown to enhance motor learning when applied immediately before repetitive task practice (RTP) [2]. The aim of this study is to determine the effects of an 8-week forced aerobic cycling intervention on post-stroke hemiplegic gait parameters. This study is part of a larger clinical trial comparing forced exercise (FE) and RTP compared to RTP alone.

While clinical tests measuring functional walking capacity can be used to assess patient performance over time, it does not provide insight into the kinematic and biomechanical changes that occur before and after intervention in individuals with hemiplegia. Given the variability observed in patients as it relates to severity of spasticity, muscle weakness, and compensatory mechanisms, unique differences in gait exist. Previous studies have yet to explore three dimensional gait analysis for patients undergoing forced exercise cycling intervention. This study provides quantitative insight into spatial, temporal, and joint angle parameters that change over the course of an 8-week FE intervention.

The Gait Deviation Index (GDI), Gait Variability Index (GVI), and Enhanced Gait Variability Index (eGVI) are validated indices proposed as tool to overall quantify gross gait pathology. Calculation of the GDI is performed using kinematic parameters whereas GVI and eGVI are calculated using solely spatiotemporal parameters. Calculation of all three of these indices involves using principle component analysis to weight the contribution of the specific variables to abnormal gait. Patient values are compared to a reference population and given a single composite score.

METHODS

Patients with greater than 6 months post unilateral stroke with residual hemiparesis underwent a trial of FE followed by upper limb RTP three times per week for eight weeks. The FE group completed a 45-minute FE aerobic cycling intervention on the FE bike followed by a 45-minute session of RTP.

6-minute walk test (6MWT) performance was assessed pre- and post-intervention to quantify functional walking ability. Spatial-temporal and kinematic data was collected at baseline and at the end of training using the Computer Assisted Rehabilitation Environment (CAREN) system (Figure 1).

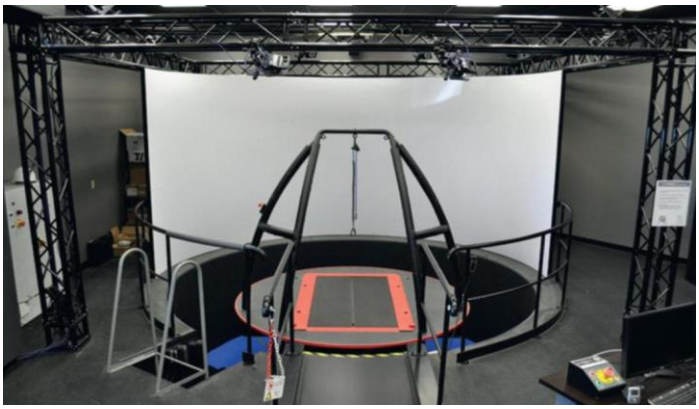

Figure 1: CAREN system is comprised of a split-belt treadmill on a tilting base, real time motion capture, and a 120-degree surrounding projection screen.

RESULTS AND DISCUSSION

Participants' performance in the 6-MWT improved by an average of 55±41 m walked at the end of the 8-week cycling trial (Figure 2). Gait velocity increased by a mean of 0.11 m/sec. All three gait index values on average changed to more closely resemble a control population after intervention (Table 1). Affected and unaffected limb values for the GDI improved by 0.32 and 0.01 standard deviations, respectively. Affected and unaffected limb values for the GVI improved by 0.1 and 0.46 standard deviations, respectively. Affected and unaffected limb values for the eGVI improved by 0.21 and 0.19 standard deviations, respectively. Forced aerobic cycling appears to have a beneficial effect on walking performance and improves biomechanical characteristics of gait.

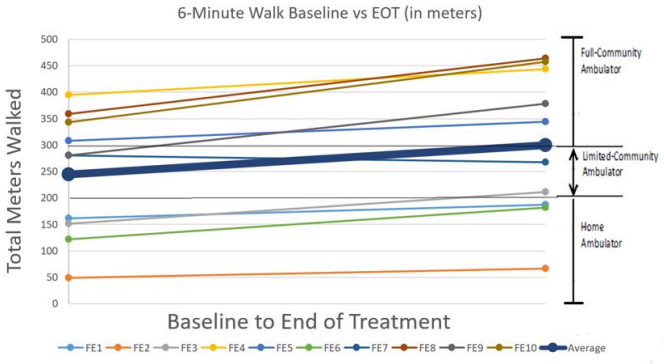

Figure 2: Representation of 6-minute walk test performance for each of the 10 participants pre- and post-intervention.

			Average Score	Change at EOT
GDI	**Affected Limb**	*Baseline*	77.2	**3.2**
		EOT	80.4	
	Unaffected	*Baseline*	79.0	**0.1**
		EOT	79.1	
GVI	**Affected Limb**	*Baseline*	81.4	**1.1**
		EOT	82.5	
	Unaffected Limb	*Baseline*	82.1	**4.6**
		EOT	86.7	
eGVI	**Affected Limb**	*Baseline*	120.2	**-2.1**
		EOT	118.1	
	Unaffected Limb	*Baseline*	119.1	**-1.9**
		EOT	117.2	

Table 1: Pre and post GDI, GVI, and eGVI scores calculated from 3-dimensional gait analysis software.

CONCLUSION

Improvements in 6-MWT performance and composite indices of gait pathology were observed following an 8-week forced exercise intervention followed by upper limb repetitive task practice. These data indicate that improvements in gait can occur with forced aerobic cycling without task specific gait training. Improvements in walking capacity were unexpected as a recently published clinical guidelines found that lower limb cycling is not efficacious in improving locomotion in post-stoke individuals [3].

REFERENCES

1. Hatem SM et al. Rehabilitation of Motor Function after Stroke: A Multiple Systematic Review Focused on Techniques to Stimulate Upper Extremity Recovery. *Front Hum Neurosci*. 2016;10:442. Published 2016 Sep 13.

2. Linder SM, Rosenfeldt AB, Davidson S, et al. Forced, Not Voluntary, Aerobic Exercise Enhances Motor Recovery in Persons With Chronic Stroke. *Neurorehabilitation and Neural Repair*. 2019;33(8):681-690.

3. Hornby, T. George et al. Clinical Practice Guideline to Improve Locomotor Function Following Chronic Stroke, Incomplete Spinal Cord Injury, and Brain Injury. *Journal of Neurologic Physical Therapy*. January 2020;44;1:49-100

Validating the Use of an IMU-based System to Capture Patient-handling Tasks

Bridget Gagnier, Reese Moschetta, Yeageon Song, Dr. Brooke Odle

Hope College, Holland, MI, USA

Email: bridget.gagnier@hope.edu

INTRODUCTION

Lower-back pain and injury is a common concern among healthcare workers. Manual patient-handling tasks often require caretakers to assume awkward postures that cause stress at the low back. OpenSim[1] is a freely available and open-source software that models human movement. Open-source, personalized computational musculoskeletal models that are capable of generating dynamic simulations of human movement can determine forces on the low back and trunk muscle activation. These models can be used to improve existing treatment methods and preventions. There are currently no publicly available models that are validated for patient-handling tasks. Advances in wireless inertial measurement unit sensor technology enables data collection in more realistic environments. This study aims to validate the use of inertial measurement units(IMUs) to capture simulated patient-handling tasks.

METHODS

Data were collected from two able-bodied male participants, both 21 years of age. Prior to data collection, both participants signed informed consent forms, which were approved by the Human Subjects Review Board at Hope College. Retroreflective markers (Optitrack, Corvallis, OR) were placed on the bony prominences of the whole body and seven inertial measurement unit (IMU) sensors (Xsens, Enschede, Netherlands) were placed on the pelvis and bilaterally on the thigh, shank, and foot. The subjects stood with each foot on a force plate. The subjects performed three simplified patient-handling tasks: a squat, a squat with an arm curl, and a reaching down motion. The knee and hip joint angles were calculated in the sagittal plane using the marker data, IMU system, and OpenSense. The marker data were filtered using a fourth-order Butterworth filter with a 10Hz cutoff frequency. The joint angles from the IMU system were compared to the ones calculated from the markers(comparison 1). The IMU orientations were put into OpenSim using its new software OpenSense. OpenSense uses the orientations to calculate joint angles. These angles were compared to the angles calculated by the IMU system(comparison 2). The lifting full-body model[2] was used for computing joint angles in OpenSim. A root mean square error (RMSE) was used to compare the joint angles.

RESULTS AND DISCUSSION

The average RMSE for comparison 1 is 8.85° for the knee joint angle and 11.67° for the hip joint angle. The average RMSE for comparison 2 is 2.09° for the knee joint angle and 1.16° for the hip joint angle. The average RMSE and standard deviation for comparison 1 is 4.44(1.82) for knee angle and 9.92(2.28) for hip angle for subject 1 and 13.25(4.52) for knee angle and 13.42(3.20) for hip angle for subject 2. The average RMSE and standard deviation for comparison 2 is 2.58(1.33) for knee angle and 1.23(0.25) for hip angle for subject 1 and 1.60(0.37) for knee angle and 1.08(0.32) for hip angle for subject 2. The results are consistent with previous sample data that were collected before subject recruitment, except for the higher knee angle error for Subject 2. High hip angle error, though, is consistent with previous sample data. The results are fairly consistent with the values that were reported in the literature[3]. The values in the literature are lower, but the pattern of the hip angle RMSE being much higher is consistent. To investigate the higher hip angle error two tests were done. First, the displacement of the markers between each trial was checked. Since the

markers were used with the Xsens system, the markers for the waist were placed on the strap that was used to secure the pelvis IMU (instead of directly on the bony landmark). It is possible that the strap moved during the data collection, potentially impacting the marker-based hip angle calculations. To determine if the strap moved at all between the trials, the maximum y-coordinate (vertical direction) of the markers for each trial were compared to the maximum y-coordinate of the static trial. After looking at the change in y-coordinates the maximum difference was only 2.33cm with an average of 0.0068cm. This likely isn't enough change to cause the errors that were given, so it was decided that it wasn't the cause of the discrepancy. Second, a goniometer test was done. A goniometer was used to compare joint angles of the IMU system and marker data with the angles of the goniometer. The hip angles at the top and bottom moments of a squat were measured using a goniometer. After comparing these angles it was noted that the angles determined from the markers are closer to the angles from the goniometer. The joint angles for the three methods can be seen in Figure 1. This leads to the possibility that the definition of the hip angle is different for the IMU system. Since the hip joint is a ball and socket joint, it is much more complicated and the definition of flexion and extension could differ. Future work involves collecting data from additional subjects, to see if these results are consistent as well as perform more sophisticated statistical analyses that require more data. The data will also be partitioned out into individual cycles in order to compare results between subjects.

CONCLUSIONS

The results of this proof of concept study show that the joint angles computed using the IMU system and OpenSense are very comparable. The joint angles from the IMU system and the marker data are fairly comparable. The knee joint angle RMSE between the IMU system and marker data is higher, but reasonable. The hip joint angle RMSE between the IMU system and marker data is very high. After some initial tests it is unknown why these errors are higher. Future data collections may provide insight on the hip angle discrepancy and whether the model is suitable for generating simulations of additional patient-handling tasks with IMUs.

REFERENCES

1. Seth et al, PLoS Comput Biol, Vol. 14(7), 2018
2. Beaucage-Gauvreau et al, Computer Methods in Biomechanics and Biomedical Engineering, vol. 22, P.451-464, 2018
3. Teufl et al, PLoS ONE, Vol. 14(2), 2019

ACKNOWLEDGMENTS

This study is supported by the Michigan Space Grant Consortium, Grant number 80NSSC20M0124 and the Clare Boothe Luce Scholars Program.

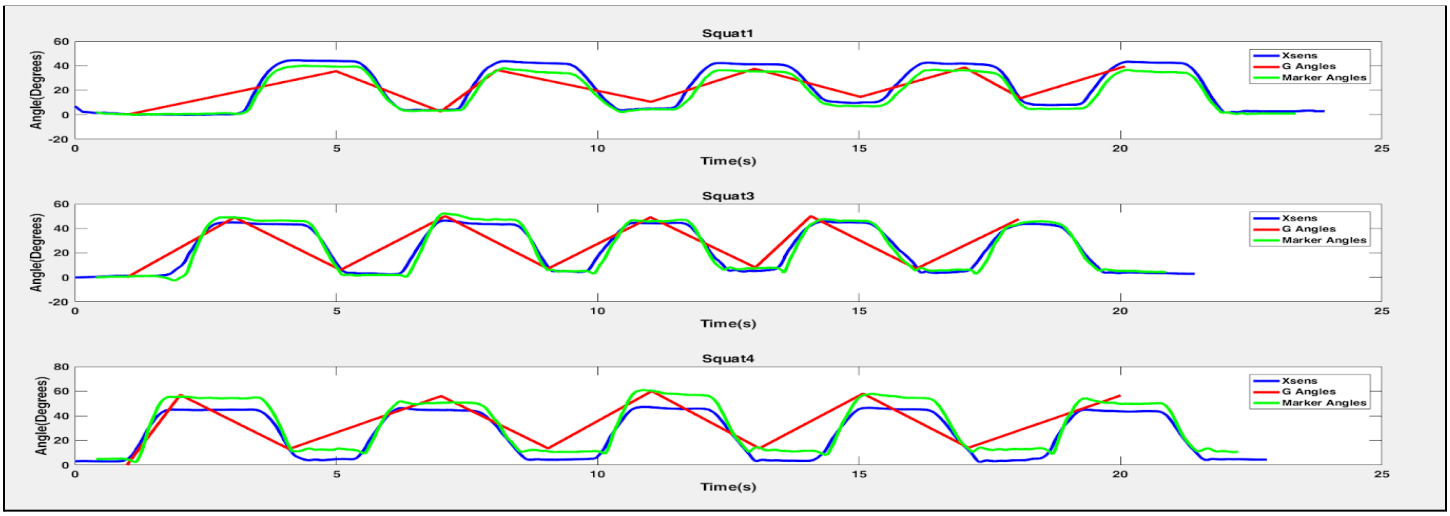

Figure 1: IMU, goniometer, and marker data angles show that the marker data is closest to the goniometer values.

Importance of Including BMI, Weight, and Height in Arthroplasty Revision Data Analyses

[1]Lauren Long (Presenter) and [1]Richard Hughes

[1]University of Michigan, Ann Arbor, MI, USA

Email: lnlong@med.umich.edu

INTRODUCTION

Arthroplasty registries are an important source of revision data for surgeons, patients, hospitals, and payers to use in selecting implants. In order to separate out patient-level factors from implant factors that affect revision risk, registries use Cox proportional hazards modeling to adjust for age, sex, and body mass index (BMI). BMI is used since it is easy and cost-effective method to measure body fat and is highly correlated with other risk factors such as elevated blood pressure and diabetes. It is very widely used in biomedical research. However, the theoretical basis for using BMI in analyses of implant revision risk is weak. In contrast, the two components of BMI (height and mass) may have a firmer theoretical basis.

The purpose of this project was to conduct an engineering analysis to determine if height and weight should be included along with BMI for the analysis of hip arthroplasty revision data.

METHODS

Engineering analyses was conducted to compute the resultant force on the hip during gait and the transfer of energy that occurs when a patient falls from a standing position to determine the theoretical effects of height and weight on revision risk.

Studies have shown that hip width is correlated to height, so as height increases pelvic width also increases [1]. Half of the pelvic width, length (b) in Figure 1, is approximately the moment arm corresponding to body weight (W) acting on the hip joint responsible for external moment. The internal moment created by the moment arm (a) in Figure 1 that corresponds to the force created by the hip abductor muscles, is correlated to the moment arm b. Thus, a is also related to height (H) [2]. In the force balance calculations at equilibrium shown in Figure 1, the internal moment must equal the external moment, so the scaling factor, k, and height, H, cancel out.

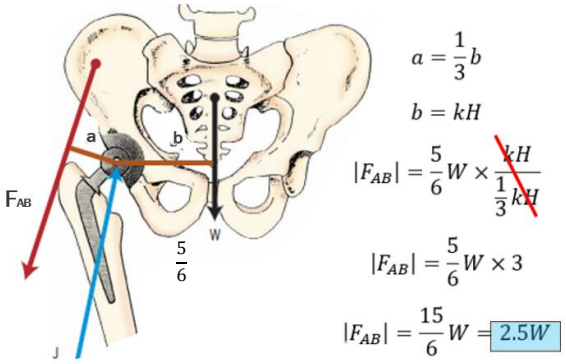

Figure 1: Simplified force diagram of the hip joint and calculations for F_{AB}, the hip joint reaction force.

Potential energy and kinetic energy are defined as mass×gravity×COM height and ½ mv^2 respectively, where COM stands for center of mass. As shown in Figure 2, when falling from a standing position all potential energy is converted to kinetic energy upon impact with the ground since energy is conserved [3].

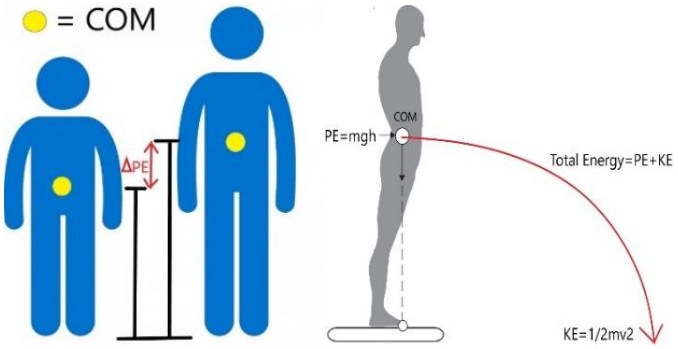

Figure 2: Depicts the change in COM with height and the transfer of energy when a patient falls.

RESULTS AND DISCUSSION

BMI is recorded at every physician visit and this metric can be used to compare patients to national averages to predict outcomes. BMI has been shown clinically to be related to dislocation, which is one reason for revision. Thus, it should be considered as a candidate for inclusion in revision risk analyses.

Body mass and height also have sound theoretical reasons to include in the analysis of hip arthroplasty implants. According to our analyses, body mass is a critical variable to consider when looking at arthroplasty revision data because the load on the hip is proportional to body mass. Our modeling is supported by in vivo studies of hip loading conducted by Bergmann et al. using instruments prostheses [4]. The correlation between body weight and load placed on implants is crucial when analyzing revision data since an increase in load increases the wear on components of the implant such as polyethylene liners. When these liners break down from cyclic motion under load, particles induce the well-known process of wear-induced osteolysis around the implant. This results in loosening of the implant, and this often results in revision of the implant.

Peri-prosthetic fracture of the femur resulting from a fall is another reason for revision, so the analysis of height, and potential energy is relevant to including height in revision analyses. As shown in the calculations in Figure 1, height does not affect load placed on the joint, but it is still a crucial data element to analyze as it is directly correlated to the position of the COM. An increase in height increases potential energy and because mass is not changing the patient is simply hitting the ground at a higher velocity. Taller and heavier patients have higher potential energy increasing their risk for peri-prosthetic hip fracture when falling.

CONCLUSION

All three variables need to be reported when analyzing hip revision data. BMI is an easy and informative metric to collect and is correlated to an increased risk of dislocation. Weight is also theoretically useful as it can be used to predict load placed on components during various activities which impacts the amount of wear on the implant that increases risk of revision. Lastly weight and height may be indicative of increased risk of peri-prosthetic fracture which is also a reason for revision.

The question of which variables to include in Cox modeling of revision risk hazard is more complicated. If these three variables are highly correlated then multicollinearity may lead to numerical instability and biased estimates in maximum likelihood estimations of the Cox model. Therefore, the variables should be selected based on their theoretical relationship of the outcome of interest.

REFERENCES

1. Ridgeway B, et al. The relationship between anthropometric measurements and the bony pelvis in African American and European American women. Int *Urogynecol J 22*:1019-24 (2011)
2. Neumann, D.A., Kinesiology of the Hip: A Focus on Muscular Actions. *Journal of Orthopaedic & Sports Physical Therapy 40*(2):82-94 (2010)
3. Agarana, M.C., Energy Conservation Analysis of Human Body Locomotion Pendulum Dynamical System. *Proceedings of the World Congress on Engineering and Computer Science Vol II* (2017)
4. Bergmann, G., et al. Hip joint loading during walking and running, measured in two patients. *Journal of Biomechanics*, *26*(8):969–99. (1993)

The Impact Balance Training Has on Kinematic Measurements Post Stroke

[1]Abigail Tolstyka, Sydney Bajusz, [2]Ann Reinthal, and Deborah Espy

[1]Cleveland State University, Cleveland, OH, USA

Email: a.tolstyka@vikes.csuohio.edu

INTRODUCTION

Stroke is a neurological disease that causes disability in adults and increases the risk of falling. The integration of technology and rehabilitation strategies are systematically used in physical therapy to target muscle activity in post-stroke patients. This addresses initial muscle weakness of the affected side of the body, as well as asymmetrical postural behavior [1]. The objective of targeting mobility control is to achieve body support, balance control, and gait progression [2].

A focus on stepping patterns in post-stroke patients is one technique in retraining balance. This includes practicing forward, lateral, and backward stepping. Stroke patients typically use a different step strategy to compensate for their affected limbs. Measuring the length of each step is necessary when analyzing a change in step reaction and adjustment over a period of time. Incorporating proper weight bearing exercises during rehabilitation is another method to restore balance. Single-leg exercises are used to train the affected side of the body and achieve symmetrical gait and weight bearing [3].

This research study used different kinematic measurements to discover whether playing motion-sensing video games while attached to a harness would improve balance in post-stroke recovery patients. The video games incorporated exercises such as kicking, multidirectional stepping, reaching, and weight shifting. Variables such as time spent in a one-leg stance and stride length were used to evaluate differences in coordination, and balance from the beginning to the end of the study.

METHODS

Participants consisted of older adults who experienced a stroke at least six months prior to enrollment in the study. The study consisted of three groups; control, slip and gaming. Along with pre and post testing, gaming participants attended ten weeks of gaming sessions, including one session to learn the game, two gaming therapy sessions with motion capture (week two and ten) and seven regular gaming therapy sessions. The games played during session 2 and 10 were played on the same level in order to compare kinematic balance data via CORTEX motion capture and MATLAB software; however, during sessions three through nine participants were able to progress to harder levels based on their reported rate of perceived stability (RPS). 20,000 Leaks and Target Kick are analyzed in this discussion.

20,000 Leaks displays an aquarium box with holes to encourage participant stepping and reaching as they plug the leaks. The leaks appear on the walls and floor of the aquarium and participants must move in all four directions and hold their hand or foot over the hole until the leak is stopped. Two rounds which last about three minutes are played at each session. For this game, pre to post session step length was used as an indicator of balance skills.

Target Kick prompts a one-leg stance with a simulation of kicking a soccer ball into a goal. The

screen shows a soccer goal with targets guarded by a goalie. The participant must aim for these targets however, they must alternate which leg they use for each kick. The amount of time spent on one leg was evaluated pre to post in order to represent balance during Target Kick.

RESULTS AND DISCUSSION

On average, the post-session results displayed longer step lengths per millimeter on the XYZ plane than the pre-session results for this participant. During the pre-session, the participant took 46 total steps with an average step length of 266.5 millimeters. A total of 30 steps were taken in the post-session with an average step length of 297.4 millimeters**.** The participant was able to complete the game by using fewer, more deliberate steps. This paired with the increased stride length suggests improved confidence, balance, and coordination moving in all four directions.

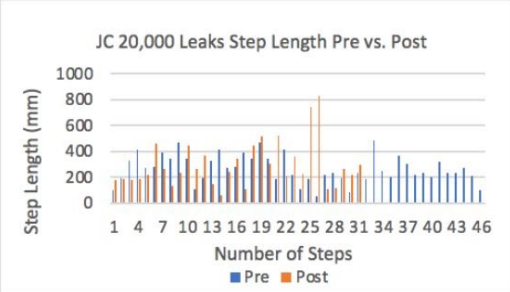

Figure 1: Graph shows length of each step during 54 seconds of 20,000 leaks for pre and post sessions.

The same participant showed improvements in one-leg stance on his hemipelagic right-side while playing Target Kick. During the pre-session, the average time in one-leg stance was longer for his non-hemipelagic left-side than his hemipelagic right-side. However, during the post-session the average time in one-leg stance was relatively the same on both sides, with the left side remaining constant and the right-side showing improvement. The reduced disparity in one-leg stance time suggests a greater sense of balance, specifically in control and coordination between both sides of the body.

JC Target Kick Average One-Leg Stance in Seconds		
	Left Leg	**Right Leg**
Pre-Session	**0.660**	**0.552**
Post-Session	**0.650**	**0.639**

Table 1: Average time spent in one-leg stance during Target Kick pre versus post-session in seconds

CONCLUSION

Overall, this participant showed notable improvement with balance related activities. The video games encouraged balance motions in a unique and engaging form, which enhanced the patient's balance abilities, as demonstrated by more purposeful and even stepping and kicking during post-session gaming.

REFERENCES

[1] Jamal, K, et al. Disturbances of spatial reference frame and postural asymmetry after a chronic stroke. P 2377-2385, 2018.
[2] Beyaert, C, et al. Gait post-stroke: Pathophysiology and rehabilitation strategies. p 335-55, 2015.
[3] Wataru, N, et al. How patients with stroke adjust their step length to step over obstacles. p 34-39, 2014.

ACKNOWLEDGEMENTS

Thank you to the American Heart Association and the Undergraduate Summer Research Association for funding this research study, Cleveland State University for providing the necessary resources, Zach Hubbard for his kinematic data analysis code that allowed data variable extraction from the motion capture data, and Dr. Espy and Dr. Reinthal for guidance.

CONTROLLING AN EFFECTOR WITH EYE MOVEMENTS: THE EFFECT OF ENTANGLED SENSORY AND MOTOR RESPONSIBILITIES

[1]John R. Schultz, [1]Andrew B. Slifkin, and [1]Eric M. Schearer

[1]Cleveland State University, Cleveland, OH, USA

Email: j.r.schultz12@vikes.csuohio.edu

INTRODUCTION

Restoring arm and hand function has been indicated as the most important factor for maintaining independence for the nearly 177,000 individuals with tetraplegia, or paralysis of all four limbs, living in the United States today [1, 2]. Assistive technologies such as robotic arms, exoskeletons, and neuroprostheses are promising solutions for regaining lost upper extremity function. However, a reliable method for sending motor commands from the user to the assistive device remains elusive. Eye movements are a candidate input signal for controlling reaching because they are naturally available, directly observable, and highly correlated with upper-extremity motor function. The current work was aimed at investigating using eye movements to directly inform effector motion.

When controlling an assistive device with eye movements, the device serves as a replacement for the function of the arm and hand. In this case, the eyes must provide the command input that determines the position of the end effector as well as observe errors in the effector position. This leads to a situation in which the responsibilities of the eyes are *entangled*, meaning, the execution of the eyes' sensory and motor roles affect each other. In this study, we addressed the following research questions: First, how accurately can humans direct an effector to a desired location with their eye movements when the eyes' sensory and motor responsibilities are entangled? Second, how does the eye fixation performance compare to hand reaching accuracy when there is no entanglement? The results of this study will inform continued research on direct eye-movement control of assistive technologies.

METHODS

To better understand how eye-responsibility entanglement affects eye-hand coordination, we recruited 7 participants (5M, 2F, ages 23-30) to look at and reach for targets displayed on a monitor. A cursor was displayed at the participant's point-of-gaze to simulate the end effector of an assistive device and to induce eye-responsibility entanglement. Eye movements were recorded with the ETL-600 head-mounted eye-tracking system (iSCAN; Woburn, MA). An Optotrak (Northern Digital; Waterloo, Canada) marker was affixed to a stylus and attached to the participant's index finger to monitor hand movement. Four experimental conditions were included in the study: 'Eye-Alone', participants simply looked at the targets as they appeared; 'Eye-Hand', participants looked at and moved their finger to the targets as they appeared; the prior two conditions augmented by the inclusion of the cursor.

We used an offline filter to extract saccades (eye movements) and fixations (stable periods between saccades) from the raw eye data [3]. The fixation error was computed as the Euclidean distance between the fixation target and the extracted eye fixation position. The hand movement endpoint was identified as the point in the movement trajectory where hand velocity dropped below a threshold of 10 cm/s. The hand movement endpoint error was computed as the Euclidean distance between the fixation target and the hand movement endpoint.

To address the first research question, we compared the group-mean eye fixation errors between experimental conditions, verified by a two-way, effector by cursor repeated-measures ANOVA. To address the second research question, we compared the group-mean eye fixation error in the 'Eye-Alone with Cursor' condition to the group-mean hand error in the 'Eye-Hand' condition, verified by a dependent samples t-test. Statistics were performed using SPSS statistical analysis software (IBM; Armonk, NY).

RESULTS AND DISCUSSION

The comparison of the average of the fixation errors in the 'Eye-Alone' and 'Hand-Alone' conditions (2.49 ± 0.53 cm) with the average of the fixation errors in the 'Eye-Alone with Cursor' and the 'Eye-Hand with Cursor' conditions (1.06 ± 0.17 cm) suggests that participants exhibited lower average eye fixation errors when the cursor was displayed compared to when it was omitted ($F(1,6) = 11.983$, $p<.05$, $\eta^2_p= .666$). The comparison of the average of the fixation errors in the 'Eye-Alone' and 'Eye-Alone with Cursor' conditions (1.71 ± 0.35 cm) with the average of the fixation errors in the 'Eye-Hand' and 'Eye-Hand with Cursor' conditions (1.84 ± 0.32 cm) suggests that participants exhibited similar average eye fixation errors regardless of whether they reached with their arm and hand or just looked at the targets ($F(1,6)=1.814$, $p>.05$, $\eta^2_p=.232$). Finally, the comparison of the eye fixation error in the 'Eye-Alone with Cursor' condition (1.04 ± 0.15 cm) and the hand error in the 'Eye-Hand' condition (0.84 ± 0.05 cm) suggests that participants' fixation accuracy when controlling the cursor was similar to the hand endpoint accuracy during reaching when the cursor was omitted ($t(7) = -1.2$, $p>.05$).

In summary, the overall quality of participants' eye-movement performance was similar whether concurrent hand reaches were made, while the addition of an eye-driven cursor resulted in a lower mean effector error across all participants. Moreover, participants' lowered eye fixation error in the 'Eye-Alone with Cursor' condition was comparable to the hand error in the 'Eye-Hand' condition (Fig. 1).

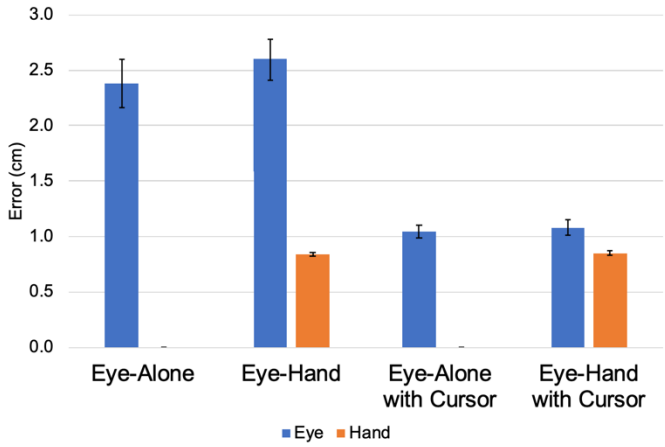

Figure 1: Group-mean eye fixation error and hand reaching error for each condition including standard error of the mean.

CONCLUSION

In the current study, we have shown that humans are able to use their eye movements to direct an effector to a desired target location despite the additional motor responsibility placed on the eyes. Moreover, with minimal task experience and training, the addition of point-of-gaze positional feedback resulted in performance gains similar to the performance of the hand during reaching with unaltered visual feedback. Although many challenges remain, the results of this study suggest that eye movements may be used to directly control an effector to desired locations and validate continued research toward extending these principles to controlling physical assistive technologies.

REFERENCES

1. *NSCISC, Facts and Figures at a Glance.* American Journal of Public Health, 2020.

2. Anderson, K. *Targeting Recovery: Priorities of the Spinal Cord-Injured Population.* Journal of Neurotrauma, 2004.

3. Olsson, P. *Real-Time and Offline Filters for Eye-Tracking*. KTH Royal Institute of Technology, 2007.

UPPER EXTREMITY MOTION ASSESSMENTS IN VIRTUAL REALITY ENVIRONMENTS

[1]Lanna Klausing and [1]Megan Reissman

[1]University of Dayton, Dayton, OH, USA

Email: klausingl1@udayton.edu

INTRODUCTION

This study examines the potential for rapid advancement and personalization in upper extremity rehabilitation by leveraging commercially available virtual reality hardware and software. The current work presents results for a baseline control population, however the goal of the work is to assess movement ability across a variety of neurological impairments. Following neurological injury or disease, a person's level of movement ability has a considerable effect on their community involvement, activities of daily living, and overall independence. Impact of deficits can vary even for individuals with the same diagnosis but typically demonstrate reductions in: speed of movement, strength, joint range of motion, and achievable workspace of the arm. Our focus is on upper extremity movements with particular focus on assessing and improving movement ability with regards to the movement aspects noted above.

METHODS

Custom movement task levels have been created using the commercially available Beat Sabers software and played on a wireless HTC Vive Pro headset. The movement task assessed was a swiping or cutting motion of the endpoint (hand). Successful completion of the task required the endpoint to move to a certain location in the upper extremity workspace and travel through that portion of the workspace in a specified direction (along a line). A grid layout (Figure 1) within the virtual environment allows for specific and repeatable placement of the movement targets with respect to the individual being tested. The movement tasks assess factors of Vertical Position (high, low), Horizontal Position (medial, lateral), and Movement Direction (up, down, in or towards midline, out or away from midline). Blocks were coded red for left arm and blue for right arm.

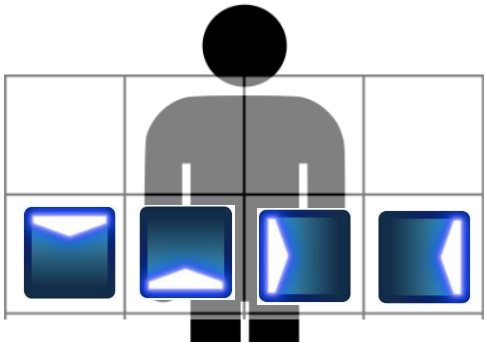

Figure 1: Grid showing location of the possible movement task locations and directions. Shown left to right: down, up, out, in.

An IRB approved validation study has been completed on a young, healthy cohort (n=10, mean age 21.9 years old). The cohort completed two levels consisting of 96 unilateral movement tasks spaced ~2 seconds apart. Several music options (all 119-139 BPM) were synchronized to the movement tasks. Task presentation order was randomized but each task was repeated 3 times sequentially to allow for multiple attempts. Movement data was collected using a commercial Inertial Measurement Unit (IMU) sensor set (XSens MTw Awinda System) placed on 11 key locations of the torso, head, and upper extremity. Biomechanics software (Visual 3D, C-Motion) was used to further analyze segment motions and determine joint angles for the shoulder, elbow, and wrist. Shoulder flexion was defined as arm movement in the anterior direction being positive. Max hand velocity and velocity at the beat were also assessed.

RESULTS AND DISCUSSION

The direction of the movement task was a significant factor for every metric examined (all $p<0.001$ and $P>0.99$). Wrist sagittal angle profiles from a representative subject for shoulder height lateral targets are shown in **Figure 2**. Kinematic plots show joint angle behaviors normalized to the beat of the movement task, where 50% mark is the beat. This subject response highlights left (red) and right (blue) arm differences that were observed even for healthy subjects. The largest mean joint angle deviations were observed specific to direction of the movement task, rather than vertical or horizontal position (max deviation shown in bold in **Table 1**). These suggest the movement direction of the tasks that might encourage increased range of motion for an individual with an upper extremity deficit.

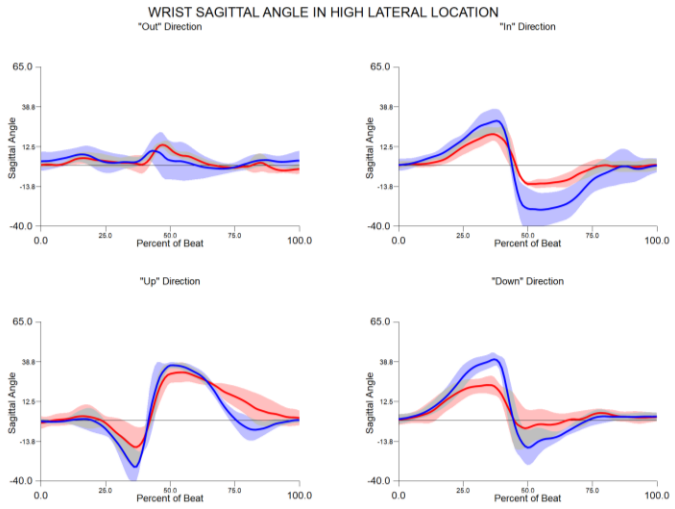

Figure 2: Wrist angle by direction for left and right arms

The vertical position of the movement target was significant for wrist medial and lateral deviation, shoulder flexion, and hand maximum velocity for both the left and right arms (all $p<0.001$ and $P>0.98$). Differences in shoulder flexion were notable with mean 48.1° for high (shoulder height) targets and 33.9° for low (elbow height) targets **(Figure 3)**. This is due to higher targets requiring greater range of motion and hand velocity to prepare for the task execution.

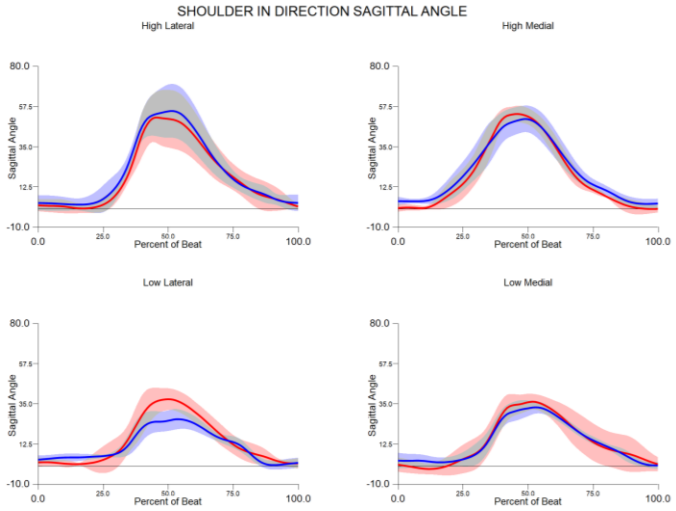

Figure 3: Inward direction task only showing shoulder angles by position for left (red) and right (blue)

The horizontal position of the movement target was a significant factor only for wrist flexion angle ($p<0.01$ and $P=0.81$) with greater flexion for lateral targets. While horizontal position did not strongly influence response in healthy controls it may be a factor for special populations with reduced achievable upper extremity workspaces.

Table 1: Mean Range of Motion by Movement Direction

	Down	In	Out	Up
Wrist Extension	**36.7**	34.9	26.1	31.6
Wrist Flexion	1.1	**-17.6**	-7.6	-5.1
Wrist Medial Deviation	21.5	24.8	20.3	**26.0**
Wrist Lateral Deviation	**-19.7**	-4.0	-6.7	-12.8
Shoulder Max Flexion	39.8	36.9	39.0	**48.4**

CONCLUSION

This study establishes baseline motion profiles and healthy range of motion for wrist, elbow, and shoulder angles. Direction of motion appears the best factor to target particular joint movements. Healthy controls adopt consistent joint profiles for a given movement task but frequently demonstrate side specific (left vs. right) differences.

Using Studies of Octopuses to Aid the Design of Smart Prosthetics

[1]Garrett Weidig, [1]Brittany Bush, [1]Emily Kelly, [1]Galit Pelled, PhD, and [1]Tamara Reid-Bush, PhD

[1]Michigan State University, East Lansing, MI, USA

Email: weidigga@msu.edu, reidtama@egr.msu.edu

INTRODUCTION

2.1 million Americans live with loss of limb [1]. The use of a prosthetic device is the most common solution for regaining motion abilities, especially for those with upper extremity limb loss. However, because of the high degree of personalization and degree of variation, smart upper extremity prostheses are expensive and can malfunction [2]. This can lead to frustration with the device, low adherence rates, inability to complete everyday activities, and a diminished sense of independence [3]. There is therefore a need for a device that is less expensive, can be 'one size fits all', and is able to complete everyday activities.

Inspiration for such an upper limb prosthetic device can be drawn from the octopus. The octopus, *octopus bimaculoides*, is a muscular hydrostat with two-thirds of its neurons located in the arms alone. They can complete many of the same tasks that humans can, especially pertaining to reach and grasp. Their arms have infinite degrees of freedom and often act independently from the brain, a requirement for improving the design of upper limb prosthetic devices.

Therefore, the goal of this study was to initiate experiments of the octopus and quantitatively define movements using curvature. Using data of this type, we aim to aid the design of an octopus arm-like prosthesis that is able to complete everyday tasks whilst being simpler and less expensive.

METHODS

A four-camera motion capture system was used to track the movements of octopus arms underwater. Four or five single reflective markers were attached to the octopus, depending on the length of the arm (Fig. 1a & b).

Two experiments were completed to understand the movement patterns of the octopus- detached arm experiments and live octopus experiments. For detached arm experiments, the arm was manually moved underwater in a fashion similar to natural octopus movements. The entire movement trial involved the octopus arm being pulled in a straight line, turning around, and being pulled back. For live octopus experiments, the octopus was allowed to move freely underwater after marker attachment.

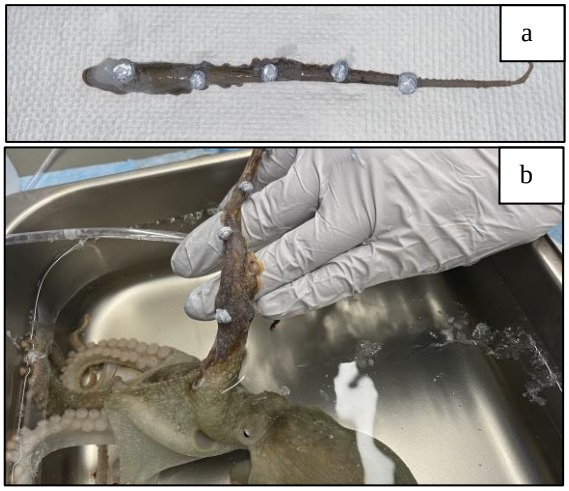

Figure 1: Marker attachment method for a) detached arm experiments and b) live octopus experiments.

Positional data were obtained to describe the movement patterns of the arms. These data were used to calculate the curvature of the arms, which is the most unique motion of the octopus. Any given curvature calculation involves the use of the 3D positional data of three reflective markers. The calculated curvature during this trial was normalized based on the maximum curvature experienced during the movement.

RESULTS AND DISCUSSION

Positional data from the detached arm experiments highlighted the characteristic curvature associated with natural octopus movements (Fig. 2a). This specific curvature plot uses the most proximal, middle, and most distal markers (1st, 3rd, and 5th) to describe the overall curvature of the leg (Fig. 2b). Similar calculations can be made for any set of three markers to obtain local curvatures.

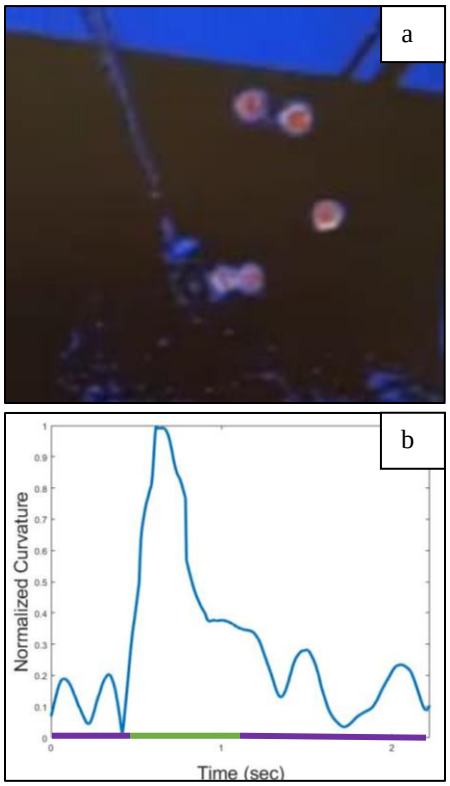

Figure 2: Curvature during detached arm experiments. a) depicts the maximum curvature during a movement trial. b) describes the calculated overall curvature throughout the entire motion, which includes straightaway (purple sections on x axis) and turnaround (green section on x axis) portions

The closer the curvature is to one, the more the arm is curving, whereas the zero value indicates the arm is completely straight. Contrary to expectation, the curvature during the straightaway (purple in Fig. 2b) portions of the movement was not zero. These local maximums indicate lateral motion of the arm, caused largely by the swaying of the distal marker. The curvature of the octopus during the turnaround (green in Fig. 2b) portion was greater than during the straightaway motion. The maximum curvature (Fig. 2a) corresponded with a curvature value that was roughly five times greater than that during the straightaway portions (Fig. 2b).

For live octopus experiments, marker attachment was successful. However, due to the varying uncooperative behaviors of the octopuses, motion capture data were not sufficient for a complete data analysis.

CONCLUSION

Understanding typical movements of the octopus is important for implementing a design for a simplified, functional upper limb prosthetic. We were able to develop a protocol to collect motion data on a live octopus. We were also able to successfully capture movements on detached arms.

Future work will focus on a more detailed evaluation of both detached arms and live octopuses. Additionally, a separate study on human reach parameters will be conducted. Together, these studies will help aid design decisions on how an octopus-arm like prosthetic can be effectively implemented.

REFERENCES

1. Ziegler-Graham, K, et al. *Arc. Phys. Med. & Rehab.*, 422-429, 2008.
2. National Academies of Sciences, et al. *The Promise of Assistive Technology to Enhance Activity and Work Participation*. National Academies Press (US), 2017.
3. Amputee-Coalition, et al. *Amputee Patient Comfort and Compliance. inMotion.* 34-39, 2011.

ACKNOWLEDGEMENTS

This work was supported by NIH grant UF1NS115817.

INITIAL WORK TOWARDS A MORE COMPLETE UNDERSTANDING OF THE HEALTHY THUMB

[1]Adam J. Chrzan, [1]Nicole Arnold, [2]Kevin Chan, M.D., [1]Tamara Reid Bush, Ph.D
[1]Michigan State University, East Lansing, MI, USA
[2]Spectrum Health, Grand Rapids, MI, USA
Email: chrzanad@msu.edu

INTRODUCTION

Radiographic osteoarthritis (OA) of the hand, characterized by damage to articular cartilage and underlying bone, affects more than 60% of Americans over the age of 55. Of those, nearly a third will suffer from OA in the carpometacarpal (CMC) joint of the thumb, making it the second most common location of hand OA [1]. CMC OA can cause decreased pinch strength, joint stiffness, and pain, rendering daily tasks difficult (i.e. open jars, writing, etc.) and limiting the ability to live independently [2].

Standard assessments of thumb kinematics include qualitative and goniometric measures, which are limited due to the subjective nature and single plane measurement, respectively. Some work has been conducted to characterize 3D kinematics of the healthy thumb, but these studies are limited by small sample sizes and age ranges [4]. Thus, there is a need for a larger study to perform a more detailed kinematic analysis of the healthy thumb.

A more thorough understanding of healthy thumb kinematics will inform treatment options for OA patients. In severe cases of thumb CMC OA, major loss of function and constant pain require surgical intervention for improvement [2]. Current standard-of-care treatments involve partial or complete removal of the damaged cartilage and bone in the CMC joint. While this and other available surgical procedures have been shown to reduce pain and increase thumb mobility, there is limited evidence showing which procedure, if any, yields superiorly improved postoperative thumb kinematics [3]. The goal of this work is to provide a more detailed 3D characterization of healthy thumb kinematics that can be used to better understand the outcomes of thumb CMC OA surgeries.

METHODS

Participant inclusion criteria for healthy thumb function included the following: no history of significant hand injury, no hand surgery, no diagnosis of arthritis, must be right-hand dominant, and not pregnant. This work was approved by the university (IRB #00006111) and all participants consented.

Fourteen participants (8F/6M, average age=30.5 STD=10.4) were recruited. Thumb kinematics were gathered using a six-camera motion capture system (Qualysis, Gothenburg, Sweden) with reflective markers. Rigid marker pods and individual markers were fixed to the hand to identify thumb and hand movements (Fig. 1).

The thumb movement performed was used to scribe out the largest space the thumb could move. To obtain this path, a maximum circle-like motion was conducted to identify the perimeter of the full kinematic space of the thumb distal phalange tip (Fig. 2). Starting with the thumb alongside the index finger (A), participants were instructed to perform a sequential series of movements. These included adducting the thumb towards the back of the hand (B), followed by a maximum ‘thumbs-up’ (C), the largest arc they could make (D) to oppose to the pad of the pinky finger (E), and sliding the thumb along the pads of the fingers (F) back to the starting position. The motion was performed three times to allow for practice and ensure participant understanding. Participant demographics (age, sex)

and hand anthropometrics (thumb bone lengths) were recorded.

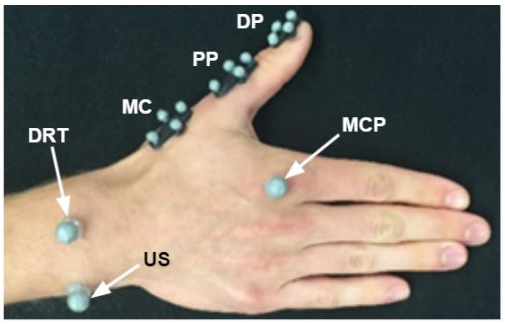

Figure 1: Rigid marker pods, each containing 4 markers, were fixed to the dorsal surface of the thumb metacarpal (MC), proximal phalange (PP), and distal phalange (DP). The palm was identified by the location of individual markers fixed to the ulnar styloid (US), dorsal radial tubercle (DRT), and the metacarpophalangeal (MCP) joint of the second digit.

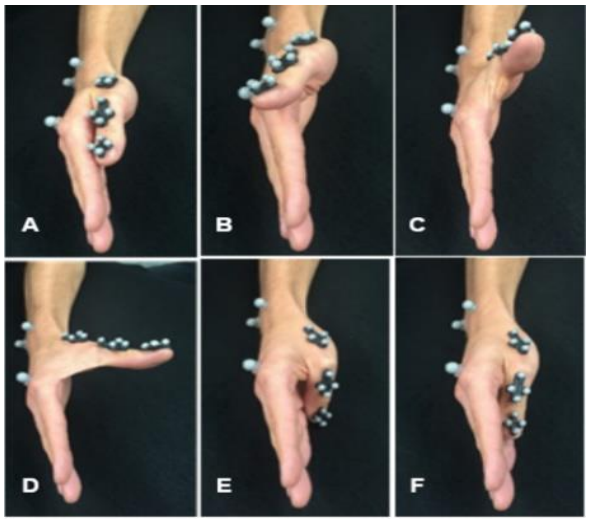

Figure 2: Steps of the maximum opposition motion. A) starting position B) adduction towards dorsal palm C) maximum 'thumbs-up' D) largest arc to oppose to the pad of the fifth digit E) completed opposition F) sliding thumb laterally along finger pads.

RESULTS AND DISCUSSION

The perimeter of the full kinematic space of the thumb tip was calculated for each participant and normalized by thumb length (unitless) (Fig. 3). The mean normalized perimeter was 4.99 (STD=0.86). Most participants had a normalized perimeter of 3.9-5.2, but a smaller group had a normalized perimeter greater than 6.0, indicating greater thumb mobility.

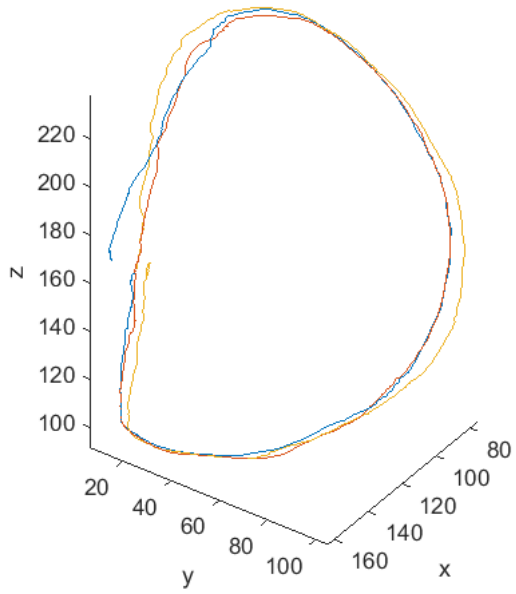

Figure 3: Time trace of the thumb tip during the maximum opposition motion. The first, second, and third repetitions of the motion are shown in blue, red, and yellow, respectively. Axes are in millimeters in reference to the global coordinate system.

CONCLUSION

The 3D kinematics of the thumb were successfully characterized using a metric of the full kinematic space perimeter. A more comprehensive understanding of 3D thumb kinematics will lead to better informed surgical treatment options for people with CMC OA.

REFERENCES

1. Haugen, I, et al. *Ann Rheum Dis.* 1581–1586, 2011.
2. Matullo, K, et al. *Hand*. 232-239, 2007.
3. Deutch, Z, et al. *Hand*. 403–411, 2018.
4. Curran, P, et al. *Clinical Biomechanics*. 63-72, 2019.

ACKNOWLEDGEMENTS

Funding was received from the Spectrum Health – Michigan State University Alliance Grant.

THE EFFECTS OF ENVIRONMENTAL FACTORS ON LADDER OVERREACHING

[1]David D. Williams, [1]Kurt E. Beschorner, [2]Daina L. Sturnieks, [2]Stephen R. Lord and [3]Erika M. Pliner

[1]University of Pittsburgh, Pittsburgh, PA, USA

[2]Neuroscience Research Australia and University of New South Wales, Sydney, Australia.

[3]University of Florida, Gainesville, FL, USA

Email: ddw28@pitt.edu

INTRODUCTION

Falls are a leading cause of fatal and nonfatal injuries. Ladder falls account for the second most common cause of all falls, accounting for 16% [1]. Ladder fall patients over 65 years were found to have both higher hospital and intensive care admission rates due to their falls [2]. In a survey given to participants who had made an emergency department visit due to a ladder fall, 37% of individuals identified overreaching as a factor in their fall [3]. Yet, there is a lack of knowledge on how the individual's environment contributes to their risk of overreaching. Thus, this study aims to further understand the effect of environmental factors on overreaching in older adults.

METHODS

104 healthy older participants were asked to complete a laboratory-based gutter clearing task on a straight ladder. The task required the participants to climb to the third step of a straight ladder and remove tennis balls from a gutter (5.8 m in length and 2.1 m above the ground) until all the tennis balls were removed. Participants were allowed to move the ladder as many times as necessary to complete the task in a safe and quick manner. The ladder was fixed to the testing apparatus but could be slid laterally along the gutter when the participant was not on the ladder.

Our preliminary analyses identified a significant positive correlation between the center of pressure (COP, kinetically derived) location relative to the ladder and the maximum reach (kinematically derived) during the gutter clearing task on a straight ladder. A greater maximum reach was associated with COP farther from the ladder's center in the lateral direction. This relationship permits the use of COP as a proxy for reaching behavior during a gutter clearing task on a straight ladder. Video and kinetic (recorded loads below the ladder feet) data was collected for each participant. Kinetic and video data was used to calculate the COP and confirm that the correct COP peak was selected. Participants were omitted if either the video or kinetic data wasn't fully available. This resulted in the inclusion of 102 participants and 828 separate reaches.

The maximum COP of each clearing attempt was used to quantify reaching, where a greater COP was associated with a farther reach laterally. Extracted environmental factors were the percent of time into the ladder task (% time), ladder position (left, mid left, mid, mid right, right), and whether debris could not be removed without moving the ladder (remaining debris). The environmental factors were entered into a multivariate linear regression with the COP values of each reach to determine if these factors influence reaching. COP values that traveled a distance outside the ladder's base of support (199 mm from the ladder center) indicate overreaches, as the ladder would have likely tipped if it was not constrained to the testing apparatus.

RESULTS AND DISCUSSION

Environmental factors had a significant impact on reach (i.e. maximum COP value of each clearing attempt per climb) ($F_{6,827}$=6.40; p<0.0001). Ladder position ($F_{4,827}$=3.68; p=0.0055) (Figure 1.a) and remaining debris ($F_{1,827}$=4.65; p=0.0314) (Figure 1.b) were both significant predictors of reach.

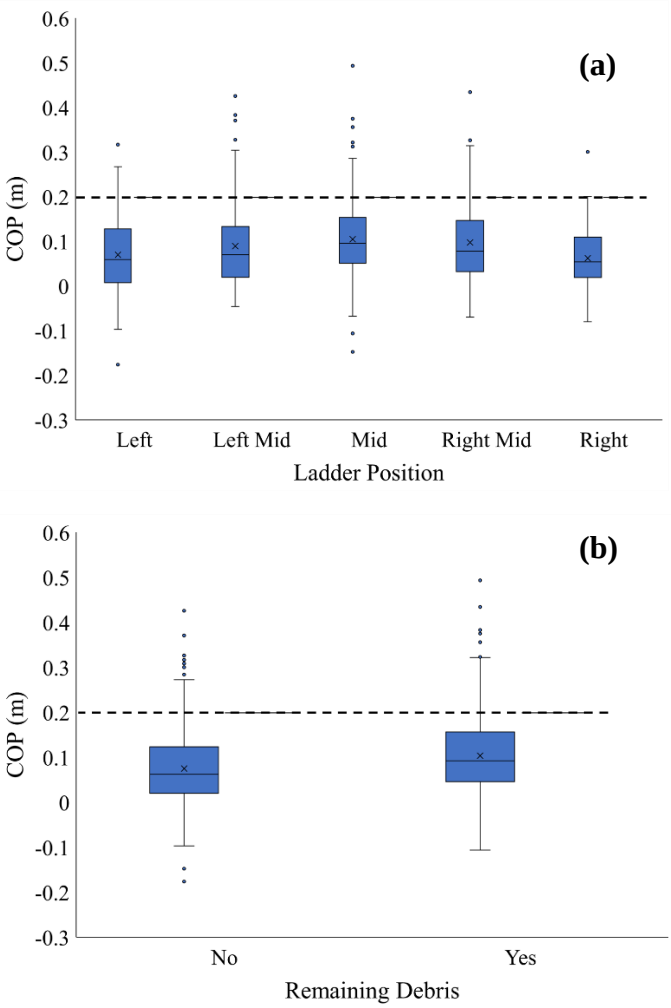

Figure 1: Box plots of COP distributions for ladder position (a) and remaining debris (b). COP values above the dashed line indicate reaching attempts that would have likely resulted in a ladder fall. A 0 value denotes that the COP is located in the center of the ladder.

The % time into the climb was not found to be a significant predictor of reach ($F_{1,827}$=0.5459; p=0.4602). COP values were significantly farther from the ladder's center when the ladder was positioned in the right middle of the gutter, compared to the right and left ends (Tukey HSD; p<0.05), and when debris still remained in the gutter after the reach (i.e. the debris was outside the participant's reach). The right middle position (15%) and remaining debris (11%) conditions had the most reaches that were classified as overreaches.

Our analysis found reach to be explained by a combination of environmental factors (i.e. ladder position and remaining debris). Previous work has shown motivation (i.e. the presence of a physical target) to increase lateral reaching while on a ladder [4]. Remaining debris may act as a motivator to overreach while ladder position may be linked to this effect as 70% of participants started in one of the middle three positions where debris was more likely to be out of their reach.

CONCLUSION

The results of this analysis draw important conclusions regarding the effects of environment on overreaching. Ladder position and remaining debris were found to impact reach during a gutter clearing task on a straight ladder. These models help illustrate how someone's environment can lead to more dangerous decision making in terms of overreaching. These findings can help guide interventions to lower overreaching risk during ladder tasks.

REFERENCES

1. Webster, T. *Compensation and Working Conditions*. p. 28-38, 2000

2. Melmer, P., et al. *The American Journal of Surgery.* p. 1103-1107, 2020

3. Cabilan, C., et al. *Emergency Medicine Australasia.* p. 95-102, 2018

4. DiDomenico, A., et al. *Professional Safety.* p. 50-53, 2013

ACKNOWLEDGEMENTS

This work was supported by the Whitaker International Fellowship Program and NIOSH R01OH011799.

EFFECT OF BONY MISMATCHES CAUSED BY OSTEOCHONDRAL ALLOGRAFT REPAIR ON CARTILAGE DEFORMATION

[1]Ryan Rosario (Presenter), [1]Ellen M Arruda, [1]John A Grant, and [1]Rhima M Coleman

[1]Univeristy of Michigan, Ann Arbor, MI, USA

Email: rhimacol@umich.edu

INTRODUCTION

Cartilage injuries commonly occur in the knee. A study reviewing over 30,000 routine knee arthroscopies found that 60% of patients had high-grade chondral lesions [1]. Of those patients with a chondral lesion, 20% had a lesion on their patellar cartilage. Because the tissue is avascular, cartilage lesions have a limited ability to heal and often need to be surgically restored.

Osteochondral allograft implantation is a form of cartilage transplant where a cylindrical graft from a cadaveric donor, comprised of live cartilage and subchondral bone, is implanted into a prepared defect site within a patient's joint. The goal of the procedure is to restore a smooth articulating surface. However, no standard exists for matching the subchondral bone of the graft and surrounding patella.

The goal of this study was to identify the effect of mismatches in the subchondral bone surface between a graft and the surrounding patella on cartilage tissue deformation. We hypothesized that large mismatches in the subchondral bone surface would result in greater deformation in the overlying cartilage as this may increase the risk of graft failure. By identifying graft characteristics that would result in lesser mismatches between the graft and patella bony surfaces, we seek to improve the long-term outcomes for patellar cartilage allograft repair.

METHODS

Two types of finite element models were used to quantify the effect of mismatches in the subchondral bone surface. A simplified model was used with an axisymmetric geometry with an 8 mm graft radius and 10 mm native cartilage radius. The graft radius was chosen to match the scans used in the 3D model. The thickness of graft cartilage was varied from 0.67 mm (proud graft subchondral bone) to 6 mm (sunk graft subchondral bone). The thickness of the native cartilage was set to 2 mm. The surface of the cartilage in the graft was matched to the surrounding native cartilage. A 1 MPa compressive traction was applied to the cartilage surface, and the patellar surface was fixed.

Ten 3D models were created from nano-CT scans of cadaveric patellar cartilage that was repaired by Dr. John Grant [2]. Scans were segmented using Dragonfly and meshed using HyperMesh. A 1 MPa surface pressure was applied to the cartilage surface, and the patellar surface was fixed. Both the simplified and 3D simulations were conducted in Abaqus 2019.

RESULTS AND DISCUSSION

The simplified model showed that a stress singularity occurred in the cartilage at the sharp bony edge between the graft and native subchondral bone, localized to the region with thinner cartilage. This concentration decayed more quickly for grafts with proud subchondral bone than grafts with sunk subchondral bone. For grafts with sunk subchondral bone, the singularity decayed more quickly for smaller differences between graft cartilage and native cartilage. Finally, lower stresses were observed in the region with thicker cartilage near the subchondral bone surface.

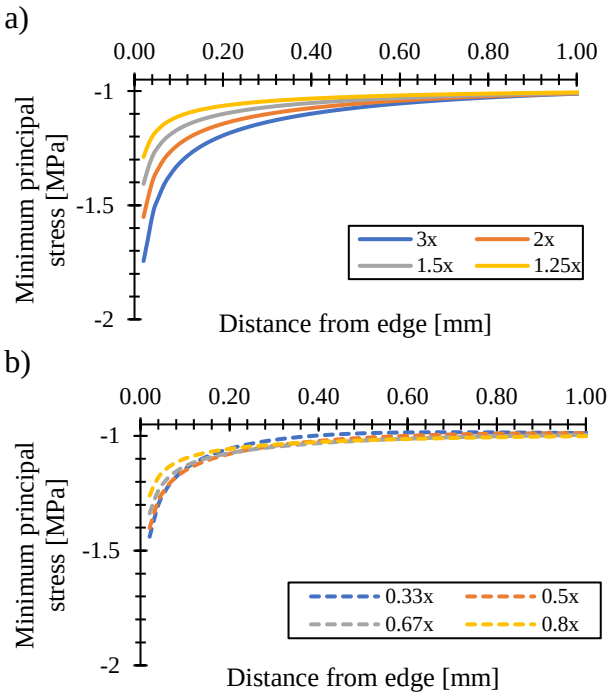

Figure 1. Minimum principal stress vs. distance from sharp edge for (a) proud subchondral bone and (b) sunk subchondral bone. Chart legends refer to the thickness of the graft cartilage relative to the native cartilage.

The 3D models reproduced key features seen in the simplified model, with stress singularities occurring at sharp edges in regions with thinner cartilage and stress reductions occurring at the subchondral bone surface in regions with thicker cartilage. Differences between the 3D and simplified models were caused by heterogeneous cartilage surface curvature and thickness.

These findings demonstrate that mismatches in the subchondral bone can produce stress increases large enough to cause local chondrocyte death, potentially leading to further cartilage degradation [2]. These stress increases can be reduced by (a) using a graft

with a thinner cartilage region (and proud subchondral bone) or (b) reducing difference in thickness between graft and native cartilage. Additionally, stress contours demonstrate that local cartilage degradation caused by mismatches in the subchondral bone would initiate at the subchondral bone surface. To identify this cartilage degradation, clinicians would need to incorporate full thickness imaging protocols, like MRI, in addition to arthroscopy.

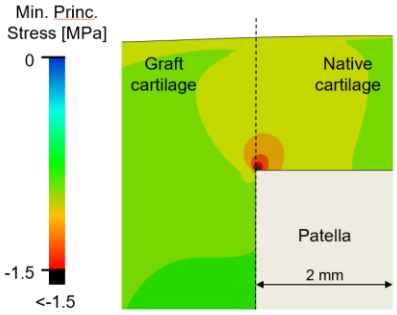

Figure 2. Minimum principal stress contours for the simplified model with graft cartilage 3x as thick as native cartilage.

CONCLUSION

This study contributes to a growing body of literature working to improve clinical outcomes for patellar cartilage allograft transplant. The findings have implications for graft selection and long-term monitoring. Future clinical examinations of patellar cartilage allograft transplant should incorporate these findings by examining the impact of subchondral bony surface mismatches and thus solidify implications for clinical practice.

REFERENCES

1. Curl, W, et al. *Arthroscopy*. 456-460, 1997.

2. Salka, N, et al. *Orthopaedic Journal of Sports Medicine*, 2020.

3. Clements, K, et al. *Osteoarthritis and Cartilage.* 499-507, 2001.

ACKNOWLEDGEMENTS

We would also like to acknowledge our funding sources: NSF GRFP #1841052, NSF Grant #1537711, ANRF Award No. 047420, Orthopaedic Research and Education Foundation Award No. 651100, NIAMS Award No. 1R21AR07401101, NIAMS Award No. P30AR069620, JRF Ortho.

Fatigue and Fracture Toughness of Cortical Bone are Radiation Dose-Dependent

[1]Dylan Crocker, [1]Isaac Hoffman, [1]Jennifer Carter, [1]Ozan Akkus, and [1]Clare Rimnac

[1]Case Western Reserve University, Cleveland, OH, USA

Email: dylan.crocker@case.edu

INTRODUCTION

Structural cortical bone allografts are a common treatment option for patients who suffer from severe bone loss resulting from trauma, cancer, and other bone-related disease [1]. Tissue banks typically aim to reduce the risk of disease transmission by sterilization with high-ionizing gamma radiation at a standard dose of 25-35 kGy [2]. However, irradiation with the standard radiation dose has a detrimental effect on important mechanical properties of cortical bone [2]. We have shown that a standard sterilization dose of 25-35 kGy is detrimental to the fatigue crack propagation resistance [3] and the high-cycle (S-N) fatigue life of cortical bone [2], reducing both by ~10-20 fold. Static fracture toughness and work-to-fracture [4] are also reduced by this standard sterilization dose (~20-35%).

We recently evaluated the high-cycle fatigue behavior of allograft cortical bone and observed a radiation dose-dependent response in the range of 0-25 kGy, with lower radiation doses exhibiting progressively longer fatigue life [5]. Radiation doses lower than 25kGy may be feasible for sterilization [6], which may be beneficial for long-term performance. The **objective** of this study was thus to determine if fatigue crack propagation, fracture toughness, and work-to-fracture of cortical bone allograft are also radiation dose-dependent.

METHODS

Three human donor femoral pairs (2 female, 45 and 61 yrs, 1 male, 61 yrs) with no known pathologies were obtained from the Musculoskeletal Transplant Foundation. Compact tension specimens were machined under constant irrigation from cortical bone rings and notched, razor sharpened and polished with alumina such that crack growth was parallel to the longitudinal direction. Specimens were allocated to four treatment groups: no irradiation (0 kGy, "control"), 10 kGy, 17.5 kGy, and 25 kGy. Fatigue crack propagation (FCP) tests were conducted with n=3 on an Instron closed-loop servohydraulic test system under 23C irrigation using a sinusoidal waveform, cyclic frequency of 1 Hz, and R-ratio of 0.1. Crack length was measured with a traveling microscope until fast fracture. FCP rate, da/dN (m/cycle), and cyclic stress intensity factor range ΔK (MPa(m)$^{1/2}$) were determined.

Data from all three specimens in each treatment group were pooled and linear regression analysis of log(ΔK) vs. log(da/dN) was determined, based on the Paris relationship $da/dN = \mathbf{C}\ \Delta K^{\mathbf{m}}$. **C** and **m** were further compared between groups using regression analysis. For fracture toughness (K_C, MPa(m)$^{1/2}$) hydrated specimens were monotonically loaded to fracture at a displacement rate of 0.34 mm min^{-1} (n = 7-9/group) [4]. Work-to-fracture (J) was determined from the area under the load vs. displacement curve (up to P_{max}). One-way ANOVA was used to compare fracture toughness and work-to-fracture between groups. Significance was taken as $p < 0.05$.

RESULTS AND DISCUSSION

During fatigue crack propagation, all treatment groups showed acceleration and deceleration of the crack (e.g., Fig. 1). However, the pattern overall became less pronounced with increasing radiation dose, consistent with progressive radiation-induced tissue damage. Overall, FCP resistance progressively decreased with an increase in radiation dose (Fig. 2). There was no difference in the exponent **m** between: 0 kGy and 10 kGy ($p = 0.43$); 0 kGy and 17.5 kGy

(p = 0.87); 0 kGy and 25 kGy (p = 0.28); 10 kGy and 17.5 kGy (p = 0.50); and 17.5 kGy and 25 kGy (p = 0.32). However, the coefficient **C** differed between 0 kGy and all other treatment groups (p < 0.001), and between 10 kGy and 17.5 kGy (p = 0.002). There was no difference in **C** between 17.5 kGy and 25 kGy (p = 0.10). Fracture toughness also decreased with increasing radiation dose: 1.97±0.29, 1.82±0.18, 1.7±0.20, and 1.61±0.22 MPa(m)$^{1/2}$ (p < 0.02), as did work-to-fracture: 7.34±1.54, 6.11±0.97, 5.52±1.41, and 4.81±1.17 J (p < 0.01) for 0 kGy, 10 kGy, 17.5 kGy, and 25 kGy, respectively.

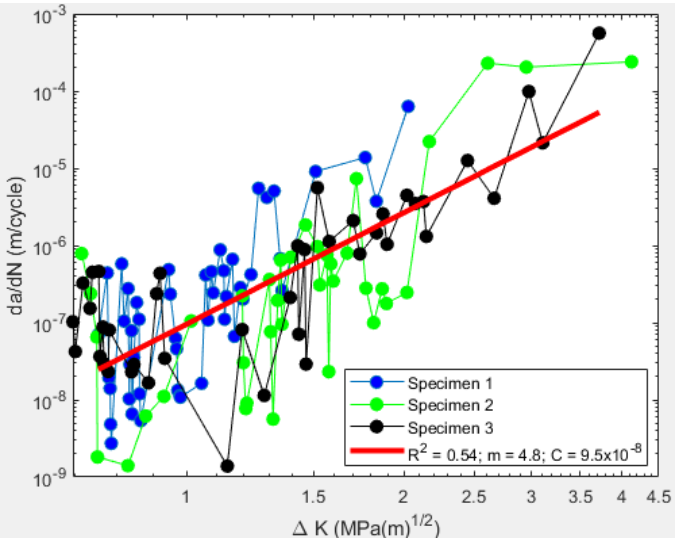

Figure 1: FCP behavior for the 0 kGy (control) group.

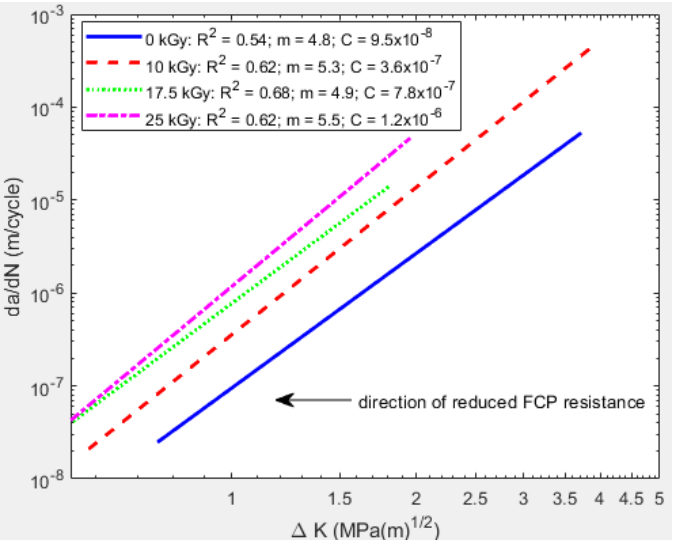

Figure 2: FCP comparison of the four radiation treatment groups (only regression lines shown for clarity).

As with high-cycle (S-N) fatigue behavior [5], we observed a dose-dependent loss of FCP resistance, fracture toughness, and work-to-fracture. The S-N and FCP findings together suggest that both crack initiation and crack propagation are impacted by radiation-induced tissue damage [1] (possibly due to collagen matrix chain fragmentation and/or crosslinking), though the relative influence as a function of radiation dose remains to be elucidated. Fracture toughness and work-to-fracture, while also radiation dose-dependent, are not as strongly impacted as fatigue properties.

CONCLUSION

An effective sterilization dose for cortical bone allografts need not be as high as 25 kGy [6]. These findings, along with our previous findings on high-cycle fatigue life [5] continue to support that a decrease in radiation dose to the lowest effective sterilization dose could potentially lead to an improvement in fatigue and fracture resistance and thus increase the functional lifetime of structural cortical bone allografts. Further studies are warranted to examine the mechanism within the collagen matrix that explains the dose-dependent loss of crack growth mechanics in cortical bone.

REFERENCES

[1] Du, J, et al. *JBJS-A*. E85(1-8), 2019.

[2] Islam, A, et al. *CORR*. 827-835, 2016.

[3] Mitchell, E, et al. *JBJS-A*. 2648-2657, 2004.

[4] Akkus, O, et al. *J Orthop Res*. 927-934, 2001.

[5] Ina, J, et al. *Fatigue Life of Cortical Bone is Radiation Dose-Dependent*. Phoenix, AZ 2020.

[6] Nguyen, H, et al. *Cell Tissue Bank*. 81-91, 2008.

ACKNOWLEDGEMENTS

NIH NIAMS T32-AR007505 (DBC), the Musculoskeletal Transplant Foundation, W.J. Austin Chair (CMR).

MESENCHYMAL STEM CELL DELIVERY VIA TOPOGRAPHICALLY TENOINDUCTIVE COLLAGEN BIOTEXTILE ENHANCES REGENERATION OF SEGMENTAL TENDON DEFECTS

[1]Phillip McClellan, [2]Jason G. Ina, [2]Derrick M. Knapik, [1]Alexis Valente, [1]Yujing Wen, [1]Cindy Wu, [1]Ruiqi Wen, [1]James Anderson, [2]Robert J. Gillespie, and [1]Ozan Akkus

[1]Case Western Reserve University, Cleveland, OH, USA

[2]University Hospitals Cleveland Medical Center, Cleveland, OH, USA

Email: pxm357@case.edu

INTRODUCTION

Injuries to the rotator cuff (RC) tendons remain a common issue encountered by orthopaedic surgeons with approximately 330,000 rotator cuff surgeries conducted on individuals each year in the United States alone [1]. In cases of massive RC tears ($\geq$ 5 cm tendon retraction or involvement of $\geq$ 2 tendons), recurrent tears following surgical repairs are a significant concern as a result of inferior tissue quality or excess mechanical stress located at the site of the repair [2].

Tissue-engineered scaffolds exhibit significant benefits in cases of RC tears where bulk tendon tissue has been lost as a result of muscle atrophy, tissue fibrosis, or fatty infiltration. Such scaffolds can restore the anatomic footprint of the native tendon and withstand the mechanical loading conditions that may otherwise lead to a recurrent failure. Additionally, scaffolds composed of biological molecules of the native extracellular matrix of tendon, such as collagen, can guide regeneration, but the use of collagen alone as a tissue engineering scaffold for bulk tendon is limited as many strategies rely on extended culture periods *in vitro* to achieve the mechanical robustness required to bridge large tendon defects.

Our laboratory has therefore developed a novel method of fabricating mechanically robust, molecularly-aligned collagen fibers by means of electrochemical compaction [3] that can be woven together to form scaffolds capable of sustaining mechanical loads of in a rabbit infraspinatus tendon defect model over the course of six (6) months *in vivo*. Additionally, the scaffolds were capable of acting as a delivery vehicle for mesenchymal stem cells (MSCs) and inducing tenogenic differentiation of said MSCs by way of topographical cues.

METHODS

Scaffolds were fabricated from electrochemically aligned collagen (ELAC) threads as detailed in a previous study [4]. Briefly, type 1 collagen (acid soluble, diluted to 3 mg/mL) was dialyzed against deionized (DI) water and the resulting solution of pure collagen was then subjected to an electric potential (30V, 90s) between two stainless electrodes to induce formation of molecularly-aligned collagen fibers. Individual fibers were combined to form 3-ply yarns and crosslinked utilizing genipin (2% w/v in 90% ethanol). Crosslinked yarns were woven into scaffolds utilizing a stainless-steel pin array.

Mesenchymal stem cells were isolated from bone marrow of New Zealand White (NZW) rabbits and adherent cells were cultured under standard monolayer conditions prior to flow sorting to obtain an enriched population of MSCs (CD44+, CD45-, and CD90-). Flow-sorted cells were seeded onto ELAC scaffolds and cultured for 3 days prior to surgical implantation.

Thirty-four (34) NZW rabbits were divided into four groups (gap = no repair, direct repair "DR" = clinical standard, ELAC = scaffold alone, ELAC+MSCs =

MSC-seeded scaffold) prior to surgical creation of a massive (≥ 5 mm) defect in the infraspinatus tendon which was then left unrepaired (gap) or repaired (DR, ELAC, and ELAC+MSCs). Shoulders were harvested at 6 months following surgery and analyzed by microCT, biomechanical testing, histology, and immunohistochemistry (IHC).

RESULTS AND DISCUSSION

Based on microCT analysis, specimens treated with ELAC showed reduced tendon retraction as compared to DR ($p < 0.05$), indicating that ELAC scaffolds are capable of withstanding native biomechanical loading conditions and may resist suture pull-through that can occur in direct repairs of native tendon tissue.

Biomechanical testing revealed shoulders in the ELAC + MSCs group likely benefited from the addition of MSCs to the scaffolds as they exhibited maximum load to failure values (178 ± 50 N) that were comparable to intact, contralateral control shoulders (199 ± 35 N; $p > 0.10$) (Fig.1).

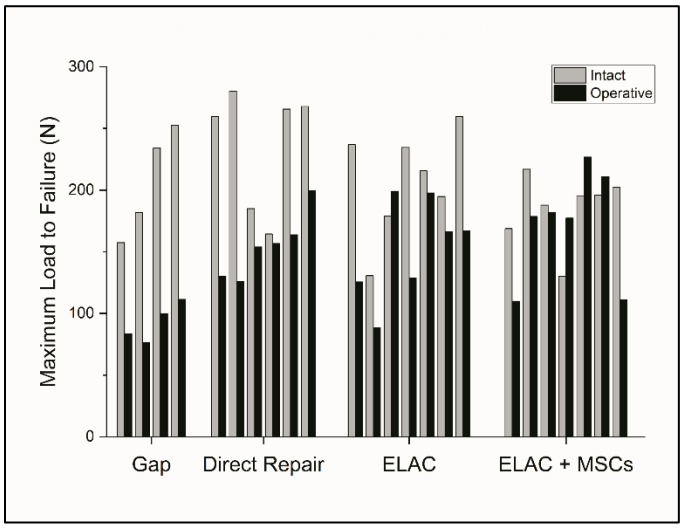

Figure 1. Maximum load to failure of individual shoulders from each group (operative and contralateral "intact" assessed as pairs from each rabbit).

Histological analyses using picrosirius red (PSR, Fig. 2A) and Masson's trichrome (MT, Fig. 2B) stains revealed well-aligned, abundant de novo collagen around ELAC threads in both ELAC and ELAC + MSC shoulders, with ELAC + MSC specimens demonstrating increased ELAC resorption (7% versus 37%, respectively; $p < 0.01$).

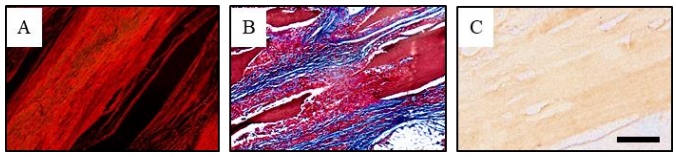

Figure 2. A) Collagen alignment visualized with PSR staining under polarized light. B) MT staining highlighting presence of de novo collagen between ELAC fibers. C) Tenomodulin staining in ELAC + MSC specimen. Scale bar = 100 um

IHC staining highlighted presence of extracellular matrix components, collagen type I and tenomodulin (Fig. 2C), indicating tendon-like tissue formation, in both ELAC and ELAC + MSC groups. Tenomodulin was absent in DR and gap groups, suggesting the ELAC scaffold provided a topographically tenoinductive effect that was sustained for up to 6 months under functional load-bearing conditions *in vivo*.

CONCLUSION

MSCs delivered locally by way of mechanically robust ELAC scaffolds enhance biomechanical and histological outcomes when compared to a current clinical standard approach.

REFERENCES

1. Colvin, A, et al. *J Bone Joint Surg Am*. 227-233, 2012.
2. Galatz, L, et al. *JBJS*. 219-224, 2004.
3. Uquillas, J, et al. *Ann Biomed Eng*. 1641-1653, 2012.
4. Learn, G, et al. *J Biomed Mater Res B Appl Biomater*. 1864-1876, 2019.

ACKNOWLEDGEMENTS

This study was supported by grants from National Institutes of Health (NIH): R01 AR063701 (OA) and T32 AR007505 (PM).

Design-specific Muscle Tissue Constructs for Treating Severe Musculoskeltal Defetcts

[1]L. Juliana Azuero and [1]Prabaha Sikder, Ph.D.

[1]Cleveland State University, Cleveland, OH, USA

Email: l.azuero@vikes.csuohio.edu

INTRODUCTION

Volumetric muscle loss (VML) is a devastating musculoskeletal injury where a substantial amount of skeletal muscle (usually greater or equal to 20%) is lost due to trauma. VML leads to functional deficits, poor muscle strength, life-long dysfunction, and ultimately hampers the life quality of individuals. The existing treatments for VML are restricted to functional free muscle transfer and advanced bracing designs, which are highly limited in their efficacy. For instance, the availability of muscle tissue is limited and even if they are engrafted, they have high chances of immune rejection by the receiver's body [1,2].

On the contrary, 3D bioprinting, the youngest variant of the well-known 3D printing, can be used to make 'live' tissues and organs [2]. Over the past few years it has been making rapid strides in the broad field of tissue engineering. Thus, 3D bioprinting can also be used to develop artificial skeletal muscle that would mimic the innate musculature in its anatomy. However, the success of developing a bioprinted tissue construct depends on numerous factors, but using the right bioink and bioprinting parameters are the critical ones [3]. In this study, we will focus on developing an optimal bioink formulation and identify the most suitable printing parameters to develop a muscle tissue construct that can help regenerate functional skeletal muscle in VML defects effectively.

We have identified alginate to be the basis of our bioink formulation. Alginate is a biodegradable and biocompatible polymer that is extracted from brown algae [4]. Due to its relative low cost, rapid gelation in the presence of Ca^{2+} ions, and low toxicity, alginate-based hydrogels have gained popularity in the 3D bioprinting field. These properties make alginate a useful candidate for bioprinting and biomaterial manufacturing.

This paper will focus on the ideal alginate bioink formulation for the bioengineering of such biomaterial targeted at VML injuries.

METHODS

Sodium alginate was purchased from Sigma-Aldrich. Calcium chloride was purchased from Thermo Fisher Scientific. Three different alginate hydrogels formulations were made, 1% w/v, 6% w/v, and 8% w/v as previously described [5]. As an example, 1g of sodium alginate was dissolved in 100mL of deionized water with one drop of blue food coloring dye, and mixed for 1h. Samples were then centrifuged to eliminate air bubbles that were formed. Then, they were loaded into a clean cartridge and were used for printing using the CellInk BIO X (CELLINK, Boston, MA, USA) bioprinter and crosslinked with 0.045M calcium chloride. All hydrogel mixtures were printed into a 20x20x0.2mm structure with a specified infill pattern to determine printability properties and structure fidelity

RESULTS AND DISCUSSION

When removed from the magnetic stirring plate, the 1% alginate showed a poor gel-like consistency, even after having all of the alginate dissolved. After bioprinting the 1% alginate hydrogel, it was determined that it was completely unfitting for any bioprinting purposes as it was exceedingly liquid and was eliminated from further analysis.

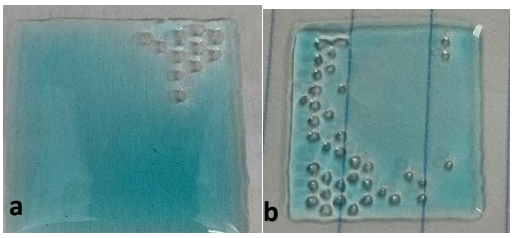

Fig 1.: Alginate formulations after printing. **a.** 6% alginate hydrogel. **b.** 8%alginate hydrogel.

The 6% alginate hydrogel showed a better gel-like consistency once it was removed from the stirring plate. In **Fig 1. a.** it is possible to see how only the upper right corner was able to hold the infill pattern after two layers. Once it was crosslinked, taking ~5 seconds, the hydrogel held its printed structure properly and it was possible to lift from the petri dish. The 8% alginate hydrogel proved to be more viscous than the other two mixtures, having a consistency closer to hair gel. **Fig 1. b.** shows the 8% alginate hydrogel with a better structure fidelity by keeping the infill pattern on most of the lower left side of the design. After crosslinking it, taking ~3 seconds, it was possible to see that the infill pattern that was printed was not affected by the procedure and the hydrogel jellified into a more solid state.

While printing, the extrusion path proved to be stable and consistent, with no skipped portions. The parameters chosen for these prints were optimized for proper accuracy for printing quality. Qualitative evaluations show that the 8% alginate hydrogel proves more promising for the purposes of bioprinting with VML injuries in mind. It is of high importance that the bioink maintains the printed structure and that this is also not affected by the crosslinking process, which the 8% alginate seems to follow. Margins of error could include not having the sodium alginate powder dissolve completely with longer stirring and low quality deionized water.

CONCLUSION

The bioprinting capabilities of alginate can be tailored according to the needs of the research. For the purpose of this project, the alginate formulation looked for strong printability and structure fidelity while remaining a relatively liquid polymer for future cell addition. The 8% alginate hydrogel seemed to fit the objectives for this project as it somewhat held the desired design after printing and crosslinking. Having visible pores that were part of the desired infill pattern, the 8% alginate hydrogel becomes the best candidate out of the three formulations made. For the future, higher percentages of w/v formulations could demonstrate better printing qualities and structural fidelity. The addition of other components to the hydrogel could also increase its mechanical properties. It is also important to keep in mind that the bioink cannot be highly viscous as it could damage cell proliferation due to poor oxygen diffusion. Further research could include incubation periods of the hydrogels after crosslinking to ensure that these will not dissolve or disintegrate at body temperature.

REFERENCES

1. Medical Technology Enterprise Consortium. *Volumetric Muscle Loss (VML) Repair Following Extremity Trauma. 2021.*
2. Ji Hyun Kim, Young-Joon Seol, In Kap Ko, Hyun-Wook Kang, Young Koo Lee, James J. Yoo, Anthony Atala, & Sang Jin Lee. (2018). 3D Bioprinted Human Skeletal Muscle Constructs for Muscle Function Restoration. *Scientific Reports*, 8(1), 1–15.
3. Parak, A., Pradeep, P., du Toit, L. C., Kumar, P., Choonara, Y. E., & Pillay, V. (2019). *Functionalizing bioinks for 3D bioprinting applications. Drug Discovery Today, 24(1), 198–205.*
4. Mallakpour, S., Azadi, E., & Hussain, C. M. (2021). State-of-the-art of 3D printing technology of alginate-based hydrogels—An emerging technique for industrial applications. *Advances in Colloid and Interface Science, 293*.
5. Shah, P. P., Shah, H. B., Maniar, K. K., & Özel, T. (2020). Extrusion-based 3D bioprinting of alginate-based tissue constructs. *Procedia CIRP*, *95*, 143–148.

Combining multiple imaging modalities to develop a finite element model of cerebral aneurysm with variable thickness and comparison to a constant thickness model

[1]Ronald Fortunato (Presenter), [2]Juan Cebral, [1]Anne Robertson, [1]Spandan Maiti

[1]University of Pittsburgh, Pittsburgh, PA, USA

[2]George Mason University, Fairfax, VA, USA

Email: rnf6@pitt.edu

INTRODUCTION

Biomechanical failure of cerebral aneurysms, a pathology of cerebral arteries (CAs), is a catastrophic clinical event with a fatality rate of 45% [1]. Thus, physicians must balance the risk of rupture under close clinical observation and the risks associated with brain surgery [2,3]. Currently published rupture risk probability models are based on patient and aneurysm characteristics discernable from current imaging modalities, such as aneurysm size and aspect ratio. From a biomechanics point of view, aneurysmal wall rupture is the mechanical failure of the wall tissue in the presence of wall stresses in excess of the tissue strength. While the presence of lipid pools or calcified regions within the wall tissue, have been variously implicated as wall-weakening mechanisms, wall thickness has typically eluded discussion because of its difficulty to be observed or measured in-vivo. Ex-vivo wall thickness measurements of excised tissue can range from 50um-2mm. In this work we are interested in how prediction of wall stress using finite element analysis can change assuming a constant thickness versus the true tissue thickness measured by a high-resolution imaging technique mapped onto the finite element mesh.

METHODS

Patient specific luminal surface geometries were created from 3-D rotational angiography (3DRA) images using MIMICS (Materialise, Leuven, Belguim) [4-5]. Aneurysm tissue was harvested after surgical clipping from a patient with unruptured cerebral aneurysm at the University of Illinois Hospital, Chicago, USA. Informed consent was signed by the patient before surgery and all study protocols were approved by the Institutional Review Board at both the University of Pittsburgh and Allegheny General Hospital. Harvested tissue was kept in 0.9% (w/v) saline solution and transported to the University of Pittsburgh within 3 hours after surgery. The sample was then scanned at a resolution of 6 μm using a high-resolution micro-CT scanner (Skyscan 1272, Bruker microCT, Belgium). After 45 minutes of scanning, a stack of 3D images was reconstructed using NRecon reconstruction software (Bruker microCT, Belgium). A series of image processing operations, including thresholding, Gaussian smoothing, and connected components filtering, were performed to clean up the segmentation mask. Triangular surface meshes and corresponding thickness maps were then generated from the segmentation masks. Using a custom algorithm and code the surface mesh from microCT was aligned with the luminal surface mesh from 3DRA. Once aligned the thickness map generated from the CT mesh was mapped onto the luminal surface mesh. Regions where interpolation was not possible due to differences in geometry between the in-vivo and ex-vivo shape was prescribed a constant thickness of 200 um. To remove artificially large gradients from this step we applied a two-ring smoothing algorithm to the thickness field variable. The thickness map on the current triangular luminal surface mesh was then mapped onto a quad surface mesh using a custom MATLAB (Mathworks, Natick, MA) script and Trelis (Coreform, Orem, UT) to create the mesh. Then another custom code projected volumetric hex elements from the quad mesh with thickness derived from the previous steps. Another volumetric hex mesh was constructed using

the same quad mesh but with a constant 200 um thickness to make comparison with the non-uniform thickness result. Finally, a custom finite element code was used to calculate maximum and minimum principal stresses, directions of principal stresses, and ratio of principal stresses under 120 mmHg of a constant pressure.

RESULTS AND DISCUSSION

Average maximum principal stress was shown to be increased in the mapped thickness model in comparison to the constant wall thickness model, 143 kPa vs. 127 kPa respectively, as well as minimum principal stress, 62 kPa vs 55 kPa respectively. One representative aneurysm with contour map of maximum (a), minimum (b), and ratio of principal components (c) of stress in both the constant, left column, and mapped on thickness, right column, are shown in Figure 1. As shown in Figure 1, stress magnitude and regions of high stress is shown to be increased in the variable thickness model.

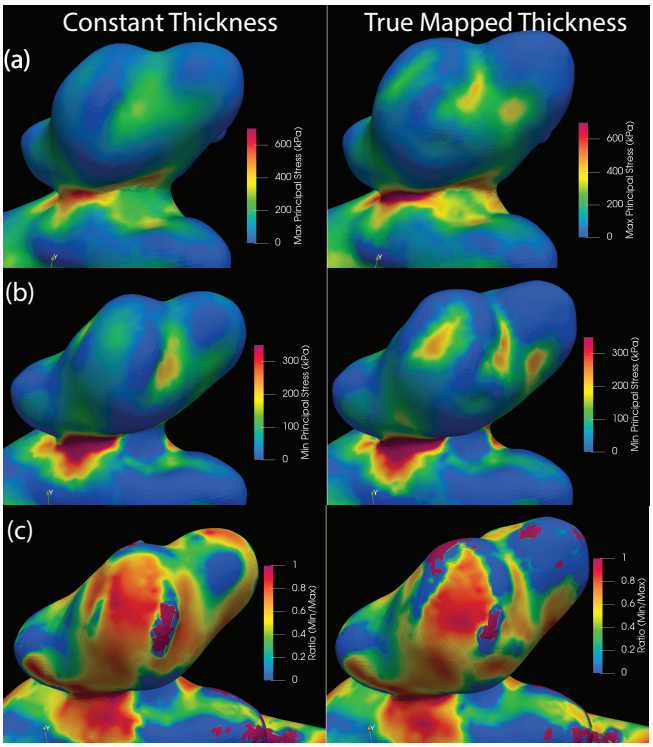

Figure 1: One representative aneurysm with a contour map of Maximum (a), Minimum (b), and ratio (c), of principal components of Cauchy stress for a 3D model constructed

CONCLUSION

While we observed in increase in average stress in the mapped wall thickness model in comparison to the constant wall thickness model this would be expected if the wall thickness in the mapped wall thickness model was always less than the constant wall thickness model. However, the range in wall thickness in the mapped model ranged from 97-610 um containing both more and less thick regions than the constant wall thickness of 200 um. Thus, further investigation is underway on how thickness magnitude and change in thickness can locally effect wall stress.

REFERENCES

[1] Kelly, P et al., *Stroke*, 32(2):530-534, 2001
[2] Broderick, J. P. et al., Stroke 40(6):1952-7, 2009
[3] Juvela, S. et al., Stroke, 44(9): 2413-21, 2013
[4] Cebral, J. et al., A J of Neuro, 26(10): 2550-2559, 2005
[5] Zeng, Z. et al., J Biomech Eng, 132(9): 2010

ACKNOWLEDGEMENTS

Research reported in this work was supported by the National Institutes of Health under award number 1R01-NS097457-01 and 5T32HL076124-12. The content is solely the responsibility of the authors and does not necessarily represent the official views of the National Institutes of Health.

ADDED MASS CHANGES KINEMATICS AND KINETICS OF ADULTS DURING WALKING

[1]Shanpu Fang, [1]Vinayak Vijayan, [1]Megan E. Reissman, [1]Allison L. Kinney, [1]Timothy Reissman

[1]University of Dayton, Dayton, OH, USA

Email: fangs4@udayton.edu

INTRODUCTION

Wearing added mass has been shown to influence walking [1-4]. Knowledge of these effects can be useful in a variety of applications ranging from improving gait exoskeleton design [5] to validating predictive musculoskeletal simulations [6]. However, while there are many studies on this topic, the majority tend to focus on metabolic changes [1-3], with only a few focusing on joint kinematics or joint kinetics [4]. While the former is important, our claim is that such knowledge is more difficult than the latter to make conclusions with respect to biomechanics or motor control. With that being said, knowledge of adaptations to joint angle or joint moment trajectories remains limited not only due to the lower number of prior studies, but also most studies being with treadmill walking [1-3] or are statistically limited with respect to their number of subjects. In this work, we aim to address this scientific gap by presenting statistical inferences from the baseline kinematic changes of a large set of young, healthy subjects who performed overground walking with 6 different conditions of laden mass on their lower body. The goal of this knowledge is to characterize the natural changes to baseline walking joint trajectories due to the location and amount of an added mass.

METHODS

Study participants included 22 young, healthy individuals (11 female, 11 male; age: 23±3 years; mass: 70.59±13.47 kg; height: 1.77±0.10 m; BMI: 22.37±3.16). Participants gave written informed consent for this IRB approved study. Each participant performed overground walking at a self-selected speed for a Baseline (no load) condition and with added masses of different levels: 2 or 4 pounds on each shank, 2 or 4 pounds on each thigh, and 8 or 16 pounds on the pelvis. Data were collected for 5 trials per condition. Motion capture data were collected using an 8-camera Vicon system with reflective markers (n=43) placed on the torso, pelvis, and lower limbs. Ground reaction forces were collected with two in-ground Bertec force plates. Sagittal plane hip, knee, and ankle joint angles and joint moments were calculated in OpenSim. Peak joint variables and spatiotemporal metrics were compared with a repeated measures ANOVA with factors of Mass Amount and Mass Location in NCSS.

RESULTS AND DISCUSSION

Statistically significant differences ($p<0.05$) in hip, knee, and ankle joint angles and joint moments were found among many added mass conditions with respect to Baseline. The focus of this abstract will be on the largest differences observed in selected conditions with changes >10% or 5-10% from the Baseline condition (Table 1). Additionally, the differences highlighted in Table 1 were statistically significant and occurred in at least two kinematic or kinetic metrics in the gait cycle. For spatiotemporal metrics (stride length, time in stance/swing phases), most conditions resulted in changes <5% from Baseline.

During early stance, the largest differences were observed in the kinematics. Low pelvis and high shank masses increased ankle dorsiflexion. Both amounts of shank masses increased knee flexion.

In mid to late stance, most changes were observed in the kinetics. Both amounts of shank mass increased the hip flexion moments, while only the high amount

increased the ankle plantarflexion moment. At mid stance, the high pelvis mass increased the hip flexion moment. None of the thigh masses had a large effect.

Lastly, with respect to kinematics at push off, there were large changes to ankle plantarflexion for the high pelvis mass and high shank mass.

CONCLUSION

Here we highlight the largest kinematic and kinetic differences from Baseline walking due to the added mass conditions considered. From the results, it is noticeable that high shank mass has large influences on multiple metrics. Conversely, within the range of thigh masses there are less influences observed. Lastly as pelvis mass increases, its influence on such metrics is measurably increased. Collectively, such findings indicate that even relatively small added mass, especially distally, can influence both kinematics and kinetics during overground walking.

REFERENCES

1. Schertzer, E, et al. *Appl Ergon*. 1422–32, 2014.
2. Mannatt, K. *The Effects of Mass Loading Distribution on Walking Energetics*. M.S. Thesis, 2015.
3. Browning, R, et al. *Med Sci Sports Exerc*. 515-525, 2007.
4. Westlake, C, et al. *Gait Posture*. 359–62, 2013.
5. Young, A, et al. *IEEE Trans Neural Syst Rehabil Eng*. 171–82, 2017.
6. Dembia, C, et al. *PLoS Comput Biol*. 1–21, 2020.

Table 1: Mean kinematic and kinetic peak values for selected conditions with changes >10% (blue) or 5-10% (yellow) from Baseline.

		Kinematics (Degrees)			Kinetics (Nm/kg)	
		Stance (~5%)	**Stance (~50%)**	**Swing (~100%)**	**Stance (~50%)**	**Swing (~95%)**
		Flexion (+)	**Extension (-)**	**Flexion (+)**	**Flexion (+)**	**Extension (-)**
Hip	**Baseline**	32.34	-14.16	32.76	0.69	-0.72
	Pelvis,High	35.58	-11.26	35.97	0.74	-0.75
	Shank,Low	32.71	-14.85	32.45	0.74	-0.69
	Shank,High	32.90	-14.36	32.73	0.77	-0.65
		Stance (0%)	**Stance (~15%)**	**Stance (~40%)**	**Stance (~15%)**	
		Flexion (-)	**Flexion (-)**	**Extension (+)**	**Extension (+)**	
Knee	**Baseline**	-11.67	-24.54	-8.48	0.54	
	Thigh,High	-10.45	-23.22	-8.85	0.52	
	Shank,Low	-12.54	-25.49	-7.92	0.61	
	Shank,High	-12.66	-26.34	-8.63	0.62	
		Stance (~10%)	**Stance (~45%)**	**Stance (~60%)**	**Stance (~50%)**	
		Plantarflexion (-)	**Dorsiflexion (+)**	**Plantarflexion (-)**	**Plantarflexion (-)**	
Ankle	**Baseline**	3.34	22.02	-12.50	-1.60	
	Pelvis,Low	4.26	22.43	-11.75	-1.69	
	Pelvis,High	4.26	23.35	-9.88	-1.74	
	Shank,High	4.43	23.30	-9.08	-1.70	

OPTIMIZATION BASED POSTURAL CONTROL SYSTEM IN AN UNDERACTUATED EXOSKELETON

Sai Kiran Gunti and Ton Van Den Bogert

Cleveland State University, Cleveland, OH, USA

Email: saigkiran13@gmail.com

INTRODUCTION

Posture control in the human body uses a complex feedback control strategy governed by its central nervous system (CNS). The CNS has complex patterns of muscle activation to balance the human body and reduce the risk of falling. Every year, thousands of people are hospitalized as a result of injuries from falls. Improving balance in exoskeletons has the potential to help people not only by assisting them in walking, but also by improving their balance and stability.

Most exoskeletons lack balance and users require crutches to balance themselves. Modeling and controls of dynamic systems can be used to design a controls strategy that helps solve some of the balance problems.

Balance control is especially challenging in underactuated exoskeletons such as Indego [1], which have actuators at the hip and knee joints but not at the ankle. In such a system, balance control is still possible, using techniques similar to high-bar gymnastics, where performers can swing up without exerting torque at the pivot. This sometimes requires movements away from the desired position, which cannot be accomplished by conventional proportional-integral-derivative (PID) control.

In this work, we develop a model-based controller with full state feedback for balancing the Indego exoskeleton.

METHODS

The exoskeleton was modeled as a three-link inverted pendulum and the equations of motion were derived with the Lagrange approach, resulting in an equation of motion in the following form:

$$M(q)\ddot{q} + G(q,\dot{q}) = \tau$$

where τ are the joint torques and q are the generalized coordinates, the joint angles in ankle, knee, and hip. M is the mass matrix, and G represents gravity, centrifugal, and Coriolis effects. Both were determined from normal human dimensions and mass properties. The state space equations of this nonlinear system are given as:

$$\dot{X} = f(X,U)$$

Where $X = (q,\dot{q})^T$. The nonlinear equation was linearized at its equilibrium point $X_o = (0,0,0,0,0,0)^T$ using a first-degree approximation of the Taylor series:

$$f(X,U) \approx AX + BU$$

where A and B are the Jacobian matrices $A = \frac{\partial f}{\partial X}$, $B = \frac{\partial f}{\partial U}$ evaluated at the point X_o. An optimal feedback controller was designed, and the control law is given as $U = -K * X$ where K is a 2 x 6 gain matrix of the optimal feedback controller designed using linear quadratic regulator (LQR) method. These gains K_{LQR} can be found in MATLAB using the inbuilt command:

```
[K,S,e] = lqr(A,B,Q,R)
```

To improve the performance of the controller in the controllable range of initial positions, a grid of initial positions, a 10 x 10 x 10 grid with a range of initial positions from 0.2 to -0.2 radians, was made to

simulate the system 1,000 times to optimize the 12 controller gains using Nelder-Mead simplex method [2]. The cost function for this optimization is given as:

$$J(K) = \sum_{grid\ points} \int_0^T X(t)^T Q X(t) + U(t)^T R U(t)\, dt$$

The control gains obtained from LQR are used as the initial simplex. The optimization was done till the user defined tolerance of 0.001 is reached and the optimized control parameters are given as K_{opt}.

RESULTS AND DISCUSSION

Based on the derived equations of motion, the dynamic modeling of the system was done in MATLAB for the underactuated exoskeleton modeled as a three-link inverted pendulum with passive stiffness at the ankle joint and actuators at the knee and hip joints. The control gain matrix K obtained from the LQR command in MATLAB for the dynamic system is:

$$K_{LQR} = \begin{bmatrix} 1590.64 & 1301.96 & 537.5 & 611.46 & 413.52 & 186.91 \\ -463.6 & -270.68 & 78.96 & -199.16 & -112.093 & -17.23 \end{bmatrix}.$$

The optimized control parameters K_{opt} are calculated as:

$$K_{opt} = \begin{bmatrix} 1650.57 & 1357.48 & 536.76 & 615.84 & 428.42 & 187.98 \\ -497.95 & -197.23 & 76.44 & -220.51 & -112.59 & -17.53 \end{bmatrix}$$

The simulated joint angle trajectories with nonzero initial position $X(0)$ = [-0.15; 0.23; -0.23; 0; 0; 0] radians with the using control gains K_{LQR} and K_{opt} are shown in figure 1 and joint torques are shown in figure 2.

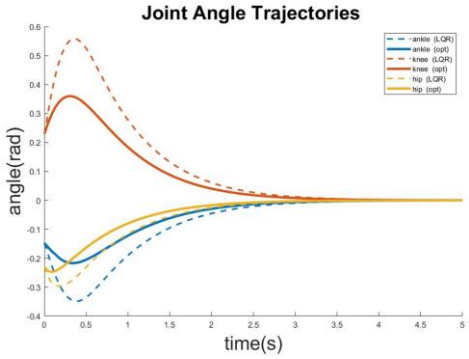

Figure 1: Joint angle trajectories using control gains from LQR method and Nelder mead optimization

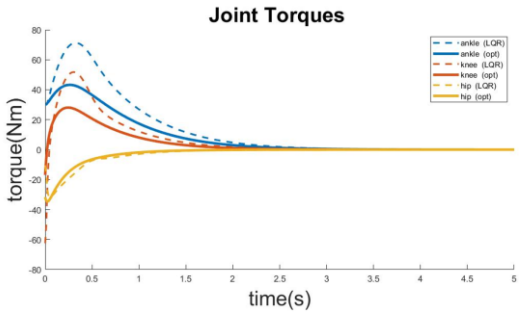

Figure 2: Joint torques using control gains from LQR method and Nelder mead optimization

CONCLUSION

The simulation results using the K gain matrix prove that the system can be stabilized at the equilibrium position with a non-zero initial position and by optimization of the control variables the overshoot is decreased by 25-30% to stabilize the system and the joint torques are reduced by 25%.

REFERENCES

[1] "INDEGO EXOSKEETON," Parker Hannifin, [Online]. Available:http://www.indego.com/indego/us/en/home.

[2] J. C. Lagarias et al., "CONVERGENCE PROPERTIES OF THE NELDER–MEAD SIMPLEX METHOD IN LOW DIMENSIONS," *Society for Industrial and Applied Mathematics Journal of Optimization,* vol. 9, no. 1, pp. 112-147, 1998.

SPATIOTEMPORAL AND MUSCLE ACTIVATION ADAPTAIONS DURING OVERGROUND WALKING IN RESPONSE TO LOWER BODY ADDED MASS

[1]Vinayak Vijayan, [1]Shanpu Fang, [1]Timothy Reissman, [1]Allison L. Kinney, [1]Megan E. Reissman

[1]University of Dayton, Dayton, OH, USA

Email: vijayanv1@udayton.edu

INTRODUCTION

Most prior studies that investigated the effects of added mass on lower body segments were performed on a treadmill, which has been known to influence gait kinematics and muscle activations. There is also limited evidence in overground studies to indicate that added mass causes changes to kinetics, kinematics, and ground reaction forces, which were previously not seen in similar treadmill studies. Specifically, one overground study found that added mass produced spatiotemporal and kinematic adjustments that caused an increase in the minimum vertical ground reaction force, the peak ankle flexor moment, first peak knee extensor moment, and peak hip flexor moment [1]. Building on this literature, we aim to characterize the impact of added mass on lower body segments during overground walking.

Lower-limb exoskeletons can provide a means of mobility, and highly reproducible rehabilitation, for patients affected by musculoskeletal and neurological disorders. However, a major impediment to exoskeleton use has been a lack of scientific understanding about the biomechanical effects of added mass, in the form of an exoskeleton, on ambulation [2]. Understanding how the body adapts to additional mass is critical for designing exoskeletons that can provide assistance without hindering the wearer's ability to volitionally move.

The purpose of this study is to characterize the effects of added mass on different segments of the lower limb. The study hopes to inform future exoskeleton design and provide insights into how mass should be distributed in an exoskeletal device to minimize the effects of added mass on a wearer's natural gait. We hypothesize that healthy young adults will be able to maintain their lower limb loading rates and spatiotemporal metrics, under added mass conditions, by modulating their muscle activity.

METHODS

Healthy, young participants (12 females and 12 males aged 22.6±3.5 years) without any lower limb injuries were recruited for the study. The subjects were fitted with 43 retroreflective markers, with at least 4 markers on each segments of interest. Surface EMG sensors were placed on Medial Gastrocnemius (MG), Rectus Femoris (RF), Soleus (SO), Tibialis Anterior (TA), Vastus Medialis (VM), and Biceps Femoris (BF) muscles on the right leg. The experimental conditions consisted of a Baseline with no added mass, and a low and high level of mass on three locations: each shank (+2lbs & +4lbs), each thigh (+2lbs & +4lbs), and pelvis (+8lbs & +16lbs). The masses were added symmetrically to the subjects by means of weight belts. Participants walked overground for up to 2 minutes to get accustomed to the additional mass before data collection. Participants completed 5 trials of overground walking, at a self-selected comfortable pace, for each experimental condition. The order of the experimental conditions was randomized.

For the purpose of analysis, the right leg gait cycle was divided into 4 phases: Phase I - first double support between right heel strike and left toe off, Phase II - single support between left toe off and left heel strike, Phase III - second double support between left heel strike and right toe off, and Phase IV - swing between right toe off and right heel strike.

Stride length, gait speed, percentage of the gait cycle spent in single and double support, area under the

curve of muscle activation within the 4 phases for the 8 considered muscles, the loading rate and loading impulse was used as metrics to compare the effects of added mass and location of added mass. Repeated measures ANOVA with Tukey-Kramer post-hoc was used to determine statistical significance.

RESULTS AND DISCUSSION

Time spent in double and single support did not change significantly with masses placed on the thigh or shank. Significant changes to the single support and double support time were observed only when adding mass to the pelvis. This could be because the maximum mass added to one side of the pelvis was 8lb, which is higher than the maximum mass added on one side of the thigh or the shank, 4lb. This adaptive change could be to improve stability, as extended periods of double support have been previously identified as key to functional stability

Table 1: Mean of percentage muscle activity.

		TA Phase I	**MG Phase II**	**RF Phase III**	**BF Phase IV**
Baseline	-	**45.78**	**53.57**	**21.26**	**27.30**
Low	Pelvis	48.31	58.02*	22.05	31.95*
Low	Thigh	48.54	51.93	20.14	28.03
Low	Shank	52.32	56.04	23.67	27.37
High	Pelvis	47.20	58.10*	22.88	30.29
High	Thigh	47.47	57.82*	30.17*	26.37
High	Shank	53.29*	54.78	18.76	27.35

With additional mass on the body, increased loading rate was a potential concern as this can lead to a higher risk for developing or worsening osteoarthritis [3]. However, none of the added mass conditions produced a significant increase in the loading rate compared to Baseline.

Muscle activity increases noticed in the earlier phases in VM, TA, MG, and SO likely reflect increased effort to support additional loading on the limb in early to mid-stance. However, the increased activity in BF in Phase IV appears to represent anticipatory changes in limb stiffening just prior to heel strike (Table 1). This suggests that healthy adults can quickly manipulate their muscle activity to prepare for support and stability demands due to altered segment masses prior to and during heel strike. The results of this study demonstrates how added mass affects muscle activity and this could supplement future design of EMG-based control systems, as such controllers have been shown to be more advantageous and better preferred by users [4]. Our initial hypothesis was partially true. Healthy young adults were able to maintain their gait speed and stride length by modulating their muscle activity and the double and single support times.

CONCLUSION

Based on our analysis, we caution exoskeleton designers against designing exoskeletons with a mass of 16lb or greater on the pelvis. We also observed that adding a mass of up to 4lb on the thigh and shank did not produce any consistent adaptive changes to the spatiotemporal metrics of healthy young adults during overground walking. However, we recommend distributing the mass across the pelvis and the thigh, as this could allow the larger muscles to absorb the work done against the added mass. The results also demonstrate how added mass affects muscle activity, and this could supplement future design of EMG-based control systems.

REFERENCES

1. Dames, K, et al. *Gait & Posture.* 207-211, 2016.

2. Yamamoto, M, et al. *Journal of Physical Therapy. 966-970, 2018.*

3. Pamukoff, D, et al. *Journal of Clinical Biomechanics.* 61-65, 2016.

4. Young, A, et al. *Frontiers in Bioengineering and Biotechnology. 5, 2017.*

ACKNOWLEDGEMENTS

We acknowledge the initial efforts of Pichayathida (Alice) Luanpaisanon in the collection of motion capture data.

An Adjustable Pelvic-Trunk Corset for Lower-Limb Exoskeletons

[1,2]Marshaun Fitzpatrick, [1]Maja Paar, [1]Umit Erol, [1]Ryan-David Reyes, [1,2,3]Nathan Makowski, [1,2]Musa Audu, [1,2]Ronald Triolo and [1]Roger Quinn

[1]Case Western Reserve University, Cleveland, OH, USA

[2]Louis Stokes Cleveland Veterans Affairs Medical Center, Cleveland, OH, USA

[3]MetroHealth Medical Center, Cleveland, OH, USA

Email: mnf13@case.edu

INTRODUCTION

Research and development of exoskeleton devices to mimic or assist walking have been ongoing since the 1960s [1]. One application for these exoskeletons is to aid individuals with spinal cord injury (SCI) to regain mobility. Our collaborative team at Case Western Reserve University and the Louis Stokes Cleveland VA Medical Center is developing a hybrid exoskeleton to enable walking [2]. The hybrid exoskeleton combines functional neuromuscular stimulation (FNS) applied to the user's muscles with assistance from motor-powered actuators at the hip, knee and ankle joints.

One of the main interface elements between the user and the motorized joints is a thoracic-lumbo-sacral orthotic corset. Trunk interface components often use a custom-fit corset or rely on a set of different sizes (e.g. small, medium, large). However, this limits the ability to optimize fit for many users. Furthermore, many of these devices limit motion to the sagittal plane. To improve comfort and balance of the user, exoskeleton developers have begun incorporating motion in the frontal plane with hip ab/adduction [3]. To accommodate the need to align ab/adduction degrees-of-freedom, adjustable mechanisms must align the joint centers of rotation. This abstract presents our design for an adjustable corset that enables hip ab/adduction through either passive or active mechanisms.

METHODS

Overall design requirements for the new trunk corset are shown in Table 1.

Table 1: Design Requirements

Requirement
Fit the 5th percentile female to the 95th percentile male
15 degrees of motion in either direction which can be locked in several locations or left unlocked for able-bodied testing
Ability to determine abduction/adduction angle
Allow hips to be moved forward and backward to align with the center of rotation
Integrate with the current device
Reduce weight from the previous corset
Make as comfortable as possible for the user

3D models of the pelvic-trunk corset were created using Solidworks. Parts critical to the structural integrity of the corset were made of 6061 aluminum for its high strength to weight ratio. These parts were manufactured in house using various machines including a waterjet cutter, CNC mill, and drill press. Human interfacing parts were made using either PLA or fiberglass. The PLA parts were made using an FDM 3D printer, while the fiberglass parts were cast using a hand-carved foam mold.

For testing, able-bodied users who had used the exoskeleton with the previous corset donned and walked with the exoskeleton using the new pelvic-trunk corset. After each trial, the users provided feedback to the design team regarding balance, comfort, and the difficulty to don and doff the exoskeleton.

RESULTS AND DISCUSSION

The completed assembly of the new corset is shown in Figure 1. The trunk portion consists of two metal backplates which allow adjustment of the width and height. Four back supports and two side supports, that interface with the user, are attached to the backplates using fasteners and Velcro straps. Around the pelvic region are a set of parts to align the joint centers and allow ab/adduction to be either locked or unlocked.

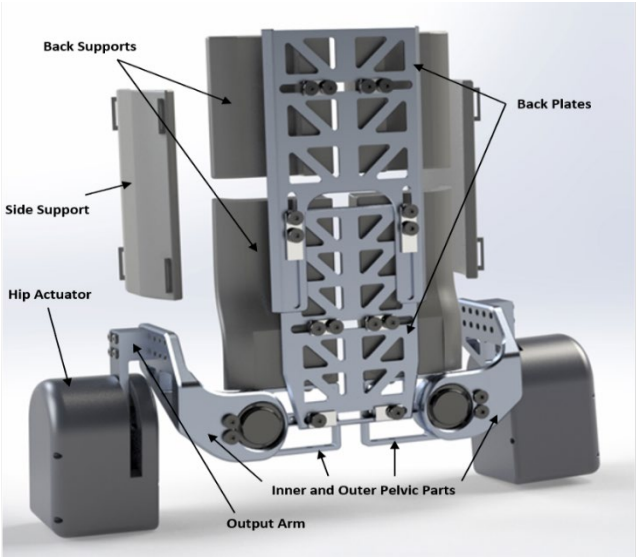

Figure 1: Finished assembly with labeled components.

This design met all the design requirements except for being able to align the hip flexion/extension actuators with the hip centers if located further than 2.8 inches away from the back supports. Fixing this issue will require extending the output arm in the anterior direction. Overall, the design allows a total adjustment range of 2.4 inches in the anterior/posterior direction, which would be enough for the 5th percentile female to the 95th percentile male.

The initial assessments of the design by the able-bodied users have indicated that having unlocked ab/adduction joints increases comfort and makes balance easier, suggesting that adding ab/adduction actuation may improve exoskeleton assisted walking for people with SCI. It was also easier to don and doff than our previous fixed-sized corset due to the side supports being attached with straps instead of being rigidly connected to the rest of the corset. Future testing will determine if removing the sagittal plane constraint has a significant effect on metabolic cost.

CONCLUSION

A new corset was designed and constructed for interfacing with hybrid exoskeletons. The corset allows a wider range of users to be properly fitted due to available adjustments for width, height, and joint alignment. It also removes the sagittal plane constraint by freeing the hip ab/adduction degree-of-freedom. These changes provided better balance and was more comfortable for able-bodied users.

REFERENCES

1. Yan, T, et al. *Robotics and Autonomous Systems*. 120-136, 2015.

2. Nandor, M, et al. *Frontiers in Robotics and AI*. 8, 2021

3. Wang, S, et al. *IEEE transactions on neural systems and rehabilitation engineering*. 277-286, 2014

4. Reyes, R-D, et al. *Frontiers in Neurorobotics*. 14, 2020.

ACKNOWLEDGEMENTS

This work was funded by VA merit review 1I01RX002275-01 and NSF grant CPS 1739800

THE EFFECT OF NIPPLE STIFFNESS AND HOLE SIZE ON INFANT SUCKING BEHAVIORS

[1]Khaled Adjerid, [1]Maxwell L. Johnson, [1]Christopher J. Mayerl, [1]Chloe E. Edmonds, [1]Kendal E. Steer, [1]Laura E. Bond, [2]Francois D.H. Gould and [1]Rebecca Z. German

[1]Northeast Ohio Medical University, Rootstown, Ohio, USA

[2]Rowan School of Osteopathic Medicine, Stratford, New Jersey, USA

Email: kadjerid@neomed.edu

INTRODUCTION

Sensory information plays an important role in successful infant feeding [1]. The nipple is one important source of sensory information that may affect feeding behavior in bottle feeding infants and can be a method for treating feeding disorders. While differences between commercially available nipples have been studied, mostly by observing external indicators of sucking behaviors, few studies have explored the *in vivo* effects of specific nipple properties on feeding behaviors [2]. Furthermore, it has been shown that milk flow rate, typically modulated by changing nipple hole size, affects feeding behaviors, including sucking rate and number of sucks per swallow [3,4]. However, it is not clear how sensory information gathered from nipple material type and hole size affects key feeding behaviors. Here, we ask: how do changes in sensory information from differences in nipple types (stiffness and hole size) affect infant nipple feeding?

METHODS

We filmed infant suckling in a seven day old validated infant pig model using highspeed video fluoroscopy in the lateral view at 100fps. Infant pigs were bottle-fed barium contrast enhanced milk replacer formula on four custom fabricated nipples. We fabricated nipples out of food-safe silicone with two levels of stiffness (327.93 MPa and 794.41 MPa) and two hole sizes (2π mm^2 and 0.5π mm^2). We also fabricated a fifth, training nipple, with intermediate properties (411.15 MPa, π mm^2) that was used for all other feeds (Fig. 1).

Figure 1: Custom fabricated nipples were used in this study. Compliant nipples (left, white) and stiff nipples (right, orange) were tested along with large hole size (top) and small hole size (bottom). A training nipple (middle, pink) of intermediate stiffness and hole size was used for all other feeds.

Each pig was recorded first on the training nipple, and then on each of the four test nipples in random order to ensure that changes in feeding behaviors were due to the properties of individual nipples rather than any particular sequence of exposure. To that end, the training nipple was also used as an experimental washout between nipple types. For each pig on each nipple type, suck timing (time from first tongue contact with the palate to just prior to the next contact) and first frame of maximum nipple compression were identified in sequences of 10 consecutive sucks. We measured nipple compression extent, representing nipple diameter at the first frame of maximum compression. We also manually traced the laterally projected nipple area (representing nipple volume) for each frame in a sequence (~200 for 10 suck cycles/pig and nipple type) to observe how the volume of the nipple changes across the

sequence. Because of size effects due to imaging, all nipples were scaled to maximum area.

To test the effect of different nipple types on sucking behavior, we used a mixed model type-III ANOVA, with scaled area as the response variable, nipple type as the fixed effect, and individual animal as a random effect.

RESULTS AND DISCUSSION

All animals drank from all nipples for at least 30 sucks, although latching was intermittent when pigs fed on the stiff nipple with the 0.5π mm^2 hole. We found that both the minimum compressed nipple diameter and nipple volume were lower in the stiff nipples than in compliant nipples ($p < .01$). Additionally, we found that hole size resulted in differences in nipple compression ($p < .05$).

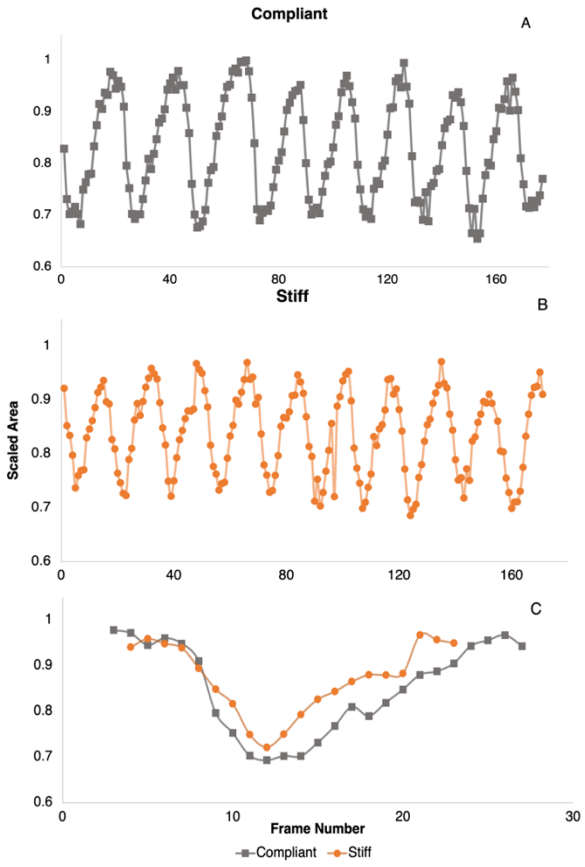

Figure 2: Lateral projected nipple area traces across a representative sequence of 10 suck cycles for compliant training nipple (A) and stiff nipple (B). Comparison of a single representative trace of a compliant and stiff nipple (C).

Our results suggest that the amount of nipple compression depends on material properties and hole size. Stiffer nipples require more force to achieve the same level of compression as more compliant nipples. We hypothesize that this requires the infant pig to use more force to achieve the same level of compression, to compensate with increased suction, or simply receive less milk per suck. Furthermore, cases of infant pigs repeatedly unlatching or refusing smaller hole/stiffer nipples suggest that sensory feedback from the nipple properties directly overall feeding patterns.

CONCLUSION

Here we show that sensory information, from different nipple stiffnesses and hole size, plays a significant role in infant suckling. Understanding this relationship of sensory feedback on feeding patterns can inform therapies in pathological cases of poor feeding performance.

REFERENCES

1. Muhle, P, et al. *Human Brain Mapping.* 2020

2. Kotowski, J, et al. *Maternal and Child Nutrition.* 2020

3. German, R.Z., et al. *Dysphagia*. 2004

4. Pados, B.F, et al. *Nursing for Women's Health*. 2021

ACKNOWLEDGEMENTS

This work was funded by the National Institutes of Health grant number R01 HD096881 awarded to R.Z.G. All work was conducted at the Northeast Ohio Medical University in accordance with the NEOMED IACUC protocol #19-03-222.

DECAY RATES OF GENERATED PARTICLES AND AEROSOLIZED DROPLETS IN DENTAL PRACTICES

[1]Homa Momeni Eskandari, [2]Darya Dabiri, [1]Omid Amili and [1]George H. Choueiri

[1] Mechanical, Industrial and Manufacturing Engineering, University of Toledo, Toledo, OH, USA

[2] Department of Dentistry, University of Toledo, Toledo, OH, USA

Email: homa.momenieskandari@rockets.utoledo.edu

INTRODUCTION

At the onset of the COVID-19 pandemic, the National Center for Immunization and Respiratory Diseases (NCIRD) recommended that elective dental procedures, surgeries, and non-urgent outpatient visits be postponed [1]. The prevalence of particles and aerosolized droplets resulting from dental procedures was thought to elevate the risk of COVID-19 transmission. Some recommendations for urgent dental procedures involved dry cutting to reduce the number of aerosolized particles; operating in a closed room with negative pressure; and waiting extended periods between patients. While these recommendations appear to be diligent, very little supporting research exists connecting which procedures may generate potentially infectious aerosols, or how quickly the concentration of these aerosols decay to safe levels in dental settings [1]. Of main concern is the production of aerosols which are less than 5–10 µm in diameter. Liquid droplets of this size quickly evaporate; however, they leave behind potentially infectious non-volatile material known as droplet nuclei [2] which remain suspended in air for extended periods of time. Due to their size, once inhaled, the droplet nuclei travel deep enough into the lungs to cause severe respiratory illnesses. In a sister study, we examined the production rate of such fine particles resulting from different dental procedures, while here we focus on the rates of decay of such particles.

METHODS

An array of particulate matter (PM), temperature and humidity sensors were set up in one of the rooms of a dental clinic having dimensions of approximately 3 × 3.5 m. The PM sensors can measure particles in the range of 10 µm or less and calculate particle size distribution. Aerosolized particles were generated using standard dental equipment such as a high-speed handpiece and an air/water syringe. Various practical considerations were tested, such as leaving the room door open or closed, activating an air purifier with and without ionization, and using an extraoral suction unit.

A baseline of airborne particles was first established by continuously running the PM sensors throughout a regular business day. An excess amount to particles was then generated and allowed to decay while keeping the room considerations constant. The decay rates of particle concentration were then observed until the number of particles reached the established baseline.

RESULTS AND DISCUSSION

While the dental clinic room was not in use, the number of particles measured by the PM sensors was monitored throughout a regular business day and for a duration of 24-hours. This test was repeated to establish the baseline cases for particle concentration when the room door was left open and closed (Fig. 1). In both cases, a particle concentration of 10 particles/cm^3 was determined to be the maximum and ~ 3–4 particles /cm^3 was the average. Therefore, in our analysis, decay rates will be established down to a particle concentration of at least 10 particles/cm^3. When determining the decay rates, the maximum particle concentration we used was over an order of magnitude higher than this baseline (specifically 200 particles/cm^3). This upper bound can be exceeded during typical dental procedures,

however only locally and for brief periods during cutting or cleaning. Globally, and on average, this limit is typically higher than what would be sustained in a clinical setting.

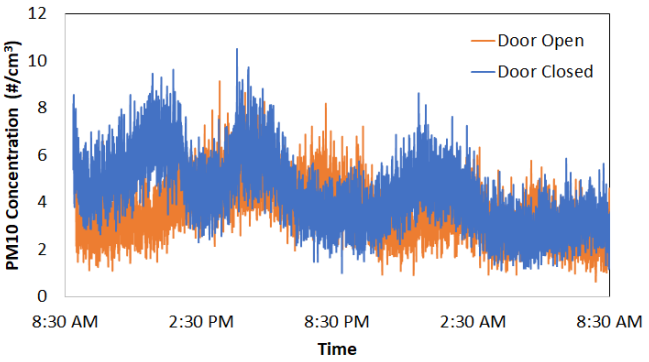

Figure 1: Number of particles with mean diameter less than 10 µm measured over a 24-hour period in a room of the dental clinic with its door open and closed.

Using a high-speed handpiece and an air/water syringe, particles were generated over a period substantially longer than what would typically be observed during routine dental procedures; the reason for this was to extend the data over a broad range of concentrations and establish more accurate trendlines in the concentration range of interest. Surprisingly, as can be seen in Fig. 2, the rates of decay when the door was closed where exponential irrespective of particle reduction considerations. Only the slopes of the decay rates were affected, and these show faster decay with the use of and air purifier and even more so when a combination of tools were used.

When the room door was left open, an unexpected power law rate of decay was observed. This means that initially, the particle concentration can decrease more rapidly than when the door was closed, however as particle concentrations decrease, the rate eventually saturates, and a slower rate of decay would be observed.

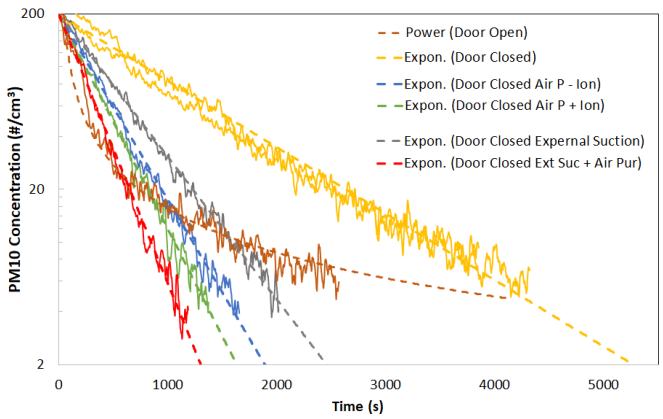

Figure 2: Number of particles with mean diameter less than 10 µm decaying over time. Appropriate exponential and power law fits were superimposed on the data.

CONCLUSION

The rate of decay of particles and aerosols generated by typical dental instruments and procedures was examined under a variety of considerations. With the door closed, an exponential rate of particle decay was observed, while with the door open, the rate of decay followed a power law. It was concluded that using readily available and cost-effective environmental management devices such as air purifiers can dramatically decrease the required wait time between patients. Combining different tools appears to further decrease this time, though only marginally.

REFERENCES

1. National Center for Immunization and Respiratory Diseases (NCIRD), Division of Viral Diseases, *Guidance for Dental Setting*, Dec. 4, 2020

2. Wells WF. *Airborne contagion and air hygiene.* Cambridge, MA: Harvard University Press; 1955

ACKNOWLEDGEMENTS

The authors thank the National Institutes of Health (grant number: X01 DE030405-01) for partial financial support through the National Dental PBRN collaborative group funding U19-DE-028717 and U01-DE-028727.

AEROSOL CHARACTERIZATION IN A DENTAL SETTING

[1]Niloufar Sadoughipour (Presenter), [2]Carol Wiese, [2]Darya Dabiri, [1]George Choueiri, and [1]Omid Amili

[1]Mechanical, Industrial and Manufacturing Engineering, University of Toledo, Toledo, OH, USA

[2]Department of Dentistry, University of Toledo, Toledo, OH, USA

Email: nsadoug@rockets.utoledo.edu

INTRODUCTION

The generation, aerosolization, and transport of virus-laden particles play a critical role in the spread of many respiratory diseases such as COVID-19. Previous studies, e.g. [1-2], have shown that the transport of a cloud of droplets may be driven by the coherent motion of the puff in a short distance from the source where droplets are large and high in concentration. As the evaporation and gravitational effects reduce the particle size and concentration in the cloud, the puff velocity decays due to the air entrainment, drag forces, etc. In such a state, the transport of the particle nuclei is predominately dictated by the surrounding air currents and turbulence intensity.

However, many physical aspects of this complex process governed by fluid dynamics fundamentals are not well understood. Such flow physics is highly sensitive to the problem boundary conditions such as the particle properties, droplet/aerosol concentration, initial hydrodynamics conditions, and environmental conditions. For example, in a dental setting where the risk of pathogen transmission is extremely high in the COVID-19 pandemic, high concentrations of aerosolized solids and liquids generated by air turbine handpieces are comparable to respiratory events like sneezing. In this study, we present the development of an experimental setup to characterize the dynamics of aerosols in a clinical setting. We report the particle topology and decay time for common dental procedures performed by our dentists on a dental manikin simulator in the absence of any biological agents. The effect of different particle-reducing strategies under well-controlled conditions are reported with the use of a combination of particle sensors and high-speed imaging.

METHODS

In order to understand the dynamics of aerosols generated and transported in a dental setting, we developed a setup consisting of 35 air quality sensors (Sensirion Particulate Matter Sensor SPS30) as well as temperature and humidity sensors. The set of sensors are systematically positioned around a dental simulator in a dental operatory in the Department of Dentistry at the University of Toledo as shown in Fig. 1. Sensors calibrated against a laser/phase Doppler anemometer are programmed to simultaneously acquire particle concentration at a frequency of approximately 1 Hz. Sensors allocate the data into five channels: 0.5 μm, 1.0 μm, 2.5 μm, 4.0 μm, 10 μm; here we only report the 10μm-channel due to the highest certainty. In addition, the setup is furnished with a high-speed camera to measure the velocity and trajectory of particles typically not detectable by the particle sensors.

The dental assistant alongside the practitioner carefully mimic the common procedures such as restoration treatments. The large parameter space includes performing dental procedures at six sextants for common treatment durations at different conditions such as using an external suction, an external fan when the room door is open or close. Each experiment is repeated multiple times for the statistical convergence, and the results are compared against a well-established benchmark baseline case. Here for brevity, we only report the data from particle sensors for select cases.

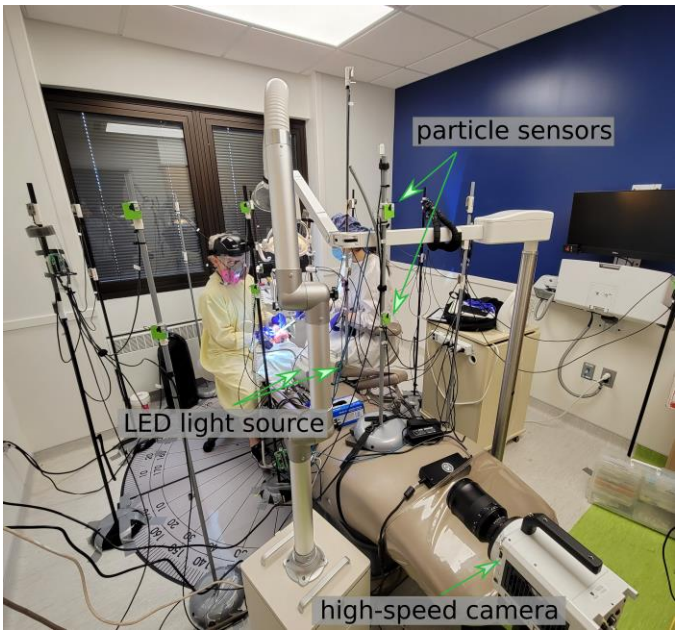

Figure 1: A snapshot of the experimental setup.

RESULTS AND DISCUSSION

Figure 2 shows a time history of the particle count measured at different locations during a set of dental procedures. As the procedure continues, particle concentration grows to reach a peak, typically towards the end of the procedure as noticed in the local maxima followed by a decay. The decay behavior of the particle concentration may be represented by an exponential function or a power-law as addressed in detail by the authors in the abstract entitled "*Decay rates of generated particles and aerosolized droplets in dental practices*".

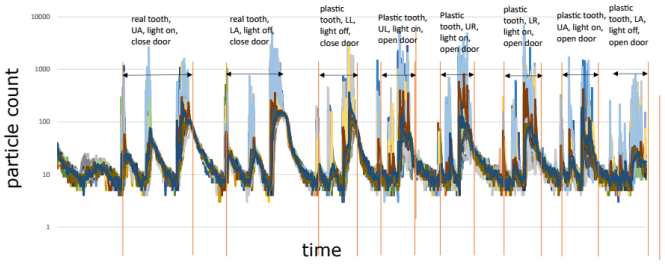

Figure 2: Temporal evolution of the particle concentration measured by different sensors for a set of dental procedures.

The spatial distribution of the measurement points allows us to reconstruct a 2D map of the particle concentration as shown in Fig. 3. In the beginning of each procedure, localized hot spots are identified near the practitioner and the assistant. Interestingly enough, these hot spots dissipate over time at one location and move to other locations showing the complex fluid dynamics of the cloud of particles.

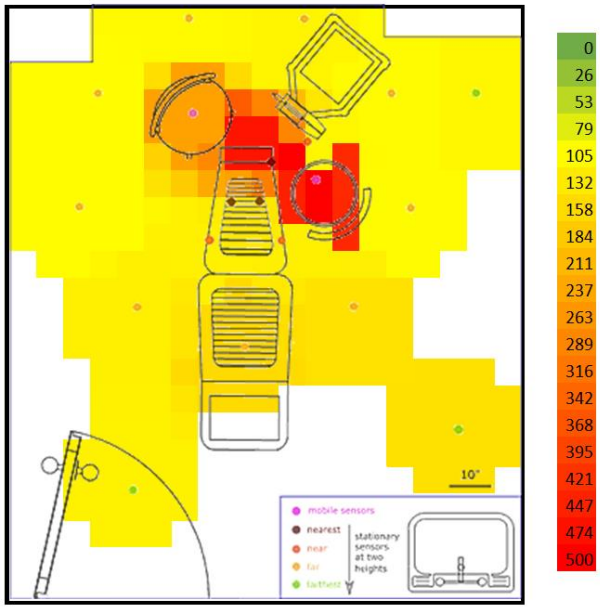

Figure 3: A snapshot of the particle concentration at one instant in time.

CONCLUSION

The spatiotemporal measurements of the particle concentration in a dental office under well-controlled conditions allows us to estimate the evolution of transport of aerosolized solids and liquids at different clinical conditions. This provides us an opportunity to carefully identify the most effective approach in limiting particle distribution.

REFERENCES

1. Bourouiba, L, et al. *J. Fluid Mech.* 537–563, 2014.

2. Balachandar, S, et al. *Int J Multiphas Flow*, 1-20, 2020.

ACKNOWLEDGEMENTS

The authors thank the National Institutes of Health (grant number: X01 DE030405-01) for the financial support for this work through the National Dental PBRN collaborative group funding U19-DE-028717 and U01-DE-028727.

OROPHARYNGEAL CAPSAICIN APPLICATION ALTERS SWALLOWING KINEMATICS TO IMPROVE PERFORMANCE

Chloe Edmonds[1], Rebecca German[1], Laura Bond[1], Francois Gould[2], Khaled Adjerid[1], Kendall Steer[1], and Christopher Mayerl[1]

[1]Northeast Ohio Medical University, Rootstown, OH, USA

[2]Rowan School of Osteopathic Medicine, Stratford, NJ, USA

Email: cedmonds@neomed.edu

INTRODUCTION

Infant mammalian feeding requires the coordinated action of lingual, oropharyngeal, and hyolaryngeal musculature to acquire milk, form a manageable bolus, and transport the bolus into the esophagus without liquid entering the trachea (aspiration). Sensorimotor feedback plays a critical role in modulating swallowing motor outputs, such that the alteration of oropharyngeal and laryngeal sensation may change swallow muscle activity [1]. Many of the pathologies that cause dysphagia (the abnormal condition of difficulty swallowing) in infants are linked to decreased sensation, including iatrogenic nerve lesions [2]. Conversely, enhancing sensation is a common method of dysphagia management, often achieved by increasing viscosity [3].

A promising method of upregulating oropharyngeal sensation is found in capsaicin, a naturally occurring compound found in pungent peppers. Capsaicin produces sensations of heat and burning when consumed because it is an agonist of Transient Receptor Potential channels of the subfamily vanilloid, member 1 (TRPV1). The internal branch of the superior laryngeal nerve (iSLN), which initiates the reflexive pharyngeal swallow, expresses TRPV1 channels [4]. Past studies have found that capsaicin exposure reduces instances of aspiration in elderly patients [5], possibly due to increased iSLN activity and subsequent limitation of bolus size. However, the effects of capsaicin have not been explored in infant populations, and the exact neurophysiological basis for changes in swallow function remains unknown. By applying capsaicin to the oropharyngeal mucosa of an infant animal model, we tested the ability of capsaicin to enhance the function of the iSLN, which is likely associated with altered oropharyngeal kinematics, decreased bolus size, and improved swallow performance.

METHODS

We trained five infant pigs to drink milk replacer from a bottle fitted with a pig-specific nipple. We sutured radiopaque beads over each pig's hyoid and thyroid, and implanted beads in the tongue (anterior, middle and posterior positions), hard palate, and nose. In a sterile surgery 14 days after birth, we unilaterally transected each pig's SLN. Infant pigs consumed formula mixed with barium while they were recorded via biplanar videofluoroscopy. We collected data prior to the application of capsaicin and immediately following the application of a capsaicin solution (capsaicin dissolved in polyethylene glycol, 10 ppm) applied to the valleculae and soft palate.

We used XMALab to track the three-dimensional translations of each marker. Data were processed in Autodesk Maya to remove the effects of extraneous skull movement and feeding posture. A custom MATLAB script extracted the total excursion of the hyoid, thyroid, and posterior tongue during each swallow and the timing of these structures' movements relative to swallow initiation. The frequency of suckling and swallowing was calculated separately using R. The size of the liquid bolus was quantified by tracing the outline of the

bolus in the lateral view in ImageJ. Swallow performance was assessed using the Infant Mammalian Penetration-Aspiration Scale (IMPAS), which classifies the degree of penetration or aspiration for each swallow.

RESULTS AND DISCUSSION

The frequency of suckling and swallowing were unchanged with capsaicin application, and the total excursion of the posterior tongue was not affected. Excursion of the hyoid and thyroid were slightly decreased in infant pigs with capsaicin applied, though the timing of hyoid and thyroid elevation was consistent across conditions. Notably, there was a significant change in the timing of posterior tongue movement with capsaicin exposure (Fig. 1), as infant pigs with capsaicin experienced a greater proportion of their posterior tongue movement prior to pharyngeal clearance of the bolus.

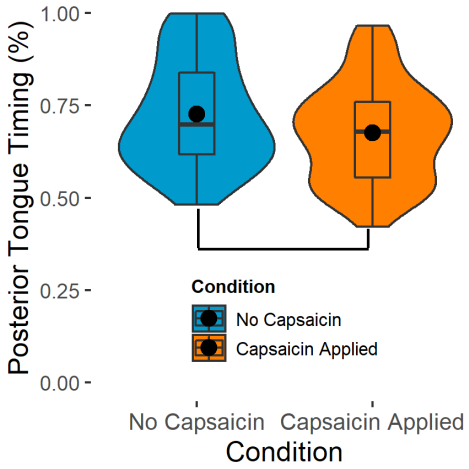

Figure 1: Timing of posterior tongue movement before and after applying capsaicin, given as the proportion of total movement completed prior to pharyngeal clearance.

Swallow performance improved after capsaicin application, such that the log odds of penetration and aspiration were significantly decreased. Capsaicin application also significantly decreased the size of the liquid bolus (Fig. 2). This reduction in bolus size resulted in improved swallow performance, such that a 1 cm^2 increase in bolus size significantly increased the log odds of penetration and aspiration.

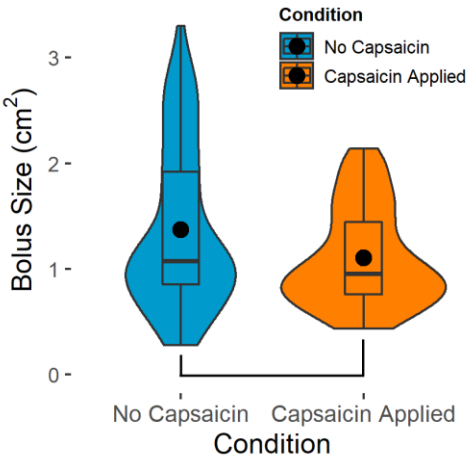

Figure 2: Changes in bolus area (as measured in the lateral view) after applying capsaicin to the infant pig model.

CONCLUSION

Capsaicin significantly altered the biomechanics of the swallow, particularly by reducing the total excursion of the hyoid and thyroid and changing the timing of posterior tongue movement. Subsequently, bolus size was reduced, which was linked to improved swallow safety. These changes may result from increased iSLN excitability caused by TRPV1 channel activation, which would allow the iSLN to more readily trigger a swallow and thus limit the bolus to a manageable size. This study provides insight into the neural control of the swallow and further demonstrates that manipulation of the peripheral nervous system may be a useful strategy to combat oropharyngeal dysphagia.

REFERENCES

1. Steele, C & Miller, A. *Dysphagia.* 323-333, 2010.

2. Gould, F, et al. *Front. Neurol.* 495-502, 2019.

3. Newman, R, et al. *Dysphagia*. 232-249, 2016.

4. Hamamoto, T, et al. *Acta Otolaryngol.* 560-568, 2009.

5. Rofes, L, et al. *Gut.* 1280-1287, 2013.

ACKNOWLEDGEMENTS

This work was supported by the National Institutes of Health [R01HD088561 to R.Z.G.].

QUANTIFYING GAIT PERTURBATION RESPONSES USING THE HOTELLING T-SQUARED STATISTIC: A NOVEL APPROACH

[1] Hala Osman MS, [2]Antonie J. van den Bogert PhD, [3] Debbie Espy PT PhD

[1] Cleveland State University, Department of Biomedical Engineering, Cleveland, OH, USA
[2] Cleveland State University, Department of Mechanical Engineering, Cleveland, OH, USA
[3] Cleveland State University, College of Sciences and Health Professions, Cleveland, OH, USA
Email: h.osman@vikes.csuohio.edu

INTRODUCTION

Stroke survivors show a high risk of falls with unexpected external perturbations during walking. Consequently, risk of falling is an important outcome variable in clinical trials for therapeutic interventions. Direct measurement of fall risk is impractical, requiring large studies with long follow up periods. Surrogate measures of gait stability, possibly related to fall risk, have therefore been proposed [1].

With modern instrumented treadmills, it becomes possible to have a more ecological, lab-based measure of gait stability, by delivering precisely timed and dosed perturbations during gait [2]. Gait stability can be measured by determining the maximum perturbation that the participant can recover from [2] but this requires a lengthy protocol, and the outcome may not be precise enough.

It would be desirable to quantify the response to a perturbation beyond a simple binary (fall or recovery) score. Conventional gait analysis might examine specific gait variables, such as a joint angle, to quantify how much, and for how long, the perturbation response deviates from the normal gait cycle.

Preliminary attempts to measure the magnitude and duration of the response, based on joint angles, suggested that these measures are poorly defined and not reliable. Here we introduce a more general, multivariate approach, inspired by the gait deviation index based on principal component analysis (PCA) [3]. Instead of joint level variables, we use raw marker trajectories, with PCA to reconstruct any missing data [2].

METHODS

Participants were tested by a progressive belt speed perturbation protocol on an instrumented treadmill [1] and optical motion capture was used to obtain 3D full body kinematics. The protocol consisted of 15 trials of 90 seconds, with a single belt speed perturbation delivered at midstance, during a random gait cycle in the middle third of the trial.

Normal gait was defined as the set of complete gait cycles except those within 10 seconds after the perturbation. From the normal gait data, the mean and covariance matrix of all marker coordinates was estimated using the ECM algorithm [4], which is available in the Matlab Financial Toolbox and can tolerate a moderate amount of missing data. Missing marker data were reconstructed by placing the entire marker vector at the minimum Mahalanobis Distance from the mean, constrained by the available measurement.

At each time point after the perturbation, the deviation from normal gait was defined using the Hotelling T-squared statistic, calculated from all marker coordinates $\mathbf{x}$, and the previously estimated mean $\boldsymbol{\mu}$ and covariance matrix $\mathbf{C}$:

$$T^2 = (\mathbf{x} - \boldsymbol{\mu})^T \mathbf{C}^{-1} (\mathbf{x} - \boldsymbol{\mu})$$

T^2 is proportional to the number of marker coordinates, and is the square root of the

Mahalanobis distance from the mean. T^2 was low-pass filtered at 1 Hz with a double second order Butterworth filter. The F-distribution was used to calculate the probability (p) that that the vector **x** represents unperturbed gait. The duration of the perturbation response was defined as the period where $p<0.001$. The magnitude of the perturbation response was defined as the maximum of the low-pass-filtered T^2. Preliminary results will be presented to demonstrate the method, and to determine the sensitivity to the marker set used.

RESULTS AND DISCUSSION

Figure 1 shows the perturbation response from a full-body marker set (47 markers) [5]. After the perturbation, the T^2 statistic is clearly elevated above the normal gait background. The duration (t_2) of the response ($p<0.001$) was 4.508s, and the magnitude ($T^2_{\max}$) was 3998.

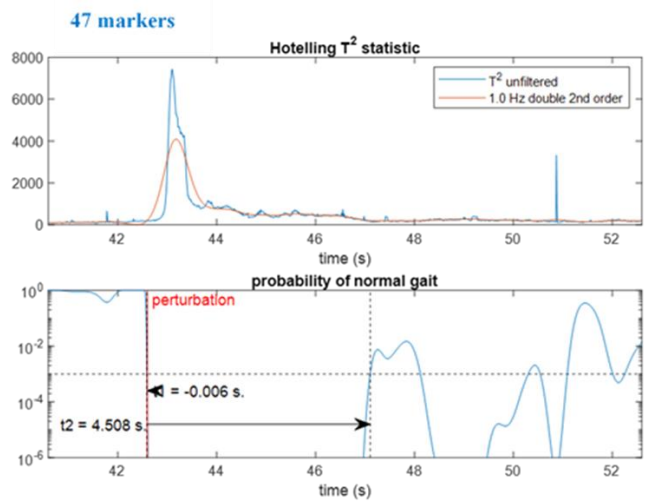

Figure 1: Response to perturbation with 47 markers

When using a smaller set of 17 markers (Fig. 2), there was still a clear response in the Hotelling statistic. The duration and magnitude of the response were, respectively, 4.036s and 990. The method was practical and can be applied with the full marker set or reduced number of markers (Fig. 3). The perturbation response depends on the number of markers that were used in the analysis.

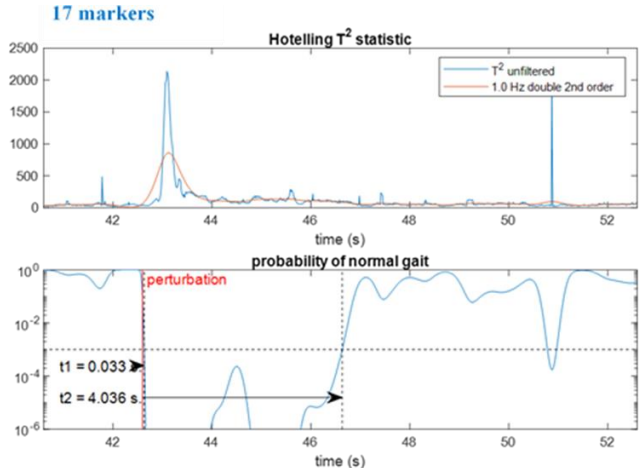

Figure 2: Response to perturbation with 17 markers

With only 17 markers, the duration of the response was shorter, and the magnitude of the response is lower. This may be because the p-values are affected by the number of markers, via the F distribution.

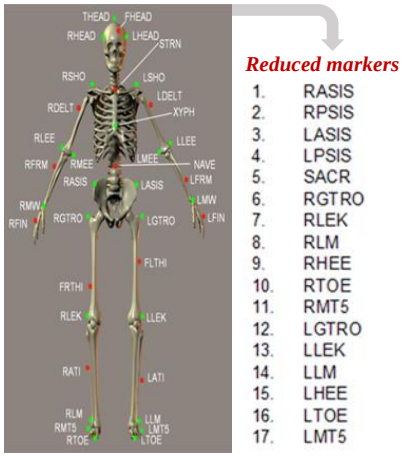

Figure 3: Marker Sets [5]

CONCLUSION

The developed approach offers both engineers and physical therapists a method to assess response to perturbation accurately. The approach appears to be robust with respect to the choice of marker set and with respect to missing data. In future work, we intend to show that there is a high correlation between the results from both marker sets, and to determine a minimal marker set that gives sufficiently reliable results.

REFERENCES

[1] Bruijn, S, et al. *J. of the Royal Society Interface*, no. 83. 2013
[2] Osman, H, et al. *J. Biomech.*, p. 110477, 2021
[3] Schwartz and Rozumalski, *Gait Posture*, pp. 351–357, 2008
[4] Sexton, J and Anders R. S. *Biometrika.*, pp. 651–662, 2000
[5] van Den Bogert, A, et al. *Med. Biol. Eng. Comput.*, 2013

A TREADMILL PERTURBATION METHOD FOR ASSESSMENT OF REFLEX MODULATION DURING GAIT

[1]Dana Lorenz and [1]Antonie van den Bogert, Ph.D.

[1]Cleveland State University, Cleveland, OH, USA

Email: d.l.lorenz@vikes.csuohio.edu

INTRODUCTION

Reflexes play an important role in the control and stability of human walking. Mathematical models have been developed [1] but were not informed by experimental data. If we can obtain mathematical models from experimental data, this will contribute to a better understanding of how locomotion is controlled. Potential clinical applications are the diagnosis of abnormal reflexes and the development of bio-inspired control systems for exoskeletons and prostheses. Here we present a method for quantification of reflexes using a forward-fall inducing perturbation, with the specific goal of detecting reflex modulation during the gait cycle [2].

METHODS

A dual-belt treadmill, with one force plate under each belt, was used to create perturbations while participants walked at a normal speed. Eight wireless EMG sensors (Delsys Trigno) were placed on the Tibialis Anterior, Lateral Gastrocnemius, Soleus, Biceps Femoris, Rectus Femoris, Vastus Lateralis, Vastus Medialis, and Gluteus Maximus of the right leg. The system detected the heel strike and toe-off using force plates and estimated the mean duration of the stance phase. After each heel strike, a random number determined (with 10% probability) whether a perturbation would be generated so that perturbations remained unexpected. Perturbations consisted of an increase of belt speed (by 0.75 m/s for 50 ms), delivered with equal probability at 10%, 20%, 30%, 40%, 50%, 60%, 70%, 80%, or 90% of the stance phase, this can be seen in Figure 1. Six 5-minute perturbed walking trials, at a speed of 1.2 m/s, were collected on one participant, with rest and instrumentation checks in between each trial. The EMG data was processed into an EMG envelope, divided into gait cycles, and separately averaged for the normal walking and each type of perturbed walking.

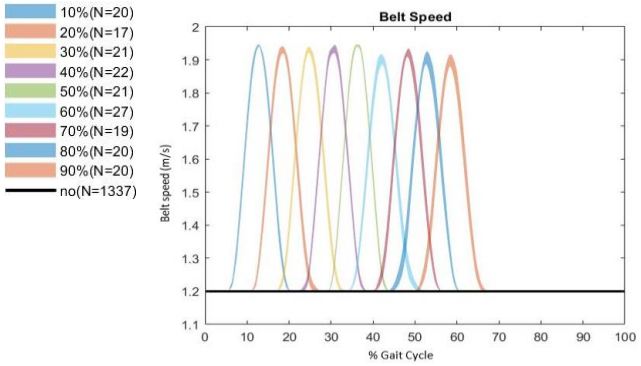

Figure 1: Average recorded belt speeds of the perturbed side for each perturbation type

RESULTS AND DISCUSSION

Each type of perturbation occurred during 20-30 gait cycles, and the remaining gait cycles (more than 1000) were not perturbed. After averaging the perturbed gait cycles, a noticeable difference could be seen compared to non-perturbed gait cycles. As seen in Figure 2, the Biceps Femoris shows increased muscle activation following most perturbation types. Specifically, the reflex response was separated by more than 2SEM from the normal EMG, making it statistically significant. The perturbation that occurred earlier in the stance phase resulted in more distinct activation changes. This could indicate that during the late stance phase, the reflex mechanism is different from during the early stance phase, suggesting that there is a complex interaction between the mechanical and neural mechanisms that

control movement during walking. From preliminary research, the muscle activation in the non-perturbed leg did not show a significant change in muscle activation.

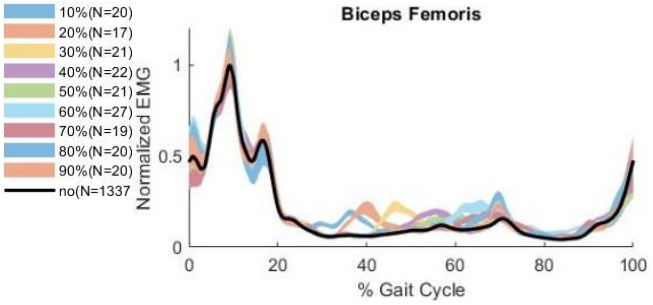

Figure 1: EMG of the Biceps Femoris during normal walking (black) compared to average EMG during perturbations at various times in the stance phase (colored, mean ± SEM).

CONCLUSION

We conclude that the protocol and data processing methods are suitable for the quantification of reflexes and reflex modulation during gait. The protocol requires 30 minutes of walking to obtain statistically valid averages, which may be a limitation for clinical applications. Future work will replicate the experiments in more participants and use the data to develop mathematical models for the reflexes that help control gait.

REFERENCES

[1] Geyer H, IEEE Trans Neural Syst Rehabil Eng, 2010, 18:263-273.

[2] Zehr EP, Prog Neurobiol 58:185-205.

ACKNOWLEDGEMENTS

The work was supported by a Faculty Research Development grant from Cleveland State University.

CONTEXTUALIZING WALKING SPEED IN THE REAL WORLD

[1]Loubna Baroudi, [1]Mark Newman, [1]Xinghui Yan, [1]Kira Barton, [1]K. Alex Shorter, and [1]Stephen Cain
[1]University of Michigan, Ann Arbor, MI, USA
Email: lbaroudi@umich.edu

INTRODUCTION

Walking is our principal mode of locomotion and is central for many clinical assessments. Walking speed is of particular interest for clinicians as a health and welfare indicator. For example, every increase of 0.1m/s in preferred walking speed at age 65 corresponds to an additional 2.5 years of life expectancy [1]. However, measurements in a clinical setting (e.g., space, timing tools, Hawthorne effect, testing protocols) may not accurately capture how humans walk. To address this issue, researchers are turning towards data collection in the real world for gait assessment. With the advancements in wearable sensing technologies, walking can be observed outside the lab during extended periods of time. However, real-world data collection brings its own set of challenges. Walking behavior in an unconstrained environment is highly variable and can be influenced by different external factors. Technologies like GPS or self-reporting can be used to gain insight into context during a walk, but can be burdensome during multi-week data collection. In this work, we present a framework to contextualize real-world walking data, collected using a single-point accelerometer, by clustering data into walking periods to capture the stop-and-go nature of real-world walks. Data from these clusters show that estimates of walking speed vary between clusters of walking periods.

METHODS

We collected 14 days of uninterrupted data using a thigh-worn accelerometer (activPAL) from 15 healthy subjects, including 5 recreational runners who also provided running logs. We used the built-in classification algorithm from the sensor to identify sitting, standing, and stepping (e.g., walking, running) events. From this initial classification, we defined what we termed stepping periods, beginning when a stepping event was detected and ending after a period of extended standing (>1min) or a sitting event was detected. This characterization was meant to regroup stepping events that were likely to belong to the same activity, such as walk through the city with stops at pedestrian crossings. Stepping periods were then divided into windows of 5 strides. A decision tree was used to classify these 5-stride windows into walking, running, or other. Other was defined as data with a high uncertainty regarding its nature. From this classification, we used the running logs to determine a threshold λ, such that stepping periods with λ% of windows labelled as walk were kept as walking periods. With this method, we were able to remove 99% of the data labelled as run data.
Walking periods were characterized by duration and continuity. Continuity was defined as a percentage:

$$Period\ Continuity = \frac{Period\ Duration - Standing\ time}{Period\ Duration}$$

Low period continuity corresponded to frequent pauses within a walk. Walking was contextualized by grouping walking periods into distinct modes based on their continuity and duration. Five modes were defined, using 10 minutes as a cut-off for period duration, and 60% and 80% for period continuity. Walking periods with 100% walking percentage were grouped in a mode as well. Finally, we calculated estimates of stride speed for each 5-stride window within the extracted walking periods using a subject-specific model [2]. A multi-level model was used to analyze the influence of period continuity and period duration on estimates of stride speed. Stride speed was normalized using leg length.

RESULTS AND DISCUSSION

An average of 290 walking periods per person (min: 153 and max: 579) were extracted from 210 days of data. The distribution of walking periods (Figure 1-a) shows a concentration of walks under 10 minutes, with an average period duration of 3.59 minutes across all walking periods. This result corroborates previous findings showing that most walks in the real world are short [3]. We also observe an ensemble of walks that have no pauses, with a period continuity of a 100%. 99% of these continuous walks are under 5 minutes. Additionally, the longer walking periods were more continuous. In fact, no walking periods longer than 30 minutes have a period duration under 50%. This observation suggests that long walks are more intentional with fewer pauses, but are also less frequent. Additional information on bout continuity provided insight into how environmental variation may impact walking behavior.

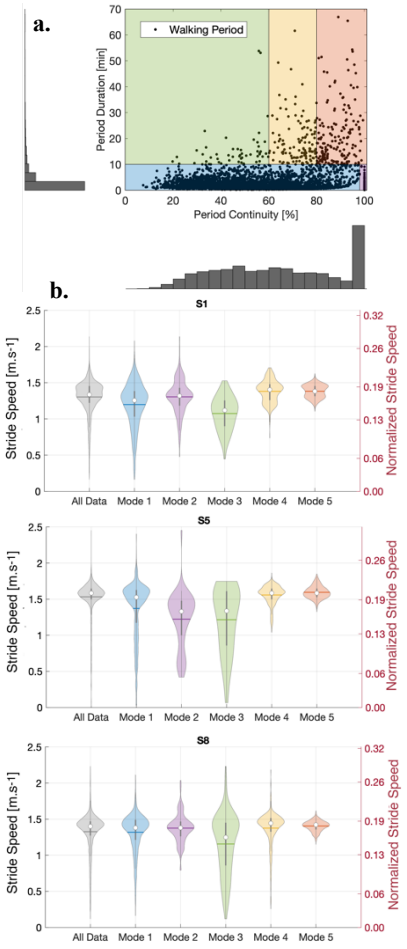

Figure 1: **a.** Map of the different walking modes. Each point represents a walking period, containing several strides. **b.** Distribution of stride speed over the different walking modes for 3 different subjects. Each shaded area represents the shape of the distribution for a mode.

When examining speed, we found a significant effect of period duration, period continuity, and the interaction between these two variables on values of stride speed. Average stride speed for all participants across all data was $1.34 m.s^{-1}$. The lowest average stride speeds and highest standard deviations were found in Mode 3 for all participants, with $1.05 \pm 0.40 m.s^{-1}$ for females and $1.14 \pm 0.41 m.s^{-1}$ for males. These values are out of the range of typical stride speed (e.g., $1.2 m.s^{-1}$ to $1.6 m.s^{-1}$) observed both in [4] and outside the lab [5]. The highest stride speeds and lowest standard deviations were found in mode 5, with $1.34 \pm 0.19 m.s^{-1}$ for females and $1.52 \pm 0.21 m.s^{-1}$ for males. Overall, we observed changes in stride speed across the modes for all participants, as well as a decrease in standard deviation for longer, more continuous bouts (Figure 1-b.). This contextualization offers a different perspective on how walking data can be grouped to gain insight into the biomechanics of an individual in the real world.

CONCLUSION

Datasets collected in the real world contain a wealth of information, but also present critical challenges. The varying nature of the environment in which humans walk in the real world requires careful characterization and data processing. Here, we created a framework to contextualize walking data in the real world by parametrizing the duration and continuity of walks, along with estimates of stride speed. Results indicate that walking speed, a critical gait parameter, varies with bout duration and continuity. This work demonstrates the importance of environmental context for the analysis of walking outside the lab and will enhance gait analysis for clinical purposes.

REFERENCES

1. Studenski, S, et al. *JAMA.* 50-58, 2011.
2. Baroudi, L, et al. *Frontiers in Sports & Active Living 2,* 2020.
3. Orendurff, M, et al. *J of Rehab R & D.* 45.7, 2008.
4. Schimpl, M, et al. *PloS one* 6.8, 2011.
5. Bohannon, R, et al. *Physiotherapie* 97.3, 182-189, 2011.

ACKNOWLEDGEMENTS

This research was funded by the Precision Health Investigators Award of the University of Michigan.

RUN TYPE INFLUENCES RUNNING AND PHYSIOLOGIC PARAMETERS FOR HIGH SCHOOL CROSS-COUNTRY RUNNERS

[1]Micah C. Garcia and [1]David M. Bazett-Jones

[1]University of Toledo, Toledo, OH, USA

Email: micah.garcia@rockets.utoledo.edu

INTRODUCTION

Running training programs are designed to manipulate running duration, frequency, and intensity. To improve performance, runners often incorporate high intensity running sessions (e.g., tempo runs, track workouts). However, running at high intensities, without adequate recovery time, places runners at a greater risk of sustaining a running-related injury (RRI) [1]. Therefore, training programs often mix in low intensity running sessions (e.g., recovery, easy runs) to allow more time for musculoskeletal structures to recover.

Running speed is typically manipulated to dictate the intensity of the running session. In the lab, running at faster speeds elicits an increase in cadence and stride length [2]. While these lab-based studies have simulated different run types (e.g., easy, typical, hard), the running conditions are often short in duration and may not fully represent these different types of running sessions. Therefore, the purpose of this study was to compare running and physiologic parameters for different types of running sessions in the wild for high school cross-country runners during a competitive interscholastic season.

METHODS

During the fall 2020 high school cross-country season, 28 runners were enrolled in our study. Participants were issued a GPS watch (Garmin Forerunner 45s) and recorded each running session with the watch. Participants were also asked to self-report the type of run (recovery/easy, tempo/speed/fartlek, set distance, hills, set time, track workout, race) and session rating of perceived exertion (sRPE) [3] following each running session using an electronic journal (Qualtrics).

For each running session recorded during the season, speed, distance, cadence, stride length, and average heart rate (HR) were extracted from the watch and matched with the self-reported run type and sRPE. Run types were then collapsed into three groups: 1) *easy* (recovery/easy), 2) *typical* (set distance, set time), or 3) *hard* (tempo/speed/fartlek, track workout). Repeated measures ANOVA compared the variables of interest among the different types of runs. Post-hoc pairwise comparisons with Bonferroni corrections were performed when significant differences were found ($p \leq .05$).

RESULTS AND DISCUSSION

Fifteen runners (F=7, M=8; age=15.7±1.2 years) completed at least one run for each type of run and were included in analysis. Significant differences among run types were found for speed ($p=.01$), distance ($p<.001$), stride length ($p=.03$), HR ($p=.01$), and sRPE ($p<.001$) while no significant difference was found for cadence ($p=.10$) [Table 1].

Pairwise comparisons showed that speed was significantly slower for *easy* runs compared to *typical* runs ($p=.03$) and *hard* runs ($p=.01$); distance was significantly longer for *typical* runs compared to *easy* runs ($p<.001$) and *hard* runs ($p<.01$) as well as *easy* runs compared to *hard* runs ($p<.001$); stride length was significantly shorter for *easy* runs compared to *hard* runs ($p=.03$); HR was significantly lower for *easy* runs compared to *typical* runs ($p<.01$) and *hard* runs ($p=.05$); and sRPE was significantly lower for *easy* runs compared to *typical* runs

(p<.001) and *hard* runs (p<.001) as well as *typical* runs compared to *hard* runs (p<.001).

Our findings indicate that running and physiologic parameters are different among different types of running sessions. *Easy* runs appear to be the least demanding type of run as running speed, distance, HR, and sRPE were lower than *typical* runs. On the other hand, fewer differences were found between *hard* runs and *typical* runs. While sRPE was higher for *hard* runs, HR was found to be similar. It is unknown if sRPE or HR provide a more appropriate quantification of running intensity.

Most surprisingly, stride length and cadence were similar among run types. It appears that runners relied more on manipulating stride length as there was a non-significant tendency for longer stride lengths at the higher intensities (faster running speed) while cadence remained mostly unchanged. Longer stride lenghts are associated with higher impact forces [4] and a greater risk of sustaining a RRI [5]. Conversely, increasing cadence reduces impact forces [4] and runners with a higher cadence are at a lower risk of sustaining a RRI [6]. Running at faster speeds has been associated with RRIs [4] and our results suggest runners may be placing themselves at a higher risk of sustaining a RRI by increasing stride length and maintaining cadence when running at faster speeds. Perhaps more focus should be aimed towards increasing cadence when running at faster speeds to reduce the risk of sustaining a RRI but further research is needed to investigate this claim.

CONCLUSION

Differences in running and physiologic parameters were found among different types of running sessions. While *easy* runs were found to be less demanding than *typical* runs, there were fewer differences between *hard* runs and *typical* runs. Adolescent long-distance runners also appear to rely more on increasing stride length than cadence for *hard* running sessions which may place them at a higher risk of sustaining a RRI.

REFERENCES

1. Bertelsen, M, et al. *Scand J Med Sci Sports*. 2017.
2. Fukuchi, R, et al. *PeerJ*. 2018.
3. Borg, G. *Borg's perceived exertion and pain scale*. 1998.
4. Heiderscheit, B, et al. *Med Sci Sports Exerc*. 2012.
5. Ferber, R, et al. *Med Sci Sports Exerc.* 2002.
6. Kliethermes, S, et al. *Br J Sports Med.* 2021.
7. Nielsen, R, et al. *IJSPT*. 2012.

Table 1. Comparison of running parameters among different types of runs.

Variable	Easy Runs	Typical Runs	Hard Runs	*p*-value
Speed (m/s)	3.28 ± 0.27	3.39 ± 0.33	3.50 ± 0.31	.01 [a b]
Distance (km)	7.5 ± 1.3	11.4 ± 3.8	5.2 ± 1.9	<.001 [a b c]
Cadence (steps/min)	167 ± 7	169 ± 7	167 ± 7	.10
Stride Length (m)	1.17 ± 0.11	1.19 ± 0.13	1.23 ± 0.13	.03 [b]
HR (bpm)	158 ± 11	165 ± 13	165 ± 11	.01 [a b]
sRPE	2.8 ± 1.3	4.3 ± 1.4	6.3 ± 1.5	<.001 [a b c]

Significant differences ($p \leq .05$): [a] *easy* compared to *typical*, [b] *easy* compared to *hard*, [c] *typical* compared to *hard*

INCORPORATING ADDITIVE MANUFACTURING IN HAND SPLINTING AND DESIGNING A NEW PALM CONE

[1,2]Mikayla Bulson, [1]Ann Reinthal, [1]Debbie Espy, [3]Prabaha Sikder

[1]Cleveland State University, School of Health Sciences, Cleveland, OH, USA

[2]Rochester Institute of Technology, Manufacturing and Mechanical Engineering Technology, Rochester, NY, USA

[3]Cleveland State University, Mechanical Engineering Department, Cleveland, OH, USA

Email: mrb1048@rit.edu

INTRODUCTION

Spasticity is a neurological condition in which muscles develop abnormal increased stiffness. Many individuals post-stroke develop spasticity and do not have the required motor control to open the hemiplegic hand. Therapeutic hand cones are used to slow and at times reverse the development of finger stiffness and contracture by opening the hand. The current materials used for hand cone splints include thermoplastics, thermosets, fabrifoam, and cloth which typically do not permit air flow through the palm allowing perspiration and creating a breeding ground for bacteria. Our goal was to design a therapeutic hand cone/splint using additive manufacturing and 3D printing that provides air flow through the palm and is sturdy enough to withstand the force applied, while at the same time having some flexibility so as to not injure the spastic hand.

METHODS

This project was a user-initiated effort carried out by a team of the user, occupational and physical therapists, a material scientist, and mechanical engineers. A three-dimensional Computer Aided Design (CAD) modeling software, Solidworks, was used to develop a design that has holes to encourage air flow through the hand as well as an opening at the top for easy cleaning. A functional prototype was manufactured using the INTAMSYS Funmat HT Fused Deposition Modeling (FDM) 3D printer. Three different materials -- Acrylonitrile Butadiene Styrene (ABS), Polycaprolactone (PCL) and Polylactic Acid (PLA) -- were analyzed on grounds of their mechanical properties to determine their suitability for the present application. As a preliminary step we used ABS to print a prototype.

RESULTS AND DISCUSSION

In researching the three different materials we discovered ABS is strong, durable, cost effective, and great for prototyping. However, it is rigid and will injure the skin if too much force is applied. PLA is also cost effective, has slightly more elasticity than ABS, and is a biodegradable material. Its main downfall is the lack of strength and durability compared to ABS. There are different grades of PCL that have different mechanical properties. Overall, it is a softer material and has a lower glass transition temperature which could allow for revisions by placing the device in boiling water and remolding, like typical thermoplastic splinting. The disadvantages of PCL are that it is not dishwasher safe and is more expensive than ABS and PLA. Different materials with different mechanical properties can be used depending on the patient's needs. For example, if the hand is more spastic, a more rigid material such as ABS can be used to withstand the extra force.

Additive manufacturing has the potential to improve splinting because of its ability to be customized to an individual's needs as well as the opportunity to mass produce identical and serial splints. A CAD file can be adjusted to the size of a patient's hand or increased in diameter to print "the next size up" as the hand is opening more over time. This design is also more hygienic than most splints on the market because the holes on the sides of the design permit air flow through the palm decreasing perspiration, and the plastic device is easy to clean with the open top design.

A model of a new palm cone was successfully created and manufactured (Figure 1) using ABS as a preliminary material. The model was created using Solidworks 2020 [a] and then converted to a Standard Triangle Language (STL) file which was placed into the INTAMSUITE slicing software [b]. This software takes the STL file and creates a code read by the INTAMSYS Funmat HT printer [c] to 3D print the prototype [d].

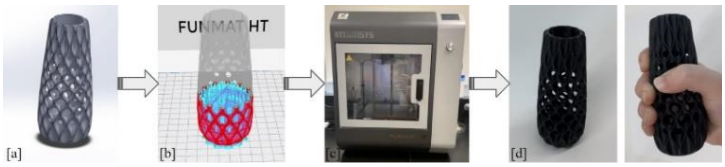

Figure 1: This figure shows the process of manufacturing the prototype of the palm cone.

CONCLUSION

This project describes a durable, hygienic, aesthetically pleasing, and safe palm cone that allows air flow through the hand of someone who has a lot of spasticity. A prototype was successfully manufactured and different materials were explored allowing modifications to fit the needs of individual patients. We believe PCL will be the best material for this application, however, testing still needs to be done to confirm this hypothesis.

ACKNOWLEDGEMENTS

We would like to thank the NSF RE@CSU Program (Award 1950558) for funding and resources, and Wayne and Roberta Cook for the concept design idea, as well as Gina Kubec and Bharath Tej Challa for their contributions to the development of this system.

ERROR IN JOINT ANGLE MEASUREMENT THROUGH SIMULATED MOTION CAPTURE

[1]Ells Mine Saint Paul, [2]Eric Schearer

[1]Regis College, Weston, MA, USA

[2]Cleveland State University, Cleveland, OH, USA

Email: esai543@regiscollege.edu

Introduction

When a cervical spinal cord injury occurs, it results in tetraplegia, causing a loss in motor and sensory function. Being the most severe type of spinal cord injury, patients see limited or absence of movement below the shoulders and the neck [1] [2]. Motion capture is used to record motion of objects, animals, or people. In motion capture, rigid bodies with sensors are placed on the participants' body, then bony landmarks are digitized as markers. The inverse kinematic solver is then used to compute the joint angles of the shoulder and elbow based on the positions of the markers. The lack of movement and control in a patient's trunk makes motion capture difficult because of the hardship when it comes to accessing these landmarks. The inaccurate placement of markers leads to inaccuracies in the inverse kinematics solution. In this project we analyzed the error associated with placing markers for motion capture and how it correlates to incorrect joint angles in a 2D kinematic model of shoulder and elbow.

Materials and Methods

The goal of this project is to understand the correlation between marker placement and joint angle error by creating a 2D kinematic model of the arm on MATLAB. The forward kinematic solver simulated the position of the markers (fig. 1). Noise was added to the marker positions' data and then an inverse kinematics solver written in MATLAB computed the shoulder and elbow joint angles. The simulation was repeated multiple times in different configurations to gather a versatile understanding of the effects marker position errors have on joint angles.

Markers position on simulated arm

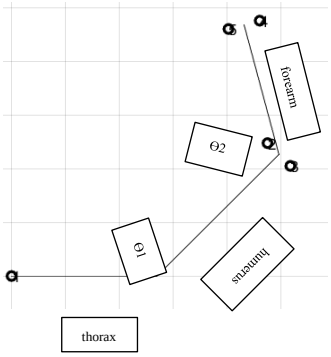

Figure 1: Forward kinematic model of arm with marker positions.

Results and Discussion

Based on the data obtained, there is a linear correlation between the marker position and measured joint angles for both joints. Marker noise had a broader effect on the shoulder than the elbow angle, which was more accurate. While the standard deviation (STD) of the marker noise increased, the STD of joint angles increased (fig. 2). The STD of the marker noise was incremented up to 100 mm and the error associated with the joint angles was recorded. With 100mm of marker noise the STD of shoulder joint angle was approximately 13 degrees and 33 degrees for the elbow.

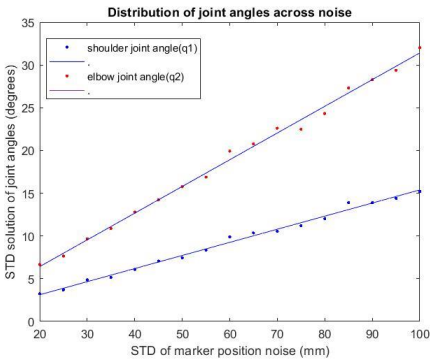

Figure 2: STD of shoulder (q1) and elbow (q2) joint angle in relation to STD of noise.

Conclusions

The project focused on how bad one can get at placing makers for motion and how that correlate to error observed in joint angles. It focused mainly on people with cervical spinal cord injuries. It was shown that the error in markers positions have a direct relationship with joint angle. Errors in joint angles are directly associated with error in marker position which makes it difficult to do motion capture on people that are paralyzed. This project can be furthered in the future by building a 3D solver for execution of inverse kinematics of joint angles. Coming up with better methods to find joint angles through an experiment with people with cervical spinal cord injuries will provide applicable data, which can later be used in the field of rehabilitation engineering to build assistive devices.

References:

[1] Kirshblum, Steven C et al. "International standards for neurological classification of spinal cord injury (revised 2011)." *The journal of spinal cord medicine* vol. 34,6 (2011): 535-46. doi:10.1179/204577211X13207446293695

[2] "Cervical Spinal Cord Injury: Symptoms and Prognosis." *What Is a Cervical Spinal Cord Injury? | Shepherd Center*, Shepherd Center, www.shepherd.org/patient-programs/spinal-cord-injury/levels-and-types/Cervical-Spinal-Cord-Injury.

Acknowledgements:

This work is supported by NSF Award 1950558.

INCREASED LOAD TRANSFER HETEROGENEITY IN CHIARI MALFORMATION SUGGESTS LESS INTERLIMB COORDINATION

[1]Maria T. Gamez, [2]Brian L. Davis, and [3]Brittany N. Sommers

[1]Cleveland State University, Cleveland, OH, USA

[2]Cleveland State University, Cleveland, OH, USA

[3]Cleveland State University, Cleveland, OH, USA

Email: mgamez3@uic.edu

INTRODUCTION

Chiari Malformation (CM) describes a congenital condition in which the cerebellar tonsils descend past the foramen magnum into the cervical canal. This may inhibit the flow of cerebral spinal fluid (CSF) [1]. Symptoms include headaches, neck pain, greater postural instability [2], and unsteady gait [1]. Decompression surgery may be performed to treat headaches, but there is no evidence of it assisting with other symptoms [2]. While CM affects approximately 1:1000 people with a potential of higher prevalence due to lack of diagnostic imaging [2], there is a significant lack of gait analysis studies done on this population. Therefore, the aim of this study is to quantify load transfer from one limb to the other to assess interlimb coordination. We hypothesized there would be increased variability in CM patients compared with age-matched controls subjects.

MATERIALS AND METHODS

GRF data for healthy controls (n=6, Group 1) and CM participants (n=6, Group 2) during normal treadmill walking were obtained. Average treadmill speeds for all groups were 1.2 m/s. Control data were recorded at 100 Hz and CM data, originally recorded at 1000 Hz, were down sampled to 100 Hz to match the control data. All groups were then filtered with a second order Butterworth filter with a cutoff frequency of 6 Hz. Fifteen consecutive strides during normal walking were plotted versus time. The points of interest were the points from heel strike to maximal weight acceptance, which made up the loading forces, and the points from peak push off to toe off, which made up the unloading forces. Once these timepoints were identified, loading versus unloading was plotted for each control and test subject. Variability was measured by examining the range of loading curves corresponding to the median of the unloading force in Figure 1. Coordination was quantified by determining coefficient of variation for each subject. Heterogeneity within each group was determined by using Levene's test for assessing variance in the coordination measurements. All functions were written using MATLAB version 2020a and statistical analysis for equal variances was completed using Minitab.

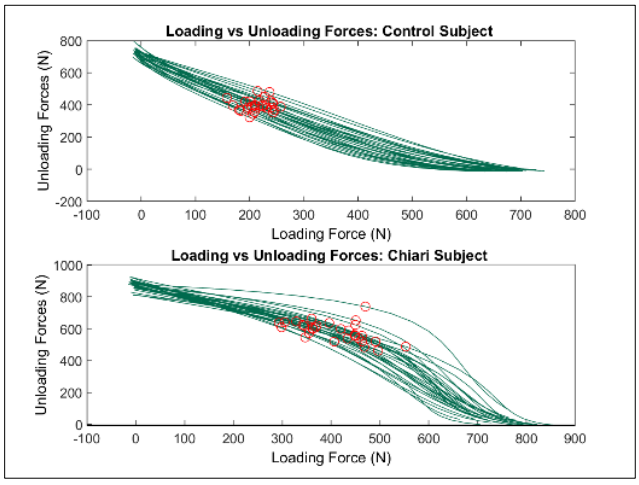

Figure 1: (Top) Loading vs. Unloading of a control subject with points of interest highlighted. (Bottom) Loading vs. unloading of CM subject with points of interest highlighted.

RESULTS AND DISCUSSION

The test for equal variances in coordination measurements showed that the variances between control and CM were significantly different, as shown in Figure 2 ($p = 0.025$ for multiple comparisons and $p = 0.050$ for Levene). This indicates that there is significantly greater heterogeneity in the CM population compared with controls.

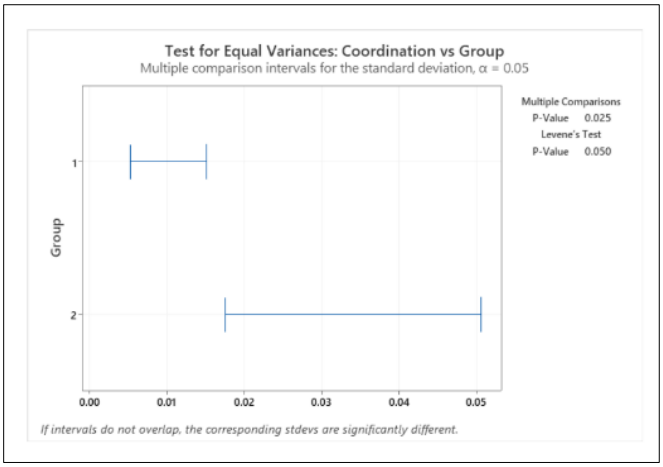

Figure 2: Results from test for equal variances between group 1 (control) and group 2 (CM).

CONCLUSION

The greater variability in how patients with CM shift weight from one step to the next may be due to decreased interlimb coordination. Future studies may be conducted to better quantify coordination heterogeneity not just at the midpoint of the gait cycle, but rather take a more cumulative approach across the entire gait cycle.

REFERENCES

1. “Chiari Malformation Fact Sheet.” NINDS. 2021.

2. Sommers, B., et al. *Gait & Posture*. 280-285, 2021.

ACKNOWLEDGEMENTS

The authors acknowledge funding from the NSF REU program grant 1950558 awarded to Cleveland State University as well as thank the students and faculty of the CHMS lab for all their guidance and mentorship.

EMG-IMU INTRUMENTATION AND SENSOR FUSION

Dawud H. Sharrieff (Presenter), Dana L. Lorenz, and Antonie J. van den Bogert

Department of Mechanical Engineering, Cleveland State University, Cleveland, OH, USA

Email: d.sharrieff@vikes.csuohio.edu

INTRODUCTION

During exercise it can be useful to monitor/measure your movement and/or muscle activity for a variety of applications. Up until recently, methods for this were only fit for a lab setting, with the equipment being expensive and not portable. Small, wearable sensors are now available for commercial use. Inertial Measurement Unit (IMU) technology is inexpensive and is gaining popularity for measurement of human motion. Dorschky et al. developed methods to process data from multiple IMU sensors using trajectory optimization [1].Trajectory optimization can make use of a mathematical model of the musculoskeletal system and provide an optimal fusion of all sensor signals that is consistent with knowledge of the dynamics of the system. The addition of electromyography (EMG) sensing to this approach has the potential to make results less sensitive to modeling assumptions. A technical demonstration of this fusion method was developed by Wisniewski, for biceps curl exercise, but only with simulated data [2]. The goal of this research was to develop inexpensive instrumentation and perform experiments to test Wisniewski's methods on real data, aiming to explore muscle force output and corresponding positional variables from forearm flexion exercise, utilizing both EMG and IMU sensors.

MATERIALS AND METHODS

To complete these trials, one MyoWare sensor (EMG) and one IMU (MPU 6050) were used to collect data from one subject, through an Arduino UNO R3 unit. All sensors were programmed to collect 100 measurements per second, displayed with one timestamp to microsecond accuracy, one raw EMG data point, and six raw IMU signals. The IMU signals consisted of 3 gyroscope readings (X,Y, and Z angular velocities) in degrees/s and 3 accelerometer readings (X,Y, and Z) in m/s^2. The IMU was placed on the distal anterior forearm with X proximal, Y dorsal, and Z lateral, accompanied by the EMG sensor on the long head of biceps brachii using adhesive pads. The MyoWare sensor was grounded at the elbow joint. Signals were recorded from one able-bodied participant performing cyclic biceps curls from full extension up to about a 90 deg angle, at fixed cadences controlled by a metronome signal (30 BPM), while holding a 5 lb.s weight, over a 30 sec period (performing 13 reps).

RESULTS AND DISCUSSION

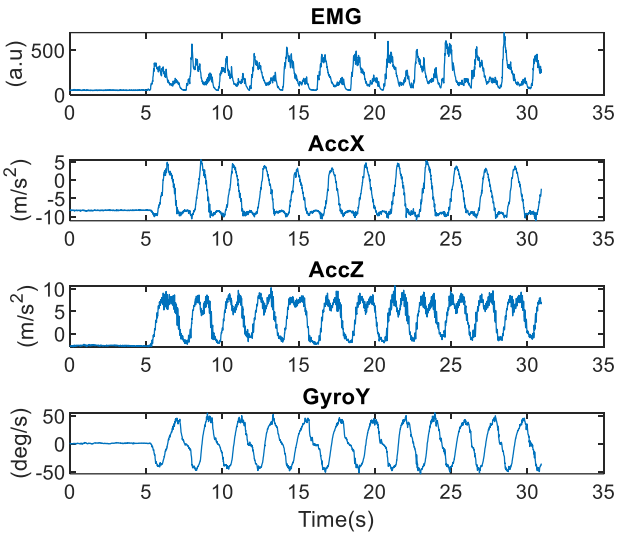

Figure 1: Time vs Significant Signals

Figure 1 above shows that the sensors successfully collected data during trials, reacting to movement. The important movement of the exercise only occurs in one plane. The only accelerometer signals

that are significant are the vertical and horizontal signals (not the sideways acceleration). The gyro Y signal is also significant, being the angular velocity in the plane, which is the rotation about the sideways axis.

Future work will be performed in multiple participants with similar procedures taken: doing repeated bicep curls, at fixed cadences controlled by a metronome signal, and different weights held in their hand. Results will be validated using conventional optical motion capture.

CONCLUSIONS

It was concluded that the EMG-IMU instrumentation system is suitable for analysis of human exercise using sensor fusion approaches.

REFERENCES

1. Dorschky, E, et al. *J Biomech* 95: 109278. (2019)

2. Wisniewski, J, et al. *Musculoskeletal State Estimation with Trajectory Optimization and Convolutional Neural Networks*. MS Thesis, Cleveland State University. (2020)

ACKNOWLEDGEMENTS

This work is supported by NSF Award 1950558.

BIOPRINTING OF A DESIGN-SPECIFIC IMPLANT FOR TREATING VOLUMETRIC MUSCLE LOSS (VML)

[1,2]Brendan Otani, [3]L. Juliana Azuero, and [1]Prabaha Sikder

[1]Mechanical Engineering Dept., Cleveland State University, Cleveland, OH, USA

[2]Mechanical Engineering and Materials Science Dept., Washington University in St. Louis, St. Louis, MO, USA

[3]Chemical and Bioengineering Dept., Cleveland State University, OH, USA

Email: bkotani@wustl.edu

INTRODUCTION

Volumetric muscle loss (VML) is the most devastating musculoskeletal injury in which a substantial amount of skeletal muscle (usually > 20%) is abruptly lost due to trauma. A recent study reported that every year approx. 250,000 U.S. civilians suffer from open fractures that commonly involve a component of VML, and 8% of evacuated military service personnel (about 14,500 annually) receive a disability rating specifically for VML injuries [1]. The aftermaths of VML are tremendous which results in functional deficits, poor muscle strength and can also lead to life-long dysfunction or disability. Notably, the defect impairs the endogenous repair (tissue regeneration) mechanisms thus mandating the need for highly effective therapies. Unfortunately, the existing treatments for VML are restricted to functional free muscle transfer and advanced bracing designs, which are highly limited in their efficacy [2]. For instance, in autologous tissue transfer, donor site morbidity is prevalent thus leaving impaired integration of the implanted muscle with the neighboring tissues. In cases where synthetic acellular scaffolds were used, pathologic fibrotic response impeded muscle healing and resulted in dysfunctional muscle formation. On the contrary, in this project, we synthesized an innovative biomaterial formulation and utilizing the powerful bioprinting technology, we developed a design-specific implant that exhibits favorable resolution and structural fidelity. Further, the implants also exhibited favorable biodegradability and biocompatibility attributes.

METHODS

The implant was designed in SolidWorks modeling software. The design is bioinspired and mimics the motif of innate skeletal muscle. Specifically, tubular structures are fabricated within the implant to hold cells in an alignment akin to that of skeletal muscle fibers (myofibers). The BIO X (CELLINK, Boston, MA, USA) printer was used to manufacture the constructs. A fine nozzle diameter of 0.2 mm was used to create precise shapes and formations that accurately represented the 3D model designs. The bioink hydrogel composition is comprised of GelMA, alginate, Poly-(L)-Lactic Acid (PLLA), and specific cytokines. A detailed analysis was performed to optimize the bioprinting parameters to get the best resolution and accuracy of the printed implants.

RESULTS AND DISCUSSION

Figure 1 shows the various design-specific structures printed with the hydrogel such as linear **(a)**, honeycomb **(b)**, and gyroid **(c)** infill patterns. **Figure 1d** shows the implant which we designed for VML treatment. Qualitative evaluations show that

the print resolution was favorable and accurate with promising structural properties (i.e. gel-like texture, high structural fidelity, and stability). The extrusion path is extremely consistent, stable, and accurately depicts the designed models. Air bubbles in the hydrogel cartridge are a known source of error and can cause missing pieces of the extrusion path, as denoted by the arrows in **Figure 1b** and **Figure 1c**, which are both missing a piece of the perimeter path. Parameters such as the printhead pressure, print speed, nozzle diameter/gauge, layer height, and first layer height percentage were optimized in the bioprinter to achieve the high-definition prints shown in **Figure 1d**.

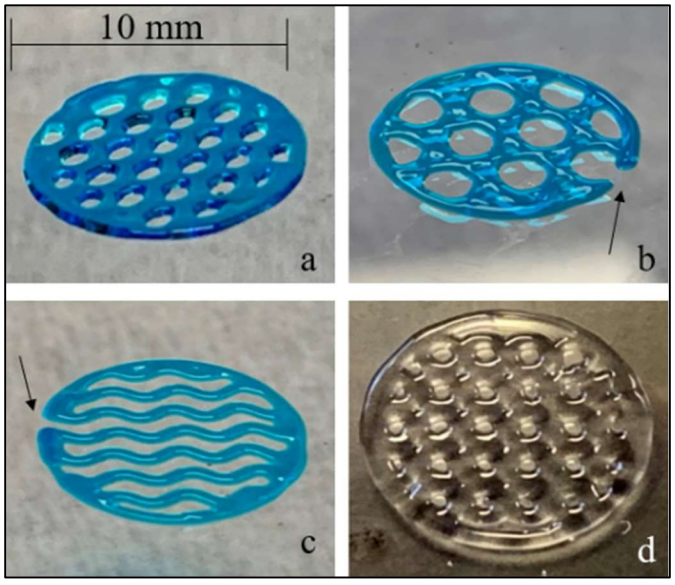

Figure 1: (a) Linear, (b) honeycomb, (c) gyroid infill patterns. (d) Custom scaffold design. This structure is 14 mm in diameter and has pores that each have a diameter of 1.5 mm. Note: Blue dye was used for better identification.

CONCLUSION

We were successful in optimizing the bioprinting parameters to obtain a good resolution of the printed structures with our novel composition. The BIO X printer was capable of successfully printing high-definition and stable bioprints with visible pores and a smooth extruder path through specific printing parameters. The printer will continue to be useful and successful at printing novel curated biomaterials in customizable scaffolds for skeletal muscle tissue implantation, which will ultimately assist with tissue restoration and regeneration. The future of this project includes varying the overall size of the implant, using other types of biomaterials and synthetic polymers for bioink hydrogel curation, and different shapes for various skeletal muscle applications throughout the human body.

REFERENCES

1. Medical Technology Enterprise Consortium. *Volumetric Muscle Loss (VML) Repair Following Extremity Trauma.* 2021.

2. Lin, C, et al. *Plastic and Reconstructive Surgery – Journal of the ASPS.* 2118-2126, 2007.

ACKNOWLEDGEMENTS

We would like to thank the National Science Foundation Rehabilitation Engineering REU Program at Cleveland State University (CSU). This work is supported by NSF Award 1950558.

DEVELOPING A BIOMECHANICAL ANALYSIS FOR SOFTBALL PITCHING

[1,2]Raven Foust, [2]Amory Starkey, [2]Bryan Opaskar, [2]Debbie Espy, and [2]Ann Reinthal

[1]North Carolina Agricultural and Technical State University, Greensboro, NC, USA

[2]Cleveland State University, Cleveland, OH, USA

Email: RNFOUST@AGGIES.NCAT.EDU

INTRODUCTION

Windmill pitching in softball is a dynamic movement in which the pitcher rapidly moves their arm in a circular motion and produce an underhand pitch. Windmill pitching in fast-pitch softball creates a great amount of strain for pitchers along their kinetic chain. A common misconception is that softball pitching is less strenuous than baseball pitching. Literature suggests that the windmill pitch generates similar forces about the shoulder such as those for baseball pitching. However, unlike baseball pitching, softball pitching does not have a mound to assist in body propulsion and force generation. This leaves softball pitchers to generate the forces needed for fast-pitch from a lower extremity push off the flat fast-pitch mound.

During the pitch, there are four phases (Fig. 1) in the motion's entirety: the windup, the stride, the delivery, and the follow through. Each phase can be further broken down into arm swing position; referenced as points on a clock. From the beginning phase to the ending phase, the lower extremity drives the sequential activation of proximal-to-distal segmental motions of the trunk, shoulder, elbow, and wrist, respectively. Previous studies on softball pitching are focused on the shoulder and upper extremity and how those movements affect ball velocity and risk of injury. There is a need to further assess the sequence of lower extremity to upper extremity motion throughout the entire pitching cycle.

The objective of this project was to develop a biomechanical analysis of critical variables throughout a windmill pitch using motion capture software.

METHODS

The project consisted of collaboration with a softball pitcher from Cleveland State University's (CSU) Women's Softball team and a physical therapy expert in softball mechanics. The data was collected via an 8-camera motion capture system and processed via CORTEX software (Motion Analysis Corp.). About 30 feet away, a ball net was set up to catch each thrown softball. A radar gun was operated by a physical therapist student that squatted behind the pitcher to capture the velocity of each pitch.

To accommodate for the rear-foot drag that occurs during a softball pitch, the medial foot marker, lateral foot marker, and toe marker were removed from both feet. The traditional Helen Hayes foot maker (top of the foot at the center) was used instead. Both the right and left anterior superior iliac spine (ASIS) markers were shifted laterally to adjust for the pitcher's tendency to drag her arm against her pelvis.

Windmill Pitching Phases

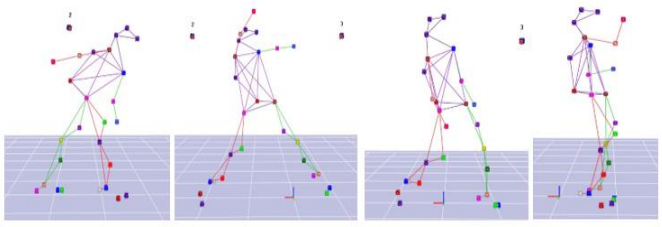

Figure 1: The phases of the windmill pitch. From left to right: The windup, the stride, the deliver, the follow through.

Through discussion with the physical therapy expert, critical variables identified were trunk flexion in the sagittal plane throughout the pitch, step distance during the stride phase, and pelvis orientation throughout the pitch and while the arm is at noon.

DISCUSSION

By using a combination of CORTEX motion capture software and MATLAB programming software, it is possible to create a biomechanical analysis of the identified critical variables.

A code was created to calculate step length at the end of the stride phase. To calculate the length, the code needed to know the precise moment of when the stride was being completed. Using the imported position calculations from CORTEX, it was determined that ideal moment to calculate the step length was when the wrist marker reached it's maximum Z axis position (arm at noon). With additional analysis, utilization of CORTEX's joint angle calculations could determine a more accurate moment for when to calculate the step distance. From brief observation, the minimum shoulder-elbow, elbow-wrist angle provided a more accurate way to determine when the step length should be calculated. For distance in a 3D space, it was ideal to use the midfoot marker. This is due to the potential problem of how the completion of the stride is defined. If a completed step is defined as when the heel is on the ground, that could prove troublesome for analyzing step length across different pitchers and for defining step in the code. Often, one or both heels were in the air. Additional review of the code is needed.

The CORTEX software contains a skeleton builder add-on that can be used to determine trunk flexion in the sagittal plane over time as well as pelvic rotation over time. Skeleton Builder uses 3 points to create segments for each marker. Withing Skeleton Builder, the user can define the orthogonal coordinate system that would rotate and move with the selected markers, representing the trunk movement throughout the pitch and the pelvic rotation.

CONCLUSION

CORTEX software contains the necessary add-ons to analyze identified, critical variables. A deeper understanding of the software is needed to maximize the benefits of using Skeleton Builder.

A standardized definition of step would aid in normalizing the code used to calculate step length at the end of the stride phase of a pitch.

REFERENCES

1. Oliver, Gretchen D., et al. "Pitching Mechanics in Female Youth Fastpitch Softball." *International Journal of Sports Physical Therapy*, vol. 13, no.3, 2018, pp 493-500., doi:10.26603/ijspy20180493.

2. Lear, Aaron, and Niraj Patel. "Softball Pitching and Injury." *Current Sports Medicine Reports*, vol. 15, no. 5, 2016, pp. 336-341., doi:10.1219/jsy.0000000000000293

ACKNOWLEDGEMENTS

Thank you to Dr. Amory Starkey and Bryan Opaskar for allowing me the opportunity to work on their project. Thank you to Sydney Bajusz and Alexa Sieger for volunteering time in obtaining pitching data. Lastly, thank you to Dr. Debbie Espy and Dr. Ann Reinthal for mentoring me throughout this process. This work is supported by NSF Award 1950558.

QUANTIFYING BALANCE THROUGH STEP LENGTH AND SINGLE-LEG STANCE

[1]Zachary Hubbard, [2]Debbie Espy, and [2]Ann Reinthal

[1]West Virginia University, Morgantown, WV, USA

[2]Cleveland State University, Cleveland, OH, USA

Email: zmh0007@mix.wvu.edu

INTRODUCTION

Quantifying and defining criteria for balance proficiency for a specific balance task is an important factor when improving one's balance. Motion-based games are selected to emphasize five distinct balance tasks as a method of improving balance and reducing fall risk in individuals' post-stroke. Prior research in the area of game-based balance training has shown that motion-based balance tasks can improve balance and stability in post-stroke individuals [1]. Variables step length and time in single-leg stance (SLS) were analyzed to identify parameters for balance proficiency in two specific balance tasks.

Research in step length and time in SLS as a method to quantify balance have also been conducted, though primarily for slip-based balance training [2]. This research concluded that decreasing step length while increasing gait speed can improve stability [2].

METHODS

Nine post-stroke participants took part in 5 video game balance tasks using Microsoft Xbox Kinect with several different surfaces. Balance tasks were organized into 5 categories: time in SLS/kicking, anterior/posterior stepping, medial/lateral (ML) stepping, feet in place, and trunk rotations with feet in place. Participants played about five minutes per task during each session for a total of 10 sessions, with the first session introducing the participants to the specific tasks. The second and last sessions used Cortex Motion Capture software (Motion Analysis Corp) with 8-cameras at 120 Hz and the 2016 Helen Hayes 37-marker set to record participants' kinematic and center of mass data. MATLAB code was created for custom analysis and graphing of kinematic data not provided by the Cortex software.

I chose two categories of the five balance task groups to analyze: medial-lateral stepping and time in SLS, both on a flat surface. The medial-lateral stepping task involved the participant using both feet to step side to side quickly in an inconsistent pattern. The time in SLS balance task involved quick kicks with each foot, alternating between the left and right foot. Within the two categories, I analyzed XYZ resultant step length in the ML stepping task and length of time in SLS in the SLS/kicking task. The participants with the highest average step length and SLS time for the tasks were used. Cortex Motion Capture doesn't calculate these variables directly, so MATLAB code was created which monitored the heel and toe markers x, y, and z positions to determine whether a given foot lifted off the surface during the task in order to calculate the two variables.

RESULTS AND DISCUSSION

Figures 1, 2, along with Table 1 summarize data for the ML stepping and time in SLS balance tasks.

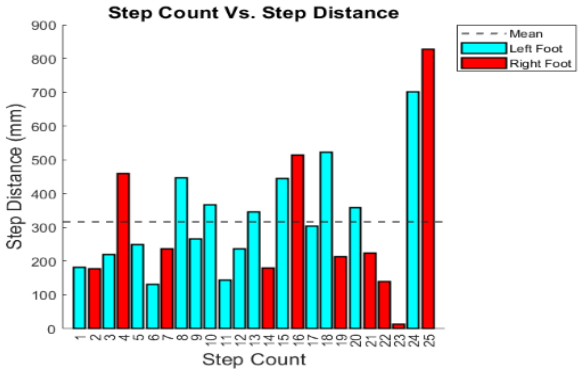

Figure 1: A bar graph plot of resultant step length distance (mm) versus step count, with mean step distance.

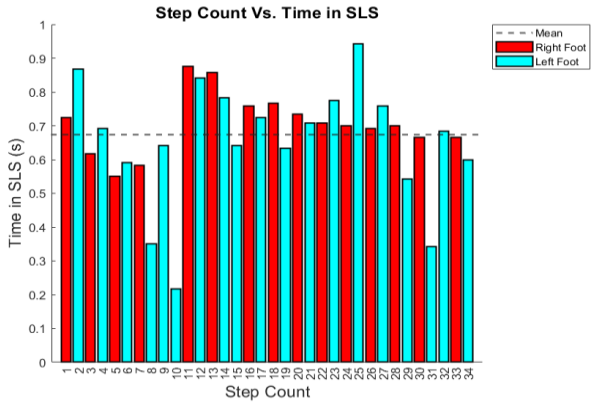

Figure 2: A graph plot of step count versus time in SLS, with mean time in SLS.

Table 1: Mean and median results for the medial-lateral stepping balance task and the SLS/kicking balance task.

Step Length Task			
Foot	**Number of Steps Taken**	**Resultant Step Length (mm)**	
		Median	**Mean**
Left	15	302.977	328.067
Right	10	219.282	298.415
Both	25	249.205	316.206
SLS Kicking Task			
Foot	**Number of Steps Taken**	**Time in SLS (s)**	
		Median	**Mean**
Left	19	0.683	0.649
Right	15	0.7	0.707
Both	34	0.696	0.674

The step length data from this participant (Fig 1.) (Table 1) shows a higher average step length with the left foot than that of the right foot, along with more steps taken. The SLS results (Fig 2.) (Table 1) display a greater number of kicks with the left foot, but a higher mean time in SLS with the right foot in less steps.

Through observing participants in both balance tasks over repeated sessions, balance proficiency criteria for the two activities can be identified. To have proficient balance at the ML stepping task, the participant must be able to take wider steps from side to side. To demonstrate balance proficiency with the SLS/kicking task, the participant must be able to kick their foot out quickly at regular intervals. The ability to perform this multiple times and with both feet consistently would be an example of proficient balance for that task. These two ways to quantify balance vary a great deal due to differences in the many types of balance tasks.

CONCLUSION

After learning the specific balance training protocol, the Cortex data collection software, and the existing MATLAB codebase, I was able to identify what data analysis scripts and functions would need to be created for the specific variables analyzed. Creating these analysis programs allowed us to quantify balance improvement related variables such as the resultant step length and time in SLS.

REFERENCES

1. Aslam. M, et al. Exer-gaming reduces fall risk and improves mobility after stroke. *Journal of the Pakistan Medical Association.* 1673-1675, 2021.

2. Espy, D, et al. Independent Influence of gait speed and step length on stability and fall risk. *Gait Posture.* 378-382, 2010.

ACKNOWLEDGEMENTS

We would like to thank Dr. Espy and Dr. Reinthal, as well as the RE@CSU program, for giving me the opportunity to contribute to this study, Thanks to Jessica Jensen, Errin Abasolo, Lauren Yeary, and Ryan Kulwicki for developing and creating portions of the MATLAB code used for data collection and analysis. This work is supported by NSF Award 1950558.

MANIPULABILITY OF A MULTILINK MOBILE ARM SUPPORT

[1]Sofia Urbina, [2]Eric Schearer
[1]Louisiana Tech University, Ruston, LA, USA
[2]Cleveland State University, Cleveland, OH, USA
Email: siu001@latech.edu

INTRODUCTION

Neuromuscular disorders such as Amyotrophic Lateral Sclerosis (ALS), Muscular Dystrophy, and Myasthenia are characterized by muscle weakness that limits upper extremity mobility, making it difficult for people to hold their arm against gravity to complete everyday tasks such as eating or brushing their hair. To solve this issue, an arm support with elastic bands is used to assist against the force of gravity, maintaining the participant's arm in a stable position at the height of their thorax; however, it simultaneously decreases the motion capability of a typical arm. Consequently, we quantify the effect of the arm support by studying the freedom of motion of the arm by itself and on the support, given any joint configuration. This helps us understand the way in which the support affects arm movement, further allowing improvements to be made to the arm support.

METHODS

The Jaeco Multilink Mobile Arm Support (MAS) is composed of a 20" MultiLink Arm, a rancho mount for a wheelchair, and a forearm support with an attached offset swivel.

Figure 1. This figure shows the arm support as it is being actuated by rubber bands.

To understand how the arm support affects arm movement, we utilize manipulability ellipses which indicate the velocities that the end-effector can instantaneously achieve in each direction at a given joint configuration.

To compute the manipulability ellipse of the closed chain formed by the arm and the support, we take into consideration the dimensions of the arm and support as well as their degrees of freedom. Both have five degrees of freedom, all of which we consider for the arm support. However, we only consider four of the five degrees of freedom for the arm, neglecting supination of the forearm as the support makes that movement impossible. We begin by identifying the actuated joints vector and passive joints vector. A constraint equation is then written to relate the actuated and passive joints. Through forward kinematics the position of the wrist, which is the end-effector of the closed chain, is determined. Taking into consideration that the chains composing the parallel manipulator have equal end-effector rotation matrices allows us to follow standard procedure suggested by F.C. Park and Jin Wook Kim [1] to obtain the dimensions of the manipulability ellipse. In a similar manner we compute the manipulability ellipse of the arm as an open chain after taking into consideration its dimensions and five degrees of freedom to study the full range of motion.

In both cases, the arm's range of motion can be computed at any given feasible position; therefore, we use the methods previously described to compute both manipulability ellipses while the arm is resting in the same position and compare them to determine the effect of the arm support in different

reaching motions.

RESULTS AND DISCUSSION

We obtained two manipulability ellipses that have different orientations as well as different dimensions. They were plotted in 3D space where the numbers on the axes represent the dimensions, measured in mm, which correlate to the directions in which the velocities for each range of motion are generated. This shows the way the support influences the velocities the wrist is allowed to achieve as well as the directions in which the support limits the range of motion of the arm.

The support makes forearm supination imposible which limits upward movements that the arm alone can easily perform. The manipulability ellipse of the arm as it is influenced by the arm support displays a small range of motion in the x direction, suggesting the support limits certain forward motions that can be used for reaching purposes (Fig. 3). The wide range of motion in the y direction illustrated on both ellipses indicate that the support has minimal effect on sideway motions.

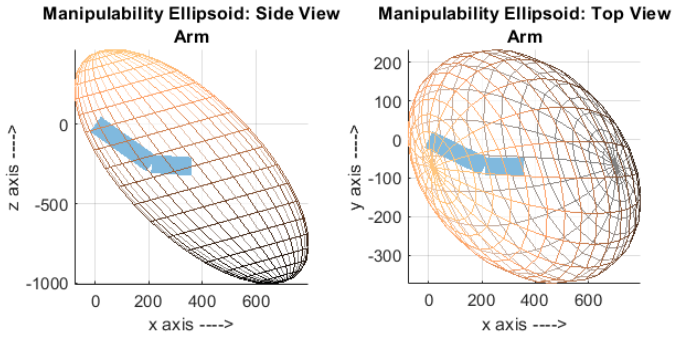

Figure 2. This figure displays the velocities and directions that a typical arm can achieve while it is in the resting position. The dimensions of the arm are displayed using blue lines, with the shoulder located at position (0,0) while the wrist is positioned at the center of the manipulability ellipse.

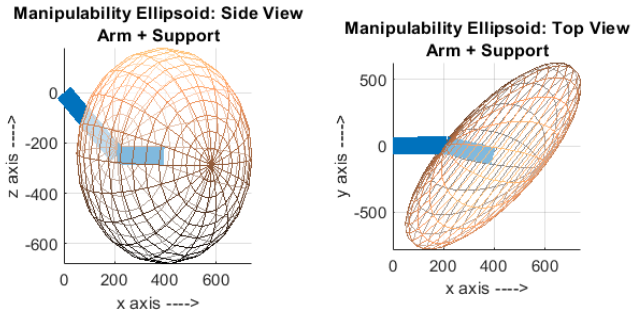

Figure 3. This figure shows the velocities and directions that the arm can achieve as it is influenced by the support while oriented in the resting position. The arm dimensions are displayed using blue lines, with the shoulder located at the position (0,0) in both plots. The wrist is positioned in the center of the ellipse.

The goal of the arm support is to assist against the force of gravity while maintaining the arm in a stable position. Obtaining two different ellipsoids indicate that the support is also affecting arm movement by limiting certain motions a typical arm could easily achieve.

CONCLUSION

The results of this study are promising, as it provides detailed information of the different ways in which the arm support affects the range of motion of the arm. This knowledge can help professionals understand the effects of the arm support on arm movement, allowing them to design new arm supports that restore the arm's full range of motion.

REFERENCES

[1] F. C. Park and J. W. Kim "Manipulability of Closed Kinematic Chains" pp. 9-12, 1996.

ACKNOWLEDGEMENTS

This work is supported by NSF grant 1950558.

Identification of Feedback Control for Human Posture Using SCONE

Isaias Trevino[1], Dana Lorenz[2], Antonie van den Bogert[2]
[1]Department of Electrical, Computer, and Systems Engineering, Case Western Reserve University, Cleveland OH
[2]Department of Mechanical Engineering, Cleveland State University, Cleveland OH

Introduction: Control of balance is an important element of human movement. Impaired balance control can lead to falls and injuries, especially in the elderly. In order to properly assist those who have these disabilities it must be understood how able-bodied persons unconsciously use their motor functions, so that one does not fall down, even with perturbations. The aim of the study is to identify the feedback control laws that humans use for standing upright.

Materials and Methods: A previously published dataset was used [1]. Human subjects were perturbed using random anterior-posterior movements of the standing surface. Surface movement and sagittal plane joint angles in hip, knee, and ankle were recorded using a 10-camera optical motion capture system. The SCONE software [2] was used to find a muscle reflex controller that could best explain the experimental results. A musculoskeletal model with nine degrees of freedom and 16 Hill-based muscles was used. The reflex controller included stretch reflexes and vestibular reflexes in all muscles. Feedback gains, thresholds, and time delays were optimized using single shooting and covariance matrix adaptation [2]. The SCONE balance control tutorial was used to find an equilibrium state for the system, which was then used as an initial condition for all simulations. Lua scripting was used to evaluate an optimization objective that was the root-mean-square (RMS) difference between simulated and measured joint angles, after subtracting the mean from all angles. This approach was evaluated on 30 seconds of data from the first participant.

Results and Discussion: The optimization time was roughly 50 minutes on a 160 180 GHz processor. After optimization, the model was able to remain standing for the entire duration. The simulated joint angles showed similar patterns to the measured joint angles (Fig. 1). The overall RMS difference between simulation and experiment was 4.83 degrees. RMS differences in the individual joint angles were 7.12 degrees (hip), 3.75 degrees (knee), and 2.26 degrees (ankle). Correlation analysis showed that the reflex control model explained 1.34%, 31.77%, and 1.90% of the variance in the hip, knee, and ankle movement, respectively. The simulated data that best represents the measured data seems to be the hip angles because we see that the angles are very close to each other; in addition, we see that the trend of the simulated data is very similar to that of the measured. The simulated data for the knee angles seem to have the correct trends; however, there is a clear vertical shift that shows all of these angles are off by a small degree. The simulated ankle angles seem more sensitive to the perturbations than in the human subject. Although there appears to be similarity between simulated and measured variations in joint angles, the variance accounted for (VAF) was poor. We expect significant improvement after implementing a reflex controller with more optimizable parameters. This added controller would allow for a closer model to the actual human neural control system. A limitation of the control model was that all muscles had the same feedback gains, thresholds, and time delays. In future work, these will be optimized independently, which will increase computation time. When a satisfactory approach is found, it will be applied to data from all participants in [1].

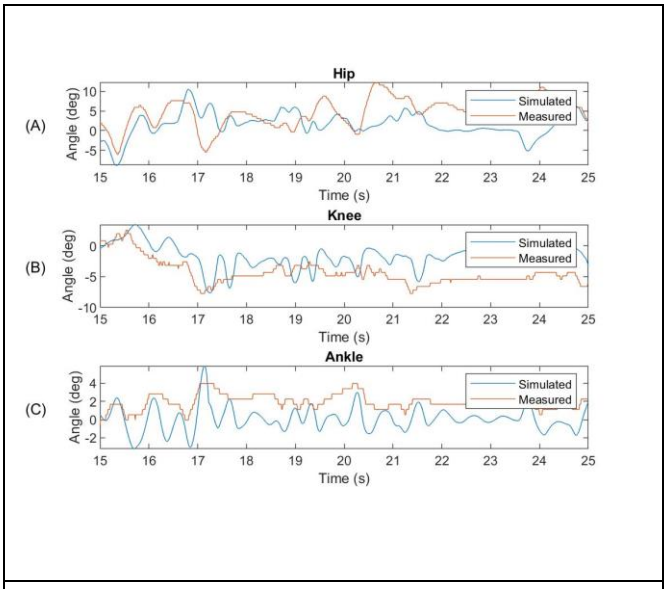

Figure 1. Simulated and measured joint angles over a 10-second portion of the experiment.

Conclusions: It was concluded that the SCONE single shooting approach can be used to identify the reflexes that are responsible for human postural control.

Acknowledgements: This work is supported by NSF Award 1950558.

References: [1] Wang H (2021) *J Biomech Eng* 143:041001. [2] Geijtenbeek T (2019) *J Open Source Softw* 4:1421.

EFFECTIVENESS OF A MOTOR POINT PEN IN FINDING MUSCLE MOTOR POINTS

[1]Kyra Stovicek, [1]Eric Schearer
[1]Cleveland State University, Cleveland, OH, USA
Email: k.c.stovicek@vikes.csuohio.edu

INTRODUCTION

There are roughly 294,000 people in the United States that are affected by spinal cord injuries [1]. Those with C4 and C5 level injuries experience upper limb paralysis, making it difficult for them to complete everyday tasks. Functional electrical stimulation is a viable technique to reanimate muscles that no longer receive electrical signals from the spinal cord. Surface electrodes are used to find the motor points and stimulate the muscles, resulting in arm movement. It is important to place the electrodes at the correct motor points in order to optimize muscle activation. Currently, the placement procedure of electrodes involves the use of an anatomical chart for reference. Motor point locations are specific to each individual, making the anatomical charts ineffective between people. Because of the variability, a procedure must be developed that is repeatable in settings that lack equipment to obtain quantitative data. Our method involves the use of a motor point pen to find motor points accompanied by the manual muscle test to score the muscle contractions in comparison to the anatomical charts.

METHODS

To determine the importance and effectiveness of electrode placement, our method involved the use of two different placement procedures where pulse width values were recorded as new manual muscle test grades were achieved, allowing for the superior method to be determined. To help reduce the possibility of extraneous data, three trials were recorded and the pulse width (PW) values for each trial were averaged together, giving one PW value per muscle at the respective manual muscle test grades. One participant was involved in the study and one researcher was responsible for finding the motor points, placing the electrodes, and collecting data.

Throughout the duration of the experiment, we used Syrtenty 1” round reusable electrodes to stimulate the forearm muscles which included: pronator teres, extensor carpi radialis, palmaris longus, flexor carpi radialis, flexor carpi ulnaris, and supinator. We used 2” square electrodes for the bicep brachii and tricep brachii. A universal external control unit controlled the electrical pulse, where the frequency and amplitude were held constant at 40 Hz and 25 mA respectively.

Anatomical charts were used for muscle stimulation first. Reference electrodes were placed on tendinous areas of the arm while the active electrodes used the anatomical charts for positioning. For the second placement procedure, we used a Compex motor point pen accompanied by electrical gel and reduced the amplitude to 5 mA to find optimal locations for the active electrodes while minimizing the discomfort of the pen. Motor points were marked with a marker before reusable electrodes were placed over the muscle.

Throughout the experiment, pulse widths (PW) were recorded with respect to manual muscle test grades associated with added gravity resistance. A grade of 3 indicates that the arm moved against the force of gravity without any external force applied. Grades of 4 and 5 allowed some applied force, with 4 being an intermediate amount of force while 5 was a strong opposing force. To obtain data about

the effectiveness of the motor point pen, the PW values obtained from the motor point pen were subtracted from the PW values found using the anatomical chart procedure. If the difference was negative, that indicated that the PW used by the electrodes in the motor point procedure was higher than the PW used during the anatomical chart procedure.

RESULTS AND DISCUSSION

This study indicated that the pulse width required to obtain each grade during stimulation using the anatomical chart was generally larger than the values obtained using the motor point pen. The difference between the two, with the exception of the tricep, was always positive (Fig. 1).

A subsequent result of this experiment is that as the manual muscle test grade increased, so did the gap between the PW required by each procedure. For example, the gap almost doubles between test grade 4 and 5 for the extensor carpi radialis. The other muscles saw similar results through each grade.

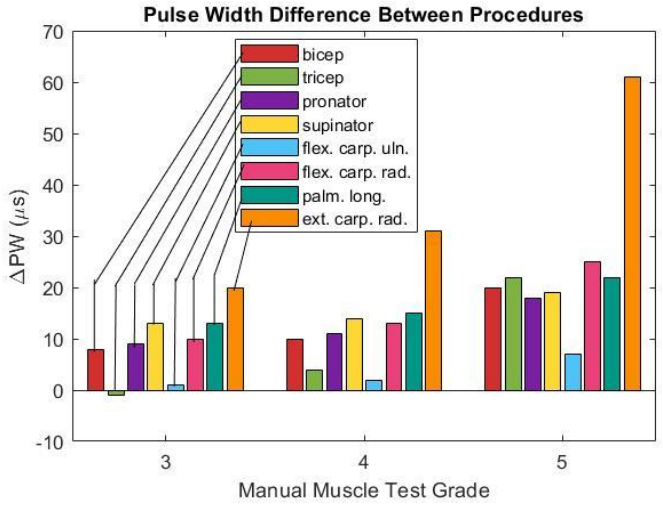

Figure 1: This plot displays the pulse width difference obtained by subtracting the pulse width value of the motor point pen from the value obtained using anatomical charts for each of the 8 muscles at the corresponding manual muscle test grades.

The goal of electrical stimulation is to reanimate muscles that are no longer controlled by the brain's electrical signal. When sending electrical current to the muscles, it is possible to send the current to neighboring sensory nerves, meaning that only trace current is sent to the motor nerve. Smaller PW values indicate that the current was sent to the correct nerve, allowing for comfortable contraction of the muscles [2].

CONCLUSION

The results of this experiment are promising, as it provides a more effective and generalizable approach to finding muscle motor points of different individuals. The data collected in this experiment was collected by someone who is not a medical professional, further proving the ease the pen provides to those searching for motor points. To improve upon the current experiment, this study could be done again with more research participants as well as more researchers, who would implement the strategies outlined above to obtain data.

REFERENCES

[1] National Spinal Cord Injury Statistical Center, Facts and Figures at a Glance. Birmingham, AL: University of Alabama at Birmingham, 2020

[2] Gobbo, M., Maffiuletti, N.A., Orizio, C. *et al.* Muscle motor point identification is essential for optimizing neuromuscular electrical stimulation use. *J NeuroEngineering Rehabil* 11, 17 (2014).

ACKNOWLEDGMENTS

This work is supported by NSF grants 2025142 and 1950558.

A case study of Chiari Malformation Type 2 gait abnormalities in a pediatric population

[1]Tayluer Streat-Ricchiuti (Presenter), [1]Dr. Doug Wajda and [1]Dr. Brian Davis

[1]Cleveland State University, Cleveland, OH, USA

Email: t.streat@vikes.csuohio.edu

INTRODUCTION

Chiari Malformation (CM) is a condition that affects the skull-spine junction and is linked to the cerebellum protruding into the top of the spine, obstructing the passage of cerebrospinal fluid. Headaches, dizziness, trouble swallowing, muscle weakness, and loss of neuromuscular coordination arise as a result of this increased pressure (Curone, 2017). There are four types of Chiari malformations:

Chiari I involves the descent of the medulla and cerebellar tonsils through the foramen magnum into the spinal cord.

Chiari II involves the descent of the inferior cerebellum and fourth ventricle through the foramen magnum into the spinal cord.

Chiari III involves the descent of most of the cerebellum through the foramen magnum causing a cervical-occipital bony defect.

Chiari IV has no herniation of the cerebellum, but rather cerebellar hypoplasia (Shah, 2017).

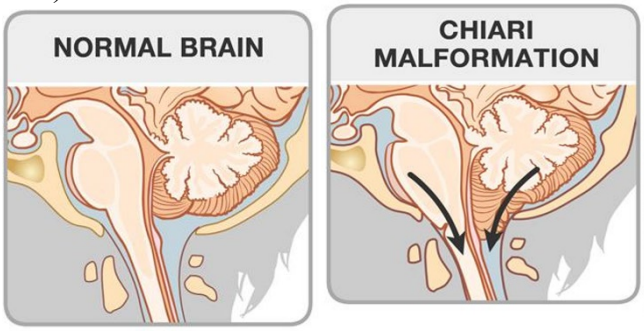

*Figure 1: Diagram of normal neurological and Chiari malformation development in patients, (*AboutKidsHealth *2009)*

The goal of this research is to measure gait stability in children with CM. Even though loss of stability and difficulty walking are common symptoms in CM patients, no previous research has investigated these issues.

Our understanding of the functional implications of CM and how it affects gait and posture is hampered by these knowledge gaps. A better knowledge of neuromuscular function will aid neurologists, neurosurgeons devising surgical therapies, and physiotherapists developing pain reduction and rehabilitative balancing approaches. This abstract analyzes walking data collected on a control and pediatric CM patient.

Type 2 Chiari Malformation has been diagnosed in the CM patient. It is typical for Chiari type 2 patients to experience cerebellar tonsils, inferior vermis, fourth ventricle, and brain stem, as well as a small posterior fossa (Cotes, 2015). It is likely the CM subject reviewed has some of these associations listed above, but we can't say for certain which without further medical records

METHODS

This study was approved by the Cleveland State University Institutional Review Board. Our control subject was 14 years old, 110 pounds, and 5'4 ft in height. Our Chiari subject was 14 years old, 224 pounds, and 5'4 ft in height. The kinematic parameters of walking, including as gait speed and step/stride parameters, were determined using a 6.1m electronic Zeno walkway (Protokinetics Inc., Havertown, PA). Individual footfalls were distinguished, and spatiotemporal aspects of the subject's gait were quantified using pressure sensors

on the Zeno walkway. Participants were told to take four walks: two at their normal walking pace and two at a faster tempo without running. The subjects were instructed to walk as fast as safely possible for the fast walk trial.

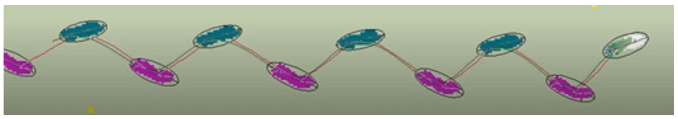

Figure 2: Control patient normal walking trial

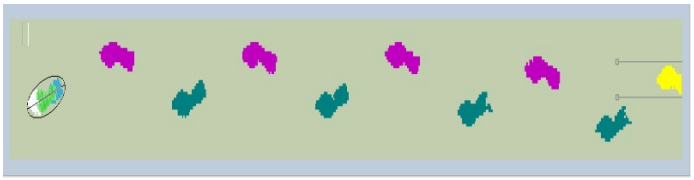

Figure 3: Chiari patient normal walking trial

Next, the walks were processed removing any uncompleted steps on the mat by marking the step as other in yellow as shown above. The stride length and width were analyzed to establish a baseline for balance stability in both subjects.

RESULTS AND DISCUSSION

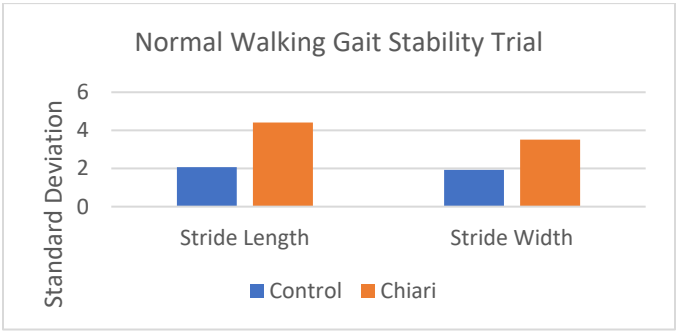

The standard deviation of the stride length and width provides a verification of the lower levels of stability in the gait of a CM patient. In the graph above, both variables of the CM subject are approximately double that of the control alluding to the lack of balance during walking.

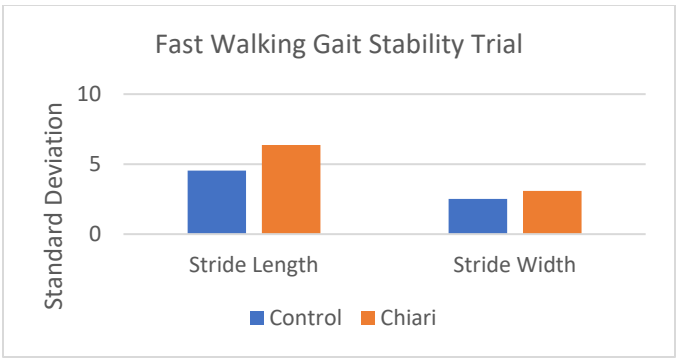

During the fast walk trial, the stride length variable showed an increase for both subjects which can be considered normal for a quick pace gait. The stride width presented no variance between the two paces.

CONCLUSION

In conclusion, The Chiari subject displayed greater walking instability as seen by the higher standard deviation values for both trials. This preliminary data suggests that a simple measurement technique involving an instrumented walkway may detect altered gait patterns in Chiari patients. In the next year collecting data on more Chiari and control subjects will be conducted, which will allow for a better understanding of the differences between the two and provide a baseline for future work.

REFERENCES

AboutKidsHealth. (2009, November 6). Retrieved fromhttps://www.aboutkidshealth.ca/Article?contentid=853&language=English

Cotes C, et al. The Neuroradiology Journal. (2015) 28(3): 238-253.

Curone, M., et al. Neurological sciences: official journal of the Italian Neurological Society and of the Italian Society of Clinical Neurophysiology.(2017) *38*(Suppl 1), 91–93.

Shah, A. H., et al. Journal of craniovertebral junction & spine. (2017) *8*(4),297–304.

ACKNOWLEDGEMENTS

This work is supported by a grant from the American Syringomyelia Alliance Project.

PEDIATRIC PARTIAL BODY WEIGHT SUPPORT SYSTEM FOR THE AID OF MOVEMENT FOR CHILDREN WITH CEREBRAL PALSY

Kaitlin Skurnak[1], Brian L. Davis[2]
[1]University of Illinois, Urbana-Champaign, IL, USA
[2]Cleveland State University, Cleveland, OH, USA
Email: skurnak2@illinois.edu

INTRODUCTION

Walking is an important milestone in the development of children, but for those with cerebral palsy (CP), development is often delayed and may slow down or stop entirely at a certain point. Approximately 41% of children with CP have limited to no walking ability without a mobility aid [1].

One form of therapy utilized for these children is the use of treadmill training in combination with traditional physical therapy. However, because lower body strength is a prerequisite for the use of a treadmill, this exercise excludes a large proportion of the population for which it is designed. Adding a partial body weight support system to treadmill training could be ideal for building lower body strength by progressively decreasing the amount of support supplied to the user.

Treadmills paired with partial body weight support systems exist, but they are very expensive and not portable, limiting their usefulness to the clinical setting. Finding a way to allow training to take place in the home or school may decrease the expense and encourage compliance [2]. This study's objective is to design a portable, lightweight, and low-cost solution that would allow a child to practice walking.

The design for this rig took inspiration from the structure and mechanisms of an Anglepoise lamp (Figure 1). This design was chosen due to its ability to support and offload a weight over an infinite range of positions [3]. Similar to the lamp, the prototype uses springs with an effective unstretched length of zero, introducing a tension force before any load is applied to the mechanism [4].

METHODS

A computer model of a body weight support rig was developed in MSC Automated Dynamic Analysis of Mechanical Systems (ADAMS) to evaluate several design iterations. The spring constants of the Anglepoise lamp were evaluated experimentally through tensile testing on an Instron Machine. The springs were stretched at a set displacement rate of 2mm/s, and the subsequent force was measured.

(a) (b)

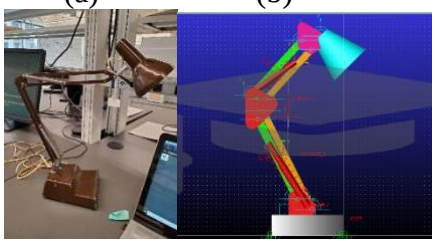

Figure 1. An Anglepoise lamp (a) and the ADAMS simulation modelling said lamp (b).

The strengths of larger springs to be used in the prototype (see Figure 4) were tested by hand, recording the displacement of the spring and measuring the amount of force applied with a force sensor. The larger springs had a k value of approximately 1.105. The springs used in the ADAMS simulation had a k value of 1.56, a difference of about 29%.

The prototype was constructed using 1" aluminum pipes for the main body, metal plates to connect the pipes, four of the larger springs mentioned previously, turnbuckle connectors to attach the springs to the pipes, and eventually a wooden frame was built to increase structural stability. A pediatric unweighing harness was attached to the end of the pipes on top in order to support the user's weight (Figure 4a).

Once the prototype was completed, it was then tested to determine its ability to support a weight, reducing the force exerted on the ground. The forces were measured in the Z-direction via an AMTI force plate. A 7.5 lb. and 10 lb. weight cuff were placed on the force plate and the forces were measured with and without support from the rig. A decrease in the force in the Z-direction on the force plate is indicative of the user experiencing a reduced body weight.

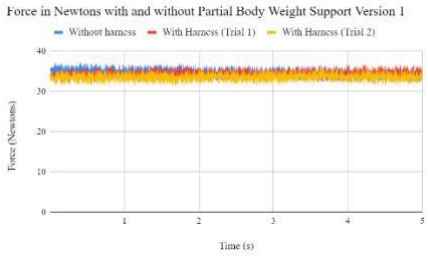

Figure 2. Force plate data for the first design iteration. Note that there is no significant difference in forces in the Z direction with and without the harness.

RESULTS AND DISCUSSION

The Anglepoise lamp design was chosen due to its ability to maintain its upright position regardless of how it is manipulated. We hypothesized that this quality would allow a rig with a similar structure to support the weight of a toddler. However, the initial test of the rig did not show a significant change between the force exerted by the weight cuff with and without support from the harness (Figure 2). Without the harness, the weight exerted an average of approximately 34.5 Newtons on the force plate. With the harness, the weight exerted an average of 33.96 Newtons (1.5% reduction in weight).

Following that test, the placement of the springs was changed, moving one end of the springs 1" further away and removing the turnbuckle connectors so as to allow them to contribute a larger force (Figure 4b). These structural changes allowed the rig to support more weight and the weight tested increased from 7.5 lbs. (≈34.5 N) to 17.5 lbs. (≈81.5 N). Without the harness, the weight exerted an average of 81.58 Newtons on the Force Plate. With the harness, the weight exerted an average of 48.75 Newtons (40.2% weight reduction).

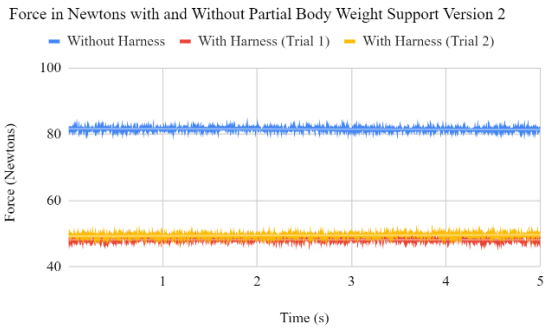

Figure 3. Data collected from AMTI force plate for Design iteration 2 with springs stretched a greater distance and wooden frame added

CONCLUSIONS

This design shows promise in reducing the amount of weight needed for a child with CP to support themselves while practicing walking. With an initial goal of supporting 50% of a 25 lb. weight, this rig currently does not meet that specification. However, the current pattern suggests that with additional improvements, this goal is achievable. Testing a version of this rig with a human subject would be ideal once the design is deemed safe enough to do so.

(a) (b)

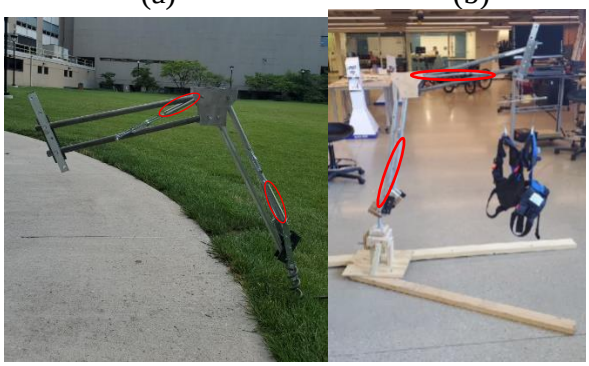

Figure 4. Design iterations 1 (a) and 2 (b) of the Portable Body Weight Support System with springs indicated in red

REFERENCES

1. Centers for Disease Control and Prevention, "Data and Statistics for Cerebral Palsy," 2020.
2. Damiano, D. et al. "A Systematic Review of the Effectiveness of Treadmill Training and Body Weight Support in Pediatric Rehabilitation," Journal of Neurologic Physical Therapy, pp. 27-44, 2010.
3. G. Cawardine, "Equipoise Mechanism". Bath, England Patent 2090439, 17 August 1937.
4. M. J. French and M. B. Widden, "The spring-and-lever balancing mechanism, George Cawardine and the Anglepoise lamp," Journal of Mechanical Engineering Science, pp. 501-506, 1989-1996.

ACKNOWLEGEMENTS

This work is supported by NSF Award 1950558.

ROBOT-ASSISTED FEEDING FOR INDIVIDUALS WITH MOVEMENT DISORDERS

[1]John R Schultz and [2]Eric M Schearer

[1]Cleveland State University, Cleveland, OH, USA

Email: j.r.schultz12@vikes.csuohio.edu

INTRODUCTION

According to the World Health Organization, there are more than 1 billion people, or 15% of the world's population, living with some sort of a motor impairment. [1]. Many of these individuals rely on a caregiver or family member for help in performing activities of daily living (ADLs), which can be costly as well as diminish a person's sense of self-worth [2]. Assistive robotic devices have emerged as a promising solution for helping people perform a wide variety of ADLs. In particular, people with movement disorders have rated the ability to prepare a meal and feed themselves as one of the highest priority features they would like an assistive device to have [3]. Our research goal is to develop a robot-assisted feeding (RAF) system that can recognize specific food items, locate them in 3D space, and feed them to the user. Our current work focuses on the methods of recognition and 3D localization of food items on a table, and concurrent strategies on robotic grasping of these food items. This work outlines the methods to picking up food items with a robot and the steps toward robot-assisted feeding for people with movement disorders.

METHODS

System Overview - Our system consists firstly of a Baxter Research Robot (Rethink Robotics; Bochum, Germany) with a L515 LIDAR camera (Intel; Santa Clara, California) mounted on its wrist. The user is seated in a wheelchair across the table from the robot. A tablet monitor is mounted to the wheelchair fit with a Tobii Eye Tracker 4 device (Tobii; Danderyd, Sweden). The user moves their eyes to select options on the tablet which control the robot to pick up and deliver food items (Fig. 1). System communication is handled by the Robot Operating System (ROS).

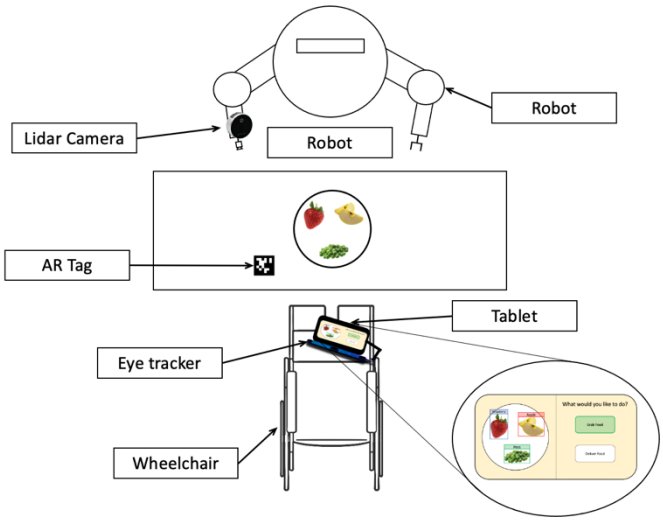

Figure 1: Robot-Assisted Feeding system top-down view.

Object Recognition – We trained a maskR-CNN based on a ResNet+FPN backbone to detect bounding boxes and instance segmentation masks of four classes: three food items (carrot, celery, pretzel) plus the robot's grippers (FacebookResearch; Menlo Park, California). Computed AP were 88.8, 94.8, 90.3, and 92.1 for carrots, celery, pretzels, and grippers, respectively (783/221 training/test images). Our network takes the Lidar camera's RGB data stream as an input and runs on a GeForce RTX 3090 GPU (NVIDIA, Santa Clara, California).

Table Plane Registration – We placed an AprilTag fiducial marker (AR tag), on the surface of the table to define the table's coordinate frame, detected using the AprilTag 3 ROS package. We then performed a Direct Linear Transformation (DLT) to map camera pixels (u, v) to table coordinates in meters (x, y). In this method, the corners of the AR tag are used as

correspondence points and the solution to a set of linear equations described by these points can be used to convert pixels to meters. Thus, any camera pixel location (u, v) can be projected to planar table coordinates (x, y).

Camera to Robot Calibration – The mount which fixes the Lidar camera to the robot's wrist allows for tuning of the camera's angle. To combat the need to frequently re-define the camera pose, we developed a calibration procedure. First, a food item such as a pretzel is placed on the table within view of the camera. The centroid of the food item in table coordinates (x, y), as well as the depth value returned from the Lidar camera (z) is saved as P_1. Then, the robot's gripper is manually moved to the center of the food item and the position of the gripper in the robot's frame (X, Y, Z) is saved as P_2. Finally, the transformation matrix (T) between the camera's frame and the robot's frame is computed using the methods described in Söderkvist, et al. for a minimum of 3 correspondence points (P_1, P_2) [4]. Thus, any camera pixel location (u, v), along with a corresponding Lidar depth value (z), can be transformed into robot coordinates (X, Y, Z) by multiplying by the transformation matrix (T).

Grasping Food Items – To properly grasp the food item with the robot's two-finger gripper, we first computed the rectangle with minimum area that circumscribes the food item's segmentation mask. The angle the longer axis of the rectangle makes with the u-axis of the camera frame is transformed to the robot's frame using the methods described in the previous section. This angle along with the centroid of the detected food item in the robot's coordinate frame define the grasp pose.

RESULTS AND DISCUSSION

We tested our combined perception and grasp methods by calibrating our robot with the four corners of a 25x25cm planar workspace on the surface of the table. We placed a pretzel centered on a point every 5 cm within the workspace for a 5x5 grid of test positions. We then attempted to pick up the pretzels for each of the 25 total test points. The grasp point error was computed as the Euclidean distance error between the transformed centroid of the detected pretzel and each grid point in robot coordinates (Table 1).

Table 1: Results

Robot Coordinate Frame	Error (mm)
X	7.3 ± 3.5
Y	2.6 ± 2.0
Z	1.6 ± 1.1
Euclidean	8.6 ± 3.6

Our method detected objects and transformed their centroid coordinates to the robot's coordinate frame with an average 3D error of less than 1 cm. The robot successfully picked up the object in 100% of trials. The robot's grippers have a clearance width of 3.5 cm, so we expect grasp performance to decline if grasp point error were to approach this threshold.

CONCLUSION

In this study, we have outlined methods to detect food items, identify their centroids, transform their pixel coordinates into a robot's coordinate system, and compute robot grasp poses that result in picking up food items with a high success rate. Future work will focus on the communication interface between the human and the RAF device.

REFERENCES

1. World Health Organization. *World Report on Disability*, 2011.

2. Lin, I, et al. *Does informal care attenuate the cycle of ADL/IADL disability and depressive symptoms in late life?*, 2011.

3. Stranger, C, et al. *Devices for assisting manipulation: a summary of user task priorities*, 1994.

4. Söderkvist, I, et al. *Determining the movements of the skeleton using well-configured markers*, 1993.

In silico modeling of Achilles tendon function in running humans: effects of foot geometry, speed, and gait

[1]Dubé MD, [2]Foster AD, [1]Young JW

[1]Deparment of Anatomy and Neurobiology, Northeast Ohio Medical University (NEOMED)

[2]Department of Anatomy, School of Osteopathic Medicine, Campbell University

Email: mdube@neomed.edu

INTRODUCTION

Previous research suggests that the length of the Achilles (calcaneal) tendon (AT) moment arm is positively correlated with energy costs of locomotion at running speeds [1,2]. This finding is hypothesized to result from a shorter AT moment arm placing larger elastic loads on the AT, increasing energy storage and return. Foster et al. [3] tested this hypothesis using inverse dynamic analyses of walking and running in human subjects, finding significant negative correlations between AT moment arm length, spring-like behavior of the ankle joint, stress on the AT, and elastic energy storage. Speed was also a significant factor explaining energy storage in the AT.

In this study, we use *in silico* musculoskeletal model in OpenSim [4], fit to motion and force data from human subjects, to explore the relationship between moment arm length and AT strain during running. Additionally, we specifically focus on AT strain during heel strike, when tendon force is greatest and tendon strain (and therefore elastic energy storage) should be maximal. We test the following hypotheses:

H_1: *In silico* models will demonstrate that AT moment arm length and tendon strain are negatively correlated.

H_2: Patterns of association between AT moment arm length and tendon strain should be most pronounced at heel strike.

METHODS

Morphometrics (body mass and AT moment arm length) and kinematic/force data were collected from n=7 human subjects (i.e., the subset of the subjects from Foster et al. [3] where motion data were suitable for simulation). *In vivo* AT strain was modeled using the inverse kinematics, inverse dynamics, and computed muscle control toolkits of OpenSim 4.2 [4]. Overall, AT strain was modeled as the mean of all instantaneous *m. triceps surae* tendon strains, weighted by force. We calculated mean and peak strain values over stance phase and mean values during heel strike (i.e., the initial 27% of stance phase).

The Campbell University Institutional Review Board approved all study methods and procedures prior to the start of research (Protocols 376 and 472) Informed consent was obtained prior to subject participation.

RESULTS AND DISCUSSION

Similar to our previous analyses of *in vivo* data, *in silico* simulation demonstrated that mean and peak tendon strain is moderated by speed, with values increasing from walking at the lowest, and jogging at the highest. Running values were lower than jogging values (Fig. 1).

There were no significant correlations between tendon strain values and walking and fast walking gaits, as expected. However unlike in Foster et al. [3], the results from this study show significant correlation between AT moment arm length and

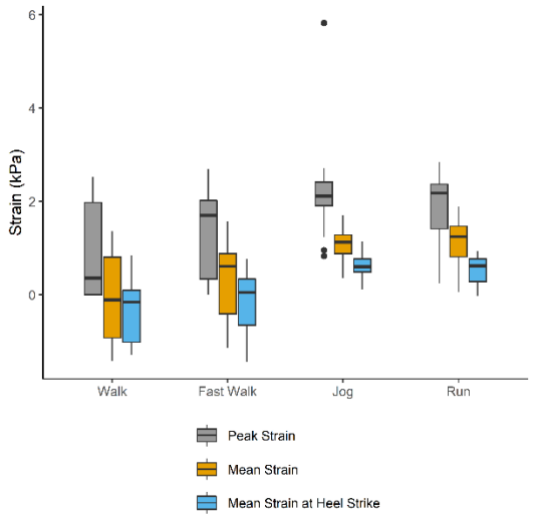

Figure 1: Boxplot of mean, peak, and heel strike values of AT strain

mean strain at heel strike in jogging gaits (Pearson's r=-0.323, $t_{[28]}$=1.801, p=0.041; Fig 2). There were no significant correlations between AT moment arm length and strain in running gaits.

CONCLUSIONS

Overall, these data suggest a functional relationship between AT moment arm length and tendon strain. Differences in results between *in vivo* and *in silico* studies may be attributed to a smaller sample size for the modeling dataset, differences in how joint work was calculated, or the inability of the musculoskeletal model to accurately represent morphometric variation among subjects. Future work should refine musculoskeletal models to more explicitly explore how foot geometry impacts AT elastic energy storage.

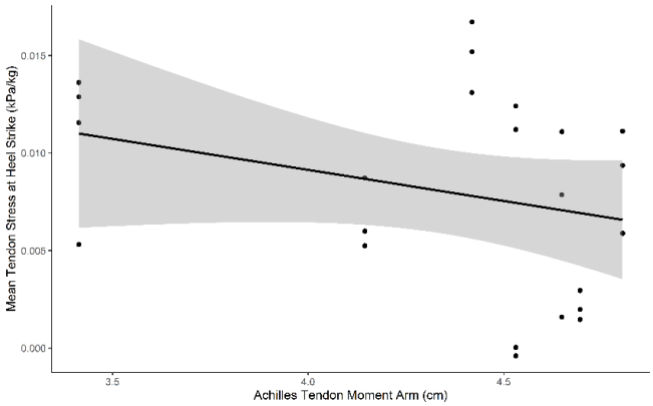

Figure 2: Scatter plot of AT moment arm length and mean mass-specific tendon strain at heel strike. The line represents the best fit line and the gray band is the 95% confidence interval.

REFERENCES

[1] Raichlen DA et al.. Calcaneus length determines running economy: Implications for endurance running performance in modern humans and Neandertals. J Hum Evol 2011.
[2] Scholz MN et al.. Running biomechanics: shorter heels, better economy. J Exp Biol 2008.
[3] Foster AD et al. Shorter heels are linked with greater elastic energy storage in the Achilles tendon. Sci Rep 2021.
[4] Delp SL et al. OpenSim: Open-Source Software to Create and Analyze Dynamic Simulations of Movement. IEEE Transactions on Biomedical Engineering 2007.

ACKNOWLEDGEMENTS

We would like to thank the CUSOM Medical Student Summer Scholars Program, the NEOMED Office of Research and Sponsored Programs Summer Fellowship Program, and the human subjects for their participation.

FEASIBILITY OF THE LIFTING FULL-BODY MODEL TO SIMULATE SQUATTING TASKS

Reese Moschetta, Yeageon Song, Bridget Gagnier, Barry Bait, Dr. Brooke Odle

Hope College, Holland, MI, USA

Email: reese.moschetta@hope.edu yeageon.song@hope.edu

INTRODUCTION

Lower back pain is one of the most common injuries involving healthcare workers. Such tasks require caregivers to squat, lift, lower, and reposition patients, which may place high loads at the low back, increasing their risk of injury (1). Experimental studies of manual patient-handling tasks can be extended with a computational model of the lumbar spine. Currently, there is not a freely available subject-specific model for patient-handling tasks. As a first step towards the development of such a model and due to the complexity of these tasks, work-in-progress from a proof-of-concept study to determine the feasibility of the OpenSim Lifting Full-Body (LFB) Model (2) to simulate squatting tasks is presented.

METHODS

Experimental feasibility tests were conducted with a 20-year-old able-bodied female volunteer. Prior to conducting the experiments, the volunteer signed informed consent forms, approved by the Human Subjects Research Board at Hope College. Thirty-nine reflective markers were placed on bony landmarks of the upper and lower body of the subject. Ten electromyography (EMG) sensors (Delsys, Natick, MA) were placed bilaterally on the following muscles; lumbar erector spinae, thoracic erector spinae, rectus femoris, rectus abdominis, and the external obliques. The participant stood with each foot on a force plate (AMTI, Watertown, MA). As the subject performed squats, body segment position (100 Hz), ground reaction forces (1000 Hz), and muscle activity (1000 Hz) data were synchronized and captured with a nine-camera motion capture system (Optitrack, Corvallis, OR). Each subject performed five consecutive squats per trial, for a total of four trials.

Kinetic data were down-sampled to 100 Hz. Kinematic and kinetic data were filtered with a fourth order Butterworth filter with a cut-off frequency of 6 Hz. EMG data was rectified and filtered with a 4th order low-pass Butterworth filter with a cutoff frequency of 6 Hz. EMG signals for each muscle were normalized to its average maximum peak value across all four trials. EMG data was resampled from 1 to 100% of the squat by noting the start and end times from the video captured by a reference camera.

There were four major steps for the OpenSim® analyses: Scaling, Inverse Kinematics, Inverse Dynamics , and Static Optimization (3). Kinematic data from a static trial was used to scale the generic LFB model to the subject's height and weight. Kinematic data from the squatting trials were used for inverse kinematics simulations. Those results and the kinetic data were used to generate inverse dynamics simulations. The static optimization simulations determined the muscle forces and activations in the trunk and low back by minimizing the squared muscle activation (3). The simulations were generated for each individual squat, the onset and offset times were determined via recordings from the reference camera. The results were resampled from 1 to 100% of the task.

RESULTS AND DISCUSSION

Due to inconsistencies with EMG sensor placement on the bilateral rectus abdominis, the data collected for those muscles were discarded. The normalized EMG data, displayed in Figure 1, demonstrate that the left lumbar erector spinae and bilateral rectus femoris were the most active during the exercise. This was expected given the task performed. A limitation of the current LFB Model is that it does not contain the lower limb musculature. The experimental EMG findings suggest that in order to

simulate patient-handling tasks, the model should be modified to include the quadriceps. This will enable validation analyses for all muscles studied.

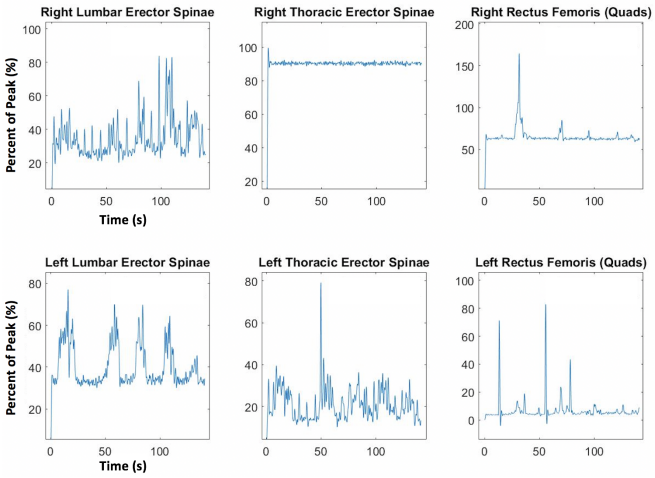

Figure 1: Normalized Experimental EMG

Figure 1 shows the profiles of the squat tasks in a single trial for Subject 1. On the top row, EMG profiles for the right lumbar erector spinae, right thoracic erector spinae, and right rectus femoris are displayed (left to right). On the bottom row, EMG profiles for the left lumbar erector spinae, left thoracic erector spinae, and the left rectus femoris are displayed (left to right).

Simulation Results

Table 1: Static Optimization L5/S1 Actuator Contribution

Flexion-Extension (%)	Lat-Bending (%)	Axial-Rotation (%)
0.0044	6.57e-04	0.0142

Reserve actuators were added to the model to help the static optimization simulations to converge. The contributions of the reserve actuators at the L5/S1 joint are listed in Table 1 and the values for each joint coordinate are less than 5% of the maximum peak of the net external forces/moments (4). These findings suggest that the reserve actuators did not contribute too much to the movement and these results are acceptable.

Future Work

In order to estimate the internal loads applied to the low back during tasks and further explore the feasibility of the LFB Model for patient-handling tasks, future work involves performing Joint Reaction Analyses in OpenSim. In order to validate the LFB Model, the experimental and simulated EMG data will be compared. Techniques under consideration include mean absolute error and cross correlation analyses. This work only addresses the experiments and findings for squat tasks with one subject. The subject also performed torso twists (to simulate twisting motions) and arm raises (to simulate lifting tasks), which are also typical patient-handling maneuvers. In addition, experimental data was also collected with two additional subjects enrolled in the study. Experimental and simulation analyses of this data are in progress.

CONCLUSION

Pilot experimental and simulation analyses suggest that the LFB Model may be used to simulate simple squatting tasks. Future work will explore feasibility of the model with additional tasks related to patient-handling maneuvers. After some modifications to the musculature, the LFB Model may ultimately be used to simulate patient-handling tasks and provide insight on low back loading during patient-handling tasks.

REFERENCES

1.Videman, T; Ojajärvi, A; Riihimäki, H; Troup J, et al. *Spine,* 2005.
2. Beaucage-Gauvreau, E, et al. *CMBBE,* 2019.
3. Delp, S, et al. *simtk.org*. 2019
4. Hicks, J, et al. *J Biomech Eng*, *2015*

ACKNOWLEDGEMENTS

This work was supported by the Michigan Space Grant Consortium, Grant number NNX15AJ20H.

IMPROVING NEUROMUSCULOSKELETAL MODELS WITH TACTILE FEEDBACK: A PROOF OF CONCEPT SIMULATION STUDY

[1]Cameron LaMack (Presenter) and [1]Eric Schearer

[1]Cleveland State University, Cleveland, OH, USA

Email: c.lamack@vikes.csuohio.edu

INTRODUCTION

In the United States alone, there are an estimated 331,000 people living with a spinal cord injury, with an additional 17,900 occurring each year [1]. For those with high spinal cord injuries resulting in tetraplegia, regaining arm and hand function is of the highest priority [2]. Regaining the use of upper extremities has high correlation with a higher quality of life [3].

A promising solution to restoring arm and hand function for those living with high tetraplegia after a spinal cord injury is neuromusculoskeletal electrical stimulation, also called functional electrical stimulation. This is a process in which a patient's muscles are sent electrical stimulation, either through surface electrodes or surgically implanted electrodes.

While it is easier to simply program a variety of pre-programmed muscle activations to be sent to the arm, a better solution is to control the tetraplegic arm by learning its inverse-dynamics with the use of subject-specific, data-driven neuromusculoskeletal models [4]. With accurate person-specific neuromusculoskeletal, it is possible to control the arm such that it can complete *any* feasible trajectory, rather than just a few pre-programmed ones.

However, learning the neuromusculoskeletal properties of an individual's arm is a challenging task. The human arm is redundantly actuated, with many muscles crossing multiple joints. Under the current state of the art, the subject-specific neuromusculoskeletal models must be remade by an expert at the beginning of each day, which is not feasible for daily use.

The goal of this work is to demonstrate that neuromusculoskeletal models improve with tactile feedback using our modelling technique. We do this first by describing a method for modelling including tactile corrective torques. We then test our method on a simulated inverted pendulum actuated by two muscles, comparing models that have received corrective torque to models which have not received corrective torque.

METHODS

In order to achieve our goal, we first created a simulation of a simple biomechanical model - an inverted pendulum with two opposing muscles acting as actuators. We then forced it along a desired trajectory in order to collect position, velocity, acceleration, and torque data. With this data, we used a modelling technique called Gaussian Process Regression (GPR) [5] to identify both the inverse dynamics and the muscle capabilities of the simulated arm. Using these predictions of the arm, we used a model-based feedforward controller to drive the arm on a desired trajectory, shown in Figure 1.

Figure 1: We give a desired angle, velocity, and acceleration, $\boldsymbol{\theta}$, to our control scheme. We can then use our neuromusculoskeletal models to find the activations to send to the arm.

After the arm traveled on a trajectory controlled by the original models, we then applied corrective torque. With this corrective torque, we re-trained our models, and then used these models updated with tactile feedback to control the arm. Using the same control scheme, the arm followed the same desired trajectory.

The core element of control of the arm is predicting torque given a current position. Using GPR as described by Rassmussen, this can be written as

$$f^* = k(X, X^*)^T * (k(X, X) + \sigma^2 I)^{-1} f$$

where X is the previously gathered training positions, f is the training torque, σ^2 is the variance, X^* is the position for which we want to predict the torque, and f^* is the torque prediction.

Similarly, we can write an equation which predicts the torque given the current position, but also includes torque supplied by a non-expert caregiver during movement correction:

$$f^* = \begin{bmatrix} k(X, X^*) \\ cov(f_{obs}, f^*) \end{bmatrix}^T \left(\begin{bmatrix} k(X, X) & cov(f, f_{obs}) \\ cov(f_{obs}, f) & cov(f_{obs}, f_{obs}) \end{bmatrix} + \sigma^2 I \right)^{-1} \begin{bmatrix} f \\ f_{obs} \end{bmatrix}$$

where we include the new term f_{obs}, torque supplied by a non-expert caregiver.

RESULTS AND DISCUSSION

Our method was capable of learning the "ground truth" of neuromusculoskeletal models, beginning with an inaccurate model and producing a much more accurate prediction, shown in Figure 2. In addition, these models resulted in more accurate trajectory tracking; the path error across 27 trials decreased by an average of 66.9238%.

CONCLUSION

The implications of this study are clear: the method presented in this paper for including mixed training data in regression makes the models better. Based on this knowledge, it is possible for non-expert caregivers to help us make better neuromusculoskeletal models.

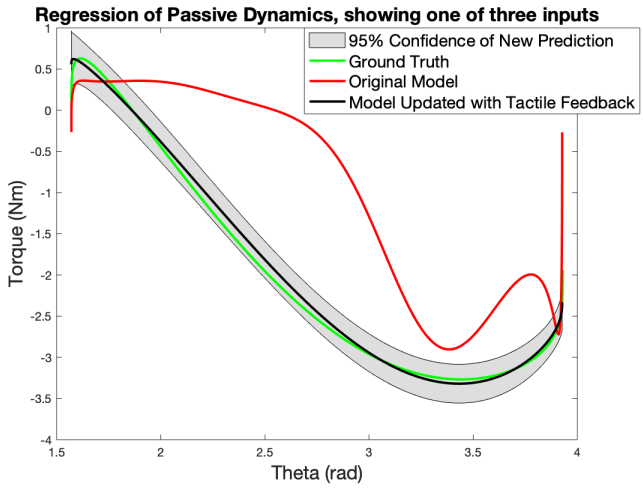

Figure 2: The initial prediction, shown in red, is inaccurate to the "ground truth," shown in green. After tactile feedback, the prediction is much more accurate, shown in black.

REFERENCES

1. NSCISC. *Spinal Cord Injury Facts and Figures at a Glance.* 2021.

2. Anderson, K. *Targeting recovery: Priorities of the spinal cord-injured population.* Journal of Neurotrauma, vol. 21, no. 10, pp. 1371–1383, 2004.

3. Dijkers, M. *Quality of life after spinal cord injury: a meta analysis of the effects of disablement components.* Spinal Cord. 1997.

4. Sartori, M., Farina, D. *Neuromusculoskeletal Modeling for Neurorehabilitation Technologies.* Converging Clinical and Engineering Research on Neurorehabilitation, pp. 1217-1220, 2013.

5. Rasmussen, C., et al. *Gaussian Processes for Machine Learning*. MIT Press, 2006

ACKNOWLEDGEMENTS

This work was supported by NSF Grant 1751821.

Kinematic Data of Healthy Thumbs

[1]Nicole Arnold, [1]Adam Chrzan, [1]Emily Kelly, [2]Kevin Chan and [1]Tamara Reid Bush, PhD

[1]Michigan State University, East Lansing, MI, USA

[2]Spectrum Health, Grand Rapids, MI, USA

Email: arnoldn5@msu.edu

INTRODUCTION

Osteoarthritis (OA) of the hand is a debilitating musculoskeletal disease that can severely impact one's ability to carry out daily activities, such as opening a bottle or food packages. The thumb, or more specifically, the carpometacarpal (CMC) joint of the thumb, located between the base of the metacarpal bone and trapezium, is the primary location for OA [1]. To understand how CMC OA impacts thumb and hand function, understanding healthy function of the hand is key. Typically, measurements that are used clinically (i.e., patient questionnaires and range of motion using goniometers) are not sufficient to quantify kinematic variations due to CMC joint OA. Thus, it is important to establish baselines of healthy function so that functional impairments can be identified and treatments can be monitored to determine if function is moving toward a normative state. The purpose of this study was to determine ranges of radial and palmar abduction/adduction of the thumb in a healthy population.

METHODS

Five healthy participants (1 female, 4 males, age 30 ± 5 years) were included in this study. A six-camera motion capture system collected three-dimensional kinematic data of the thumb's movements. A custom testing device was constructed to isolate the movement of the hand and thumb. Three reflective marker pods were attached to the distal phalange, proximal phalange and metacarpal of the thumb on the right hand. Additionally, four single markers were attached to the sides of the wrist and the 2nd and 5th finger joints (Fig. 1). Participants were instructed to perform their maximum palmar and radial abduction to the best of their ability. Palmar abduction/adduction was defined as thumb motions away from and toward the plane of the hand, (Fig. 2, left). Radial abduction/adduction occurs in the plane of the hand with the thumb moving away from or toward the rest of the hand, respectively (Fig. 2,

Figure 1: Marker pods on the thumb and single markers located on the base of the 2nd and 5th metacarpophalangeal joints and the medial and lateral sides of the wrist.

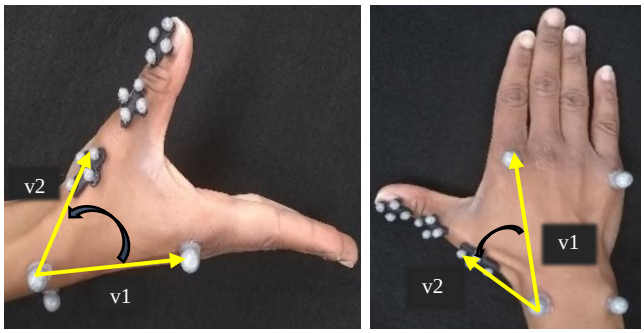

Figure 2: Hand with marker pods demonstrating palmar abduction/adduction (left) and radial abduction/adduction (right). Vectors for range of CMC abduction/adduction angles are shown in yellow and the black arrow shows the angle between the two vectors.

right). Marker locations used for vector analysis are shown in Figure 2. The angle between the two vectors was calculated using Eq 1.

$$\theta = \cos^{-1}\left(\frac{v1 \cdot v2}{|v1||v2|}\right) \qquad \text{Eq 1.}$$

RESULTS AND DISCUSSION

The average ranges of motion for thumb CMC radial and palmar abduction/adduction were 13º±5º and 11º±2º, respectively.

Table 1: Maximum, minimum, range and average values of thumb CMC palmar and radial abduction/adduction

Subject	Palmar abduction/adduction thumb CMC Angle (deg)			Radial abduction/adduction thumb CMC Angle (deg)		
	Max	Min	Range	Max	Min	Range
1	45	34	10	47	36	11
2	42	30	12	45	32	13
3	40	29	11	45	34	11
4	50	37	14	56	34	22
5	39	31	8	40	34	6
Average	43±4	21±3	11±2	46±5	34±1	13±5

Figures 3 and 4 show radial and palmar abduction/adduction, respectively, for a single participant. Radial abduction/adduction had a greater range of motion than palmar for all participants.

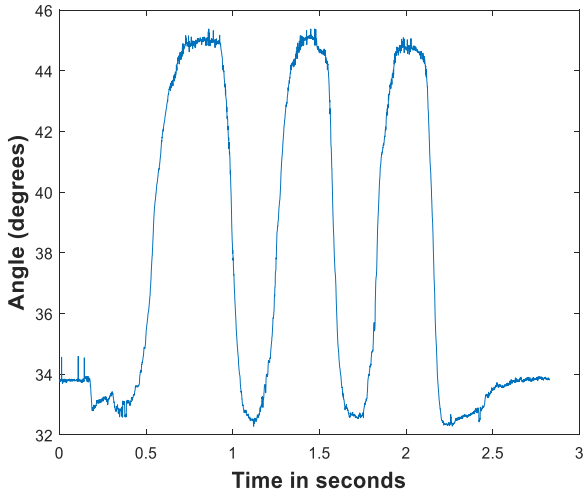

Figure 3: Range of motion of the thumb CMC joint during radial abduction/adduction. Peak maximum and minimum values were used to calculate the range.

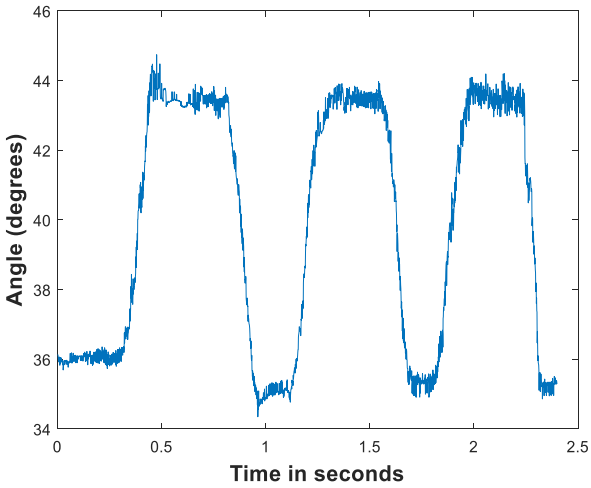

Figure 4: Range of motion of the thumb CMC joint during palmar abduction/adduction. Peak maximum and minimum values were used to calculate the range.

However, people with thumb OA typically have limited or a reduction in range of motion of palmar abduction/adduction, which significantly impacts a person's ability to execute certain activities of daily living, such as gripping and grasping tasks.

CONCLUSION

This research provides information on how healthy thumbs function. Understanding healthy function is important when monitoring treatment effects or designing therapies. Our future goals include testing participants with thumb CMC OA. Data from the healthy and arthritic groups will be compared to determine differences in kinematic motions and help improve treatment protocols.

REFERENCES

[1] Dias, R., et al. *Postgrad Med J*. 40–43, 2007.

ACKNOWLEDGEMENTS

This work is funded by the Spectrum Health – Michigan State University Alliance Grant.

UNDERSTANDING HEAD MOVEMENT AND SHOULDER ROUNDING IN SEATED AND STANDING POSTURES

[1]Archana Lamsal (Presenter) [1]Sloan Kanat, [1]Katharine Walters, [2]Teresa Bellingar, PhD, and [1]Tamara Reid Bush, PhD

[1]Michigan State University East Lansing, MI, USA

[2]Haworth, Holland, MI, USA

Email: lamsalar@msu.edu, reidtama@msu.edu,

INTRODUCTION

Being sedentary for long periods of time and poor postures are two of the biggest health issues for office workers. Sedentary positions have been linked to various cardiovascular and metabolic diseases [1]. Poor posture during office work has also been shown to cause pain and musculoskeletal disorders of various body parts, including the neck and back [2,3]. Although shoulder rounding, head tilting and head rotation are believed to be linked to neck pain and postural deformities, little quantitative data on these movements are available. The goal of this study was to analyze how head rotation, head tilt, and shoulder rounding are affected by typing and using a mouse (called mousing) in seated and standing postures.

METHODS

Thirty consenting adults (15 males and 15 females) participated in this study (IRB 3325). A motion capture system and reflective markers attached on anatomical landmarks (Figure 1) were used to gather kinematic data. The participants conducted computer tasks in a seated posture for one hour, followed by a standing posture for 30 minutes. While in both positions, participants alternated between typing and mousing tasks every 15 minutes. Prior to the start of testing, all equipment was set at the lowest height setting, forcing participants to adjust the chair and desk height to their comfortable position before starting. Marker position data were collected for the entire testing period.

After the completion of both tasks, individuals were positioned into a reference ergonomic position in both seated and standing postures [4]. In the seated posture, the ankle, knee, thigh-to-torso and elbow angles were at 90 degrees. In the standing posture, the ankle and elbow angles were at 90 degrees, and the knee and torso angles were 180 degrees. Additionally, the top edge of the monitor was aligned with eye height. This ergonomic position was used as a baseline comparator for the motion data.

The shoulder rounding angle was defined as the angle between the vectors formed by the seventh cervical vertebra and the top of the glenohumeral joint on each side (Fig 1a).

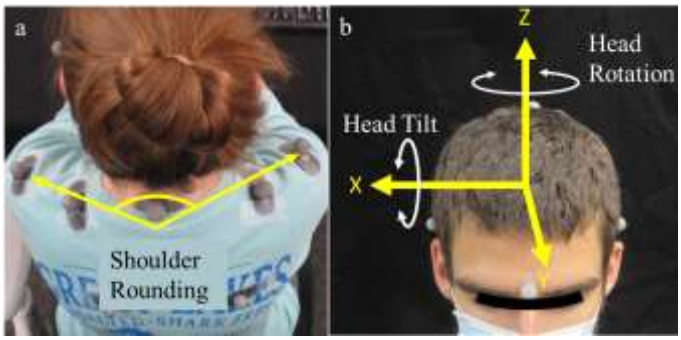

Figure 1: (a) shoulder rounding angle was calculated using markers on seventh cervical vertebra (C7) and glenohumeral joint on either side of the shoulder. (b) head tilt (rotation about X) and head rotation (rotation about Z) were calculated with respect to the local co-ordinate system created on the head using four markers shown (crown of the head, glabella, left and right posterior temples-just above the ears).

A local coordinate system was created in the head, as defined in Fig 1b. A rotation matrix was created, and Euler angles were used to calculate head tilt and head

rotation. The head tilt was defined as the rotation in the sagittal plane (about the X-axis) and head rotation was defined as the rotation about transverse plane (about the Z-axis).

The ranges of the shoulder rounding angle, head tilt and head rotation were calculated for both sitting and standing postures. Head tilt and head rotation are presented as the maximum movement in up/down, left/right direction whereas the range of shoulder rounding is presented as the difference of maximum and minimum values. To calculate the average deviation of the angles, the average angle over the entire time while typing/mousing in each posture was calculated. The magnitude of difference between the angles in reference ergonomic posture and the averages are reported as deviation of the angles from reference posture.

RESULTS AND DISCUSSION

The range of shoulder rounding was larger in the seated posture than while standing. Increased ranges of head rotation also occurred while seated (Fig. 2a).

When comparisons of average angles were made to the reference posture, again, more shoulder rounding occurred while seated than standing (Figure 2b). This suggests that a more upright posture was maintained while in the standing position. A previous study showed increased slouching in the seated posture compared to standing, and the results of this study support that previous finding [5].

The difference between the average and reference for forward head tilt was similar for seated and standing postures during the typing task, but the deviation was larger in the seated posture for the mousing task.

CONCLUSION

The angular range of shoulder rounding, head rotation and head tilt were largest while seated and conducting the mousing tasks. The largest deviation from the ergonomic position was found in the seated position for shoulder rounding and for head tilt, however head rotations deviated more while standing. The results of this work provide important information regarding the natural movements that occur during different types of office tasks. These findings can be used to design office systems that not only allow but encourage healthy motions while discouraging movements that have been shown to cause injury and pain.

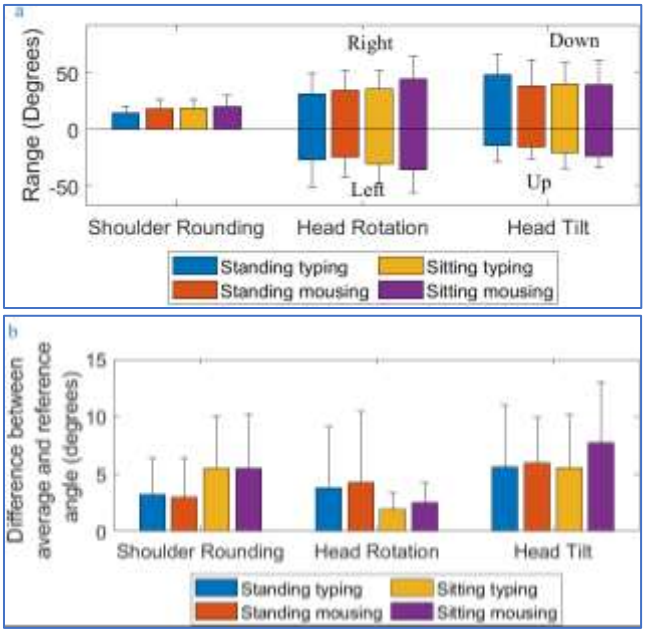

Figure 2: (a) The range of angles during typing and mousing tasks in seated and standing postures. Shoulder rounding is presented as the difference of maximum and minimum angle whereas head rotation and head tilt are presented as maximum value in left/right, up/down direction. (b) The difference between average and reference angle during typing and mousing tasks in seated and standing postures. Both charts indicate that largest movement occurred during mousing task in the seated posture.

REFERENCES

1. Hamilton MT, et al., Diabetes, 2007
2. Lou, E., et al., Med and Bio Eng Comput, 2012
3. Cagnie, B., et al., European Spine Journal, 2007
4. OSHA,https://www.osha.gov/etools/computer-workstations/positions
5. Lamsal A., et al., ASB, 2020

ACKNOWLEDGEMENTS

Financial support for this research was provided by Haworth Inc.

MODELING HUMAN ARM CONFIGURATION HOLDING A TENNIS RACKET USING A 2-DIMENSIONAL 4-SEGMENTS COUPLED PENDULUM SYSTEM

[1]Loay Al-Zube (Presenter)

[1]University of Mount Union, Alliance, OH, USA

Email: alzubelo@mountunion.edu

INTRODUCTION

Human motion analysis and modeling using mathematics, coupled with theoretical concepts in physiology and mechanics is constantly expanding and becoming more and more important in human performance and rehabilitation studies.

Mathematical description helps us understand and quantify the physical upper and lower extremities disability. Furthermore, mathematical models provide a framework to design and quantify the best training strategies and motor tasks to find optimal movement patterns that can prevent injury and improve performance.

To test the hypotheses that an arm and tennis racket configuration can be modeled using a 2-dimensional representation of 4 segments coupled pendulum system, a mathematical model of human arm configuration holding a tennis racket was developed along with constructing the equations of motions for this model using the energy (work) based approach of Lagrange.

METHODS

The human arm holding a tennis racket was idealized as a 2-dimensional four segments coupled pendulum system where the branching pattern of those segments is shown in Figure (1) with four mass points one on each segment. The connected pattern corresponds to an acyclic graph and that one segment is anchored to the origin of the coordinate system Point (A), the player shoulder.

The relation matrix [R] (Equation 1) shows the relationship of connection between segments of the system, where each row of [R] represents a point mass of the system, and has the information about the path from the origin (A) of the system to the point mass. Each column represents a segment, and has the information about the usage of the segment for every path to point masses.

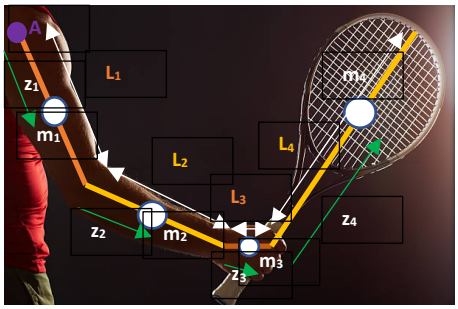

Figure 1: Arm segments (L_1, L_2, L_3, & L_4) and mass distributions (m's & z's).

$$R = \begin{bmatrix} z_1 & 0 & 0 & 0 \\ L_1 & z_2 & 0 & 0 \\ L_1 & L_2 & z_3 & 0 \\ L_1 & L_2 & L_3 & z_4 \end{bmatrix} \cdots\cdots\cdots (1)$$

The energy (work) - based approach of Lagrange was used to formulate the equations of motion of the suggested mechanical system. Since the choices of independent dynamic variables are position only, then the equations of motion that are formulated are of second order.

The energy (Work) – based approach of Lagrange is based on the difference between the kinetic and potential energy of the system. More precisely the Lagrangian function (L) is defined as:

$$L = K - P \cdots\cdots\cdots (2)$$

Where, (K) represents the kinetic energy and (P) represents the potential energy

Using the above equation of Lagrangian function, the i^{th} equation of motion corresponding to the i^{th} degree of freedom takes the form found in Equation (3):

$$\frac{d}{dt}\left(\frac{\partial L}{\partial \dot{\theta}_i}\right)-\frac{\partial L}{\partial \theta_i}=0 \quad \text{..... (3)}$$

In the suggested model, i = 1, 2, 3, 4 according to 4 segments used, and (θ_i) represents the segment angle with the vertical axis viewing the segments from the lateral view.

$$\frac{d}{dt}\left(\frac{\partial L}{\partial \dot{\theta}_1}\right)-\frac{\partial L}{\partial \theta_1}=0 \cdots\cdots\cdots \text{(4)}$$

$$\frac{d}{dt}\left(\frac{\partial L}{\partial \dot{\theta}_2}\right)-\frac{\partial L}{\partial \theta_2}=0 \cdots\cdots\cdots \text{(5)}$$

$$\frac{d}{dt}\left(\frac{\partial L}{\partial \dot{\theta}_3}\right)-\frac{\partial L}{\partial \theta_3}=0 \cdots\cdots\cdots \text{(6)}$$

$$\frac{d}{dt}\left(\frac{\partial L}{\partial \dot{\theta}_4}\right)-\frac{\partial L}{\partial \theta_4}=0 \cdots\cdots\cdots \text{(7)}$$

The kinetic and potential energies of the system are found according to Equations (8) and (9), respectively:

$$K=\frac{1}{2}\sum_{i=1}^{3} m_i(\dot{x}_i{}^2+\dot{y}_i{}^2) \cdots\cdots\cdots (8)$$

$$P=\sum_{i=1}^{3} g m_i y_i \cdots\cdots\cdots (9)$$

RESULTS AND DISCUSSION

The following Lagrangian function (L) was obtained after substituting the formulated kinetic and potential energies of the 2-dimensional 4 segments coupled pendulum system.

$$\begin{aligned}L=&\frac{1}{2}\dot{\theta}_1^2(m_1z_1{}^2+m_2L_1{}^2+m_3L_1{}^2+m_4L_1{}^2)+\frac{1}{2}\dot{\theta}_2^2(m_2z_2{}^2+m_3L_2{}^2+m_4L_2{}^2)+\frac{1}{2}\dot{\theta}_3^2(m_3z_3{}^2+m_4L_3{}^2)+\frac{1}{2}\dot{\theta}_4^2(m_4z_4{}^2)\\&+\dot{\theta}_1\dot{\theta}_2\cos(\theta_1-\theta_2)(m_2z_2L_1+m_3L_1L_2+m_4L_1L_2)+\dot{\theta}_1\dot{\theta}_3\cos(\theta_1-\theta_3)(m_3z_3L_1+m_4L_1L_3)+\dot{\theta}_1\dot{\theta}_4\cos(\theta_1-\theta_4)(m_4z_4L_1)\\&+\dot{\theta}_2\dot{\theta}_3\cos(\theta_2-\theta_3)(m_3z_3L_2)+\dot{\theta}_2\dot{\theta}_4\cos(\theta_2-\theta_4)(m_4z_4L_2)+\dot{\theta}_3\dot{\theta}_4\cos(\theta_3-\theta_4)(m_4z_4L_3)\\&-g\cos\theta_1(m_1z_1+m_2L_1+m_3L_1+m_4L_1)-g\cos\theta_2(m_2z_2+m_3L_2+m_4L_2)-g\cos\theta_3(m_3z_3+m_4L_3)-g\cos\theta_4(m_4z_4)\end{aligned}$$

After evaluating equations (4), (5), (6) and (7), equations (11), (12), (13) and (14) were found respectively (Table 1), which represent the system of equations that is used to solve for the trajectories of motion and the angular velocities needed to produce them.

Table 1: The equations of motion for a 2-dimensional arm and racket model consisting a 4-segments coupled pendulum system

$\ddot{\theta}_1(m_1z_1{}^2+m_2L_1{}^2+m_3L_1{}^2+m_4L_1{}^2)+\ddot{\theta}_2(m_2L_1z_2+m_3L_1L_2+m_4L_1L_2)\cos(\theta_1-\theta_2)$ $+\ddot{\theta}_3(m_3L_1z_3+m_4L_1L_3)\cos(\theta_1-\theta_3)+\ddot{\theta}_4(m_4L_1z_4)\cos(\theta_1-\theta_4)=g\sin\theta_1(m_1z_1+m_2L_1+m_3L_1+m_4L_1)$ $-\dot{\theta}_2^2(m_2L_1z_2+m_3L_1L_2+m_4L_1L_2)\sin(\theta_1-\theta_2)-\dot{\theta}_3^2(m_3L_1z_3+m_4L_1L_2)\sin(\theta_1-\theta_3)$ $-\dot{\theta}_4^2(m_4L_1z_4)\sin(\theta_1-\theta_4)$	11
$\ddot{\theta}_2(m_2z_2{}^2+m_3L_2{}^2+m_4L_2{}^2+m_4L_3{}^2)+\ddot{\theta}_1(m_2L_1z_2+m_3L_1L_2+m_4L_1L_2)\cos(\theta_1-\theta_2)$ $+\ddot{\theta}_3(m_3L_2z_3+m_4L_2L_3)\cos(\theta_2-\theta_3)+\ddot{\theta}_4(m_4L_1z_4)\cos(\theta_2-\theta_4)=g\sin\theta_2(m_2z_2+m_3L_2+m_4L_2)$ $-\dot{\theta}_1^2(m_2L_1z_2+m_3L_1L_2+m_4L_1L_2)\sin(\theta_1-\theta_2)-\dot{\theta}_3^2(m_3L_2z_3+m_4L_2L_3)\sin(\theta_2-\theta_3)$ $-\dot{\theta}_4^2(m_4L_1z_4)\sin(\theta_2-\theta_4)$	12
$\ddot{\theta}_3m_3z_3{}^2+\ddot{\theta}_1(m_3L_1z_3+m_4L_1L_3)\cos(\theta_1-\theta_3)+\ddot{\theta}_4(m_4L_3z_3)\cos(\theta_3-\theta_4)+\ddot{\theta}_2(m_3L_2z_3)\cos(\theta_2-\theta_3)=g\sin\theta_3(m_3z_3+m_4L_3)$ $-\dot{\theta}_1^2(m_3L_1z_3+m_4L_1L_3)\sin(\theta_1-\theta_3)-\dot{\theta}_2^2(m_3L_2z_3)\sin(\theta_2-\theta_3)$ $-\dot{\theta}_4^2(m_4L_3z_4)\sin(\theta_3-\theta_4)$	13
$\ddot{\theta}_4(m_4z_4{}^2)+\ddot{\theta}_1(m_4L_1z_4)\cos(\theta_1-\theta_4)$ $+\ddot{\theta}_3(m_4L_3z_4)\cos(\theta_3-\theta_4)+\ddot{\theta}_2(m_4L_2z_4)\cos(\theta_2-\theta_4)=g\sin\theta_4(m_4z_4)$ $-\dot{\theta}_1^2(m_4L_1z_4)\sin(\theta_1-\theta_4)-\dot{\theta}_2^2(m_4L_2z_4)\sin(\theta_2-\theta_4)$ $-\dot{\theta}_3^2(m_4L_3z_4)\sin(\theta_3-\theta_4)$	14

It was hypothesized that an arm and tennis racket configuration can be modeled using a 2-dimensional representation of a 4-segments coupled pendulum system. We were able to show that such system can be constructed. More research is currently being done to determine if the system is stable and solvable with the condition of selecting the appropriate set of dynamical variables and initial and boundary conditions.

CONCLUSION

The equations of motion for a 2-dimensional 4-segments coupled pendulum system were derived. To the best of my knowledge, this is the first study to investigate the use energy-based approach in constructing the equations of motion of an arm configuration holding a tennis racket.

DETERMINATION OF L5/S1 LOADS DURING LIFTING USING A SIMPLIFIED CONSERVATIVE MODEL

[1,2]Harper Calhoun, [1,2]Lauren Eichaker, [2]Cameron Trepeck, [2]Dawn Freyder, [2]Douglas Morr

[1]The Ohio State University, Columbus, Ohio, USA

[2]SEA, Ltd., Columbus, OH, USA

Email: hcalhoun@sealimited.com

INTRODUCTION

The ability to estimate the forces and accelerations the human body experiences during activities of daily living is important for the analysis and design of new devices. For example, in the field of rehabilitation engineering, the position in which a device orients an individual is important because the range of abilities may be limited. Additionally, in the general population it is known that repetitive loading, including that sustained during activities of daily living, can result in chronic pathological conditions. The ability to equate these activities to quantitative, yet conservative values can provide engineers with suitable estimates that influence that design process.

Furthermore, being able to utilize a simplified, conservative model is useful in the educational process; students may estimate the loading on the human body as part of biomechanics education and the product design process. Hand calculations may be used as starting points for computational modeling, injury assessment reference value, and kinematic description considerations [1].

The relevance and validity of such a simplified model is important for carrying over this knowledge from the design process into physical prototyping. This work describes the comparison of a simplified, rigid anatomy model in a squatting scenario to literature values derived from more complicated methods [2-5].

METHODS

The height (5 foot, 9 inches) and weight (About 177 lbs) of a Hybrid III, 50th percentile male anthropomorphic test device will be used for demonstrative purposes. When lifting an object from the ground in the sagittal plane, the moments and forces depend upon the lifting mechanics utilized. The highest joint loading occurs when lifting while simply bending at the waist, while the lowest occurs when in a squat (bent knee) position. Calculations were made relative to the L5-S1 joint for compressive forces. The initial conditions for the model are presented in Table 1.

Table 1: Initial conditions for calculations.

Variable	Value	Description
g_c	32.2 ft/s^2	Acceleration of gravity
r_{cg_eff}	14 inches	Approximate moment arm from effective center of gravity of upper body to L5/S1
r_{muscle_eff}	3 inches	Effective moment arm of posterior lumbar muscles
r_{object}	20 inches	Effective moment arm from center of gravity of object to L5/S1
W_{2_mst}	177 lbs	Estimated weight of Hybrid III male
W_{object}	11-27 kg 24-59 lbs	Weight of object
M_{2mst_up}	$0.6*(W_{2\_mst}/g_c)$	Mass of the upper body portion of the Hybrid III male
θ_{lift_bent}	$90*(\pi/180)$ degrees	Back angle for lifting by bending over
θ_{lift_squat}	$45*(\pi/180)$ degrees	Back angle for lifting from squat position

Eq. 1-2 and Eq. 3-4 show the moment and force equations used in the conservative rigid model respectively.

(Equation 1)

$$M_{L5\_lift1\_mst} = \frac{r_{cg\_eff}}{12} * M_{2mst_{up}} * g_c * \sin(\Theta_{lift\_bent}) + \frac{r_{object}}{12} * W_{object} * \sin(\Theta_{lift\_bent})$$

(Equation 2)

$$M_{L5\_lift2\_mst} = \frac{r_{cg\_eff}}{12} * M_{2mst_{up}} * g_c * \sin\left(\Theta_{lift\_squat}\right) + \frac{r_{object}}{12} * W_{object} * \sin(\Theta_{lift\_squat})$$

(Equation 3)

$$F_{L5\_C\_lift1\_mst} = M_{2mst_{up}} * g_c * \cos\left(\Theta_{lift\_bent}\right) + W_{object} * \cos(\Theta_{lift\_bent}) + \frac{12M_{L5\_lift2\_mst}}{r_{muscle\_eff}}$$

(Equation 4)

$$F_{L5\_C\_lift2\_mst} = M_{2mst_{up}} * g_c * \cos\left(\Theta_{lift\_squat}\right) + W_{object} * \cos\left(\Theta_{lift\_squat}\right) + \frac{12M_{L5\_lift2\_mst}}{r_{muscle\_eff}}$$

The resultant force outputs over the range given in Table 1 were compared to values from the literature [2-5] to validate the conservative estimates using a 1-sample t-test with α=0.05.

RESULTS AND DISCUSSION

The simplified rigid anatomy model provided values between 2.5 kN and 3.8 kN of compression at L5-S1 during squatting using mass values from 11 kg to 27 kg. Literature values from 4 separate studies employing comparable conditions ranged from 2.3 kN to 4.0 kN at L5-S1 for similar mass values [2-5]. The literature values were not statistically different from the computed results using this simplified analysis technique (P>0.8) (Fig. 1).

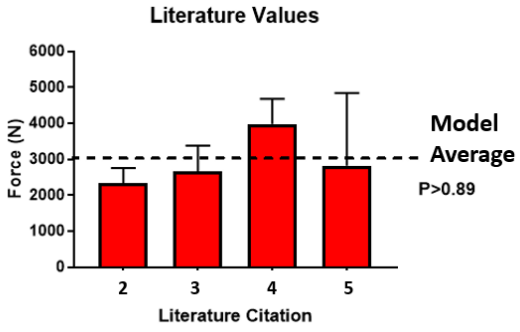

Figure 1: Graphical depiction of literature values compared to average output of simplified model.

Additional data to be presented at the conference.

CONCLUSION

A simplified rigid anatomy model can be used reliably to estimate loads within the lumbar spine.

REFERENCES

1. Hall, S. *Basic Biomechanics*. 6th ed., McGraw-Hill, 2012.

2. Gomez, L, et al. *Dynamic analysis of forces in the lumbar spine during bag carrying.* Int J Occup Safe and Ergo, 2018;24: 605-613.

3. Kermit, D, et al. *Evaluation of spinal loading during lowering and lifting.* Clin Biomech. 1998;13:141-152.

4. Kingma, I, et al. *Can Low Back Loading During Lifting Be Reduced by Placing One Leg Beside the Object to Be Lifted?* Phys Therap, 2006;86:1091-1105.

5. Marras, W, et al. *Spine Loading Characteristics of Patients with Low Back Pain Compared with Asymptomatic Individuals.* Spine, 2001;26:2566-2574.

APPLICATION OF ARTIFICIAL NEURAL NETWORKS IN ESTIMATING GROUND REACTION FORCES USING INERTIAL DATA OF THE LOWER BODY

Kenneth Munyuza, Trevor Palmatier, Bridget Gagnier, Reese Moschetta, Yea Geon Song, Brooke Odle, Omofolakunmi Olagbemi

Hope College, Holland, MI, USA

Email: olagbemi@hope.edu

INTRODUCTION

Manual patient-handling tasks have been associated with low-back pain and injury in caregivers, like nurses. Although camera-based marker systems can be used within research laboratory settings to further explore mechanisms of injury during these tasks, the expanded use of IMUs in biomechanics enables data collection in the laboratory as well as clinical settings. IMU-based capture systems are also advantageous to camera-based marker systems because they avoid marker occlusion during more complicated patient-handling tasks. However, the force plates which are used for measuring the ground reaction forces (GRFs) are not as amenable to being transported back and forth for collection of required data outside of the lab. Pressure insoles may be used, but they are bulky and require extra instrumentation, which may not be ideal for data collection in clinical settings. Recently, biomechanists have explored machine learning techniques to estimate GRFs. In [1], Wouda et al applied machine learning techniques in the estimation of vertical ground reaction forces during running to overcome the limitation of being confined to a gait laboratory while performing analysis of running mechanics. Similarly, Matijevich et al in [2] applied machine learning techniques in the estimation of tibial bone force and damage during running. The objective of this proof-of-concept study is to develop and validate an artificial neural network (ANN) that estimates the ground reaction forces exerted while participants perform tasks and motions that simulate those that might be performed by a caregiver performing patient-handling tasks.

Table 1: Tasks performed and their categories.

Category of Task	Task Name
Squatting	Squats
	Squat Curls
Leaning	Lean
	Shift
	Twist
Lifting	Arm Curls
	Left Arm Raise
	Right Arm Raise
	Row
	Reach

METHODS

For our preliminary model, data was collected from two 21-year-old, able-bodied male volunteers who were fitted with 7 IMU devices on the pelvis, upper and lower legs, and feet. They then performed 10 different squatting, lifting, and leaning tasks while standing on two force plates placed side by side, with a foot on each force plate.

Table 1 provides details of the respective categories and tasks. For each of the 10 tasks, 10 trials were performed, with 10 repetitions per trial. The data was filtered using a fourth-order Butterworth filter with a 10Hz cutoff frequency. The force plate data was down-sampled from its native 1000Hz sampling rate to the 100Hz sampling rate of the IMUs. Then 500 samples were taken from every trial for each participant, resulting in a total of 100,000 samples from both participants.

Each of the 7 IMUs placed on the participants provided 7 data items resulting in a total of 49 position and orientation data items. These served as inputs to the ANN. Each of the two force plates provided 5 data items (giving a total of 10) which were the outputs from the ANN. The ANN was first constructed using TensorFlow with a normalization layer and two hidden layers which had 98 and 49 neurons respectively. After training and evaluating the performance of this model, a second ANN was constructed with a normalization layer and four hidden layers which had 196, 147, 98, and 49 neurons respectively. Both models used ***Glorot Uniform*** for weight initialization, ***ReLU*** as the activation function, ***Adam*** for the learning function, and ***Huber*** for the loss function. Each model was trained on 64% of the data, with a separate 16% used as a validation set. The remaining 20% of the data (which were not used in training the model) were used to test the performance of the ANN.

RESULTS AND DISCUSSION

Training and evaluating our preliminary model demonstrated a good fit between ANN-estimated GRFs and corresponding GRF values measured by force plates. The model with two hidden layers achieved a model score of 0.8633 (where the model scores range from 0 to 1, with 1 indicating perfect estimation accuracy). The average loss for this model was 5.065. The second model with four hidden layers achieved a model score of 0.9263, with an average loss of 2.912. The second model achieved a higher model score with a lower loss value than the first model, indicating that it performed better at estimating the ground reaction forces than the first model. These results demonstrate that the deeper model (one with more hidden layers) provided more accurate estimates. These results are encouraging and motivate further exploration. We therefore plan to obtain additional data from a more diverse range of participants and include these in training the ANN with the hope of obtaining an ANN that can generalize more accurately when estimating ground reaction forces (as opposed to being too closely fitted to data from just a few participants). Future work will also investigate dynamic simulations of manual patient-handling tasks with musculoskeletal models, the experimental IMU signals, and the estimated/predicted GRFs from the machine learning algorithm. Combined with electromyography, this may provide insight on low back loads applied to caregivers while performing manual patient-handling tasks.

CONCLUSION

Preliminary ANNs that estimate GRFs with an acceptable level of accuracy when provided with IMU input data were developed. Future work will seek to enhance the generality of the ANN by training it on data obtained from a higher number of participants. We are also considering creating task specific ANNs and evaluating their performances when compared to the more generalized non-task-specific ANN.

REFERENCES

1. Wouda, F. J. et al. *Estimation of Vertical Ground Reaction Forces and Sagittal Knee Kinematics During Running Using Three Inertial Sensors*. Frontiers in Physiology, 9.218, 2018.

2. Matijevich, E. S. et al. *Combining wearable sensor signals, machine learning and biomechanics to estimate tibial bone force and damage during running*. Human Movement Science, 74 (2020) 102690.

ACKNOWLEDGEMENTS

This work is funded by the Dean of Natural and Applied Science and the Department of Computer Science, both of Hope College.

EEG Analysis of Referred Sensations Caused by Electrical Stimulation for Treatment of Phantom Limb Pain

[1]Grace VanDellen, [1]Peter Ruffolo, and [1]Katharine Polasek

[1]Hope College, Holland, MI, USA

Email: polasek@hope.edu

INTRODUCTION

Phantom limb pain is experienced by more than 80% of amputees. It is a painful sensation felt in the amputated limb. Current treatments include medication, surgeries, and invasive stimulation. Each of these treatments can be expensive and have negative side effects.

Targeted surface electrical stimulation is being investigated as a potential treatment option for phantom limb pain. Electrical stimulation has been shown to evoke hand sensation from electrodes placed at the elbow (referred sensation) [1]. Different techniques have been investigated and it was found the pulse trains at 1 to4 Hz produced a tapping sensation in most subjects [2].

The overall goal of this research is to investigate cortical changes due to treating phantom limb pain using electrical stimulation. The goal of this project was to look at cortical responses to touch in different locations in able-bodied individuals and compare those to sensations evoked using electrical stimulation.

METHODS

Thirteen subjects between the ages of 18 and 65 were recruited from the Hope College community. Informed consent was received from each subject. A 96 electrode EEG cap was used to record cortical activation during trials consisting of physical or electrically evoked sensations.

Prior to stimulation trials, the voltage was slowly increased to estimate threshold and maximum comfortable stimulation levels. A 2Hz frequency pulsetrain was then sent at 5V below the maximum voltage while the electrodes were adjusted in order to evoke a referred sensation in the subject's hand. A larger stimulation voltage targeted the nerve and caused sensation in the subject's hand (deep stimulation). A smaller voltage was sent that the subject only felt under the electrodes (skin stimulation). The frequency of the pulses was random but between 1 and 3 Hz. For the entire trial, the subject's hand was blocked from view and the subject was reading.

Following the stimulation trials, the subject underwent a series of tapping trials using Arduino programmed solenoids. The solenoids were placed over 4 hand locations, the thumb, the index finger, the ring finger, and a match location corresponding to where the subject felt the sensation during stimulation. Trials were performed with the subject watching their hand as it was being tapped and when the subject's hand was blocked from view and they were reading.

EEG data was collected during all sessions. The data was then filtered and plotted in Matlab. The correlation between the different trials was determined to compare stimulation of touch to actual touch.

RESULTS AND DISCUSSION

Looking at the results of the R-values for the 13 different subjects, four gave results showing a correlation between the deep stimulation and the tapping of the match location. Table 1 shows the R-value for these correlations for all 13 subjects. In nine of the 13 subjects, the highest correction with the deep stimulation was the skin stimulation. This would be expected because both stimulations are

being sent through the electrodes at the same location on the subject's elbow. For subjects 2139 and 2142 the second highest correlation was seen with the match location. The deep stimulation having a high correlation with match location shows that the subject's brain is responding in a similar way to the referred sensation as it is to the actual tapping of the finger. Subjects 2143 and 2146 had their correlation with the match location be one of the greatest R-values. These four subjects that had higher correlation values with the deep stimulation and match location show that it is possible for the brain to respond in a similar manner to the deep stimulation as actual tapping.

Table 1: R-values for all subjects showing the R-value for the correlation of the deep stimulation to the surface stimulation and match location.

	2139	2140	2141	2142	2143	2144	2145	2146	2147	2148	2149	2150	2151
Surface Stim	0.96	-0.1	-0.04	0.33	0.89	-0.11	0.09	0.33	0.17	0.01	0.19	0.24	0.27
Match Location	0.62	0.2	0.22	0.15	0.54	-0.07	0.07	0.3	-0.07	0.05	0.05	-0.09	-0.06

The quality of the deep stimulation sensation will determine the brain's response to the stimulation. Low correlation could be the result of the subject not feeling the sensation in their hand. Subjects have reported feeling the referred tapping sensation at the beginning of the trial but by the end the sensation is no longer present. Without the sensation the brain would not respond as if the hand is being tapped, causing a low correlation with the brain's response to actual tapping.

CONCLUSION

The brain's response to electrical stimulation producing a referred sensation can produce a similar response to the brain's response to tapping on the location of the referred sensation. The high correlation R-values between the deep stimulation and match location tapping show that the brain is responding in a similar way to the referred sensation of tapping as it is to the physical tapping of a finger. This project is ongoing and the future work will include similar experiments conducted on an amputee in order to see if the brain's response to stimulation and tapping of the prosthetic changes over time.

REFERENCES

[1] J. C. Forst *et al.*, "Surface electrical stimulation to evoke referred sensation," *J. Rehabil. Res. Dev.*, vol. 52, no. 4, 2015.

[2] J. P. Slopsema *et al.*, "Natural Sensations Evoked in Distal Extremities Using Surface Electrical Stimulation," *Open Biomed. Eng. J.*, vol. 12, no. 1, pp. 1–15, 2018.

ACKNOWLEDGEMENTS

This material is based upon work supported by the National Science Foundation under Grant No. 1805447.

The Viability of In-Shoe Insoles to Measure Pressure and Shear in Patients with Charcot Arthropathy

[1]Jessi Martin, [1]Brian Davis, [2]Grant McMillan, and [2]Larry Goss
[1]Cleveland State University, Cleveland, OH, USA
[2]Innovative Scientific Solutions Inc., Dayton, OH, USA
Email: j.k.martin42@vikes.csuohio.edu

INTRODUCTION

Peripheral neuropathy is a condition that occurs as a complication of diabetes mellitus due to prolonged periods of elevated blood glucose. It has been demonstrated that peripheral neuropathy disrupts the sensory, autonomic, and motor systems. Clinical symptoms of peripheral neuropathy can include Muscle weakness, numbness, lack of coordination, and pain.

Charcot arthropathy can develop when an injury occurs in a patient with peripheral neuropathy. Repeated loading on this injury creates an inflammatory response and eventual bone resorption. If left untreated, this disease can progress to the collapse of the medial arch. Once the longitudinal arch has collapsed, high-pressure concentrations can occur due to abnormal loading at the sites of protrusions from misaligned bones. If left untreated, these pressure concentrations can result in ulceration, infection, and subsequent limb loss. At this stage, the only treatment option is surgical intervention.

To date, about 60% of surgical implants used in the correction surgery for Charcot Arthropathy fail. The failure can be attributed to the unnatural loading of the implants. The foot contains a complex load-sharing system between the bones, muscles, tendons, nervous system, and cardiovascular system. All the above systems are disrupted in Charcot neuroarthropathy. When implants are utilized, they are prone to failure as they are not designed to handle the entire load in the foot. Ergo, the best treatment for Charcot arthropathy is prevention and early detection before the foot collapses.

Davis et al.[1] showed that in neuropathic patients, the difference in shear between the 1st metatarsal and the heel increases when the arch is collapsing. The limitations in their approach is that patients must walk across a stationary platform. To be able to truly detect early signs of arch collapse in patients with Charcot arthropathy, an in-shoe insole would be a preferred solution. This abstract assesses the viability of the use of in-shoe insoles to measure pressure and shear as compared to the over-ground shear-measuring platform.

METHODS

Ten healthy participants were recruited for this study. Subject ages ranged from 20 to 42 years old. The average subject weight was 148.6 ± 20 lbs for women and 170.0 ± 11 lbs. These subjects had no history of lower-limb surgeries, history of diabetes mellitus, or possessed any illness that would alter their gait. The study was conducted in accordance with an IRB-approved protocol.

The two instrument systems used in this study were the shear platform utilized in Davis et al.[1] created by ISSI in Dayton, Ohio, and in-shoe insoles, also created by ISSI in Dayton, Ohio. Both the shear platform and the insoles measure shear and pressure.

The shear platform measures shear and pressure across the entire foot whereas the insoles measured pressure and shear from sensors placed under the heel, first metatarsal, and fifth metatarsal. The insoles were designed around a size 8 women's foot. The insoles are connected via Bluetooth to the

ISSI insoles website which collects data from the insoles and exports the data to an excel sheet.

Each participant took 1 step barefoot over the shear platform with one foot. The participant repeated this five times. Then, the participant placed the insoles in both shoes, barefoot, and took approximately 5-7 steps while the website was recording. These set of steps were repeated twice.

Pressure and shear data from each sensor (heel, first metatarsal, and lateral metatarsal) were analyzed using custom software. Shear values from the platform were extracted to match data from corresponding sensor locations in the insoles.

Since the data of interest corresponds to when the foot arch could be "collapsing" the focus was on data collected during the midstance of gait. Time intervals corresponding to when both the heel and metatarsal were registered on the plate/insoles were selected. To assess the shear ratio and accurately compare the platform to the insoles, the difference in anterior/posterior (a/p) shear for the first metatarsal and the heel were calculated and compared. The peak difference was then recorded.

RESULTS AND DISCUSSION

There was no significant difference in shear differences (1st MTH – heel) when comparing insole and overground data (Figure 1).

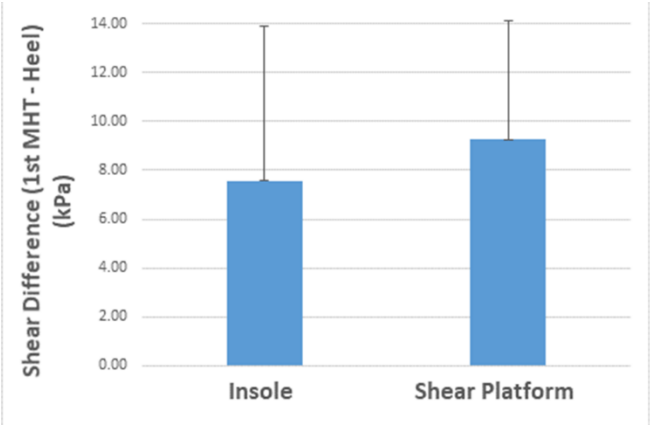

Figure 1: Shear Difference for the Insoles and the Shear Platform Between the 1st Metatarsal and the Heel

The peak shear difference for the insoles was approximately 7 kPa with standard deviation of approximately 7 kPa, whereas the peak shear difference for the shear platform was about 9 kPa with a standard deviation of approximately 5 kPa. There was therefore more variation in the difference measurements for the insoles compared to the shear platform. These differences can be attributed to the fact that the participants had varying shoe sizes, but only one insole size was used. Additionally, the a/p shear difference results for control subjects obtained in Davis et al.[1] were approximately about 5 times larger than the peak a/p shear difference from the insoles and approximately 4 times larger than the peak a/p shear differences from the platform.

These differences can be attributed to the difference in a/p shear calculation for the heel and 1st metatarsal. Davis et al.[1] calculated their a/p shear values using the first 50% of stance. This includes the events of heel strike until midstance. This study calculated a/p values using the period where both the heel and 1st metatarsal are on the ground. This excludes heel strike and toe-off.

CONCLUSION

The results indicate that in-shoe insoles are a viable option for measuring shear and pressure forces under the foot. Further studies should be conducted with diabetic neuropathic patients to assess the same viability at detection in disease state. Additionally, studies should be conducted to assess the interference of socks inside the insoles.

REFERENCES

[1] Davis B, Crow M, Berki V, Ciltea D. Shear and pressure under the first ray in neuropathic diabetic patients: Implications for support of the longitudinal arch. Journal of Biomechanics. 2017;52:176-178. doi:10.1016/j.jbiomech.2016.12.024

ACKNOWLEDGEMENTS

This work was supported by the National Institutes of Health.

3D PRINTING OF BIOMEDICAL IMPLANTS

[1]Sudeep Kumar Gummadi and Bharath Tej Challa, Prabaha sikder, PhD

Mechanical engineering department, Cleveland State University, Cleveland, OH, USA

Email: s.gummadi56@vikes.csuohio.edu

INTRODUCTION

Over the past few years, there have been significant advances in the development of advanced polymer materials. These materials have received attention for use as implants to aid regeneration of orthopaedic defects. Every year more than 3.1 million orthopaedic surgeries are performed in the United States alone [1]. However, although current treatments using nondegradable fixation materials have proven efficacious, tissue-engineering approaches with advanced polymer material are being considered as promising future alternatives. One possible advantage of these systems is that advanced polymer materials can be engineered to provide temporary support for bone fractures, and because they can degrade at a rate matching new tissue formation, their use can eliminate the need for a second surgery. Polyether-ether-ketone (PEEK) is a high strength semi crystalline thermoplastic and is one of the most common materials used for orthopaedic devices. PEEK is a promising biomaterial that could potentially be replaced with the metal or ceramic parts [3].

MATERIALS AND METHODS

Compared to other processing technologies for manufacturing PEEK parts, fused deposition modelling FDM method was applied to achieve 3D Printing of PEEK. Several FDM experiments were performed to study the effects of various printing parameters, including the printing temperature, printing speed, and layer thickness and mechanical properties, microstructure, and surface quality of printed PEEK parts. The parts manufactured from PEEK have excellent dimensional stability even under environments since changes in temperature and humidity has little impact on the deformation of PEEK.

The 3-D printer used for printing the PEEK was INTAMSYS FUNMAT HT and the filament diameter is 1.75 mm which is purchased from vision miner. The nozzle heating temperature (380℃-400℃) and the printing speed (40mm/s) were obtained through printing head. The slicing software for the printer which we use is INTAM SUITE. The layer thickness of 0.1 mm and initial layer thickness of 0.2 mm are used for printing. The designs of the implants were obtained from internet.

RESULTS AND DISCUSSIONS:

The fabrication results showed that the 3D printed PEEK was of a smooth finish without any irregularities. No black specks formations nor any

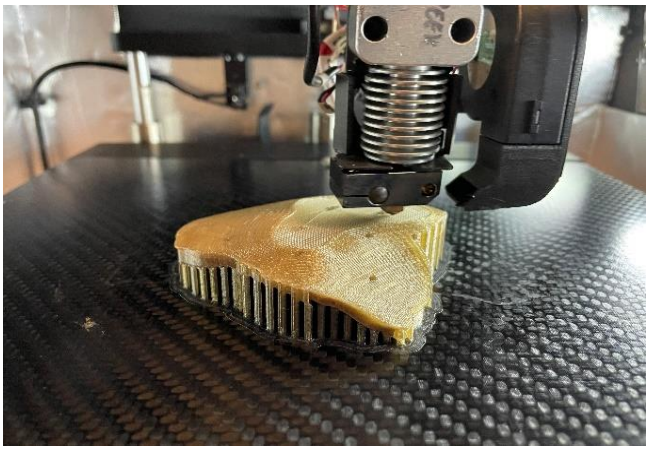

Fig.1: Craniofacial while printing.

discolorations were detected in parts. All the 3D printed parts were without any deformation. As, in **Fig.1** and **Fig.3** the printer is printing the craniofacial implant and Tibia implant with the help of support material. In **Fig.2** and **Fig.4** they were printed completely, and the support material was removed.

Fig.2: Craniofacial after printing.

Over the past few years PEEK has attracted a great deal of interest from scientists and orthopaedists. It is suitable for load bearing implants because of

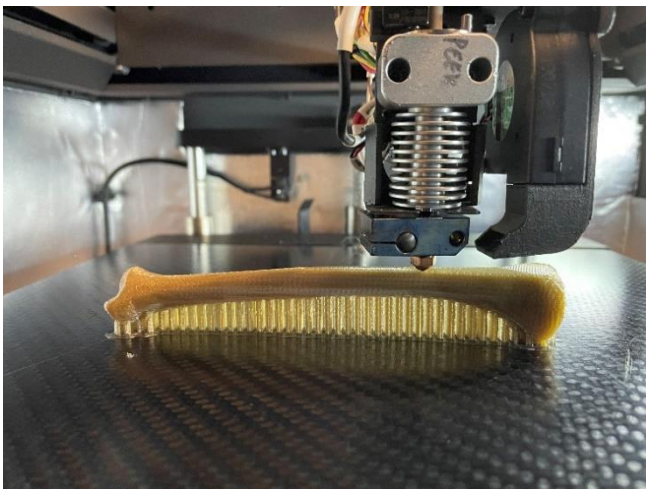

Fig.3: Tibia while printing.

favourable biomechanical properties, MRI compatibility, and chemical inertness. PEEK has primarily been used for interbody fusion cages and been used in combination with other materials such as carbon fibre PEEK [2]. PEEK is suitable biomaterial and an appropriate alloplastic material for reconstructive and orthopaedic surgeries.

Fig.4: Tibia after printing.

CONCLUSION:

Although we had some issue removing the support material from the implant, but we found some good techniques to remove them easily. It is also important to consider the maintenance of 3D printer time by time and the PEEK filament should always be placed inside the oven at 110℃ when it's not in use. In future we are planning to do more mechanical studies in various implants.

REFERENCES:

1.Honigmann, Philipp, et al. "Patient-specific surgical implants made of 3D printed PEEK: material, technology, and scope of surgical application." *BioMed research international* 2018 (2018).

2. Stepashkin, A. A., Chukov, D. I., Senatov, F. S., Salimon, A. I., Korsunsky, A. M., & Kaloshkin, S. D. (2018). 3D-printed PEEK-carbon fiber (CF) composites: Structure and thermal properties. *Composites Science and Technology, 164*, 319-326.

3.Singh, Sunpreet, Chander Prakash, and Seeram Ramakrishna. "3D printing of polyether-ether-ketone for biomedical applications." *European Polymer Journal* 114 (2019): 234-248.

ADDITIVE INSERT MOLDING: FEASIBILITY AND APPLICATIONS

Ryan O'Quinn and Saeed Farahani

Cleveland State University, Cleveland, OH, USA

Email: r.oquinn@vikes.csuohio.edu

INTRODUCTION

Additive and traditional manufacturing are often regarded as separate schools of thought in end-part production, each with its own advantages and shortcomings. However, several attempts have been made to combine these two approaches in a complementary manner to improve upon their respective downfalls. Motivated by this concept, this work introduces a new hybrid approach, called Additive Insert Molding (AIM), that combines best in class plastic manufacturing process, injection molding, with additive manufacturing. AIM is the process of additively manufacturing inserts, placing the inserts into a mold for subsequent injection molding, and finally ejecting a single, combined finished part out of the mold. By this integration, the customizability and geometric freedom of additive manufacturing is combined with the reliability and speed of injection molding.

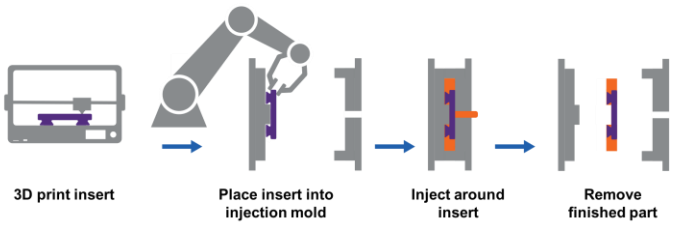

Figure 1: The schematic of AIM process.

AIM can be applied for personalization, part consolidation, reduction of tool complexity, and reinforcement. AIM is most valuable when complexity or customization is needed in a component but is not necessary throughout the entire component. Such may be the case in some orthoses and protheses where customization to individualized needs is required, yet some standardization can occur without limiting the required design envelope for customization.

Three case studies were carried out to demonstrate and explore AIM's applications. Finally, a literature review was conducted to explore AIM's potential in the manufacture of custom foot orthoses.

METHODS

All three case studies were performed using a model car mold and various 3D printed inserts made using fused deposition modeling (FDM). The car was injection molded using a polypropylene compound and the inserts were bonded to the injection molded matrix via mechanical interlock.

In the first study, an insert was designed to build personalized text or images into the top of the car. This personalized insert was printed using orange ABS filament. In the second case, an insert was designed to add greater detail to the wheels of the car. This insert consolidated two parts, which would typically be made through multiple injection molding processes using more complex tools. It was printed using grey and black ABS. In the third case study, an insert was designed to reinforce the car using continuous fiber 3D printing. Specifically, inserts were printed on a Markforged printer using their proprietary Onyx (Nylon 6 with chopped carbon fiber fill) matrix with continuous fiberglass reinforcement. 4 versions of the reinforcement insert were made, one with 0° draft on the walls of the mechanical interlock cutouts, one with 30°, one with 30° and larger window-like cutouts, and one with 45°. After injection molding the reinforced specimens were compression tested according to ASTM D695. Note the ribs and bottom portion of the car were removed in the preparation of compression specimens.

RESULTS AND DISCUSSION

Figures 2 and 3 show the results of the 3 case studies. Both the personalization and reduction of tool complexity/part consolidation case studies successfully demonstrated AIM's application in

Figure 3: AIM's applications as explored through 3 case studies.

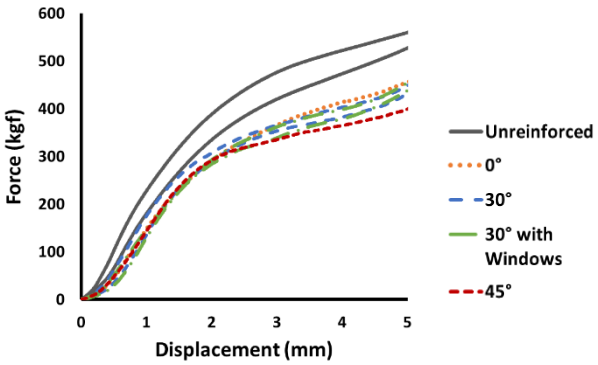

Figure 3: Compression testing results for reinforcement study.

these areas. Note that the tire and rim insert in the latter study features undercuts between the spokes, a fine tread design, and multiple materials, all of which would require special consideration (i.e. part divisions/complex tooling) to injection mold. The reinforcement study did not demonstrate greater strength in reinforced specimens relative to unreinforced specimens. This may be due in part to the limited continuous fiber content that could be printed into the reinforcement inserts. This was a result of limitations in Markforged's continuous fiber printing, both in unalterable slicer settings not suited for printing a continuous fiber preform (as opposed to a finished part) and in the combined hardware/software limitation of 2.5 axis printing, which limits fiber layouts to parallel 2D planes. Figure 3 also suggests that the draft angle on the mechanical interlocks was unnecessary or dysfunctional, as no or lower draft angles appeared to perform better. Thus, better understanding at the insert and injected matrix interface is required. In the future, we would like to explore fusion bonding between compatible thermoplastics as opposed to mechanical interlock as the bonding mechanism.

Many publications were found demonstrating and evaluating 3D printed foot orthoses. Perhaps most extensive is Przestrzelski's dissertation which developed and evaluated a 3D printed orthosis design to treat diabetic patients with foot ulcers [1]. Material jetting was used to print the orthosis. In a clinical trial, the 3D printed orthosis performed similarly to a traditional custom orthosis and provided greater comfort than a mass-produced, non-custom orthosis. In evaluating the commercial potential, Przestrzelski found the technology could enable millions of diabetics to have access to affordable custom orthoses. However, Przestrzelski identified issues in her 3D printed orthoses' wear resistance.

An AIM produced orthosis, consisting of a custom FDM printed reinforcement insert encapsulated in an injection molded matrix, may be able to provide similar customized support with improved wear resistance and reduced cost. This could be of value considering 3-6 months is often the recommended life of foot orthoses.

CONCLUSION

AIM, a hybrid manufacturing process combining additive manufacturing and injection molding was developed. The process was successfully demonstrated for personalization and reduction of tool complexity/part consolidation, but not for reinforcement, likely due to limitations of the 3D printer used. AIM has potential to offer value where customization and complexity is needed at scale. This includes custom foot orthoses, which have already been demonstrated with 3D printing, but could benefit from the scale and reliability of injection molding through AIM.

REFERENCES

1. Przestrzelski, B. *In-shoe innovation: 3D-printed foot orthoses*, (2017).

ACKNOWLEDGEMENTS

We would like to thank Dr. Srikanth Pilla and Clemson University's undergraduate research grant program for their support on this work.

PIVOT SHIFT AND ANTERIOR DRAWER TEST SIMULATIONS IN JUVENILE PATIENT POPULATIONS

[1]Alexandria Mallinos (Presenter), [1]Brian Davis, PhD, and [2]Kerywn Jones, MD

[1]Cleveland State University, Cleveland, OH, USA

[2]Akron Children's Hospital, Akron, Ohio, USA

Email: admallinos@gmail.com

INTRODUCTION

Every year, there will be more than 200,000 Anterior Cruciate Ligament (ACL) tears in the US alone. In this study, the goal was to develop baseline, specimen-specific knee models that accurately predict anterior tibial displacement when undergoing an anterior drawer test (ADT) and pivot shift test (PST). In doing so, these novel finite element models will provide a foundation for further knee model investigations. This study utilized data on normal ACL laxity measurements obtained using knee arthrometers [1,2] and experimental pivot shift simulations [3,4]. The ADT and PST data were used to compare the anterior translations of the finite element representations (FER) of the pediatric knee joints under specific simulation conditions.

METHODS

A total of 22 CT images of juvenile knees were utilized. The patients selected had no ACL pathologies and no bony deformations (ages: 9-18, males: n=16, females: n=6). 3D Slicer was used to convert the CT images into a three-dimensional representation of the bony anatomy. The bony anatomy was uploaded into FEBio to construct each tibiofemoral joint (Fig.1).

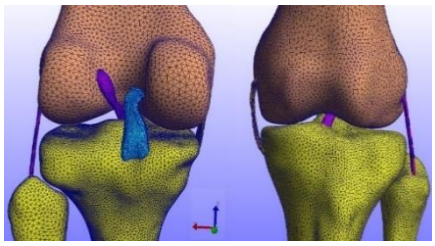

Figure 1: Frontal plane views of the developed juvenile FER.

The bones were defined as rigid bodies while the ligaments were modeled as incompressible transversely isotopic Mooney-Rivlin. The material properties of each of the bones and ligaments were obtained from the Open Knee User's Guide and the ligament stl files were utilized for each model [5]. To replicate the ADT, the femur was fixed in all degrees of freedom while the tibia-fibula was left unconstrained. An anteriorly directed force was applied to the tibia-fibula at 67, 89, and 133 N. At the current time, 10 out of the 22 subjects have completed the anterior drawer test simulations. Protocols established in the literature were used to simulate the PST [3,4]. This consisted of fixing the femur in all degrees of freedom and applying a 133 N anteriorly directed force to the tibia with a combination of 10 Nm valgus and 4 Nm internal tibial torques.

RESULTS AND DISCUSSION

The FER of the juvenile knees provides a realistic depiction of the ADT. The model predicted tibial displacement fell within the 95% confidence interval range of the experimental data (Fig. 2). The computer simulated models exhibited similar behavior to the experimental data by increasing in anterior tibial displacement with each loading force level: 5.5 mm, 6.55 mm, and 7.38 mm. The 95% confidence interval data demonstrates that the simulated anterior tibial translations reflect what has been established experimentally for all force levels.

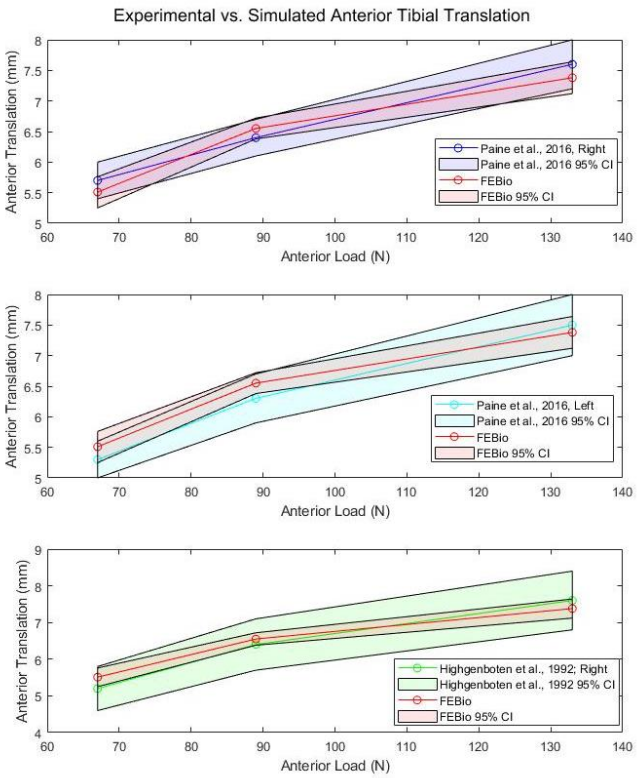

Figure 2: 95% confidence intervals for experimental and simulated anterior drawer test anterior tibial translation.

In addition, the anterior tibial translations measured during the pivot shift simulations reflects what has been established experimentally as well (Fig. 3).

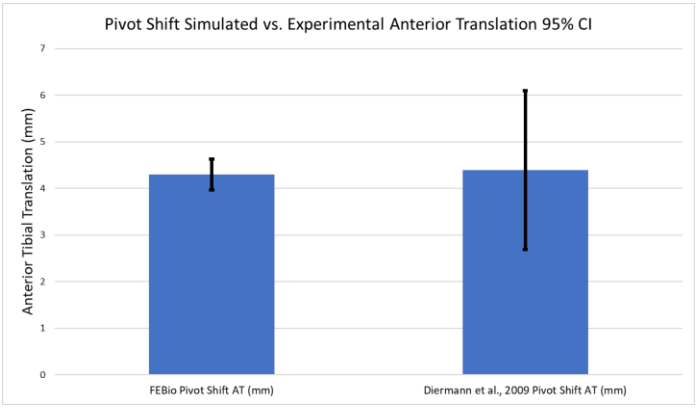

Figure 3: 95% confidence intervals for experimental and simulated pivot shift anterior tibial translation.

Compared to the experimental PST that obtained an average anterior tibial translation of 4.3 mm, the FEBio models averaged 4.4 mm when subject to the same testing protocols. This is further supported by the overlapping of the 95% confidence intervals between the simulated and experimental data.

Thus, the accurate and realistic simulations of the ADT and PST further supports the validity of these novel juvenile knee models.

CONCLUSION

The novel finite element representations of juvenile tibiofemoral joints were able to accurately simulate the ADT and PST. In doing so, this further demonstrates the validity of the juvenile knee models in that it can predict tibial displacement that is representative of the clinical data available in the literature.

REFERENCES

1. Highgenboten, C. L., et al., (1992). KT-1000 arthrometer: conscious and unconscious test results using 15, 20, and 30 pounds of force. *Am J Sports Med*, 20(4), 450-454.

[2] Paine, R., et al. (2012). Comparison of Kneelax and KT-1000 knee ligament arthrometers. *J. Knee Surg*, 25(2), 151.

[3] Diermann, N., et al. (2009). Rotational instability of the knee: internal tibial rotation under a simulated pivot shift test. *Arch Orthop Trauma Surg*, 129(3), 353-358.

[4] Wan, C., et al. (2017). Finite element simulations of different hamstring tendon graft lengths and related fixations in anterior cruciate ligament reconstruction. *Med Biol Eng Comput*, 55(12), 2097-2106.

[5] Schwartz, Ariel, Snehal K. Chokhandre, and Ahmet Erdemir. "Modeling and Simulation Workflow Using Open Knee (s) Data." simtk.org.

KNEE MECHANICS DURING ANTERIOR AND POSTERIOR LUNGE

Stephen Barnes[1] and Mohamed Samir Hefzy[2] (presenter and corresponding author)

Biomechanics and Assistive Technology Laboratory[1, 2]

Dept. of Bioeng.[1] and Mechanical, Ind. and Mfg. Eng.[2], Univ. of Toledo, Toledo, Ohio, USA

Email: mohamed.hefzy@utoledo.edu

INTRODUCTION

When a patient is attending rehabilitation, the therapist will prescribe either closed or open kinetic chain exercises. A recent systematic review found that there was insufficient evidence to suggest one was superior to the other after anterior cruciate ligament reconstruction [1]. This in turn, leaves the exercise prescription at the therapist's discretion and any previously known conditions.

An example of a commonly closed kinetic chain exercise that is used for the lower limbs strengthening is the lunge. There are numerous styles and forms of lunges including the lateral lunge, the forward anterior lunge (FL) and the reverse posterior lunge (RL).

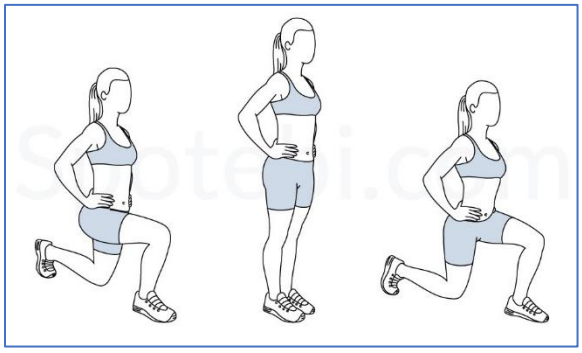

Figure 1: The right leg during a right leg FL (left) and a right leg RL (right) [2]

During FL, subjects stand in an upright position. They would then step forward with the lead foot to a distance that would allow them to bend both knees to an ideal 90 degree angle for both. They then return to an upright position. During a posterior reverse lunge, individuals step behind themselves so that the leading foot's placement mimics that of the FL and allows for the patient to descend so that both knees are bent to a 90 degree angle. Individuals then return to the upright position to conclude the exercise. Figure 1 shows a schematic displaying a right leg FL (on the left) and a right leg RL (on the right).

Few studies provided a biomechanical analysis of the forward lunge as well as a comparison only between the forward and lateral lunges. The objective of this paper is to describe the mechanics of both knee joints during forward and reverse lunges.

METHODS

Given that the worldwide pandemic, COVID-19, took place during the conduct of this study, both CDC guidelines and the University of Toledo (UT) guidelines were followed. The testing protocol was approved by the IRB of the UT.

An integrated human motion analysis was used to collect motion, ground reaction forces and EMG data. The system includes ten Raptor-E digital cameras from Motion Analysis, Inc., two Optima digital force platforms from Advanced Mechanical Technology, Inc., and EMG sensors from Delsys, Inc. Cortex software from Motion Analysis, Inc. was used to simultaneously collect the motion data from the cameras, the ground reaction forces from the force platforms, and the data from the EMG sensors.

Eight males and seven females were recruited for this study. The average age of the fifteen subjects was 22.4 years. Subjects were instrumented with 16 reflective markers on the left and right sides of the body in order to identify key bony landmarks for motion analysis. Ten EMG sensors were placed on the surface of the skin to collect activation from 5

muscles on the left and right sides of the body. Subjects were then instructed to stand still on a force plate. During FL, subjects performed the lunge on their dominant foot and returned to a complete up-right standing position, and then performed the lunge on the non-dominant foot. This process was repeated to conduct the RL.

RESULTS AND DISCUSSION

Figure 2 shows how the knee angles change during FL and RL for one of the subjects. Figure 2a and 2b show how the knee angles change during a FL with the right and left legs, respectively. Figure 2c and 2d show how the knee angles changes during a RL with the right and left legs, respectively. The blue and orange curves are for the left and right knees, respectively

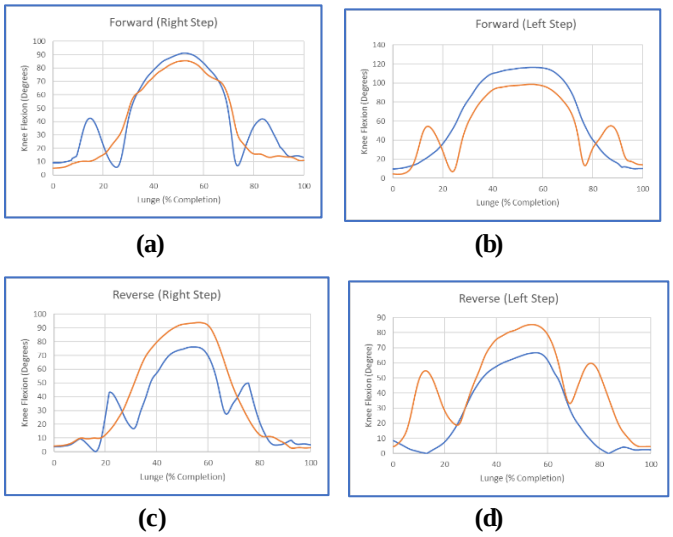

Figure 2: Knee angles during forward lunge (a and b) and reverse lunge (c and d). The blue and orange curves are for left and right knees, respectively.

The results of figure 2.a and 2.b show that the forward knee during the forward lunge gradually flexes to a maximum flexion, sustains that position, and then gradually extends to full flexion. The other knee flexes, then extends, then flexes to a maximum flexion position, then extends, then flexes, then extends to full flexion. A similar pattern is shown for the reverse lunge in figures 2.c and 2.d.

Figure 3 shows the normalized knee flexion moments during forward lunge with right step (a) and with left step (b). The results shown in this figure correlate with the results of figure 2. For instance, during a forward lunge with a right step, figure 2.a shows that the right knee goes into flexion and maintains that position before extending. Figure 3.a shows that during a forward lunge with a right step, the flexion moment on the right knee increases to a maximum and remains constant before decreasing as the knee moves to full extension.

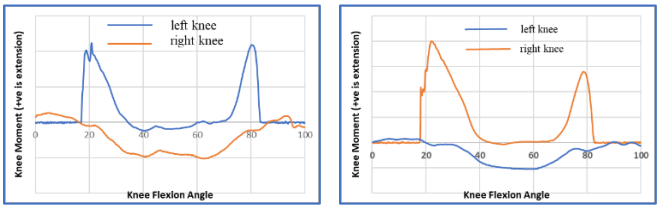

Figure 3: Normalized knee moments with respect to body weight and body height during forward right step lunge (a) and forward left step lunge (b).

CONCLUSION

The results shown in this study indicate the knee angles and knee flexion moments for the anterior and posterior knees have different patterns during both forward and reverse lunges. It is thus important to study how these findings correlate with the EMG measured muscle activities, and to determine the shear forces acting at the knee joints during both forward and reverse lunges in order to determine their efficacy and efficiency.

REFERENCES

1. Jewiss, D., et al. Hindawi J. of Sports Medicine, Vol. 2017, Article ID 4721548

2. https://www.spotebi.com/exercise-guide/lunges/

ACKNOWLEDGEMENTS

This work was supported by the Bioengineering and Mechanical Eng. departments at the Univ. of Toledo.

NOVEL IMPLANT DEVICE FOR PLANTAR PLATE REPAIR

[1]Skye Carlson (presenter) and [2]L. Dickinson, Z. Kozar, J. Wayne, V. Wang, [3]D. Poulos, [4]R. Clements

[1]Cleveland State University, Cleveland, OH, USA,

[2]Virgina Polytechnic and State University, Blacksburg, VA, USA

[3]University of Tennessee, Knoxville, TN, USA

[4]Carilion Clinic Orthopedic Surgery, Roanoke, VA, USA

Email: s.a.carlson@vikes.csuohio.edu

INTRODUCTION

The plantar plate is a fibrocartilaginous structure located at the underside of the forefoot. A plantar plate tear is a common injury that may occur with excessive force and trauma to the forefoot. This injury can cause immense discomfort and pain, as well as alter the appearance of the toe. In many cases surgery to repair the plantar plate is recommended. [1][2].

However, the existing surgical methods may cause post-op complications, such as phalanx fracture, avascular necrosis, and patients that are unsatisfied with the results. Surgeons have noticed a sawing effect on the dorsal side of the phalanx and hypothesized the cause of this to be a combination of the suture tension and the repetitive compressive and tensile loads applied to the fixation site. These complications can lead to continuous pain and discomfort, further alter the appearance of the toe, or loss of toe function. Although current devices on the market simplify the overall surgical procedure and restore toe function, they do not limit the risk of the suture sawing effect on the dorsal and/or plantar side of the proximal phalanx and offer limit fixation and operation space.

Our objective was to create a durable solution to plantar plate tears that restores foot function and patient comfort. The primary deliverables included reducing or eliminating the dorsal saw effect, minimizing the common postoperative complications, and creating a prototype to meet the needs of our clients.

METHODS

The proposed design, Figure 1, uses a two-piece implant that sits in the phalanx to secure the sutures and torn plantar plate. The female piece sits on the top, dorsal side, of the bone while the male piece sits on the bottom, plantar side. The implant features a variable height snapping mechanism. These two pieces are designed to be manufactured in PEEK (Polyether ether ketone), however for testing they were manufactured using Rigid 4000, a Formlabs resin.

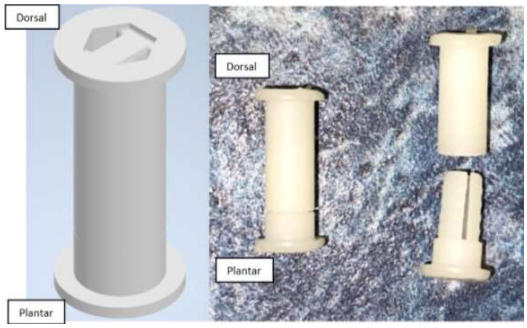

Figure 1: model and print of implant

Computational Testing Computational analysis was performed using Autodesk Inventor to predict the implant's reaction under various stresses. A -20 N load was applied in the -y direction and 3 N load was applied in the x-direction to represent the sutures being pulled toward the plantar plate. The force values were evaluated using a free body

diagram of the implant and expertise from Dr. Clements.

Mechanical Testing A displacement-controlled tensile test was performed using an MTS Insight 10 machine to record the load at implant separation. Sutures were woven through the implant and tension was applied to the sutures, simulating loads that will be placed on the implant in dorsiflexion when in vivo. A total of 48 implants were tested at 0-, 40-, and 80-degrees dorsiflexion.

RESULTS AND DISCUSSION

Computational Analysis The maximum Von Mises stress was 18.83 MPa. The yield strength for PEEK is greater than the max stress determined by the computational model. Therefore, it can be concluded that the material would not plastically deform when under the applied load. In addition, the maximum stress was also used along with a fatigue strength between 40-80 MPa to calculate a factor of safety of 2.7**.** These results concluded that the implant would be able to withstand the forces in practice.

Mechanical Analysis In over 87% of the tests, suture failure occurred, while the rest of the tests experienced implant failure, revealing that the implant is strong enough to hold load as high as 300N without failure (Fig. 2). No significant ($p > 0.05$) differences in max load or stiffness were observed between different dorsiflexion angles. In addition, tests with implant failure only occurred near the failure load of the size 2 sutures. According to Dr. Clements, the most common form of failure for plantar plate repairs are sutures pulling out of the plantar plate. Since our data shows suture breakage as the point of failure, this suggests the implant will not fail when in implanted.

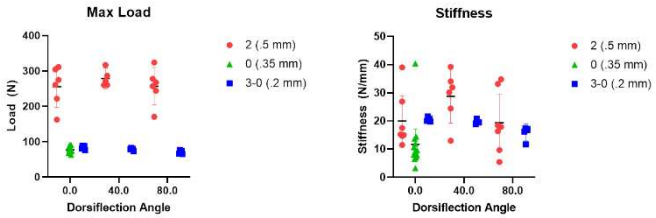

Figure 2: Max load and stiffness results from mechanical testing, colors represent suture sizes (diameter)

CONCLUSION

On April 8, 2021, a simulated use test was conducted with Dr. Clements. The purpose of this simulated use test was to determine the effectiveness of the implant at shielding the bone from the sutures, observe how a surgeon would interact with the implant, and the time it takes to insert and secure the implant into the phalanx. This test was extremely successful; Dr. Clements was able to implant and secure the device into a sawbone.

This implant is intellectual property of the Virginia Polytechnic and State University, VTIP: 21-106.

REFERENCES

[1] Doty, Jesse. Operative Techniques in Sports Medicine, Vol 22, Issue 4, pgs. 339-347. December 2014.

[2] Weil Jr, Lowell. PodiatryToday, Vol 25, Issue 4, pgs. 62-72. March 23 2012.

ACKNOWLEDGEMENTS

I would like to express my very great appreciation to my Plantar Plate Team: Logan Dickinson, Zach Kozar, Demi Poulous, for their teamwork on this project and our advisors: Dr. Jennifer Wayne, Dr. Vincent Wang, and Dr. Randy Clements, for their constructive suggestions and expertise throughout the design process.

SENSITIVITY OF ACL FORCE AND STRESS TO KINEMATIC ERROR

[1]William Zaylor (Presenter), [1]Snehal K. Chokhandre, [1]Ellen M. Klonowski, [1]Kayla Malby, [1]Ahmet Erdemir, [1]Jillian E. Beveridge

[1]Musculoskeletal Research Center & Department of Biomedical Engineering, Cleveland Clinic, Cleveland, USA

Email: zaylorw2@ccf.org

INTRODUCTION

Diminished anterior cruciate ligament (ACL) function following surgery is likely a contributing factor to long-term joint damage and post-traumatic osteoarthritis [1]. The function of the native ACL during common activities remains unclear, and an improved understanding of native ACL function could inform clinical interventions to improve outcomes. Kinematically-controlled computational knee models could be used to evaluate ligament function during common activities; however such models are generally avoided because previous work has shown that predicted tibiofemoral contact forces are sensitive to kinematic errors [3]. The sensitivity of ligament function metrics to kinematic errors has not been evaluated; therefore, the purpose of this study was to evaluate the effect that kinematic errors have on an ACL model's predicted force and stress distribution.

METHODS

One 18 month old male Yucatan minipig was used for this study. All animal procedures were reviewed and approved by our institutional animal care and use committee. In vivo magnetic resonance (MR) images of the right hind limb were acquired using a 3T scanner where two sequences were used [4]: 1) a double echo steady state (DESS) sequence with a resolution of 0.36x0.36x0.7 mm was used to generate the knee model geometry; 2) a gradient multi-echo T_2* sequence with a resolution of 0.42x0.42x0.8 mm and TEs=2.48, 6.86, 11.24, 15.62 ms) was used to calculate the T_2* relaxation time throughout the ACL. The femur, tibia, and ACL were manually segmented from the DESS images, and the segmentations were used to generate surfaces of the corresponding geometry. The femur and tibia were modeled as rigid bodies, and contact between the bones and ligaments was neglected. The ACL surface was used to generate a linear tetrahedral mesh, and the ACL mesh nodes at the femoral and tibial insertions were rigidly attached to the corresponding surface. A heterogeneous transversely isotropic Mooney-Rivlin material model was assigned to the ACL, where T_2* relaxation times were used to assign each element's material properties throughout the ACL mesh [5]. The knee model was used to simulate an anterior drawer test, where a 3 mm anterior tibial translation was assigned, and the remaining kinematic degrees of freedom (DOF) were fixed, and this was taken as the nominal model.

The model was iteratively evaluated to assess the sensitivity of the predicted force and stress distribution to errors in the assigned kinematics. A total of 1000 iterations were evaluated, where each iteration assigned a set of six randomly selected errors to the model's kinematics. Errors were sampled from a normal distribution, where the mean was 3 mm for anterior tibial translation and zero for the remaining DOF. The standard deviation for translational and rotational DOF was 0.47 mm and 0.4°, respectively, which is similar to previous work [6]. For each iteration, the assigned kinematic pose and the total force carried by the ACL was recorded.

The predicted forces from the 1000 simulation results were used to identify two representative simulations to evaluate the stress distribution. The mean and standard deviation of the predicted force across the 1000 simulation results was calculated and

used to identify representative simulations with high and low force predictions. The two representative simulations were identified as the iterations where the ACL carried force closest to the mean force ±2 standard deviations. The distribution of the first principal stress at the high and low predicted-force iterations was qualitatively compared to the stress distribution from the nominal simulation's results.

RESULTS AND DISCUSSION

The ACL showed a wide range of forces due to kinematic error. The mean (±stdev) ACL force across the perturbed iterations was 674 (±139) N, which was similar to the 670 N predicted by the nominal (zero error) simulation. The magnitude of the first principal stress varied between the results, whereas the distribution of stress appearing to be similar (Figure 1).

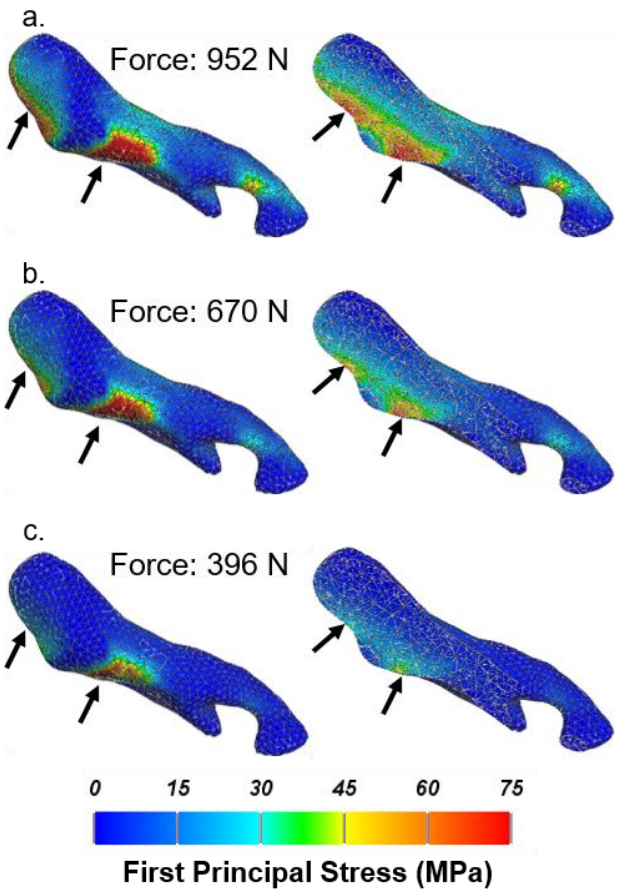

Figure 1: A lateral view of the ACL showing the (left) exterior ACL and (right) a representative interior view. The distribution of the first principal stress in the ACL for the (a) simulation with force results near mean force+2stdev, (b) the nominal simulation, (c) mean force-2stdev. Arrows indicate areas where the stress distribution is similar between results. Note that deformation are not shown to enable comparisons.

Our results showed that an ACL model's predicted force is sensitive to kinematic errors on the order of 140 N, but the predicted stress distribution within the ligament may not be sensitive to kinematic errors. The variation in ACL force is consistent with a previous study which showed a wide range of predicted forces due to kinematic errors in a spring-based knee model [6]. The model's predicted forces were higher than the failure load measured in experimental studies of the same animals [4]. The high loads could be due to taking prestrain to be uniformly zero across the ACL model. Previous work has shown that kinematics are sensitive to variations in a knee model's prestrain [2]. This study indicates that ligament function metrics based on stress distribution may be less sensitive to kinematic errors compared to metrics based on overall ligament force. Future work could include more subjects and also utilize quantitative measures of the stress distribution to compare values across every kinematic pose. Additionally, future work could calibrate the ACL model's prestrain to potentially yield more physiologic predictions of ligament force.

CONCLUSION

The forces predicted from a kinematically controlled ACL model appear to be sensitive to kinematic errors, however the predicted stress distribution may not be as sensitive.

REFERENCES

[1] Beynnon, B, et al. Am. J. Sports Med., pp. 1579–1602, 2005.
[2] Dhaher, Y, et al. J. Biomech., pp. 3118–3125, 2010.
[3] Fregly, B, et al. J. Orthop. Res., pp. 1173–1179, 2008.
[4] Beveridge, J, et al. J. Orthop. Res., pp. 1701–1709, 2018.
[5] Beveridge, J, et al. The International Society of Biomechanics (ISB), Stockholm, 2021.
[6] Zaylor, W, et al. J. Biomech., pp. 1–5, 2019.

ACKNOWLEDGEMENTS

We thank our funding agencies: NIH NIAMS R00AR069094, R01EB024573 and the Cleveland Clinic MSRC Pilot Program.

ANATOMICAL CHARACTERISTICS CONTRIBUTING TO PATELLAR DISLOCATIONS FOLLOWING MPFL RECONSTRUCTION

Jeffrey C. Watts[1], John J. Elias[1], Lutul D. Farrow[2]
[1]Departments of Research and Orthopedic Surgery, Cleveland Clinic Akron General, Akron, OH,
[2]Department of Orthopaedic Surgery, Cleveland Clinic Foundation, Cleveland, OH
Email: wattsj3@ccf.org

INTRODUCTION

Medial patellofemoral ligament (MPFL) reconstruction is growing in popularity for surgical patellar stabilization following a lateral dislocation. Continued dislocations following MPFL reconstruction have been noted for approximately 5% of patients [1], and alternative procedures involving bone cuts are commonly considered for knees with high levels of anatomical pathology. The current study focuses on identifying anatomical characteristics that place the knee at risk of a patellar dislocation following MPFL reconstruction.

METHODS

Knee function was simulated with thirteen multibody dynamic simulation models (RecurDyn) representing subjects being treated for recurrent patellar instability. The study was IRB approved. Ligaments, tendons, and retinacular structures were represented by tension-only springs, including assigned properties for stiffness, damping, and pre-strain at full extension (Fig. 1). A fixed ankle joint was represented with three rotational degrees of freedom. A hip joint was represented, allowing vertical translation, flexion/extension, and abduction/adduction.

During simulations, simplified Hertzian contact governed patellofemoral and tibiofemoral reaction forces and moments, guiding patellofemoral and tibiofemoral motion. The models were individually validated for patellar tracking by comparisons to data measured from the subjects [2].

A pivot landing was simulated with each model to represent an activity that places the knee at risk of patellar dislocation. The motion was initiated by a 3200 N gravitational force at the hip. The quadriceps force increased from 180 N at 5° of flexion to 1000 N at 90°, with 40% of the quadriceps force applied through the hamstrings. A 12 N-m external torque was applied to the tibia to represent pivoting around a planted foot, thereby applying a large lateral force to the patella. A gracilis tendon MPFL graft was represented by a rigid surface from the Schöttle point on the femur to a wrapping surface on the femur, with two springs extending to the medial edge of the patella.

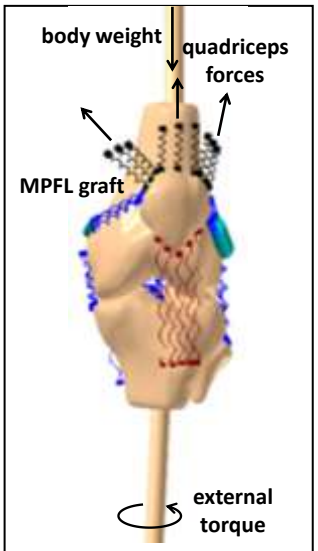

Figure 1: Model for dynamic simulation of knee function.

Multibody dynamic simulation output was post-processed with automated algorithms (Matlab) to characterize parameters related to lateral patellar tracking and pathologic anatomy at each flexion angle. Patellar tracking was characterized based on the bisect offset index (percentage of patellar width lateral to the deepest point of the trochlear groove) in an axial plane. Lateral position of the tibial tuberosity was characterized based on the tibial tuberosity to trochlear groove distance (medial/lateral distance from the center of the tibial tuberosity to the deepest point of the trochlear groove). Trochlear depth was characterized based on the lateral trochlear inclination angle (orientation of the lateral facet of the patella with respect to the posterior condylar axis of the femur). Patellar height was quantified based on the Caton-Deschamps index (ratio of the distance from the most distal point on the cartilage to the superior-anterior tibia to the articular length along the patella) (Figure 2). Linear regressions were used to relate patellar tracking to knee anatomy at both 5° and 45° of flexion. Tension within the graft was also quantified as the knee flexed.

RESULTS AND DISCUSSION

The simulated pivoting maneuver produced a patellar dislocation for all thirteen models without an MPFL graft represented. Two of the models also experienced a dislocation with an MPFL graft represented, with dislocation occurring beyond 45° of flexion. The

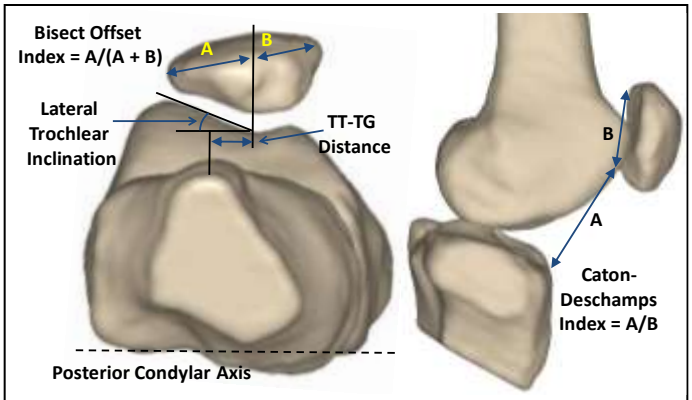

Figure 2: Parameters of patellar tracking and anatomy from the knee models.

average (± standard deviation) tension within the graft peaked at 10° (52 ± 26 N) and varied dramatically among the knees at 45° (35 ± 63 N).

Patellar tracking was significantly correlated with anatomy at 45° of flexion, but not at 5° (Fig. 3). At 45°, bisect offset index was significantly correlated with both Caton-Deschamps index ($r^2 = 0.40$, $p = 0.02$) and lateral trochlear inclination angle ($r^2 = 0.48$, $p = 0.01$), but not with tibial tuberosity to trochlear groove distance ($p > 0.8$). No significant correlations were identified between anatomy and patellar tracking at 5° ($p > 0.1$).

The analysis indicates that a high patella and a shallow trochlear groove are significantly correlated with lateral patellar maltracking at 45° of flexion for a pivot landing following MPFL reconstruction. Both a high patella and shallow trochlear groove limit the articular constraint provided to the patella by the trochlear groove to resist lateral translation. At 45°, the patella should be captured by the trochlear groove, so lateral maltracking indicates a risk of post-operative patellar dislocations. The position of the tibial tuberosity was not significantly correlated with patellar tracking, which was not expected due to the lateral force generated with external tibial rotation. Lack of significant correlations with the knee extended is likely related to relatively high and consistent graft tension. The graft shortens as the patella enters the trochlear groove, with the reduced tension making the patella more vulnerable to dislocation.

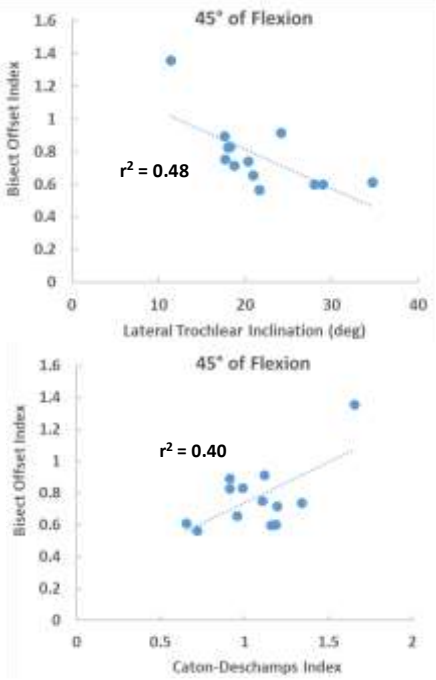

Figure 3: Correlations relating bisect offset index to lateral trochlear inclination and Caton-Deschamps index at 45° of flexion during simulated pivoting following MPFL reconstruction.

CONCLUSIONS

The current study identifies two anatomical parameters associated with lateral patellar tracking during a pivot landing following MPFL reconstruction, indicating a risk of additional patellar dislocations for athletic patients. These are a high patella and shallow trochlear groove with the knee flexed. For athletic patients displaying these characteristics, alternative surgical procedures involving bone cuts may be required to stabilize the patella.

REFERENCES

1. Schiphouwer, L, et al. *Knee Surg Sports Traumatol Arthrosc*. 25:245–250. 2017
2. 2. Tanaka, M.J., et al. *J Knee Surg* doi: 10.1055/s-0040-1702185 [online ahead of print].

ACKNOWLEDGEMENTS

Funding was provided by Department of Defense, Peer Reviewed Medical Research Program Discovery Award W81XWH2010

A PRELIMINARY STUDY ON MEASURING NORMAL AND TANGENTIAL FORCE USING STRETCHABLE POLYMERIC SENSORS FOR SMART INSOLES

[1]Jae-Won Choi and [2]Omar Faruk Emon

[1]The University of Akron, Akron, OH, USA

[2]University of New Haven, West Haven, CT, USA

Email: jchoi1@uakron.edu

INTRODUCTION

Foot plantar pressure measurements can provide important information on biomechanics that could be used for medical assessments, footwear evaluation, clinical gait analysis, and athletic performance enhancement. There have been some studies on platform-based and in-shoe foot plantar pressure measurement systems. In most cases, these solutions only work with normal or resultant force applied by the foot. Moreover, they either do not provide a real walking/running experience or they are not comfortable. In this work, a polymeric stretchable sensor was developed that is capable of measuring the normal and the tangential force applied by the foot. These two force measurements can also be used to determine the shear force. The developed sensor is believed to be superior over the existing solutions for foot plantar pressure measurement as it provides multi-directional force measurements and could be used for a comfortable and/or customized in-shoe systems.

METHODS

An acrylate-based monomer/oligomer composition was developed to achieve flexibility and stretchability in the sensor. A photo-initiator and a cross-linker were used with the prepolymer to achieve proper elasticity and strength. An ionic liquid (IL) was incorporated into the polymer for inducing pressure sensitivity in the polymer membrane. Carbon nanotube (CNT)-based polymer composite was developed to fabricate stretchable electrodes. Various material formulations were investigated to check the sensitivity of the sensor. The sensor design and wiring diagram are shown in Fig. 1. When force is applied to the sensor, its electrical resistance changes due to the deformation in the IL layer. The sensor was fabricated via photocuring the prepolymer in a mold and screen-printing the CNT-based electrodes [1]. A sandwich of two electrodes with an IL-layer is referred to as a *taxel* [2].

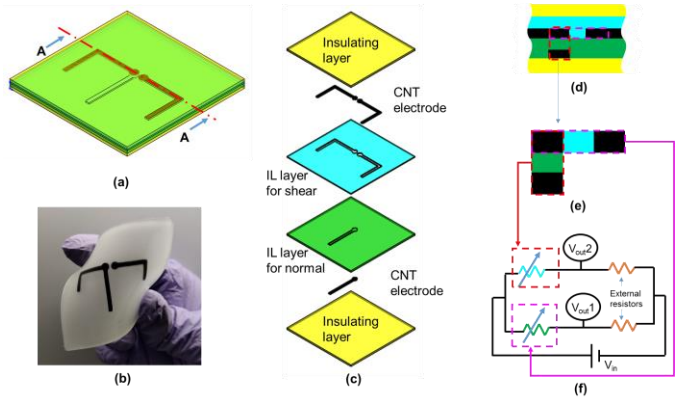

Figure 1: Sensor configuration: (a) sensor schematic; (b) fabricated sensor; (c) different layers of the sensor; (d-e) cross section of the sensitive zone; (f) wiring diagram.

Fig. 2 shows the experimental setup for the sensor evaluation. It consists of two motorized stages (X and Z), a force gauge for normal compressive force

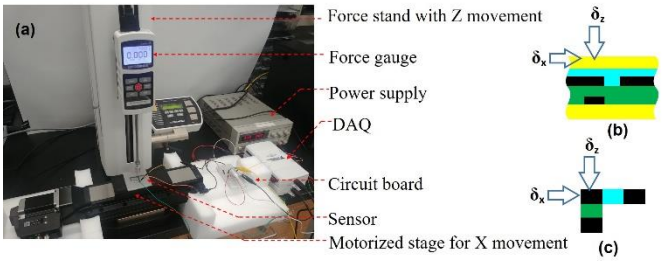

Figure 2: Experimental (a) set-up (b-c) strain application shown in cross-sectional schematic.

measurement, circuitry for the sensor, and a power supply. δ_x and δ_z in Fig. 2(b-c) are applied strain in the normal and tangential direction, respectively.

RESULTS AND DISCUSSION

Fig. 3 shows the experimental results for the fabricated sensor. Initially, ~1 mm of δ_z was applied and normal compressive force got increased. Fig. 3(d) and (e) show the normal and tangential taxel output, respectively. With the initial δ_z and compressive normal force, Fig. 3(d) shows the normal taxel output where voltage increases according to the applied normal strain. Next, a set of three slide/tangential cycles was applied by applying 2 mm of δ_x three times as shown in Fig. 3(b). The normal strain (δ_z) affected both normal and shear/slide taxel. Because of the shear effect, the normal taxel voltage went down due to the increase in resistance. However, the tangential taxel voltage went up as one electrode moved closer to the other in the same layer. Voltage reduction only in the normal taxel does not provide enough information to detect the slide/shear, since the reduction can come from unloading in the Z direction. But combining normal and tangential taxel outputs in Figs. 3(d) and (e) give additional information to define the direction of the strain. Tangential taxel output in Fig. 3(e) shows some electrical noise. Noise is prominent because of the small voltage deviation. However, this noise could be reduced in future experiments by adding filters.

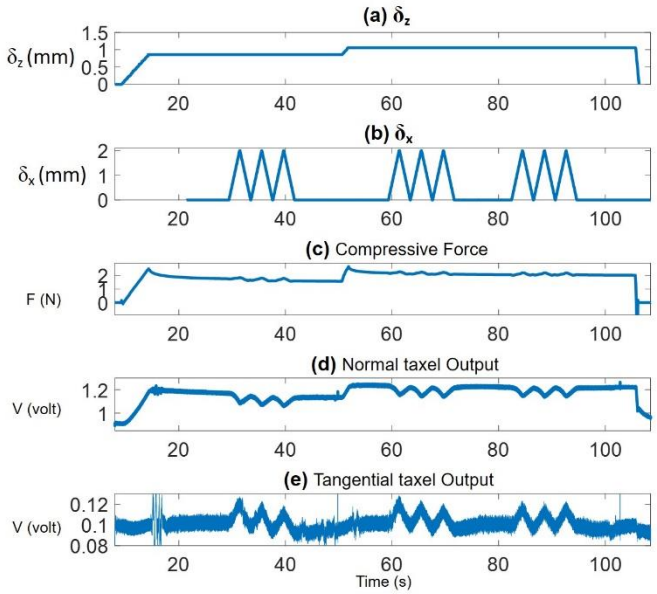

Figure 3: Sensor evaluation for simultaneous normal and tangential strain

CONCLUSION

This work shows the development of a polymeric force sensor that is capable of measuring normal and tangential force. A combination of these two measurements could be used to identify and measure shear force. A potential application of this sensor could be in an insole where the obtained data can be used for the analysis of biomechanics. Ongoing work includes sensor characterizations for shear force measurement.

REFERENCES

1. Emon, M.O.F., et al. *IEEE Sensors Journal*, Vol. 19, Iss. 15, pp. 6076-6084, 2019

2. Emon, M.O.F., et al. *Additive Manufacturing*, Vol. 6, pp. 629-638, 2019.

ACKNOWLEDGEMENTS

This work was supported by the National Science Foundation under Grant No. #1914165 through eSens.

ISOLATED SEAT PAN TILT REDUCES BUTTOCK AND LOWER BACK PRESSURE ON ABLE-BODIED INDIVIDUALS AND WHEELCHAIR USERS WHILE SEATED

[1]Justin Scott, PhD and [1]Tamara Reid Bush, PhD

[1]Michigan State University, East Lansing, MI, USA

Email: scottju5@msu.edu, reidtama@msu.edu

INTRODUCTION

Wheelchair users experience pressure injuries (PIs) at a staggering rate, with a prevalence as high as 47% in care facilities [1]. As a result, PIs cost the United States healthcare system about $1.3 billion annually [2]. PIs are caused by sustained external pressure on the body, so wheelchair design has tried to reduce pressure on areas that experience large pressures while seated. Half of PIs occur in the buttocks and lower back, so those areas are of particular concern [3]. Back recline and whole-body tilt (simultaneous back recline and seat pan tilt) are the most common movements used to relieve pressure while seated [4].

Despite the popularity of back recline and whole-body tilt, there is little research demonstrating their efficacy. Notably, most studies do not have pressure data in the neutral (no back recline or seat pan tilt), reclined, and tilted positions; and most studies have no data from wheelchair users. Commercial wheelchairs include back recline and whole-body tilt, but PIs are still prevalent in wheelchair users. Thus, we propose an isolated rearward seat pan tilt to offload the buttocks and lower back while seated. The goal of this work was to evaluate the efficacy of back recline and whole-body tilt in reducing the maximum pressure on the buttocks and lower back while seated and to compare them to a position with an isolated seat pan tilt.

METHODS

Twenty able-bodied individuals (ABs) (ten males, ten females) and ten male wheelchair users (IRB #15-889) participated in this study. An articulating chair was constructed with independent rotations of the back and seat pan (Figure 1). Data were collected on participants in nine positions with varying back recline angles and seat pan tilt angles. Three angles of back recline (0°, 10°, 20°) and three angles of seat pan tilt (0°, 15°, 30°) were tested, with 0° back recline and seat pan tilt shown in Figure 1.

Pressure mats were placed on the back support and seat pan of the chair to collect pressure data in each position. Each pressure mat was an array of 42 rows with 48 sensors. Pressure data were split into three regions: the thighs (anterior half of the seat pan mat), buttocks (posterior half of the seat pan mat), and lower back (inferior third of the back mat). The maximum pressures in each region were determined by calculating the maximum average measurement over any three by three set of sensors in the region.

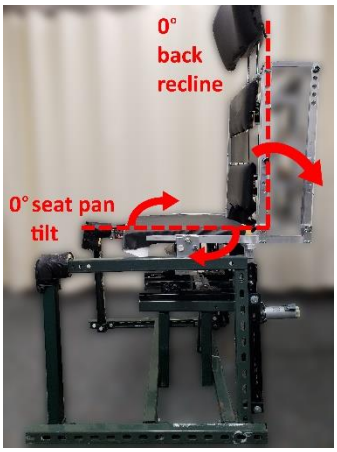

Figure 1: Side view of the articulating chair, with the top arrow showing the back recline and bottom arrows showing seat pan tilt. The vertical dashed line shows 0° recline, and the horizontal dashed line shows 0° seat pan tilt

RESULTS AND DISCUSSION

Increasing back recline increased the maximum pressures in the lower back and buttocks of ABs and wheelchair users, while decreasing maximum pressure in the thighs (Figure 2). Increasing seat pan tilt had the opposite effect, seen in Figure 3.

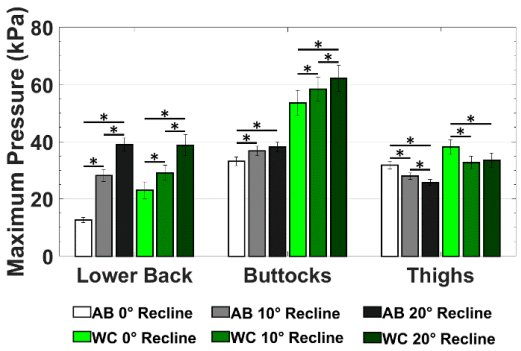

Figure 2: Max pressure values for each region in each recline angle, with ABs in greyscale and wheelchair users in green. Significant differences denoted by asterisks (*)

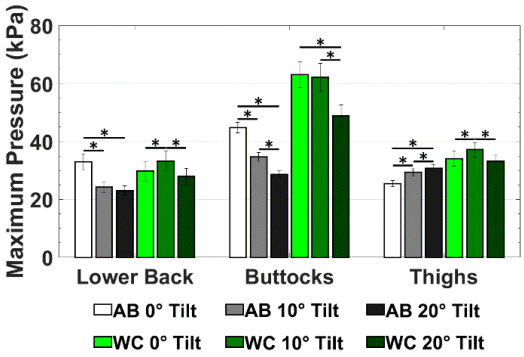

Figure 3: Max pressure values for each region in each pan tilt angle, with ABs in greyscale and wheelchair users in green. Significant differences denoted by asterisks (*)

The collected data are critical because they include data from ABs and wheelchair users in several positions. The maximum pressures on wheelchair users were generally larger than those of ABs. These pressures indicate an overall increase in PI risk for wheelchair users that may not be captured by testing only ABs. Meanwhile, there were common trends in pressure shifts between the two groups. The reported data support the use of an isolated seat pan tilt to reduce the maximum pressures on the buttocks and lower back of ABs and wheelchair users. However, increasing back recline, which is most often used to relieve pressure on the body, does not offload the pressure on the buttocks or lower back. Whole-body tilt did not have any consistent pressure changes relative to a neutral position with no back recline or seat pan tilt, indicating that it does not decrease the risk of PIs in seated individuals.

Both back recline and seat pan tilt increased the maximum pressure in one region while decreasing it in another. There is previous work showing that soft tissue is more resilient to higher pressures if those pressure are intermittently relieved [5]. Because of this, there is a need for a position change regimen that moves between several positions, to reduce the risk of a PI in any single region.

CONCLUSION

When considering the design of equipment such as wheelchairs, it is important to include the intended users in data collection. This work was vital because it included data from wheelchair users while investigating the effects of chair movements on seated pressures. In doing so, this work showed that there are larger seated pressures on wheelchair users as compared to ABs. The trends recorded support the use of an isolated seat pan tilt to relieve the pressure on the buttocks and lower back while seated; and the use of a movement regimen to reduce the risk of PI formation in any region.

REFERENCES

1. Cowan, L.J., et al., *Wound Care*, 32, 2019.
2. S.D. Horn, et al., *J. Am. Ger. Soc.*, 50, 2002.
3. Peart, J. *Br. J. Nursing*, 25, 2016.
4. Ding, D., et al., *J. Rehab. Res. Dev.*, 45, 2008.
5. Linder-Ganz, E., et al. *J Biomech*., 39, 2006.

ACKNOWLEDGEMENTS

Research was funded by NSF Grant CBET-1603646.

DEVELOPMENT OF FOOT DISPLACEMENT DETECTION ALGORITHM FOR POWER WHEELCHAIR FOOTPLATE PRESSURE AND POSITIONING

[1,2]Jeremiah Ukwela, [2]Steve J. A. Majerus, [2]Joseph Lerchbacker, [2]Kath M. Bogie and [2]M. Kristi Henzel

[1]Case Western Reserve University, Cleveland, OH, USA

[2] Advanced Platform Technology Center, Cleveland VA Medical Center, Cleveland, OH, USA

Email: jeremiah@case.edu

INTRODUCTION

Power wheelchairs (PWC) are critically important for independent mobility and quality of life for persons with spinal cord injuries and disorders (SCI/D), but even optimally configured PWC's can be dangerous during operation by users who cannot feel, see, or easily reposition their lower limbs when driving conditions, e.g., rough terrain, cause inadvertent lower extremity displacement (ILED) from the PWC footplates. After ILED from the footplates, traumatic fractures, wounds, abrasions, pressure injuries, and amputations may occur [1].

There are no current systems to help users replace the missing sensory feedback of the nervous system which is lost after SCI/D. Safe wheelchair use relies upon users consistently implementing safe operation techniques, which requires intact vision, cognition, and impulse control [2]. Development of smart footplate position sensing and feedback provides the basis for developing active safety interventions to address the unmet clinical need for real-time prevention of lower limb injuries during PWC use [3], first by helping define incidence of lower limb injuries and near misses and, once optimized, by helping to prevent ILED-related injuries.

The FootSafe system combines force and proximity sensors with a wirelessly connected smartphone application with adjustable alarm options to provide continuous real-time monitoring of foot position on the footplate. The device was designed to fit a commonly used PWC footplate. Each half of the FootSafe system includes an array of 24 low profile piezoresistive force sensing regions (FSR) and 14 infrared (IR) proximity sensors to detect foot position above the footplate [3].

METHODS

Seven individuals, one of whom was an experienced PWC user with SCI/D participated (3 women, 4 men). Participants were of varying heights (157-183 cm) and shoe sizes and had varying fits in the PWC (oversized to undersized). All recordings were performed using a Permobil F5 PWC and the FootSafe device affixed to the footplate tray using 3M VHB. One recording of simulated daily PWC use was made for each study participant, and three 10-minute recordings at rest were made for the experienced PWC user. The experienced PWC user with SCI/D had several sets of simulated daily PWC use collected to account for potential bias. Each participant performed a set of movements known to provoke ILED.

To test each foot position classification algorithm, we defined a figure of merit (FOM) to emphasize the importance for true positive detection (Table 1).

TABLE I: TERMS USED IN ALGORITHM FIGURE OF MERIT

Term	Name	Description
α	True Negative	Correctly detected as misplaced
β	True Positive	Correctly detected as correctly placed
K	False Positive	Incorrectly detected as correctly placed
γ	False Negative	Incorrectly detected as incorrectly placed
L	Frame Length	Number of frames in recording
M	Normalization Constant	Maximum value the fitness function produces for a completely accurate detection

The FOM, σ, with range [-1 1] was calculated as:

$$\sigma = \frac{\frac{\alpha - K}{L} - \left(\frac{\gamma}{L}\right)^2 + \left(\frac{\beta}{L}\right)^3}{M}, \quad M = \frac{\alpha_{max}}{L} + \left(\frac{\beta_{max}}{L}\right)^3.$$

Six algorithms were evaluated with the human dataset. Five algorithms were developed heuristically based on a priori knowledge of safe foot position and general foot shape and pressure distribution (Fig. 1). A cubic k-nearest neighbors (KNN) algorithm was also studied to evaluate the potential accuracy improvement in using a machine learning approach. The KNN essentially considers the correlation of a given footplate state to known states within its training set.

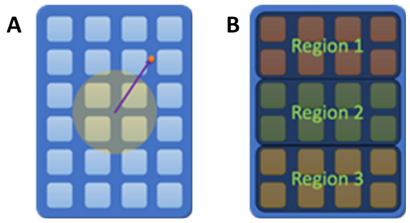

Figure 1: A centroid algorithm (A) was evaluated in addition to algorithms which compared differences between FSR regions on the footplate (B), as well as others.

RESULTS AND DISCUSSION

The mean FOMs, accuracies, and positive detection rates (PDR) for each algorithm were calculated (Table 2). The PDR described the percentage of ILED properly detected by each algorithm, as opposed to the percentage of all frames properly detected that the accuracy represents.

TABLE II. AVERAGE ALGORITHM PERFORMANCE MEASURES

	Mean	Centroid	Relative
FOM	0.62±0.10	0.25±0.16	0.20±0.13
Accuracy	84.2±4.1%	68.8±7.4%	67.2±6.3%
PDR	77.5±6.8%	29.5±10.5%	48.8±7.8%
	Ratio	**MSE**	**KNN**
FOM	0.29±0.12	0.37±0.10	0.78±0.08
Accuracy	70.7±5.0%	72.9±4.5%	95.3±2.7%
PDR	51.6±8.1%	63.0±8.2%	90.5±3.9%

The algorithms which relied on information from Region 2 (Fig 1.) of the force matrix tended to score lower. This may be due to the geometry of the footplate surface and the user's footwear. These algorithms worked under the assumption that the user's foot makes full contact with all regions of the footplate surface, which may not be the case depending on footwear. For example, when the arch of the user's shoe spanned Region 2 of the footplate, as prevalent with athletic shoes and shoes with heels, the center portion did not make contact. When the threshold value for Region 2 was decreased for these algorithms, an improvement in determining ILED correctly was obtained.

The Centroid algorithm had the lowest FOM, but also had the highest standard error, indicating a higher variance in the recorded values. Even considering the standard error, the PDR of the Centroid algorithm was the lowest out of all tested algorithms. It's possible this may be attributed to footwear geometry, or the Centroid calculations may be inaccurate due to the low resolution of the force sensing matrix.

CONCLUSION

As compared to the manually programmed algorithms which only required a few cycles of computation time, the machine learning model required approximately 40-60 ms for classification on a modern mobile device (Apple iPod Touch). When this level of computational power is available, machine learning algorithms like KNN are feasible in a real-time application. However, implementing the algorithm on the low-power microcontroller running the FootSafe system was not feasible. Feature reduction could potentially reduce the computational burden of the ML algorithm. The KNN model consistently outperformed the other algorithms, however, the KNN model would be significantly more complex to implement in a real-time classification task due to the large number of features and calculations required. Of the simpler algorithms, the Mean and MSE approaches showed reasonable performance.

REFERENCES

1. Paparone, P., et al. *Geriatric Nursing, 34(1), 2013.*
2. Simpson, R.C., et al. *Journal of Rehabilitation Research and Development, 45(1), 2008.*
3. Majerus, S.J.A, et al. *IEEE Eng. in Med. and Biology Soc, Proceedings, pp. 4367–4370, 2018.*

Accuracy of Cranial and Brain Morphometric Measurements across Parasagittal Planes as compared to Midsagittal Plane Measurements on Adult Females with Chiari I Malformation

Authors: [1]Mark Morkos, [1]Maggie Eppelheimer, ,[1]Blaise Nwotchouang , [1]Dorothy Loth, [1]Francis Loth
[1]University of Akron, Akron, OH, USA

Introduction: Chiari malformation type I (CMI) is a neurological condition, typically characterized by cerebellar tonsils that extend below the foramen magnum at the base of the skull. CMI patients often experience a range of symptoms which could include neck pain, balance problems and numbness. The current process of diagnosis involves evaluating MR images, and morphometric measurements from a reconstructed midsagittal image of the brain. The objective of this study is to determine whether MR images obtained at either left or right of the midsagittal plane of the brain significantly affect morphometric measurements.

Materials and Methods: A total of thirty female individuals were involved in this study, ranging from 23 to 55 years. All of the MRI slices evaluated were taken before any surgical procedures were performed. The MRI images were obtained from the Chiari 1000 database collected by the Conquer Chiari Research Center in Akron, Ohio. MRI sequences were imported into a DICOM medical image viewer (Horos). The sequences were segmented using a segmentation tool that allows slices at specified intervals along the coronal plane to be obtained. This segmentation tool is shown in Figure 2. For the first part of the study, five cases were segmented to obtain, for each case, a total of 21 slices, one at the midsagittal and ten at 1mm intervals away from the midsagittal towards the left side of the midsagittal plane, and ten at 1mm intervals towards the right side of the midsagittal plane. For the second part, an additional twenty-five cases were segmented to obtain, for each case, five slices, one at the midsagittal, two at 1mm and 2mm away to the left, and two at 1mm and 2mm away to the right of the midsagittal plane. After obtaining the individual slices, a set of 14 morphometric measurements were obtained for each slice, using a custom in-house software developed in MATLAB (MathWorks, Natick, MA) at the University of Akron.

Results and Discussion: Statistical analysis was performed on the morphometric data obtained. Firstly, the first set consisting of five cases was analyzed using a MATLAB code to find the difference between each morphometric measurement at consecutive slices (1mm,2mm,3mm,.. etc.) and at the midsagittal, then this difference was compared to the mean difference between Chiari and control patients outlined in 'A morphometric assessment of type I Chiari malformation above the McRae line' (Houston et al., 2018). The parasagittal distance at which the measured error exceeds the mean difference between Chiari and controls was identified, and then an average parasagittal distance for each of the 14 measurements was calculated using data from the five cases. Secondly, symmetry analysis plots were created using the measured data at 1mm intervals to evaluate symmetry of each of the 14 measurements on either side of the midsagittal up to 10mm on each side. Statistical analysis was then performed on the second set consisting of 25 cases to calculate the average absolute differences between parasagittal and midsagittal planes up to 2mm on each side and compare it to the average difference between Chiari and controls. Lastly, the difference between measurements at 1mm and 2mm and at the midsagittal was analyzed by performing a t-test analysis on the set of 25 cases.

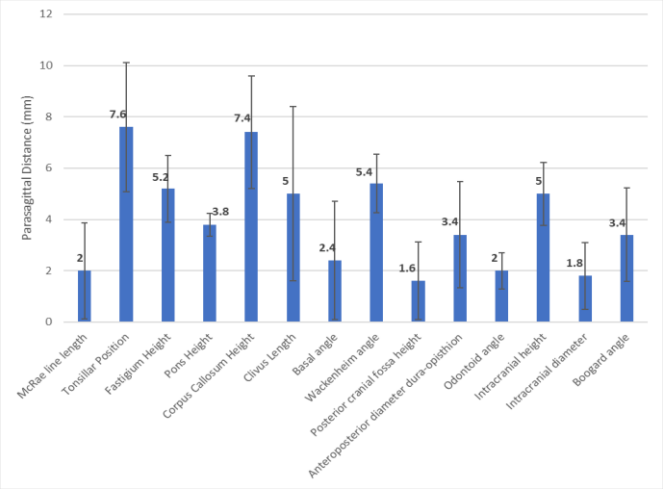

Figure 1. The average parasagittal distance (distance between parasagittal and midsagittal planes) at which the measured error (difference between parasagittal and midsagittal measurement of a given parameter) exceeds the mean difference between Chiari and controls for that given parameter.

Conclusions: For years, morphometric measurements were obtained at the midsagittal plane because it is identifiable, however no studies were focused upon the importance of this plane, and the degree to which measurements vary away from it. This study identified the morphometric measurements that vary the most away from the midsagittal, and the parasagittal distance away from the midsagittal within which an operator can make accurate morphometric measurements.

References:

1. Houston, J et al., *A morphometric assessment of type I Chiari malformation above the McRae line: A retrospective case-control study in 302 adult female subjects*. 2018

THE EFFECT OF COMPRESSION GARMENTS ON HIP AND KNEE KINEMATICS DURING A SWIM START

[1]Shraddha Sudhir, B.S., [1]Brenda J. Peters, PhD, [1]Amy M. McCormick, DNP, ARNP, CPNP-PC, and [1]Rhiannon M. Seneli, PhD, ATC.

[1]St. Ambrose University, Davenport, IA, USA

Email: sudhirshraddha@sau.edu

INTRODUCTION

The use of compression technical swimsuits in swimming has become very prevalent because of their hydrodynamic nature and their ability to reduce drag forces. With their evolution and consistent success at world championships and the Olympics, several top brands are constantly improving and redesigning these technical swimsuits with an aim to increase the swimmers' efficiency and performance. With most research focused on the hydrodynamic and physiological effects these swimsuits provide, there has not been sufficient research on the effects of compression during a swim race and start. The mobility of joints in a swimmer's race is very crucial in terms of not causing discomfort to the swimmer, allowing for a full range of motion, while reducing the risk of injury.

Combined with this, the significance of the swim start in the swim race has become apparent and crucial. The swim start offers the initial kinetics and kinematics needed to help gain momentum for the race. With a paucity of data identifying the biomechanical effects of compression garments, it becomes crucial to investigate the biomechanics of a swimmer at various parts of the swim race with a compression swimsuit.

It was thus the purpose of this study to investigate the effect of compression garments on hip and knee kinematics during the push off phase of the swim start. To help conduct this in a water-free environment, countermovement jumps were employed as an alternative to the swim start. It was hypothesized that the compression swimsuit will result in increased jump height, increased hip flexion, decreased knee flexion and decreased hip and knee velocity and decreased hip and knee acceleration.

METHODS

A sample of 20 collegiate swimmers, 10 males and 10 females, (mean age, 20.4 ± 1.3 years) were included in this study. Participants with any prior surgeries or lower extremity injuries in the 6 weeks prior to the study were excluded from the study.

Each swimmer performed three countermovement jumps in two conditions, one with a practice swimsuit and one with a technical compression swimsuit. Three-dimensional hip and knee kinematics were collected using inertial measurement units (myoMotion, Noraxon, Scottsdale, AZ) placed on the sacrum, and bilaterally on the thigh, shank, and foot segments. Jump height was also recorded using a Vertec. Each participant was tested in a single session and the order of the condition was randomized. Alpha was set at .05.

RESULTS AND DISCUSSION

Jump height significantly increased from 42.74 ± 13.7 cm with normal swimsuits to 44.55 ± 14.8 cm ($P<0.01$) with compression swimsuits (*Figure 1*). Additionally, compression swimsuits resulted in a significantly decreased hip flexion from 89.1 ± 12.1° to 77.3 ± 13.6° ($P<0.01$)), and significantly increased peak knee extension velocity from 1079 ± 192°/s to 1174 ± 242°/s ($P=0.03$) during the push-off phase of the countermovement jump (*Table 1*).

No statistically significant differences between the two conditions were found in peak knee flexion,

maximal hip extension velocity, maximum hip acceleration and maximum knee acceleration.

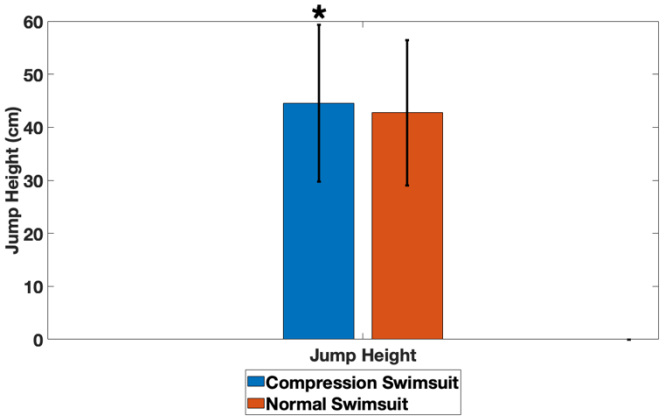

Figure 1. Average jump heights of swimmers in the compression swimsuit (blue) and normal swimsuit (red).
* Indicates a significance difference in jump height from the normal swimsuit condition ($p<0.01$).

Table 1: Peak hip flexion and maximum knee extension velocity values (average ± SD) during the push off phase of the countermovement jump during two conditions- Compression Swimsuit and Normal Swimsuit.

Parameter	CS	NS
Hip Flexion	77.3 ± 13.6°	89.1 ± 12.1°
Knee Extension Velocity	1174 ± 242°/s	1079 ± 192°/s

* Indicates a significance difference in jump height from the NS condition ($p<0.05$).

The elastic component in the swimsuit could have helped produce an increased propulsive force that resulted in an increased jump height [1]. The increased knee extension velocity found in this study could be a direct result of the antagonist co-contraction of the biarticular muscles that span both the hip and knee joint. The decreased hip flexion with compression swimsuits found in this study could suggest a potential injury prevention effect of compression swimsuits and this kinematic alteration could indicate a potential change in motor control strategy [2]. The more popular explanation today for the change in mechanics with compression garments is their proprioceptive abilities. Research has shown indication towards compression garments having the ability to improve awareness of joint position in space and thereby alter muscle contraction [3].

CONCLUSION

Investigating the effect of compression garments on knee kinematics and kinetics can provide valuable insight on the other effects technical swimsuits have on the swimmer's race. Prioritized for its hydrodynamic drag resistance, the effect the technical swimsuits have on joint kinematics and kinetics can prove to be of great importance in the future engineering of compression swimsuits. This study, having investigated the effects of compression garments on hip and knee kinematics found a significant increase in jump height, decrease in peak hip flexion, and increase in peak knee extension velocity while performing the countermovement jumps with the compression swimsuits. More studies are required to further investigate the effects of compression swimsuit on the kinematics and kinetics of a swimmer during the various phases of the swim race. This will not only help evaluate the injury risk to a swimmer but could also help improve performance and better engineer technical swimsuits.

REFERENCES

1. Doan, B, et al. *Journal of Sport Science.* 601-610, 2003.

2. Zamporri, J, et al. *Orthopedic Journal of Sports Medicine.* 2018

3. MacRae, B, et al. *Sports Medicine*. 1-29, 2011.

ACKNOWLEDGEMENTS

I would like to thank my advisor Dr. Rhiannon Seneli for being extremely supportive and patient with me throughout this study. I would also like to thank my secondary advisor Dr. Brenda Peters and my Honors reader Dr. Amy McCormick for their valuable feedback and guidance. Finally, I would like to thank the SAU Honors Program for funding software and materials needed for this study.